

**Investigation of Tribological Performance of Ti-6Al-4V Alloy
Processed by Selective Laser Melting and Electron Beam
Melting Processes**

Hua Li

A thesis submitted to Auckland University of Technology in fulfilment of the requirements for
the degree of Doctor of Philosophy (PhD)

2021

School of Engineering, Computer and Mathematical Sciences

Abstract

Powder bed fusion (PBF) additive manufacturing (AM) or 3D printing, either laser based or electron beam based, is a recent advanced manufacturing process and is being more widely applied industrially. Ti-6Al-4V alloy is a printable alloy and is the most commonly used alloy in PBF-AM for a wide range of applications. However, microstructures of the alloy manufactured by different processes are different and properties including tribological properties relating to the different microstructures need to be well understood. Furthermore, relevant to wear resistance of PBF processed Ti-6Al-4V alloy, applying physical vapor deposition (PVD) coating and ion implantation surface treatment commonly applied to conventional processed Ti-6Al-4V parts need to be evaluated for AM parts. Thus, through a comprehensive series of wear testing and analysis, this study aims to understand the tribological behaviors of the Ti-6Al-4V samples processed by PBF and further by surface treatments.

Dry linear reciprocating (sliding) wear tests were conducted to evaluate how wear rate (WR) of the alloy samples processed differently by selective laser melting (SLM), electron beam melting (EBM) and processed conventionally (CP) may differ under room temperature or elevated temperatures. The tests were conducted with a wide range of test conditions using WC-Co as counter material. Furthermore, dry sliding wear tests were conducted on PVD TiN coated and nitrogen ion implanted samples processed either by SLM or by CP, also using WC-Co as counter material. After wear testing, wear rates were measured and surface and cross-sectional features of wear tracks were examined in detail.

Results have shown the expected increase in WR as applied normal load increases, but the dependence of WR on sliding frequency has been found very weak. The major finding is that WR is not affected by the alloy processed in different manufacturing routes having different microstructures and hardness values. It will be shown that under a same wear test condition for the three different samples, their deformation behaviors leading to fracture and thus wear loss differ significantly. It will be reasoned that WR does not only depend on strength and thus hardness, but also ductility of the alloy.

It has been observed that test temperature has not affected WR significantly, although it appears that the wear debris layer has become richer in oxygen content as test temperature increases. Thus, it will be suggested that although a higher testing temperature may soften the sample, a more stable oxide layer as temperature increases is more wear resistant.

TiN PVD coating has provided a significant protection of wear for both SLM and CP samples. It has been found that local fracturing of TiN coating after being thinned to 0.4-0.5mm in both coated SLM and CP samples is similar. The major wear mechanism leading to a gradually rapid increase in wear rate of the coated samples will be demonstrated through a wear process as thinning and local fracturing of the coating before the widening of the wear track, while substrate deformation underneath the coating for the case of the low hardness substrate will be illustrated affecting little the overall wear rate.

Surface treatment by nitrogen implantation however has not provided a significant effect on increasing wear resistance of SLM and CP samples. Nanoindentation test data have revealed that, overall, the implantation has not resulted in a significant increase in hardness even in the top layer of 200-300nm. Thus, it is suggested that the implantation treatment used in this study has not resulted in forming a wear resistant layer and thus has an insignificant effect on WR.

List of Publications

- [1] H. Li, M. Ramezani, and Z. W. Chen, “Dry sliding wear performance and behavior of powder bed fusion processed Ti–6Al–4V alloy,” *Wear*, vol. 440–441, no. July, p. 203103, 2019.

- [2] H. Li, Z. W. Chen, and M. Ramezani, “Wear behaviors of PVD-TiN coating onTi-6Al-4V alloy processed by laser powder bed fusion or conventionally processed,” *Int. J. Adv. Manuf. Technol.*, vol. 113, no. 5–6, pp. 1389–1399, 2021.

- [3] H. Li, Z. W. Chen, H. Fiedler, and M. Ramezani, “Wear behaviour of n ion implanted ti-6al-4v alloy processed by selective laser melting,” *Metals (Basel)*., vol. 11, no. 10, 2021.

Acknowledgement

First of all, my deepest gratitude goes to my primary supervisor Associate Professor Maziar Ramezani and co-supervisor Professor Zhan Chen. I really appreciate the opportunity you granted me to have PhD study experience, which has changed my whole life. Your consistent supports and guidance were the most essential to my PhD study and research. Your patience and encouragement were the biggest motivation whenever I came up against difficulties. Without your constant and illuminating instructions, this thesis could not have been achieved in its present form.

Second, I would like to express my heartfelt thanks to AUT lab technicians especially Yuan, Mark, Ross, Stephen, etc., they have granted their great help to facilitate my experimental research work. I would also appreciate AUT that provides us such advantageous research environment and gave me a fantastic overseas study experience and countless colorful and treasurable memories.

My sincere thanks also go to my husband Minglei Li, thanks for your whole year's company when the stressful life came from my new job, the anxiety mood resulted from writing thesis, and the inconvenient circumstance taken from COVID-19. You always behaved by not too many words, but by an understanding heart with firmly holding my hands and providing me the warmest and the most stable life to let me focus on writing.

Last but not least, I cannot find any proper words to express my gratitude to my parents. No matter how far away I live from you, your deepest love is engraved in my heart and makes me brave and confident forever. Whenever I experience rain and wind outside, you are always my peacefully warm harbor and give me eternal acceptance and tolerance.

In addition, the most special person I would like to express my wish to is my cute daughter Chengxue Yang, you always occupy the softest place in Mom's heart, please strengthen your heart, be brave, as healthy and happy as possible when growing up and passing your whole life.

Table of Contents

Abstract	ii
List of Publications.....	iv
Acknowledgement	v
Table of Contents	vi
List of Figures.....	ix
List of Tables.....	xvi
Nomenclature.....	xvii
Attestation of Authorship.....	xix
Chapter 1 Introduction.....	1
1.1 Titanium and titanium alloys.....	1
1.2 Powder bed fusion (PBF) additive manufacturing.....	3
1.3 Powder bed fusion of Ti-6Al-4V.....	6
1.4 Aim of the research and thesis structure.....	8
Chapter 2 Literature Review	9
2.1 Wear, wear mechanisms and sliding wear testing of metallic alloys	9
2.1.1 Wear and basic wear processes	9
2.1.2 Typical wear types	10
2.1.3 Methods of evaluating wear	14
2.2 Wear behaviors of PBF and conventional processed titanium alloys	16
2.2.1 Wear behaviors of conventional processed titanium alloys under room temperature	16
2.2.2 Wear behaviors of PBF Ti-6Al-4V alloys under room temperature.....	18
2.3 Wear of titanium alloys at elevated temperatures.....	23
2.3.1 Wear behavior of conventional processed titanium alloys at elevated temperatures	23
2.3.2 Wear behavior of PBF Ti-6Al-4V at elevated temperatures	30
2.4 Wear performance of PBF Ti-6Al-4V alloy surface treated by PVD coating and ion-implantation	32
2.4.1 Wear performance of PBF Ti-6Al-4V alloy surface treated by PVD coating.....	32
2.4.2 Wear behavior of nitrogen ion implanted Ti-6Al-4V alloy	39

2.5 Summary of the literature review and research questions.....	46
Chapter 3 Research Methodology.....	49
3.1 Samples, counter material and wear test equipment.....	49
3.2 Sample preparation and nanoindentation.....	52
3.3 Tests conditions.....	54
3.4 Wear measurement.....	55
Chapter 4 Dry Wear Behavior of SLM, EBM and CP Samples.....	58
4.1 Wear rate.....	58
4.1.1 Wear rate as a function of applied load.....	58
4.1.2 Wear rate as a function of sliding frequency.....	59
4.2 Wear track surface appearance.....	61
4.3 Cross sectional features of wear tracks and shear layer.....	64
4.3.1 Cross sectional features.....	64
4.3.2 Shear layer.....	65
4.4 Wear mechanisms governing the measured wear rates.....	71
Chapter 5 Effect of Temperature on Wear Behavior.....	77
5.1 Wear rate at various test temperatures.....	77
5.2 Wear track appearance and wear debris on track surface.....	81
5.3 Further analysis on wear debris and oxide in cross sections.....	85
5.4 Chapter Summary.....	92
Chapter 6 Wear Behavior of PVD-TiN Coated SLM and CP Samples.....	94
6.1 Wear volume data.....	94
6.1.1 Initial data for comparison with uncoated samples.....	94
6.1.2 Wear volume, wear depth and wear width vs. sliding distance/time.....	95
6.2 Track surface, thinning and breaking of coating, and substrate wear.....	100
6.3 Mechanism and subsequence of coating protection and deterioration.....	105
Chapter 7 Wear behavior of nitrogen ion implanted SLM and CP samples.....	107
7.1 Wear test data and track examination.....	107
7.1.1 Comparative wear rate data.....	107
7.1.2 Track surface appearance.....	108

7.1.3 COF and wear process	111
7.2 Further analysis on effect of ion implantation on wear.....	114
7.2.1 Hardening profile resulting from ion implantation	114
7.2.2 Effectiveness of ion implantation on wear reduction	116
Chapter 8 Conclusions.....	117
References	120
Appendix.....	131
Appendix 1 Whole wear tracks from top view	131
Appendix 2 Cross-sections of worn tracks	142

List of Figures

Fig. 1.1 Titanium alloys categories by phases [7]	2
Fig. 1.2 The schematic of SLM process.....	4
Fig. 1.3 Schematic of an Arcam A2XX EBM machine [24]	5
Fig. 1.4 Ti-6Al-4V continuous cooling transformation curve [7]	7
Fig. 1.5 SEM micrographs of (a) SLM sample showing α' martensitic structure, (b) EBM sample showing lamellar $\alpha+\beta$ structure, and (c) CP sample showing fine and irregular β particles in α -matrix.....	7
Fig. 2.1 Schematic illustration of a hard object forcefully sliding against the surface of a body with lower hardness, indicating various features of stress-strain leading to fracture and material loss.....	10
Fig. 2.2 Adhesive wear.....	11
Fig. 2.3 Abrasive wear.....	12
Fig. 2.4 Fatigue wear.....	12
Fig. 2.5 SEM images of a wear test for Ti-6Al-4V alloy (a) wear debris and (b) wear track; EDX spectrum and inserted XRD patterns of two locations indicated in (a) are shown in (c) and (d), respectively [24]	14
Fig. 2.6 The schematic of ball-on-plate linear reciprocating sliding wear test.....	15
Fig. 2.7 Schematic diagram of rotary pin-on-disk wear tester.....	16
Fig. 2.8 Wear rate versus sliding speed for Ti-6Al-4V alloy sliding against EN31 steel under different loads with dry condition [48]	18
Fig. 2.9 SEM images of the Ti-6Al-4V worn surfaces under different wear conditions (a) dry sliding condition, (b) water lubricated condition, (c) dry sliding condition but the location is at the ends of the worn track [39]	18
Fig. 2.10 Vickers hardness of Ti-6Al-4V specimens obtained by casting, HP (Hot Pressing) and SLM (a); the specific wear rates of these samples when sliding against Al_2O_3 ball (b) [51]	19
Fig. 2.11 Microhardness (a), and wear volume (b) of horizontal and vertical built specimens at different loads [52]	20
Fig. 2.12 Specific wear rates and Vickers hardness of EBMed and conventional processed	

Ti-6Al-4V samples (a) [24] ; specific wear rates of conventional processed and EBMed Ti-6Al-4V samples tested under the same conditions (b) [53].....	20
Fig. 2.13 Hardness and wear rate of Ti-6Al-4V samples fabricated by forging, SLM and EBM [55]	21
Fig. 2.14 Cross-sections of Ti-6Al-4V alloy produced by (a) forging, (b) SLM and (c) EBM [55]	21
Fig. 2.15 Wear rate results for the Ti-6Al-4V samples in contact with brass (a) and 38CrMoAl (b) [56]	22
Fig. 2.16 Vickers hardness distribution away from the worn surface of Ti-6Al-4V in contact with 38CrMoAl [56]	22
Fig. 2.17 SEM images of cross sections of (a) CP, (b) as prepared SLM, and (c) heat treated SLM samples in contact with 38CrMoAl [56]	22
Fig. 2.18 Wear rates of Ti-6Al-4V alloy as a function of temperature and load [44]	24
Fig. 2.19 SEM images of worn surfaces of Ti-6Al-4V alloy sliding under various conditions: (a) 200°C, 100 N, (b) 400°C, 100N; (c), (d) are their cross-sections respectively [44]	25
Fig. 2.20 Wear rate versus applied load for titanium alloy under various test temperature conditions [43]	26
Fig. 2.21 Morphology, EDS line analysis and XRD patterns of tribo-layers under sliding wear tests: at room temperature (a, b); at 600°C (c, d); first sliding at 600°C and then sliding at room temperature (e, f) [43]	26
Fig. 2.22 Tribo-layers typical status of: (a, b) sliding at room temperature, 150 and 250N, respectively; (c, d) sliding at 600°C, 150 and 250N, respectively [43].....	27
Fig. 2.23 Wear rate versus temperature of Ti-6Al-4V alloy pin when sliding against SS316L disk in vacuum condition [64]	28
Fig. 2.24 SEM images of mechanically mixed layer (MML) when the tests were conducted at 25°C (a), 100°C (b), 200°C (c), 300°C (d), 400°C (e) [64]	29
Fig. 2.25 Volume wear rate and depth of wear profiles versus temperature when WC-6Co pin slides against Ti-6Al-4V disk [65]	30
Fig. 2.26 Elemental composition profiles of cross-sectional view of Ti-6Al-4V, (a) 320 °C, (b) 920 °C [65]	30

Fig. 2.27 Wear rate versus temperature when steel or alumina counter ball sliding against EBM Ti-6Al-4V disk (error bars represents standard deviations) [66]	31
Fig. 2.28 Friction coefficient versus traversals during multi-scratch test on TiN coated Ti-6Al-4V; a SEM image inside showing worn surface morphology with micro cracking and delamination of TiN films after 400 passes [69]	33
Fig. 2.29 Wear volumes measured for untreated Ti-6Al-4V and TiN-coated TPN and TPON samples, tested against WC-Co at a normal load of 13.5N [70]	34
Fig. 2.30 SEM image of the wear track (a) and corresponding X-ray maps of elemental distribution (b) to (f) for the wear test of CrN/NbN-coated Ti-6Al-4V sliding against SAE52100-EN100Cr6 steel under 40N applied load [71]	35
Fig. 2.31 Cross-section of the TiN PVD coated Ti-6Al-4V sample [72]	35
Fig. 2.32 Optical microscope (a) and SEM (b)–(e) images of wear track obtained for TiN coated Ti-6Al-4V alloy after 263.7 m sliding distance in dry condition [72]	36
Fig. 2.33 SEM cross-sectional micrographs of: (a) 3DT, (b) N3DTs, (c) CN-N3DTs and (d) DLC-N3DTs [74]	38
Fig. 2.34 Wear depths of all specimens when sliding against 316L, Si ₃ N ₄ and 3DT balls. (S.D. denotes standard deviation) [74]	38
Fig. 2.35 SEM images for wear surfaces on: (a) DLC-3DT, (b) DLC-3DT (1000×), (c) DLC-N3DTs and (d) DLC-N3DTs (1000×) when sliding against 3DT ball, and the EDS analysis results for the regions marked in the corresponding Figures (labelled 1 or 2), respectively [74]	39
Fig. 2.36 Ion implantation beam scanner [77]	40
Fig. 2.37 Schematic of ion-solid interactions [77]	41
Fig. 2.38 Knoop surface microhardness of Ti-6Al-4V alloy with and without ion implantation [79]	42
Fig. 2.39 AFM image of worn Ti-6Al-4V surface (a) and N ⁺ ion-implanted Ti-6Al-4V surface (b) [79]	42
Fig. 2.40 Adhesion work variation of implanted Ti-6Al-4V [84]	43
Fig. 2.41 Relation between load and penetration depth of indenter [88]	45
Fig. 2.42 Wear values of implanted and unimplanted samples after 2000 cycles [86]	45

Fig. 2.43 Mean wear of Ti Grade 5 samples with standard deviations [87]	45
Fig. 3.1 Micro-hardness tester	51
Fig. 3.2 Linear reciprocating tribometer	52
Fig. 3.3 Cross sections of PVD TiN coated on: (a) SLM martensitic and (b) CP $\alpha+\beta$ Ti-6Al-4V samples	53
Fig. 3.4 Simulated nitrogen concentration vs. depth for the two implantation processes	53
Fig. 3.5 Curves for nanoindentation test of a SLM N2 ion-implanted sample	54
Fig. 3.6 Olympus SZX9 stereomicroscope	56
Fig. 3.7 A sectional profile for a CP sample wear track tested under 200°C and 2N load	56
Fig. 3.8 Hitachi SU-70 field emission scanning electron microscope (FE-SEM)	57
Fig. 4.1 Values of WR plotted as a function of test load	58
Fig. 4.2 Values of WR plotted as a function of test frequency	59
Fig. 4.3 COF values plotted as a function of time for test conditions: (a) 6N at 5Hz and (b) 10N at 2Hz	60
Fig. 4.4 Appearances of selected wear tracks showing various track features, (a) SLM sample tested at 2Hz and 6N - straight track, (b) CP sample tested at 2Hz and 6N - straight track with edge pieces, (c) SLM sample tested at 5Hz and 2N - width variation, and (d) EBM sample tested at 8Hz and 6N - width and height variations	62
Fig. 4.5 Measured depth, calculated depth and calculated wear volume plotted vs. track width	63
Fig. 4.6 Average measured width and standard deviation values plotted as a function of (a) test load and (b) test frequency	64
Fig. 4.7 Cross sectional SEM micrographs showing: (a) SLM sample tested at 2Hz and 6N - little debris, (b) CP sample tested at 2Hz and 6N - discontinuous debris layer, (c) SLM sample tested at 5Hz and 2N - uneven and discontinuous debris layer, and (d) EBM sample tested at 8Hz and 6N - uneven and discontinuous debris layer	65
Fig. 4.8 Examples of surface cross sections of tested samples (a) SLM sample tested at 2Hz and 6N, (b) EBM sample tested at 5Hz and 6N and three EDS spectra of points as indicated and (c) CP sample tested at 5Hz and 2N	66
Fig. 4.9 SEM images of wear debris from tests conducted at $F_N=6N$ and with $f=5Hz$ using (a)	

SLM, (b) EMB and three EDS spectra of points as indicated, and (c) CP samples.....	68
Fig. 4.10 An illustration of shear strain in shear layer, (a) shear distance in the shear field measured in the micrograph in Fig. 4.8(b) and (b) increase in shear strain towards the Ti-6Al-4V/debris interface.....	70
Fig. 4.11 Values of shear layer thickness (h_{sh}) plotted as a function of (a) F_N with $f=5$ Hz and (b) f with $F_N = 6$ N, for SLM, EBM and CP samples as indicated.....	71
Fig. 4.12 Schematic illustration of (a) sliding wear test with forces, shear stress-strain ($\tau_{ad}-\gamma_{ad}$) field causing adhesive wear, shear layer thickness (h_{sh}), and stress-strain ($\sigma_{ab}-\epsilon_{ab}$) causing abrasive wear indicated, (b) stress-strain curves of Ti-6Al-4V alloy, and (c) stress (σ_n) corresponding to hardness value of the alloy.....	72
Fig. 5.1 Values of WR plotted as a function of test loads (a) and test temperatures (b).....	78
Fig. 5.2 Measured (a) track depth and (b) track width plotted as a function of test temperature. In (b) standard deviation values are also plotted.....	80
Fig. 5.3 SEM images and EDS spectra of the SLM sample tested at 400°C and 6N: (a) the whole wear track with area outlined/shown in a higher magnification and a further high magnified area marked 'A' selected for EDS analysis and (b) EDS spectra from points (1, 2, and 3) marked in the SEM image (of area 'A')	81
Fig. 5.4 Whole wear track SEM images of EBM sample tested at 400°C and 6N observed from top (top image) and mid cross section (bottom image)	83
Fig. 5.5 Whole wear track SEM images of CP sample tested at 400°C and 6N, observed from top.....	84
Fig. 5.6 Whole wear track SEM images of EBM sample tested at 200°C and 10N, observed from top.....	84
Fig. 5.7 Whole wear track SEM images of SLM sample tested at 600°C and 2N, observed from top.....	84
Fig. 5.8 SEM cross sectional images and EDS spectra from analysis of points (1, 2, and 3) marked in the SEM image of SLM samples tested at (a) 200°C, (b) 400°C and (c) 600°C, and under the test load of 6N.....	85
Fig. 5.9 SEM cross sectional images and EDS spectra from analysis of points (1, 2, and 3) marked in the SEM image of EBM samples tested at (a) 200°C, (b) 400°C and (c) 600°C, and	

under the test load of 6N.....	87
Fig. 5.10 SEM cross sectional images and EDS spectra from analysis of points (1, 2, and 3) marked in the SEM image of CP samples tested at (a) 200°C, (b) 400°C and (c) 600°C, and under the test load of 6N.....	89
Fig. 5.11 Oxide content determined by EDS-ZAF analysis on wear debris in cross sectional samples plotted vs. tested temperature.....	92
Fig. 6.1 Wear rate for SLM and CP samples with and without PVD coating.....	95
Fig. 6.2 Measured data of (a) WV, (b) h_{Max} and (c) W_{Track} plotted as a function of time for the two types of coated samples. In (b), a horizontal line representing $h_{Coating}$, outline of group 1 data with $h_{Max} < h_{Coating}$, outline of group 2 data with $h_{Max} > h_{Coating}$, a regression line labelled as h_C based on data below $h_{Coating}$ line are drawn.....	96
Fig. 6.3 Coefficients of friction during testing of SLM samples for (a) 900s, (b) 2219s and (c) 5000s.....	96
Fig. 6.4 A trace from the profilometry measurement for a CP sample wear track with sliding wear stopped at 2747s. Line A is the suggested base line and curve B is the suggested trace for the condition that the coating had not fractured in the central location.....	98
Fig. 6.5 Schematic illustration of a cross section of a wear track showing h_C ($=h_{Max}$ when $h_C < h_{Coating}$). Note: W_{Track} and h_{Max} are not drawn in proportion.....	99
Fig. 6.6 Measured and calculated (a) depth and (b) wear volume plotted against track width for both SLM and CP samples.....	99
Fig. 6.7 SEM images of track surfaces of SLM samples tested for (a) 900s and (b) 2219s, (c) 2268s and (d) 5000s.....	100
Fig. 6.8 SEM micrographs of track cross sections of SLM samples tested for (a) 900s, (b) 2105s, and (c) 2219s, (d), (e) and (f) are high magnification micrographs in local area marked with a small square in (a), (b) and (c), respectively.....	102
Fig. 6.9 SEM images of track surfaces of CP samples tested for (a) 900s and (b) 1958s, (c) 2401s and (d) 5000s. In (a), two EDS spectra from the spots indicated as 1 and 2 are shown.....	103
Fig. 6.10 SEM micrographs of track cross sections of CP samples tested for (a) 900s and (b) 2401s, (c) and (d) are high magnification micrographs in local area marked with a small square	

in (a) and (b), respectively.....	104
Fig. 6.11 Schematic illustration of wear track before (top schematic) and after the coating having locally broken in mid track (mid schematic), respectively, and continuation of wear with the portion of coating resisting wear becoming less and less (bottom schematic)	106
Fig. 7.1 Wear rate of eight tests conducted with $F=1N$ and $f=5Hz$ for 40m and on samples with (a) N1 and (b) N2 nitrogen concentration profile after ion implantation and (c) with samples without ion implantation. Note: data with * mean their track appearances will be shown.....	108
Fig. 7.2 SEM images of SLM-N1 sample wear tracks after (a) first, (b) second, (c) third and (d) fourth experiments.....	109
Fig. 7.3 SEM images (a) and (b) in higher magnifications taken in SLM-N1 track from the second test and EDS spectra in locations of (c) point 1, (d) point 2 and (e) point 3 as indicated in (b)	110
Fig. 7.4 SEM images of wear tracks of (a) CP N1, (b) SLM N2, (c) CP N2, (d) SLM non-treated and (e) CP non-treated samples, after the first respective wear experiment.....	111
Fig. 7.5 COF plots for (a) SLM and CP N1 first tests, (b) SLM and CP N1 second tests, (c) SLM N1 the third and fourth tests, (d) SLM and CP N2 first tests, (e) SLM and CP N2 second tests, (f) SLM and CP non-treated sample first tests, and (g) SLM and CP non-treated sample second tests.....	112
Fig. 7.6 P_{Max} vs. h_{n-i} from nanoindentation measurements for various samples.....	115

List of Tables

Table 1.1 Similarity and difference of these SLM and EBM techniques.....	5
Table 1.2 The structure of SLM, EBM and CP Ti-6Al-4V and their hardness values measured from our samples.....	7
Table 2.1 Volume loss of various materials compared with Grade 2 pure titanium and Ti-6Al-4V [11]	17
Table 2.2 Thickness, hardness and oxide level of tribo-layer in Ti-6Al-4V alloy under various test conditions [44]	25
Table 2.3 Papers about ion implanted Ti or Ti-6Al-4V samples wear tests.....	44
Table 3.1 SLM process parameters.....	50
Table 3.2 EBM process parameters.....	50
Table 3.3 Micro-hardness test.....	50
Table 3.4 Sliding wear conditions.....	55
Table 4.1 Average tensile strength and elongation values from literature [25] and from manufacturer.....	72
Table 4.2 Summary of mechanical properties, and the suggested behavior during wear test...	75
Table 5.1 Compositions (at%) from semi-quantitative analysis of the three points in the SEM image and based on the EDS spectra in Fig. 5.3b.....	82
Table 5.2 Compositions (at%) from semi-quantitative analysis of the points in the SEM images and based on the EDS spectra in Fig. 5.8 to Fig. 5.10.....	91

Nomenclature

AM	additive manufacturing
bcc	body-centred cubic
CP	conventional processing
EBM=EBPBF	electron beam melting =electron beam powder bed fusion
e	engineering strain
e_f	fracture engineering strain
e_{ah}	normal engineering strain worked out from shear field
f	Frequency
F_{Sh}	shear (friction) force
F_N	normal force
hcp	hexagonal close-packed
h	wear track depth
h_{sh}	shear thickness
h_c	the track depth related to the ball diameter
h_{Max}	maximum track depth in a wear track cross section profile
$h_{Coating}$	the thickness of coating
$h_{Coat.Tr}$	the remaining thickness of a coating in the central location of a track
h_{n-i}	the depth which the indenter can penetrate during nanoindentation test
MAM	metal additive manufacturing
PBF	powder bed fusion
PVD	physical vapor deposition
P_{max}	the indenter penetrates under a specific maximum load during nanoindentation test
SLM =LPBF	selective laser melting =laser powder bed fusion
t	Time
T	test temperature
T_{Rm}	room temperature
WR	wear rate
WV	wear volume
W_{Track}	wear track width
W_{Worn}	the width of the coating having been worn
γ_{ad}	adhesive shear strain
ϵ	true strain

ϵ_{ab}	abrasive strain
ϵ_{ah}	normal strain worked out from shear field
ϵ_y	yield strain
ϵ_f	fracture strain
ϵ_{eff}	effective strain
ϵ_{max}	the maximum strain during an indentation test
σ	Stress
σ_{WT}	standard deviation of track width
σ_{ab}	abrasive stress
σ_y	yield stress
σ_f	fracture stress
σ_n	stress corresponding to hardness value
σ_{max}	the maximum stress during an indentation test
σ_{flow}	flow stress
τ_{ad}	adhesive shear stress

Attestation of Authorship

I hereby declare that this submission is my own work and that, to the best of my knowledge and belief, it contains no material previously published or written by another person (except where explicitly defined in the acknowledgements), nor material which to a substantial extent has been submitted for the award of any other degree or diploma of a university or other institution of higher learning.

Signature _____

Date: 30 July 2021

Chapter 1 Introduction

1.1 Titanium and titanium alloys

Titanium and titanium alloys, due to their high strength to weight ratio, biocompatibility, and high corrosion resistance, are widely used in many areas such as aerospace, power generation, transport industries, and biomedical applications [1-6]. Titanium alloys are specifically used in applications where lightweight but high strength materials are needed or in corrosive environments.

Pure titanium at room temperature has a hexagonal close packed (hcp) structure, which is called α -phase. α -phase can transform to a body centered cubic (bcc) structure at elevated temperature (around 900°C), called β -phase. Titanium alloys consist of alloying elements which can be the stabilizers of either the α or β phases, resulting in changes in the phase for final parts. Commercially available titanium alloys categories are divided by the contribution of the α - and β -phases, this includes (i) α alloys, (ii) near- α , (iii) α - β (including Ti-6Al-4V), (iv) near- β , and (v) β alloys. Sometimes when the alloy was cooled from above the β -phase transus temperature (around 900°C) very fast, then β -phases undergo a diffusionless transformation to the martensitic phase, α' (hcp). α' martensitic is with great interest to scientists, because a part containing α' martensitic structure has higher hardness, but with the expense of ductility [7]. Fig. 1.1 shows the categories of titanium alloys by phases and M_s/M_f shows the quite close martensitic start and finish lines.

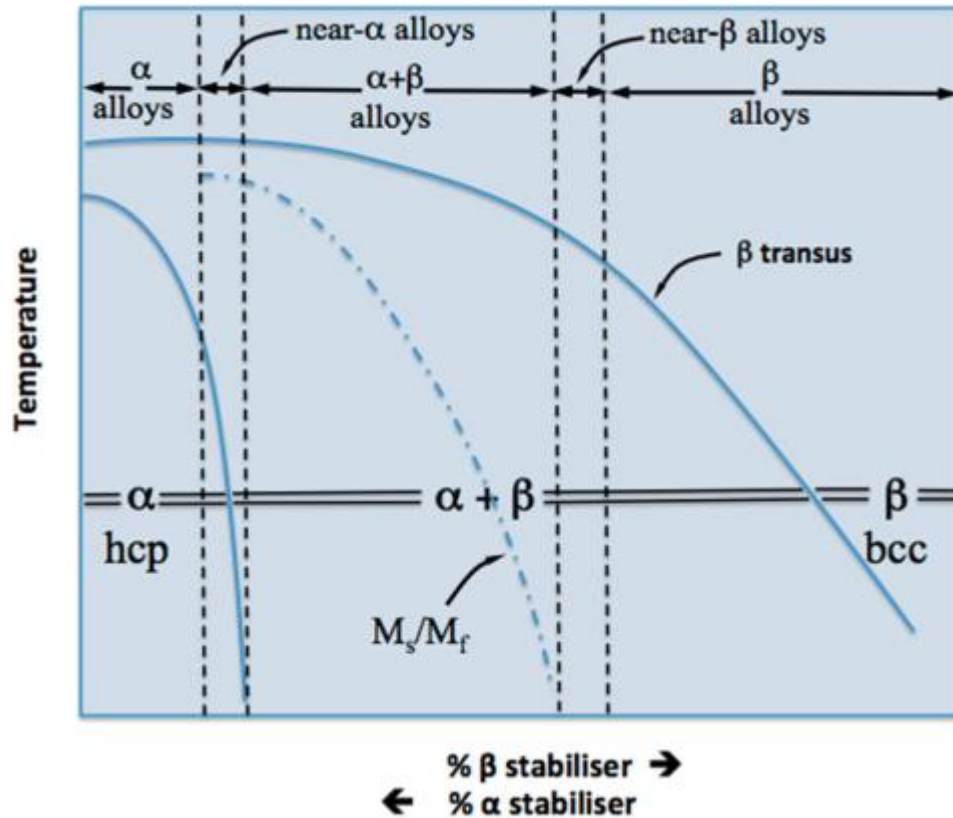


Fig. 1.1 Titanium alloys categories by phases [7].

Titanium and titanium alloys are produced in a wide variety of forms, including bars, billets, sheets and plates [8]. For load bearing applications, titanium parts will be in contact with other materials, resulting in friction and wear. Wear is a continuous damage process to the surfaces, which happens when there is a contact and a relative movement at the same time, and it is the inevitable result of friction. Wear is the largest factor (60-80%) of the three main mechanical failures (wear, fatigue and corrosion) [9]. Tribology is the science and engineering of friction, wear and lubrication in interacting surfaces in relative motion.

However, wear resistance of titanium alloys was proved to be poor due to their low shear strength and low work hardening, as well as weak surface oxides protection due to friction heat [10][11], and poor abrasion resistance [12]. For example, when titanium alloys are used in total joint replacement prosthesis, the wear debris produced by the cyclic movement of the implant might result in inflammation, pain and loosening of the implant. Also, their poor wear properties limits their applications as bone fixation materials such as bone screws, plates and similar applications [2][3]. However, if their tribological performance could be improved, they are

excellent candidates for implants inside body environment, due to their biocompatibility and corrosion resistance. The most commercially used titanium alloy (Ti-6Al-4V) was proved to have some Al and V ions released from the alloy when under wear and corrosive environment, which are found to be associated with long-term health problems [13]. By the above concerns about the tribological performance of titanium alloys, the service period when used for implants is limited to 10 to 15 years [3], and the service life and their functions for other applications are also crucially influenced by their poor tribology performance.

1.2 Powder bed fusion (PBF) additive manufacturing

Powder bed fusion (PBF) metal additive manufacturing (MAM), also known as 3D printing, is increasingly being applied in industry. This is because of their ability for manufacturing parts with highly complex shapes [14-18].

Due to the huge demands for alloy parts with complex and precise geometries, in the past decade, there has been a rapid development in powder bed fusion (PBF) additive manufacturing technologies [19]. During PBF, an energy beam fully and rapidly fuses the powder in a selective path instructed by a program that interpret parts designer's instruction in 3D CAD models [20][21]. Through geometry optimization of the parts made by PBF techniques, lighter and more complex precision parts can be produced [22]. In PBF, the energy beam can either be laser or electron beam. Thus, there are two PBF processes: laser powder bed fusion, which is also called selective laser melting (SLM) and electron beam powder bed fusion, which is also called electron beam melting (EBM). The additive principle is the same for both SLM and EBM.

Fig. 1.2 shows the schematic of SLM process. A high energy laser beam scans the powder layer based on a sliced model of a CAD file. This results in rapid melting and solidification of the metallic powder. The fabrication bed will then move down by a certain distance, and another layer of the metal powder will be deposited and the high-power laser beam scans continuously layer by layer to achieve the final part. The non-fused metal powder remains in the build chamber and can be collected and reused for the next manufacturing project. By using this laser beam welding process, it is possible to achieve a fully dense structure [23].

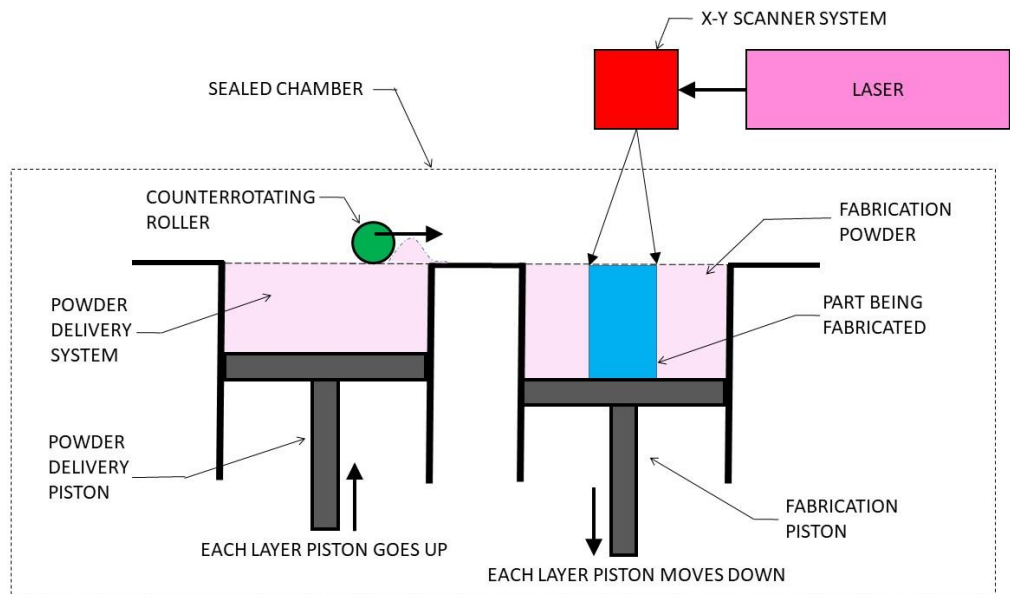


Fig. 1.2 The schematic of SLM process.

Fig. 1.3 shows the schematic of an EBM machine. EBM has the similar melting principle with SLM by using an electron beam heating source, however, the thermal environments of their chambers differ considerably. Table 1.1 lists the similarities and differences of these two PBF techniques.

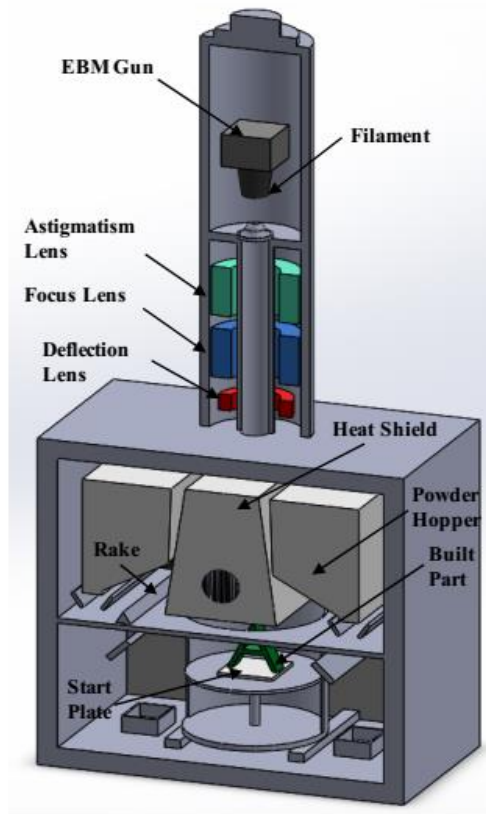


Fig. 1.3 Schematic of an Arcam A2XX EBM machine [24].

Table 1.1 Similarity and difference of these SLM and EBM techniques.

Technique	Heat source	Differences [25][26]	Similarities
SLM	Laser beam	<ol style="list-style-type: none"> 1. Lower preheat temperature (around 100°C) 2. Super-fast cooling rate (10⁵K/s or even higher) 3. With an inactive gas fill the chamber, final parts are easy to get porosity defect. 4. Due to the drastic solidified process, the final parts usually contain big residual stress. 	<ol style="list-style-type: none"> 1. Metallic powder melting. 2. Heat source scanning the metallic powder layer by layer. 3. The processing parameters (heat source parameters, hatch space, layer thickness) have big effect on the final parts.
EBM	Electron beam	<ol style="list-style-type: none"> 1. High preheat temperature (above 600°C in chamber) 2. Cooling rate is fast until reach the chamber temperature (above 600°C), and the rest of cooling from chamber temperature to room temperature is quite slow. (normally more than ten hours before taking out the finished parts from the chamber) 3. More sensitive with the processing parameters, and more processing parameters (such as beam power, beam scanning velocity, beam focus, beam diameter, beam line spacing, plate temperature, pre-heat temperature) than SLM 4. Vacuum atmosphere 5. Due to the very long cooling time in 600°C chamber, the residual stress is almost eliminated from the final parts. 	<ol style="list-style-type: none"> 1. Metallic powder melting. 2. Heat source scanning the metallic powder layer by layer. 3. The processing parameters (heat source parameters, hatch space, layer thickness) have big effect on the final parts.

1.3 Powder bed fusion of Ti-6Al-4V

There are different types of titanium alloys suitable for specific applications; however, Ti-6Al-4V alloy which contains 6% aluminum and 4% vanadium is the most commonly used titanium alloy. Until now, with about 45% of the total weight of all titanium alloys shipped in the second half of the twentieth century is Ti-6Al-4V [8]. Ti-6Al-4V can be highly weldable, and the narrow freezing range of the alloy means the alloy is highly printable. Thus, AM technologies are particularly suitable for Ti-6Al-4V parts manufacturing for a wide range of applications. The combination of PBF and Ti-6Al-4V gives Ti-6Al-4V a huge application stage, much more than before when titanium alloys were manufactured by conventional techniques [6][27-30].

Ti-6Al-4V is an α - β alloy. As shown from Fig. 1.4, when liquid Ti-6Al-4V starts to cool down, at above around 980°C (β transfer temperature), it consists of 100% β phase (bcc), when the temperature goes below 980°C, α phase (hcp) starts to transform from the previous β phase, and the final alloy structure depends on the cooling speed from above the β transus temperature. Conventional processed Ti-6Al-4V alloy is normally used in annealed condition, the annealed temperature is below the β transus temperature which is in $\alpha + \beta$ phase region, the microstructure consists of a mixture of equiaxed α and β phases [3].

It should be pointed out that for SLM technique, the cooling speed is around 10^5 K/s or even higher [27][31]. During this extremely fast cooling process, vanadium in β phase cannot have enough time to diffuse out of the cell, thus transform to α' (hcp) martensite as the main structure of SLMed Ti-6Al-4V [7][32]. While temperature goes up to around 600°C, α' martensite can start to transform back to $\alpha+\beta$ structure, and the transform speed is increased with increasing temperature [33]. Thus, as to the cooling speed for EBM and conventional processing (CP) of Ti-6Al-4V, the main structure for both is $\alpha+\beta$. However, EBMed Ti-6Al-4V usually has finer grain size than CP samples. The hardness of Ti-6Al-4V alloy depends on the percentage of α' in its structure, thus in these three manufacturing methods, SLMed Ti-6Al-4V has significantly higher hardness [34], followed by EBMed Ti-6Al-4V, and CP samples [35][36]. Table 1.2 shows the structure of SLM, EBM and CP Ti-6Al-4V and their hardness values measured for our

samples. Fig. 1.5 are SEM images of their microstructures, and these pictures were taken from the samples with their fabricated details introduced in Chapter 3.

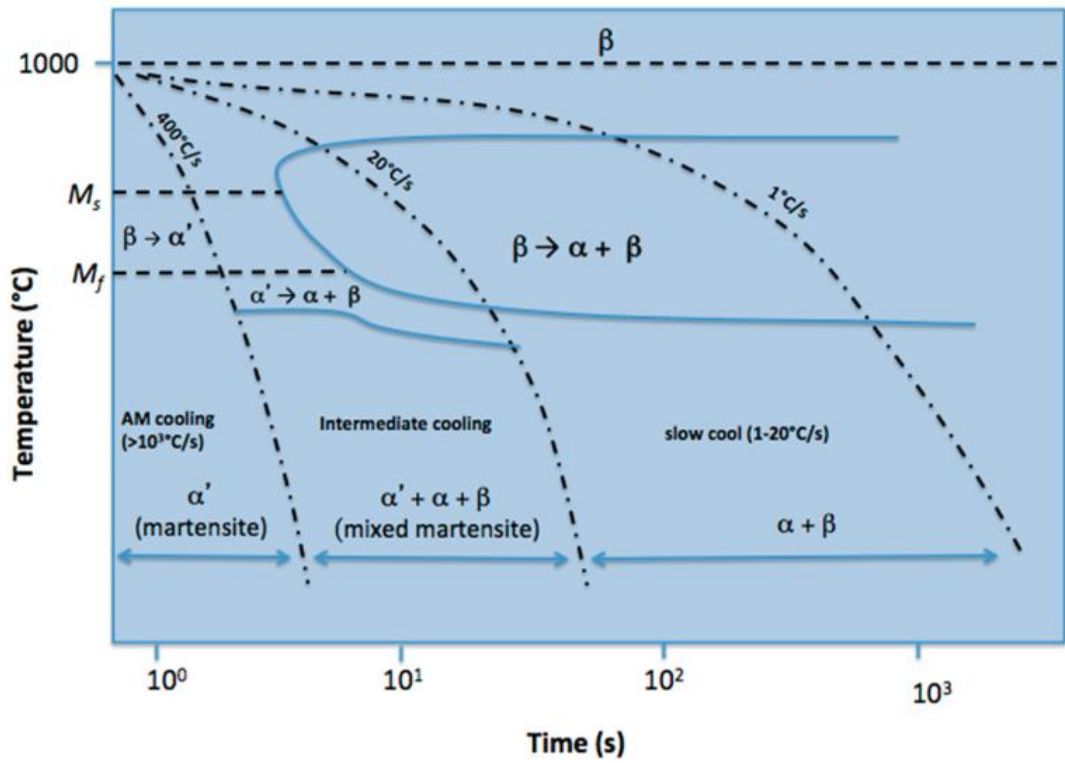


Fig. 1.4 Ti-6Al-4V continuous cooling transformation curve [7].

Table 1.2 The structure of SLM, EBM and CP Ti-6Al-4V and their hardness values measured from our samples.

Manufacturing process	Structure	Grain size	HV Hardness
SLM	α' martensite	Fine needle shape	428±17
EBM	$\alpha+\beta$	laminar structure	359±16
CP	$\alpha+\beta$	irregular β particles in α -matrix	324±8

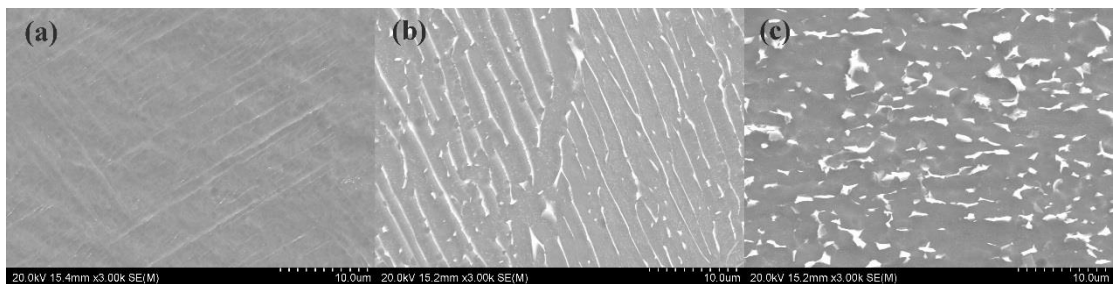


Fig. 1.5 SEM micrographs of (a) SLM sample showing α' martensitic structure, (b) EBM sample showing laminar $\alpha+\beta$ structure, and (c) CP sample showing fine and irregular β particles in α -matrix.

1.4 Aim of the research and thesis structure

With the rapid development of PBF additive manufacturing, there have been a number of studies on tribological performance of both SLM and EBM processed Ti-6Al-4V alloy. It is important to investigate whether PBF techniques can improve the tribological performance of the Ti-6Al-4V alloy, as these manufacturing techniques produce samples with higher hardness and finer structures.

Chapter 1 is the general introduction of Ti-6Al-4V alloy and its applications, followed by PBF technique and its processing on Ti-6Al-4V alloy are introduced. And then in Chapter 2, recent studies about the tribological performance of Ti-6Al-4V alloy including manufacturing routes by both conventional processing and PBF technique are discussed. The subsections of Chapter 2 are correlated with the research topics presented in Chapter 4 to Chapter 7 respectively. Research questions and research gaps are then introduced at the end of Chapter 2. After the research methodology chapter (Chapter 3), the tribological performance of PBF Ti-6Al-4V alloy compared with conventional processed at room and high temperatures is discussed in detail in Chapters 4 and 5, followed by tribological performance of samples with PVD coating and ion implantation in Chapters 6 and 7. Finally, the conclusion of this research are summarized in Chapter 8.

This thesis will provide systematic tribological testing results based on the design of the tests with samples manufactured by different routes, various test conditions, and different surface treatments. The analysis of these results will thus shed light into the tribological performance of PBF Ti-6Al-4V. Furthermore, the wear mechanisms are also going to be discussed in this thesis to support the observed wear behaviors. This thesis will thus provide a contribution to the tribology of SLMed and EBMed Ti-6Al-4V alloy by comprehensive analysis of sliding wear tests results.

Chapter 2 Literature Review

As sliding wear is the focus of this thesis, the relevant studies of sliding wear testing and wear mechanisms of metallic alloys in literature will first be briefly reviewed. The various tribological studies of Ti-6Al-4V and other Ti alloys that are processed by additive manufacturing (particularly powder bed fusion processes), as well as traditional manufacturing techniques will then be reviewed in detail. The coverage of the review will start with the studies on sliding wear testing at room temperature and the effect of increasing testing temperature on wear rate and the associated wear mechanisms will then be discussed in detail. The review will continue by examining the literature on the wear performance of coated Ti-6Al-4V alloy manufactured by different process routes. This will then extend to reviewing the effect of surface treatment by ion implantation on wear performance of Ti-6Al-4V alloy. The comprehensive review will then be summarized for the knowledge gap in the literature to be identified. This serves the base for the research questions to be asked and stated.

2.1 Wear, wear mechanisms and sliding wear testing of metallic alloys

Reciprocating sliding wear test is the method that has been used in this research to evaluate the wear behavior and wear rate of PBF Ti-6Al-4V alloy, in comparison to CP Ti-6Al-4V alloy. Thus, after a discussion on the commonly recognized wear and wear mechanisms of metallic alloys in literature, widely used testing methods are discussed.

2.1.1 Wear and basic wear processes

Wear is continuous damage of surfaces, which are in contact with a relative movement and it is the inevitable result of friction between the two surfaces. To better illustrate the wear phenomenon, a schematic is drawn in Fig. 2.1 showing the process of a hard object under force sliding against a softer body as well as illustrating the possible stresses, deformations, and fractures leading to material loss (thus wear). As shown in Fig. 2.1, the hard object's bottom

surface is embedded into the softer material by the softer material surface deformation and the applied normal force. The two materials stick together and then have relative micro movement, until the driving force is larger than the adhesive shear force, thus this relative movement will cause abrasive wear. This embed and driving model causes a compressive area on the surface of the softer material in front of the driving hard object, which results in mainly abrasive failure of the surface, and a tensile area in the back due to the two materials' adhesion, resulting in mainly adhesive wear.

The amount of wear (volume loss) per unit sliding distance, which is commonly defined as wear rate (WR), is the primary focus of most studies on wear and is also the major parameter to quantify wear in this work. Coefficient of friction (COF), which is a measure of resistance to motion is another important parameter to be considered in tribological studies and is the ratio of shear (friction) force (F_{sh}) to normal force (F_N). WR is a complex function of test parameters including applied normal load (F_N), sliding speed, hardness, ductility/toughness of the body, type of motion, surface roughness, etc.

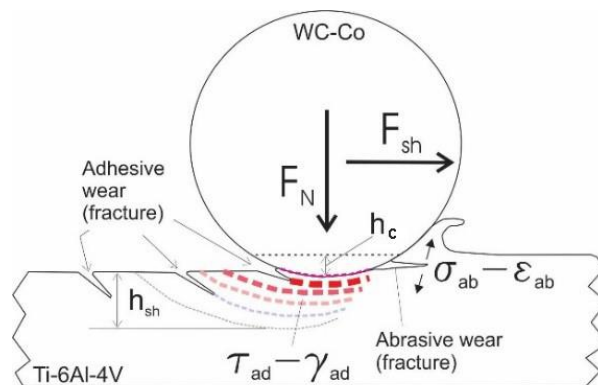


Fig. 2.1 Schematic illustration of a hard object forcefully sliding against the surface of a body with lower hardness, indicating various features of stress-strain leading to fracture and material loss.

2.1.2 Typical wear types

There are four basic types of wear: adhesive wear, abrasive wear, corrosion wear and fatigue wear (by a cyclic loading during friction) [37].

- Adhesive wear

Adhesive wear readily happens when asperities at the interface of the sliding pair stick and cold welded together by the contact pressure, and then sheared (fractured) with one material migrating from one surface to another causing material loss (Fig. 2.2). This adhesion normally causes a deformed layer with a certain thickness beneath the surface. Archard proposed an adhesion model to calculate adhesive wear rate as expressed by equation 2.1. In this model, V is wear volume, s is sliding distance, dV/ds is wear capacity rate, W is the normal load, σ_s is the yield stress of the softer material, and k_s is adhesive wear constant [9]. From equation 2.1, the material with higher yield stress should have relatively lower wear loss.

$$\frac{dV}{ds} = k_s \frac{W}{3\sigma_s} \quad (2.1)$$

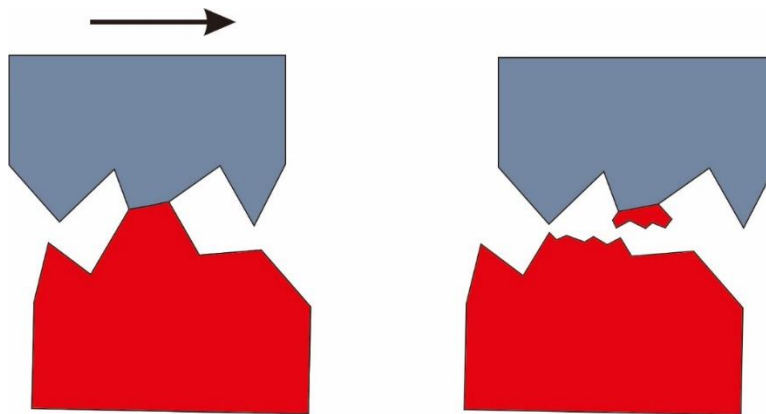


Fig. 2.2 Adhesive wear.

- Abrasive wear

When a hard and rough material slides over a softer material, the asperities of the softer material break and the presence of these particles at the contact interface causes progressive loss of material, which is called abrasive wear (Fig. 2.3). Due to the presence of the particles beside the two materials sliding over each other, this type of wear is usually called three-body abrasive wear. A conical counterface sliding over a flat surface is used to develop an abrasive wear model. The model is presented in equation 2.2, where V is wear volume, W is the normal load, H is hardness, and k_a is a constant determined by the hardness, shape and number of abrasive particles at the interface. Based on this equation, a material with higher hardness should exhibit

better wear resistance [9].

$$\frac{dV}{ds} = k_a \frac{W}{H} \quad (2.2)$$

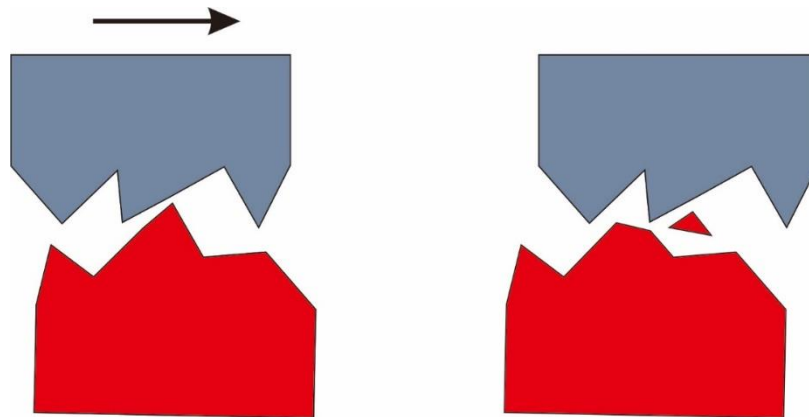


Fig. 2.3 Abrasive wear.

- Fatigue wear

Fatigue wear happens when materials are under cyclic loading during friction contact. The material loss is usually not occurred immediately, but after a considerable number of loads cycles. Fatigue wear usually causes crack initiation in sub-surface and then propagate to the surface. The connection of these cracks would cause delamination and peeling of the surface material resulting in wear loss (Fig. 2.4). The cracks initiated and propagated due to fatigue wear are usually normal to the wear track.

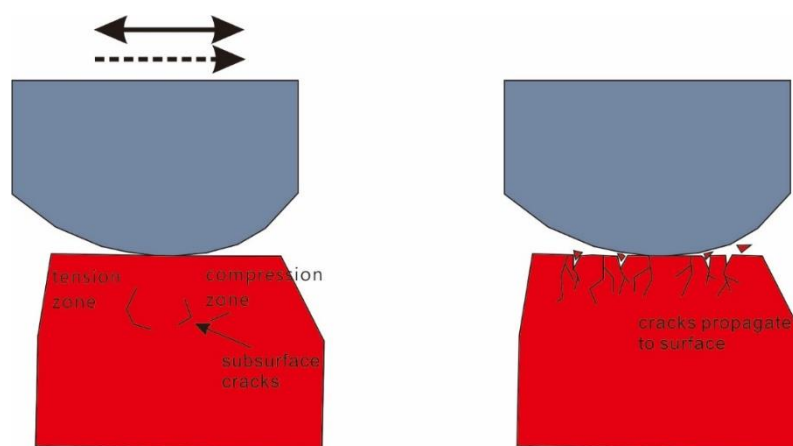


Fig. 2.4 Fatigue wear.

- Corrosive wear

Corrosive wear happens when the sliding mates operate in a corrosive environment, which could be liquid or gas. Corrosive wear sometimes can accelerate the wear process under dry contact, when the friction increases the surface temperature, which is in favour of the formation of oxides. The rubbing surfaces would remove these oxides, which will make the underneath layer of the material exposed to air and make the oxides formation continued. Corrosive wear can also occur under lubricated condition, due to the presence of dissolved oxygen or corrosive liquids.

When sliding wear happens, several types and mechanisms of wear occur together, resulting in mass loss. Firstly, the abrasive and adhesive actions cause plastic deformation on the surface which makes the material surface hardened and brittle; or cause elastic deformation when fatigue damage takes place. Secondly, friction heat will increase the temperature at the interface and high friction temperature can soften the contact surfaces. Thirdly, the ambient environment causes surface oxidation and other chemical reactions [37][9].

Fig. 2.5(b) shows a typical wear surface. Traces of ploughs and deep grooves along the sliding direction are the typical indications of abrasive wear, while the cracks perpendicular to the rubbing direction were caused by fatigue wear. The adhesion wear is usually combined with other wear mechanisms and not easy to be identified, but the composition of wear debris can help to define adhesive wear clearly from other types of wear. As shown from Fig. 2.5(a), large flake shape debris with chemical composition similar to the base material (Fig. 2.5(c)) is produced by peeling from the surface, which was caused by adhesive wear. Wear debris with high oxygen level shown in Fig. 2.5(d) indicates the oxygen in air caused oxidation of the surface of wear track.

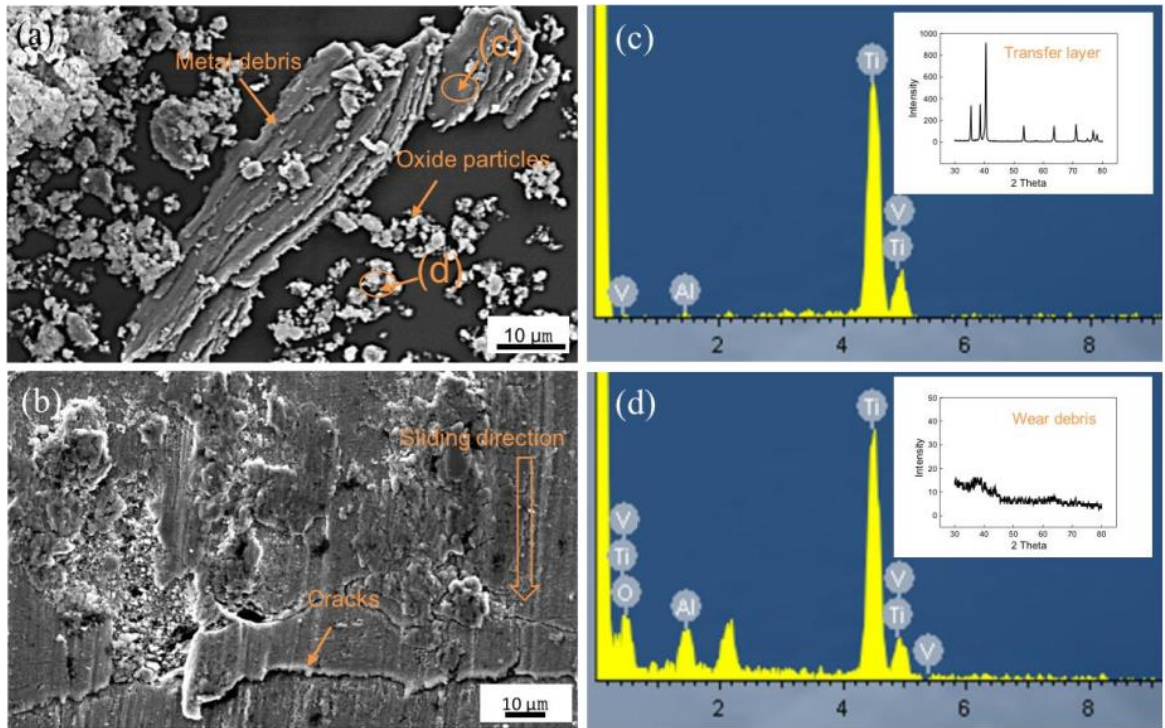


Fig. 2.5 SEM images of a wear test for Ti-6Al-4V alloy (a) wear debris and (b) wear track; EDX spectrum and inserted XRD patterns of two locations indicated in (a) are shown in (c) and (d), respectively [24].

2.1.3 Methods of evaluating wear

Sliding wear tests can be conducted by different sliding mates, different loads, temperatures, and sliding speeds. It gives you a convenient way to systematically study and analyse the wear happened between specific sliding materials under specific wear conditions. The results from the wear tests can evaluate the wear performance of sliding mates by analyzing the material loss, wear products on wear surface and wear morphology etc. after a series of wear tests, thus give constitutive guideline for wear couple selection and wear control [9].

Wear tests can be carried out on a sliding wear tester. These equipment, some of them are multi-functional under dry condition, some can do tests with liquid environment, some can be connected to electrodes to do tribocorrosion tests, but from the literature review, the sliding wear test is mainly from two ways -linear reciprocating and rotatory.

Fig. 2.6 shows a schematic of linear reciprocating tribometer. During wear tests, the sample is

fixed tightly into the sample bed, the counter material is fixed by the holder, and is applied on the sample surface with a specified normal load. The sample bed is normally connected to a heater that the test temperature can also be elevated. There is a motor connected to the counter material holder, draw and pull the counter material rubbing against the sample surface linearly forward and backward. The sliding frequency, stroke length, and temperature can be controlled through a software, and at the same time, the computer will record the necessary real time data like COF, bed temperature, friction force etc. [38-42].

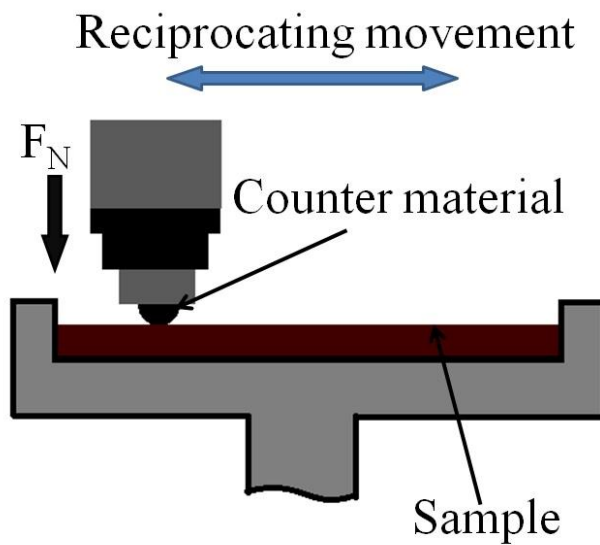


Fig. 2.6 The schematic of ball-on-plate linear reciprocating sliding wear test.

Fig. 2.7 is the schematic of rotatory tribometer, compared with the linear reciprocating tribometer, the wear couple are usually a disk and a pin, the sample or the counter material rotate, resulting in a relative sliding movement on the other material surface. The relative movement is through a single direction [43-47].

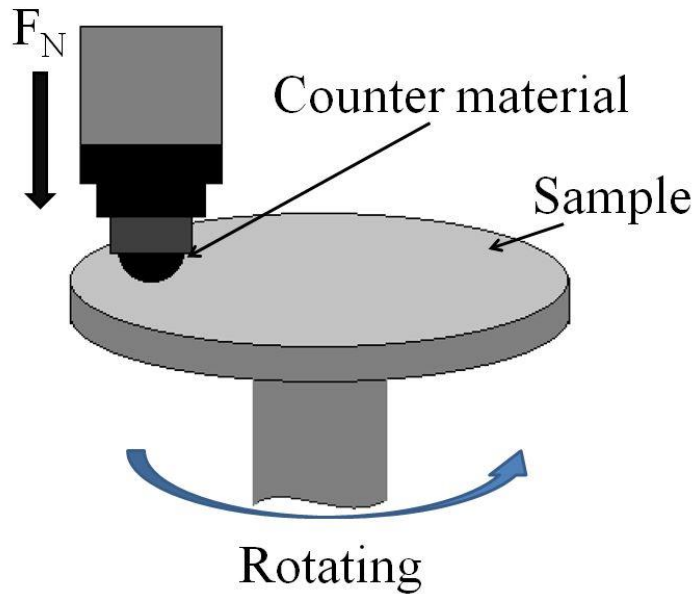


Fig. 2.7 Schematic diagram of rotary pin-on-disk wear tester.

After wear tests, wear performance of different materials should be evaluated. Comparing wear rate (WR) which is the material loss per sliding distance is a numerical way to evaluate wear performance of materials with same wear test conditions. Material loss usually is calculated by weight loss or volume loss [43-45]. Sometimes, specific wear rate which is WR divided by applied normal load is also used to evaluate wear loss [24].

2.2 Wear behaviors of PBF and conventional processed titanium alloys

This section is going to discuss relevant published papers about wear performance of conventional processed Ti alloys and PBF Ti-6Al-4V alloy at room temperature. Wear performance of conventionally processed Ti-6Al-4V alloy is discussed in section 2.2.1, followed by the wear performance of PBF Ti alloy in section 2.2.2.

2.2.1 Wear behaviors of conventional processed titanium alloys under room temperature

Titanium and titanium alloys are high strength and high corrosion resistant materials, but as reviewed by Budinski [11] and Dong [12], their tribological properties are known to be poor due

to their poor abrasion resistance. Table 2.1 shows the wear volume loss of pure Ti and Ti-6Al-4V after dry sand-rubber wheel abrasion tests followed by ASTM G65. It is clear that both Ti and Ti alloy show poor abrasive wear resistance, which is almost 7 times volume loss than that of 1080 carbon steel. In Budinski's [11] study, the incongruous of Archard's law which predicts the wear loss inversely proportional to material hardness is also been noticed, since the soft stainless steel showed better wear resistance than those material with higher hardness.

Dong [12] also cited the results from Budinski's [11] study, but he still points out the well-known softness of Ti alloys (200-350 HV) to be the reason for their poor abrasive wear resistance. Dong [12] also points out the good ductility of Ti alloys as c/a ratio of hexagonal Ti being less than the closest value making prismatic $\{10\bar{1}0\}$ and pyramidal $\{1011\}$ slips easy to operate. Dong [12] further points out that high plasticity and good junction bonding at high temperatures due to low thermal conductivity of Ti result in the poor adhesive wear resistance of the Ti alloys.

Table 2.1 Volume loss of various materials compared with Grade 2 pure titanium and Ti-6Al-4V [11].

Material	Hardness	Volume loss(mm ³)
6061 T6 aluminium alloy	60HRB	1220
Ti-6Al-4V	36HRC	650
Grade 2 Ti	90 HRB	550
316 austenitic stainless steel (SS)	90 HRB	260
17-4 precipitation hardening SS	43 HRC	220
1080 carbon steel	24 HRC	67
D2 tool steel	60 HRC	33

Since Dong's comprehensive review, there have continuously been tribological studies on Ti alloys, particularly on Ti-6Al-4V alloy. Sharma and Sehgal [48] conducted dry sliding wear tests to evaluate the effects of sliding speed and loading on the coefficient of friction (COF) and wear loss. Their study did not explain the reason of their results but show a series of plots to demonstrate that loads, speed have considerable influence for wear rate, Fig. 2.8 is one of their pictures for the lower loads up to 40N, the wear rate decreases with increasing velocity, however, for the load of 50N, wear rate decreases first until the velocity goes to 1.25m/s, and then, the wear rate increases abruptly and reach to its peak value at velocity of 2.1m/s, after that, the wear rate decreases as the velocity goes to 2.6m/s.

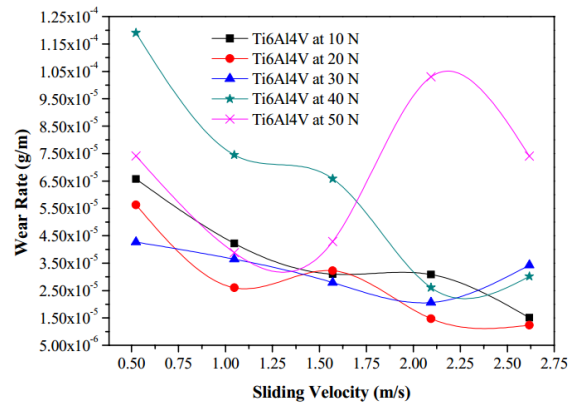


Fig. 2.8 Wear rate versus sliding speed for Ti-6Al-4V alloy sliding against EN31 steel under different loads with dry condition [48].

Niu et al. [38][39] and Fellah et al. [49] conducted sliding tests comparing COF in dry and water environment and under different applied loads. In their studies, wear surfaces were carefully examined and wear has been suggested to be in various forms of abrasion, adhesion and their combination. Fig. 2.9 shows the wear track of Ti-6Al-4V when sliding against WC ball from the study of Niu et al. [39]. Deep grooves left by ploughing and tiny particles showing sever abrasive wear can be seen in Fig. 2.9.

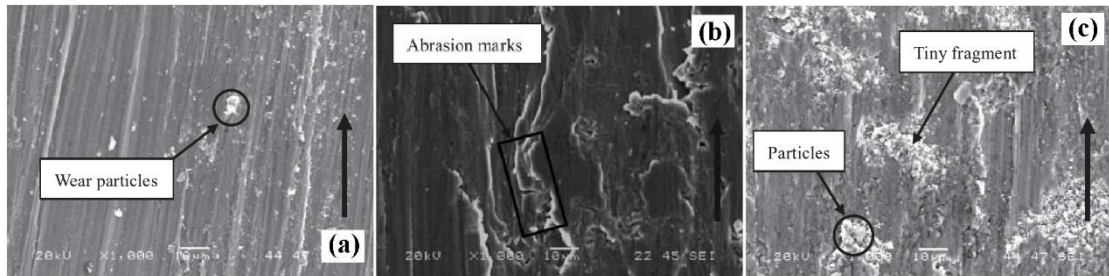


Fig. 2.9 SEM images of the Ti-6Al-4V worn surfaces under different wear conditions (a) dry sliding condition, (b) water lubricated condition, (c) dry sliding condition but the location is at the ends of the worn track [39].

2.2.2 Wear behaviors of PBF Ti-6Al-4V alloys under room temperature

Powder bed fusion AM technique can change the cooling process from traditional processed Ti-6Al-4V, which can lead to different microstructures of Ti-6Al-4V alloy and can also increase the hardness of the alloy. Thus, understanding the wear performance of Ti-6Al-4V made by AM technique is very important.

With the rapid development of PBF additive manufacturing, there have been a number of studies on tribological performance of both SLM and EBM processed Ti-6Al-4V alloy. On SLM, the early study by Kumar and Kruth [40] explained that samples were not fully dense by SLM and suggested that wear resistance may increase in fully dense samples. That denser SLM samples performed better in terms of lower wear volume has later been confirmed in Gu et al.'s study [50]. The major defect relating to lowering density is the lack of fusion for both SLM and EBM. Thus, for EBM, less dense parts should also be expected to result in lower wear resistance. For both SLM and EBM, with proper selection of processing conditions, nearly fully dense parts can now be readily produced, thus the wear performance of PBF alloys are expected to have better wear resistance if they can show higher hardness.

Two wear studies on SLM Ti-6Al-4V [51][52] were later reported, showing contradictory results. In Bartolomeu et al.'s work [51] of Ti-6Al-4V / Al₂O₃ sliding pairs, a higher hardness value (390 HV) results in a significantly lower wear rate (WR) compared to that of CP materials with hardness values of ~340HV and ~360HV (Fig. 2.10). They suggest that this is largely the result of wear resistance following Archard's linear relationship that wear volume being inversely proportional to hardness. However, Palanisamy et al. [52] produced SLM samples and hardness values of the samples vary from 310HV to 405HV. Their dry sliding tests with three different loads show no dependence of wear volume on hardness as shown in Fig. 2.11.

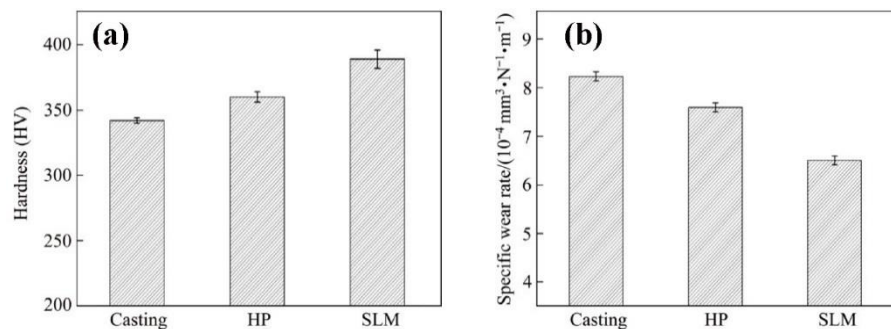


Fig. 2.10 Vickers hardness of Ti-6Al-4V specimens obtained by casting, HP (Hot Pressing) and SLM (a); the specific wear rates of these samples when sliding against Al₂O₃ ball (b) [51].

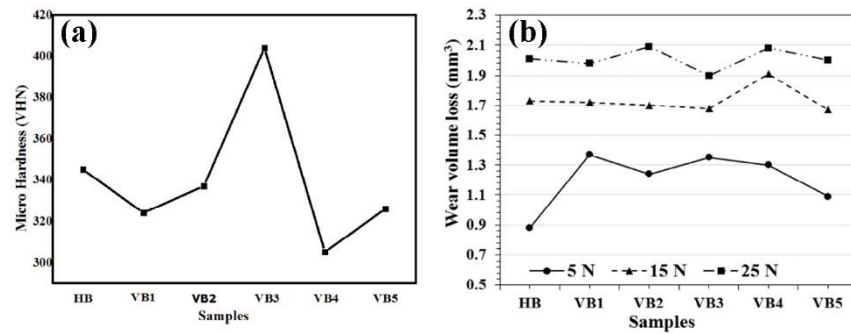


Fig. 2.11 Microhardness (a), and wear volume (b) of horizontal and vertical built specimens at different loads [52].

Comparing performance of EBM to cast Ti-6Al-4V in dry sliding wear tests, the relationship between hardness and wear rate is also not clear. Toh et al.[24] showed the normally observed inversely proportional relationship of hardness and wear volume shown from Fig. 2.12 (a). This relationship is however not followed when test was conducted with Hank's solution, as demonstrated by Khun et al. [53] in Fig. 2.12 (b). Furthermore, Ryu et al. [54] also showed that hardness (450HV) of mill-annealed (conventional) Ti-6Al-4V is higher than the hardness (400-410HV) of EBM samples, but WR is lower for the EBM samples in dry sliding test. More recently, data of Ti-6Al-4V rotation wear test from Zhang et al. [55] showed forged/annealed samples (~370HV) worn more than SLM (~400 HV) and EBM (~380HV) samples, while EBM samples worn less than SLM samples (Fig. 2.13). The better performance of EBM samples were simply linked to horizontal cracking and delamination of the tribo-layer in SLM samples (Fig. 2.14). How continuous the layer is and what the mechanism is for cracking to result in less wear loss are however not clear and these studies are not providing detailed mechanistic explanations.

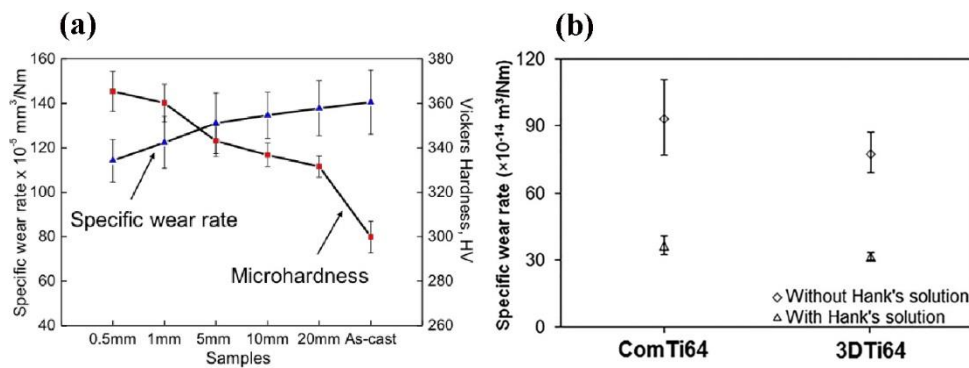


Fig. 2.12 Specific wear rates and Vickers hardness of EBMed and conventional processed Ti-6Al-4V samples (a) [24] ; specific wear rates of conventional processed and EBMed Ti-6Al-4V samples tested under the same conditions

(b) [53].

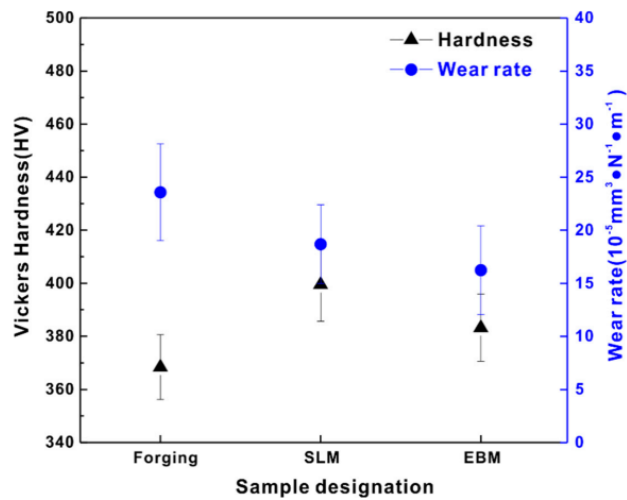


Fig. 2.13 Hardness and wear rate of Ti-6Al-4V samples fabricated by forging, SLM and EBM [55].

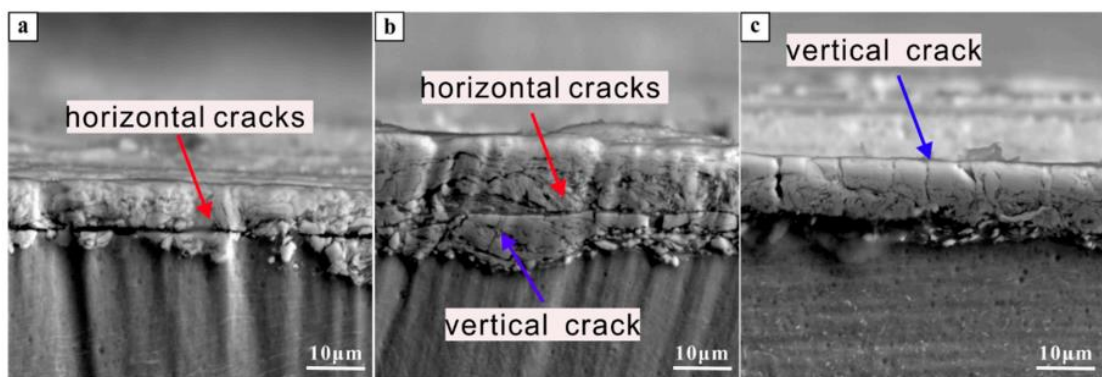


Fig. 2.14 Cross-sections of Ti-6Al-4V alloy produced by (a) forging, (b) SLM and (c) EBM [55].

More recently, Zhu et al. [56] conducted extensive testing comparing wear rate of SLM Ti-6Al-4V alloy samples to that of conventional processed (CP) Ti-6Al-4V alloy samples with wear mechanism explanation. Hardness of the SLM alloy samples was 450HV comparing to 350HV for the CP alloy samples. Wear rate of SLM alloy samples was significantly lower than that of CP alloy samples when counterface material was brass, but was only slightly lower when the contact was with 38CrMoAl (Fig. 2.15). For the test with 38CrMoAl, their data show a hardened layer of $\sim 100\mu\text{m}$ in thickness with hardness of $\sim 530\text{HV}$ for SLM samples and a hardened layer of $\sim 40\mu\text{m}$ with hardness of $\sim 410\text{HV}$ for CP samples shown from Fig. 2.16. However, the cross sections of their test samples do not show thick wear interaction/deformation layers as shown in Fig. 2.17 correlated with the hardened thickness they demonstrated before. It is known that Ti alloys do not work harden significantly and thus Zhu et al.'s hardness data may be seen unexplainable.

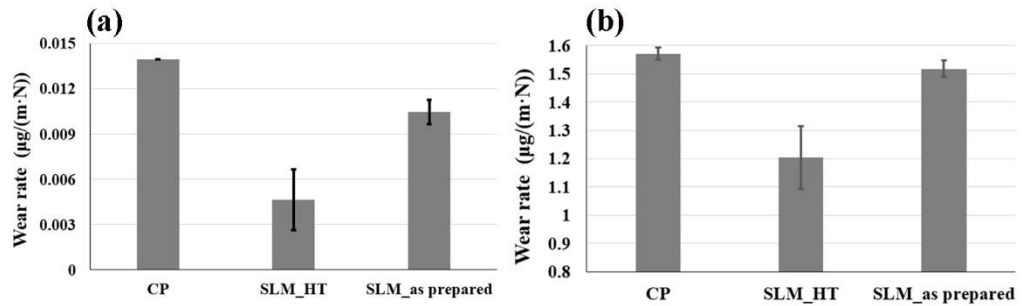


Fig. 2.15 Wear rate results for the Ti-6Al-4V samples in contact with brass (a) and 38CrMoAl (b) [56].

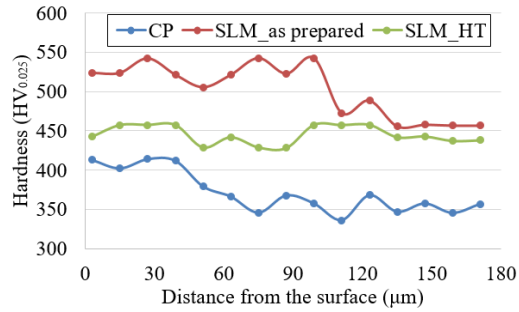


Fig. 2.16 Vickers hardness distribution away from the worn surface of Ti-6Al-4V in contact with 38CrMoAl [56].

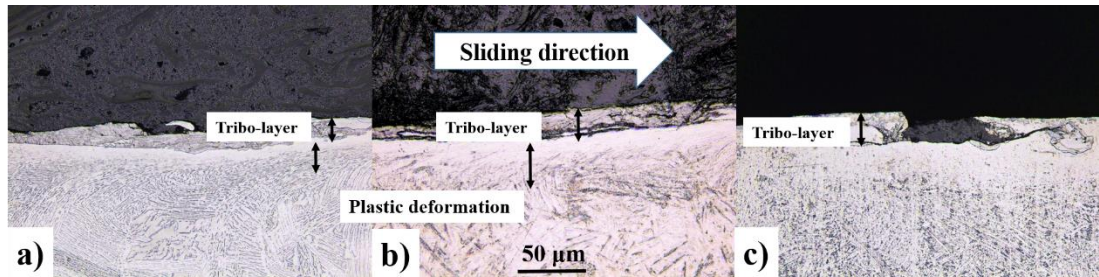


Fig. 2.17 SEM images of cross sections of (a) CP, (b) as prepared SLM, and (c) heat treated SLM samples in contact with 38CrMoAl [56].

It could be seen from the studies above that wear rate inversely follows hardness trend (Archard's law) or the trend is not clear and there is also a lack of wear mechanism explanation for Ti-6Al-4V samples made by PBF techniques. Besides, it has widely been demonstrated that the cooling rate during SLM is sufficiently high and therefore the solidified cubic β phase largely transforms to martensitic α' phase [7]. Hardness should normally be $>400\text{HV}$. From the articles above, various hardness of Ti-6Al-4V are reported, SLM samples could be 390HV [51], 310HV to 405HV [52], $345\text{--}355\text{HV}$ [57], 450HV [56], 400HV [55], and EBM samples could be 300 to 365HV [24], 376HV [53], 400 to 410HV [54], 380HV [55].

2.3 Wear of titanium alloys at elevated temperatures

In some industries such as aerospace, automotive, and power generation, depending on the applications, the operating temperature may reach up to 500°C or even higher [58][59]. These elevated temperatures can have detrimental effects not only on the mechanical properties of the materials, but also their surface morphology. This in turn can affect the wear performance of each component [60]. High temperature tribological processes are common phenomena in these applications. For example, apart from the significant effect on fuel economy, high temperature wear loss is considered to be one of the most critical barriers that restricts engines' reliability and service life [14][58], because the geometry change due to wear influences the workability and reliability of components working in a system.

In high temperature tribo-systems, the elevated temperature causes material softening, thus will influence the mechanical strength of the material, leading to higher wear rates. Besides, high temperatures will cause higher level of surface oxidation, affecting the wear process. Therefore, limited workability of titanium alloys at elevated temperatures is one of the main concerns of the designers and engineers [8][61][62]. There have been some previous studies on wear resistance of titanium alloys at high temperatures under different working conditions that will be reviewed in this section.

2.3.1 Wear behavior of conventional processed titanium alloys at elevated temperatures

Cui et al. [63] and Mao et al. [44] conducted dry sliding Ti-6Al-4V pin on GCr15 steel disk wear tests under 50-250N applied load and measured the volume loss of the pins. Their results showed that at 400°C and 500°C and in the mid-range of loading (100-200N), the average WR is only up to $\sim 5 \times 10^{-6} \text{mm}^3/\text{mm}$, while at room temperature, average $\text{WR} = (15-35) \times 10^{-6} \text{mm}^3/\text{mm}$. This is a considerable reduction in WR when temperature increases to 400°C and 500°C. Also, at these temperatures, as shown in Fig. 2.18, a significant reduction in WR is observed at higher applied loads (100-200N) compared to the WR at 50N load, which is very different from the

general trend of increasing WR with increasing applied load.

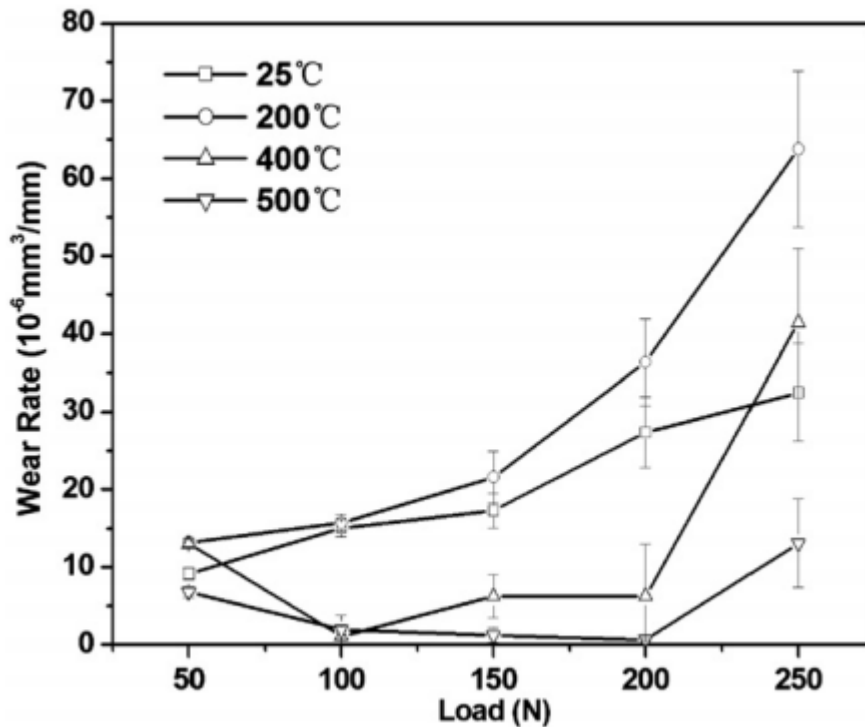


Fig. 2.18 Wear rates of Ti-6Al-4V alloy as a function of temperature and load [44].

During dry sliding of metallic alloys, tribo-layers are usually formed on the worn surface. Table 2.1 evaluates the hardness of tribo-layer and base material, under 400-500°C temperatures and 100-200N applied loads. A significant difference in hardness was observed, and a significant amount of oxygen was found in the tribo-layers. Fig. 2.19 shows the surfaces and cross sections of some test samples from Mao et al.'s work [44]. In Fig. 2.19(a), which is the test with 200°C and 100N load, the wear tracks mainly show abrasive wear with furrow and ridge along sliding direction, while its cross section image in Fig. 2.19(c) shows there is only a thin tribo-layer. On the other hand, the sample tested under 100N load at 400°C shows relatively smooth wear surface with delaminated wear regions (Fig. 2.19(b)). The correlated cross-section morphology (Fig. 2.19(d)) also shows the presence of a thick and dense tribo-layer.

Cui et al. [63] and Mao et al. [44] pointed out that only a tribo-layer with enough amount of oxygen and high hardness can prevent metal-metal adhesion at the contact interface and possess self-lubrication function, thus providing good protection from wear. That is the reason that 100-200N load tests have lower wear when under high temperatures of 400 to 500°C.

Table 2.2 Thickness, hardness and oxide level of tribo-layer in Ti-6Al-4V alloy under various test conditions [44].

Testing conditions	25°C		200°C		400°C		500°C	
	50N	100–200N	50N	100–200N	50N	100–200N	50N	100–200N
Thickness of the tribo-layer (mm)	3–6	20–25	5–8	15–20	15–20	20–30	10–15	10–15
Hardness of the tribo-layer (HV)	325	410–440	330	385–440	375	520–570	225	325–475
Hardness of the tribo-layer (HV)	280	340	320	340	350	320–360	175	175–210
Hardness difference of the tribo-layer and the substrate	45	70–100	10	45–100	25	200–210	50	150–265
Amount of tribo-oxides	no	No	trace	Trace	No	more	trace	More

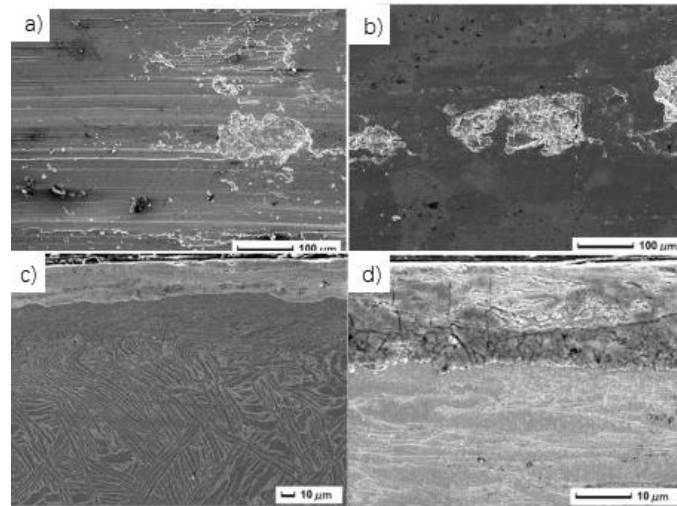


Fig. 2.19 SEM images of worn surfaces of Ti-6Al-4V alloy sliding under various conditions: (a) 200°C, 100N, (b) 400°C, 100N; (c), (d) are their cross-sections respectively [44].

Zhang et al. [43] conducted dry sliding Ti-6.5Al-3.5Mo-1.5Zr-0.3Si pin on AISI52100 steel disk tests and measured the wear volume of the pins. They showed an increase of WR from $15 \times 10^{-6} \text{mm}^3/\text{mm}$ to $65 \times 10^{-6} \text{mm}^3/\text{mm}$ when load increases from 50N to 250N for tests conducted at room temperature. For tests conducted at 600°C, WR is close to zero for the whole range of loading (50N-250N). Furthermore, they conducted sliding wear tests at a starting temperature of 600°C and then the same sample was kept being tested, but the temperature was lowered to room temperature. Their data showed that wear resistance in this condition is similar to the single temperature sliding test at 600°C, with WR values close to zero (Fig. 2.20). Their results suggest that exposing the sample to the elevated temperature of 600°C prior to or during sliding

tests has basically prevented wear to occur.

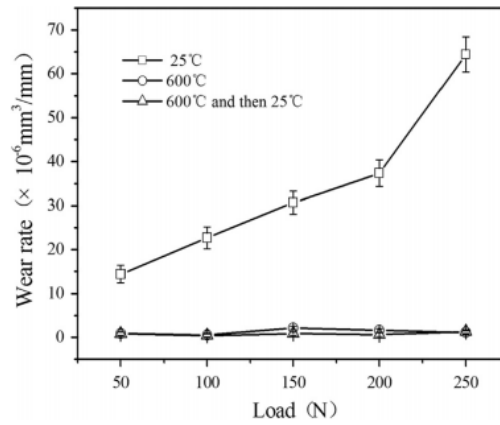


Fig. 2.20 Wear rate versus applied load for titanium alloy under various test temperature conditions [43].

Fig. 2.21 shows EDS and XRD results of the study carried by Zhang et al. [43]. In (c) and (e) (which are the tests with 600°C or first with 600°C), the green lines which indicate the amount of oxygen in the tribo-layer region are both higher than the substrate material, which shows the tribo-layers are with higher oxygen content.

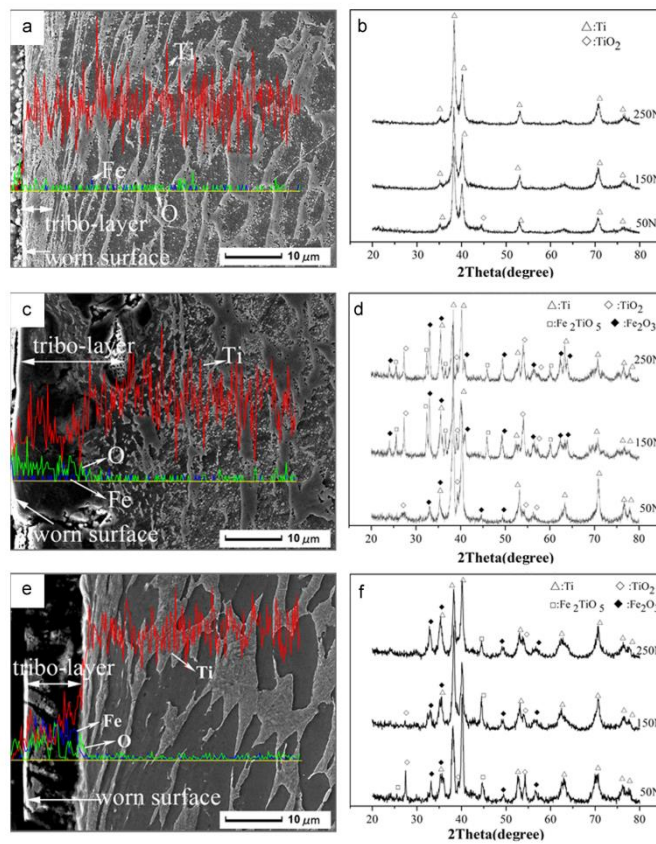


Fig. 2.21 Morphology, EDS line analysis and XRD patterns of tribo-layers under sliding wear tests: at room temperature (a, b); at 600°C (c, d); first sliding at 600°C and then sliding at room temperature (e, f) [43].

Fig. 2.22 also shows the plastically deformed layers beneath the tribo-layer (red arrow lines show the deformed layers). These deformed layers appear to be associated with the load-bearing capacity of tribo-layers. In Fig. 2.22(a) and (b), which are for 150N and 200N tests under room temperature, in which the tribo-layers have very tiny oxides, the deformed layer thickness is around 30 and 80 μm , respectively. On the other hand, oxide layers which are compact and continuous, can be seen in Fig. 2.22(c) and (d), which are for 150N and 200N tests under 600 $^{\circ}\text{C}$ temperature and the thickness of the deformed layers beneath them are less than 10 μm for both. Thus, Fig. 2.22 can show that hard tribo-layer would possess high load-bearing capacity, and the force was prevented to transfer to the substrate material underneath the tribo-layers. So, a thin plastically deformed layer was presented when there is a hard oxide layer on top of it (Fig. 2.22(c) and (d)).

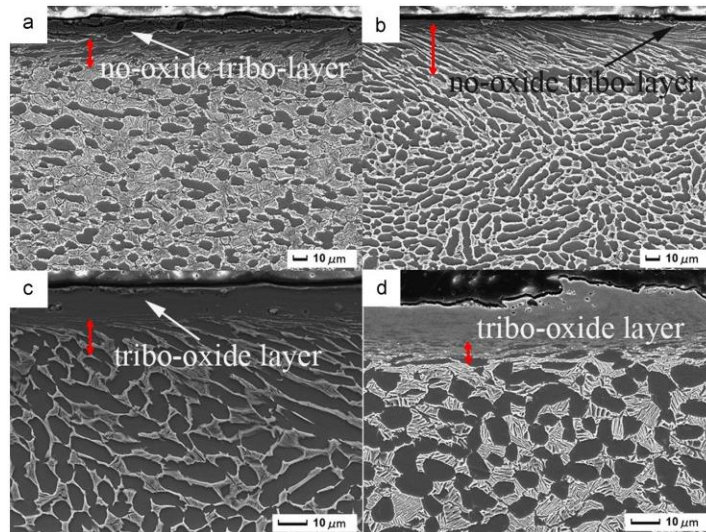


Fig. 2.22 Tribo-layers typical status of: (a, b) sliding at room temperature, 150 and 250 N, respectively; (c, d) sliding at 600 $^{\circ}\text{C}$, 150 and 250 N, respectively [43].

Thus studies [43][44][63] concluded that high temperature results in high level of oxygen in the tribo-layer, which can act as a protective layer and improve wear resistance.

Kumar et al. [64] conducted dry sliding Ti-6Al-4V pin on SS316L stainless steel disk linear reciprocating wear tests in vacuum to filter out the effect of oxidation due to increasing temperature and measured the volume loss of the pins. Their results also show a rapid decrease in WR as temperature increases from room temperature to 200 $^{\circ}\text{C}$ and at 400 $^{\circ}\text{C}$, WR is close to zero (Fig. 2.23).

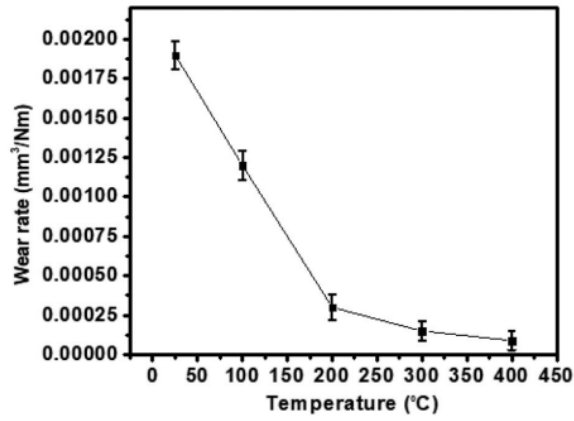


Fig. 2.23 Wear rate versus temperature of Ti-6Al-4V alloy pin when sliding against SS316L disk in vacuum condition [64].

Kumar et al. [64] presented mechanically mixed layer (MML) as can be seen in Fig. 2.24. MML, which is the term they used for tribo-layer, was formed by tribo-chemical reactions during the sliding wear tests. They stated that this layer is surface oxides layer and its thickness increased with increasing temperature. However, they didn't test the oxygen amount of the layers, and due to their tests being conducted at vacuum environment, it is not clear how oxygen is present in the MML layer. They concluded that a thicker tribo-layer with high oxygen is better as it can prevent adiabatic shear band and thus reduce wear loss.

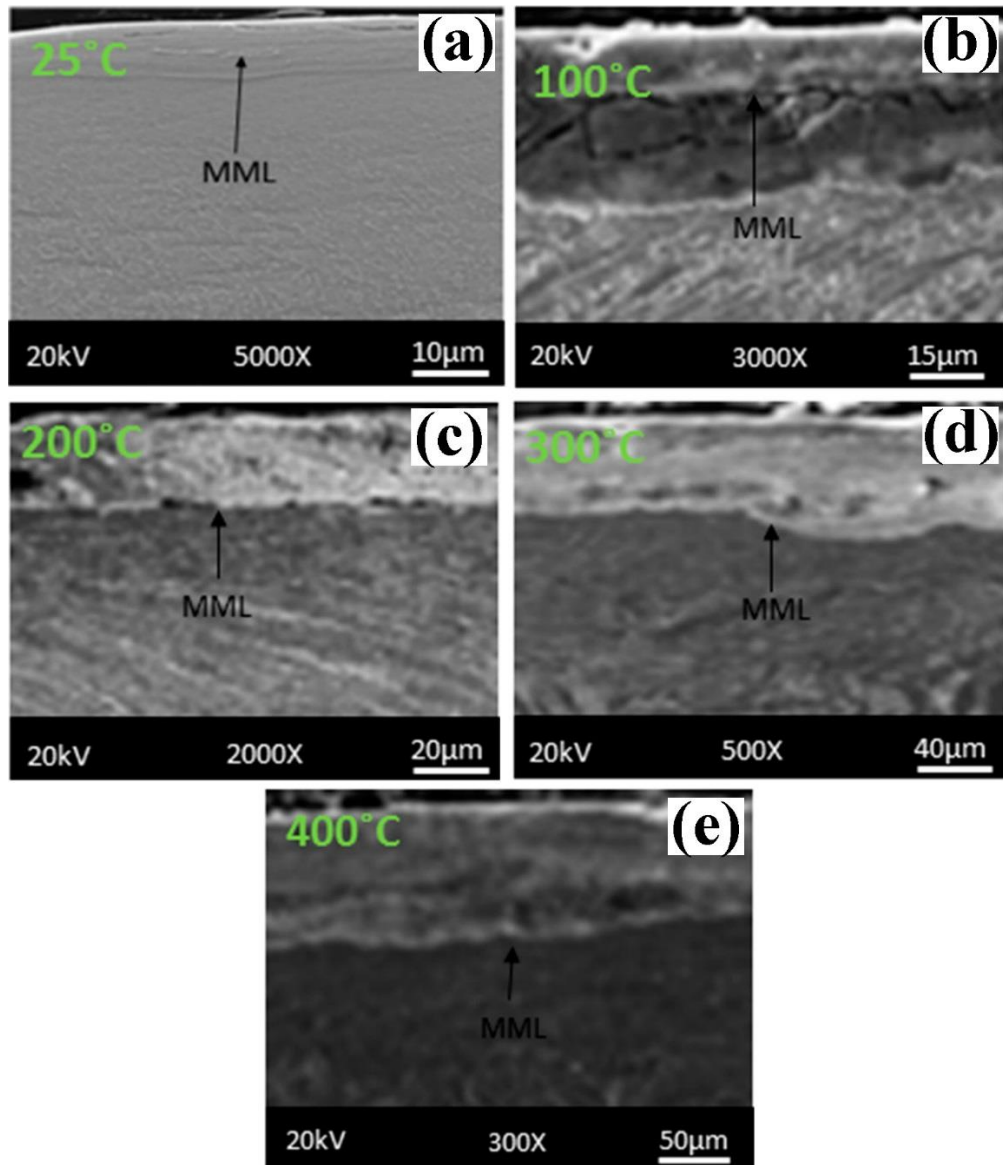


Fig. 2.24 SEM images of mechanically mixed layer (MML) when the tests were conducted at 25°C (a), 100°C (b), 200°C (c), 300°C (d), 400°C (e) [64].

More recently, Liang et al. [65] conducted pin-on-disk rotatory testing with WC-6Co as pin and Ti-6Al-4V as the disk at temperatures up to 900°C and traced the 3D wear tracks to convert to wear volume rate. Fig. 2.25 shows that increase in temperature from room temperature to 320°C slightly increases the wear volume from $\sim 5 \times 10^{-3} \text{mm}^3/\text{s}$ to $\sim 7 \times 10^{-3} \text{mm}^3/\text{s}$. By further increasing the temperature to 600°C, wear volume increased significantly to $\sim 17 \times 10^{-3} \text{mm}^3/\text{s}$. Increasing the temperature to 900°C resulted in a considerable increase in wear volume to $\sim 42 \times 10^{-3} \text{mm}^3/\text{s}$ (Fig. 2.25). Thus, the effect of increasing T on increasing WR by Liang et al. is strong when $T > 320^\circ\text{C}$ and is completely opposite to the observations by Cui et al. [63], Mao et al. [44] (Fig. 2.18), Zhang et al. [43] (Fig. 2.20) and Kumar [64] (Fig. 2.23).

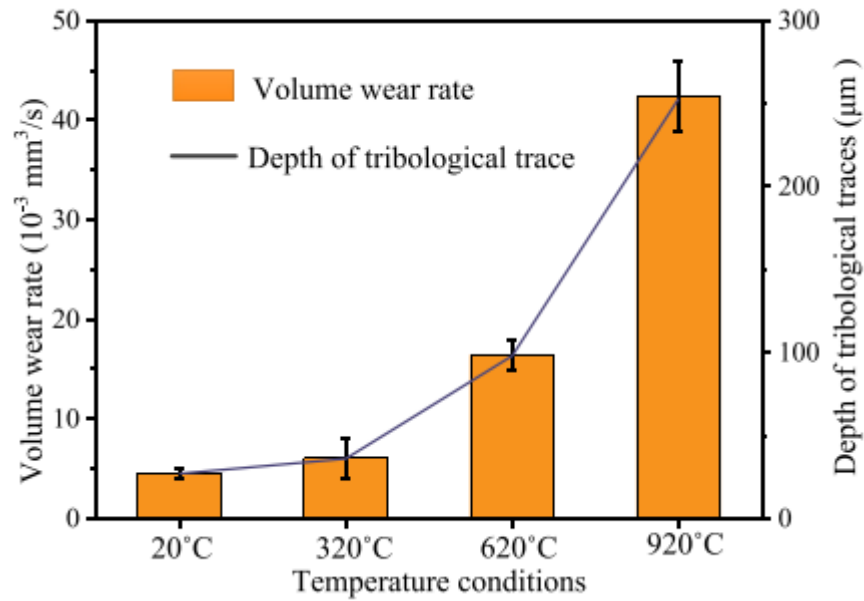


Fig. 2.25 Volume wear rate and depth of wear profiles versus temperature when WC-6Co pin slides against Ti-6Al-4V disk [65].

Further to measuring wear rates, Liang et al. [65] conducted EDS/SEM analysis and observed that oxidation phenomenon increased as the temperature increased (Fig. 2.26). The contents of element O reached up to 20%–30% in contact surfaces at the high temperature of 920°C. Thus, unlike research [43][44][63][64], study [65] gives an opposite relationship between temperature and wear loss.

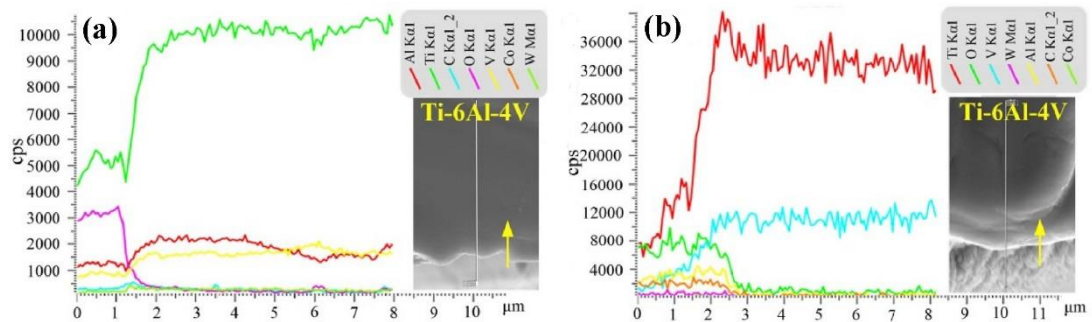


Fig. 2.26 Elemental composition profiles of cross-sectional view of Ti-6Al-4V, (a) 320 °C, (b) 920 °C [65].

2.3.2 Wear behavior of PBF Ti-6Al-4V at elevated temperatures

Due to increased applications of AM techniques, many load bearing parts working at elevated

temperatures are produced by PBF manufacturing methods [15]. However, limited data are available on high temperature tribological performance of PBF Ti alloy in literature, and only one article was found. Alvi et al. [66] conducted ball-on-disk rotary sliding wear experiments with EBM Ti-6Al-4V as disk and steel or alumina as ball materials at temperatures up to 500°C. Their wear rate was determined based on track volume, taking the product of average depth and area of track. Their results showed that wear rate at room temperature to be $(7.0\pm 6.5)\times 10^{-4}\text{mm}^3/\text{Nm}$ and $(8.3\pm 6.8)\times 10^{-4}\text{mm}^3/\text{Nm}$ sliding against steel and alumina balls, respectively. However, as can be seen in Fig. 2.27, standard deviation values were very high. At 200°C and 400°C, deviation values were lower and average wear rate values were within $(0.4\text{-}0.9)\times 10^{-4}\text{mm}^3/\text{Nm}$. At 500°C, the average values were $(3.5\text{-}4.5)\times 10^{-4}\text{mm}^3/\text{Nm}$ with a medium level of standard deviation at $\sim 4\times 10^{-4}\text{mm}^3/\text{Nm}$ for the case of alumina ball experiments (Fig. 2.27). They conducted two tests for each condition, and it is thus unclear how standard deviation values were obtained. With this uncertainty but the very large deviation values for some tests, the effect of temperature on wear rate from Sajid et al.'s study [66] may be difficult to ascertain.

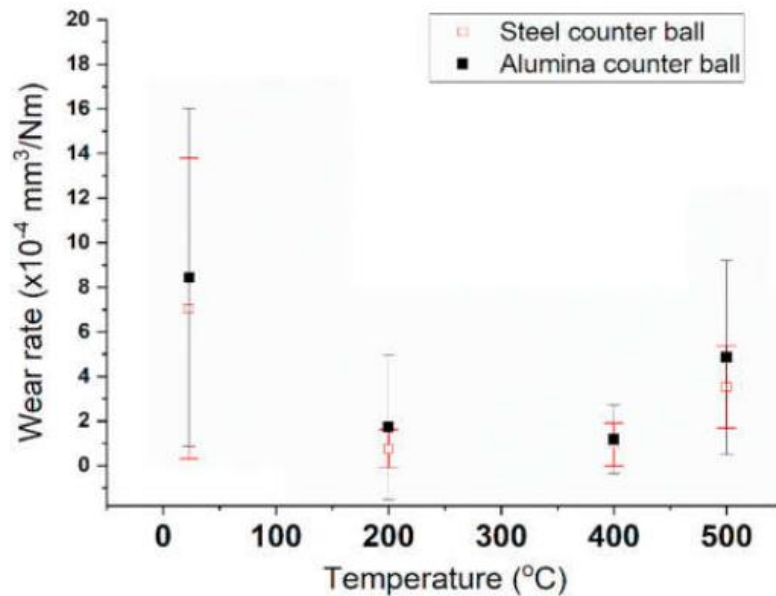


Fig. 2.27 Wear rate versus temperature when steel or alumina counter ball sliding against EBM Ti-6Al-4V disk (error bars represents standard deviations) [66].

By summarizing the studies above, the current understanding on the effect of temperature on wear rate from literature may be viewed contradictory from different studies. A number of

studies measured the volume loss of the Ti alloy pins from pin-on-disk experiments have shown that wear rate generally decreases as temperature increases, although it depends also on the level of load applied [43][44][63][64]. On the other hand, study [65] based on directly measuring the wear volume of the wear track in the Ti-6Al-4V disk clearly shows that wear rate is directly proportional to test temperature. The effect of the formation of the tribo-oxide layer to reduce wear rate also seems unclear from the literature data. Besides, tribological data for PBF Ti alloys are very limited.

2.4 Wear performance of PBF Ti-6Al-4V alloy surface treated by PVD coating and ion-implantation

This section is going to introduce several papers about the wear performance of surface treated Ti-6Al-4V. The wear performance of TiN PVD coating is introduced in section 2.4.1 and ion-implantation surface treatment is in section 2.4.2.

2.4.1 Wear performance of PBF Ti-6Al-4V alloy surface treated by PVD coating

As mentioned in section 2.2.1, wear resistance of titanium and Ti alloys are known to be poor primarily due to the low hardness values (200-350 HV) of the alloys, thus applying surface coating to CP Ti-6Al-4V for improving wear resistance is a natural way. It has been commonly recognized that PVD coating can prevent the base material from wear and is widely used in industry for improving tribological performance, particularly for tooling [67][68]. Several studies have been conducted on PVD coating and how it affects the wear resistance of the base Ti alloy.

Though PVD coating can prevent the base material from wear, under some test conditions PVD coating could fail. Studies have revealed that the failure of coating can cause abrupt change of COF or rapid increase in wear volume. Liu et al. [69] conducted dry “multi-scratch test” to investigate tribological performance of PVD TiN coating on Ti-6Al-4V samples against a

hemispherical diamond as counter material [69]. It was shown in this study that there is a certain value of load, when the applied load is bigger than that value, there is a sharp increase in coefficient of friction (COF) after a certain number of passes, which indicates the time of coating failing. As shown in Fig. 2.28, where the coating failure happened at around 390 traverses.

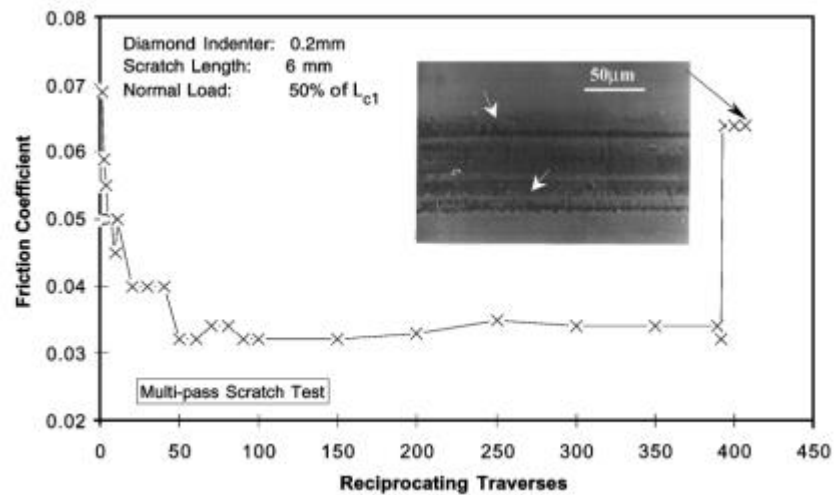


Fig. 2.28 Friction coefficient versus traversals during multi-scratch test on TiN coated Ti-6Al-4V; a SEM image inside showing worn surface morphology with micro cracking and delamination of TiN films after 400 passes [69].

Cassar et al. [70] conducted dry reciprocating sliding wear tests to investigate the tribological performance of TiN and CrAlN PVD coating sliding against WC-Co ball. These coatings were with different nitride bias potential: low voltage (LV) and high voltage (HV), or different triode-plasma diffusion process: nitrided (TPN) or oxidized first then nitrided (TPON). Fig. 2.29 shows PVD TiN coating provides a high resistance to wear up to the sliding distance of 300m and beyond this distance, wear volume rapidly increases.

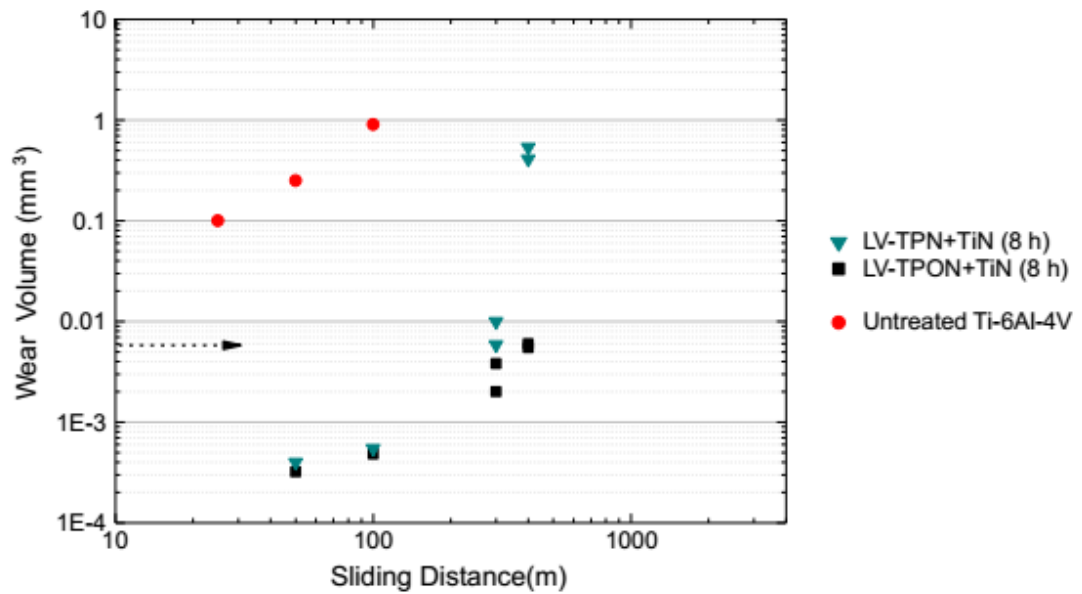


Fig. 2.29 Wear volumes measured for untreated Ti-6Al-4V and TiN-coated TPN and TPON samples, tested against WC-Co at a normal load of 13.5N [70].

Previous studies also tried to discuss the reasons PVD coating fails. Martini and Ceschini [71] examined the worn surfaces of PVD coated Ti-6Al-4V after testing using dry rotatory flat-on-cylinder configuration with bearing steel as the cylinder material. They investigated different types of PVD coating, including CrN single layer, CrN/NbN alternative nanolayers and WC/C multiple layers coatings. Fig. 2.30 shows the worn surface of CrN/NbN coating, they reveal that there is a high level of iron oxides, which is from the counter material surface, in the worn surface. They predicted that the higher hardness of coating caused abrasive action when contacted with steel counter material and made the steel debris, then the steel debris turned to iron oxides and were pressed on the coating surface by the friction heat and contact pressure forming a compact oxide transfer layer. Under higher load, this unstable oxide transfer layer is non-protective, it was delaminated and broke with cracks been observed.

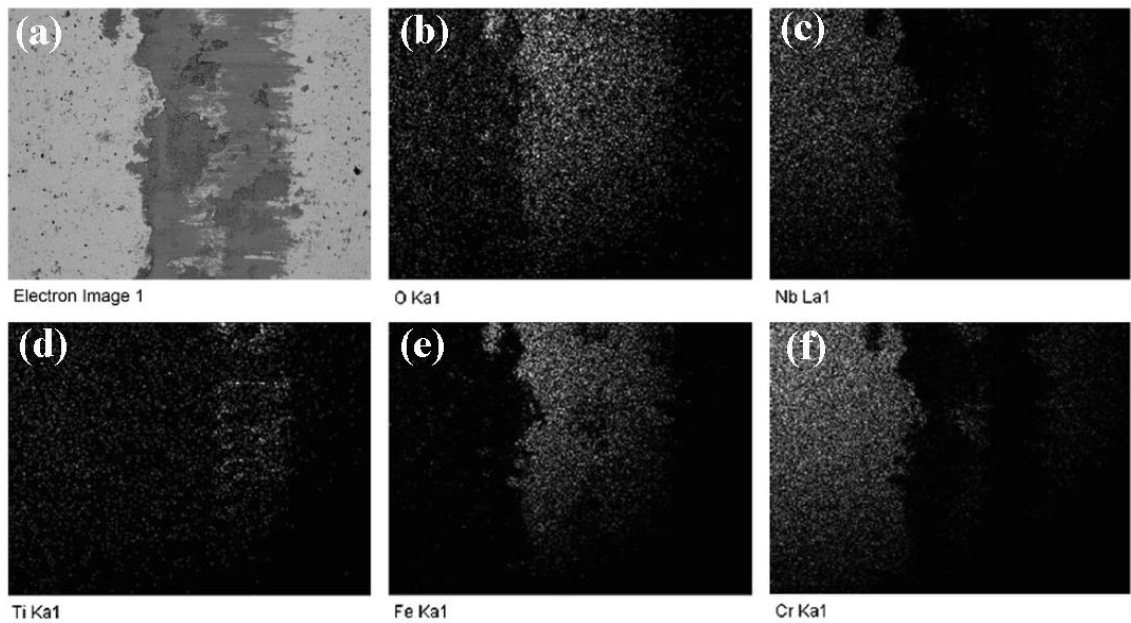


Fig. 2.30 SEM image of the wear track (a) and corresponding X-ray maps of elemental distribution (b) to (f) for the wear test of CrN/NbN-coated Ti-6Al-4V sliding against SAE52100-EN100Cr6 steel under 40N applied load [71].

Recently, Lepicka et al. [72] analyzed the completely worn surface more closely after dry rotary ball-on-disk testing with PVD TiN coated Ti-6Al-4V disk and WC-Co ball. Fig. 2.31 shows the thickness of the PVD coating is about 2 μ m. Fig. 2.32 shows the surface has been completely worn out after the sliding wear test. The worn surface shows the abrasive ploughing grooves, oxygen intensive debris, adhesive cracks which are perpendicular to the sliding direction and tensile cracks which are along the sliding direction.

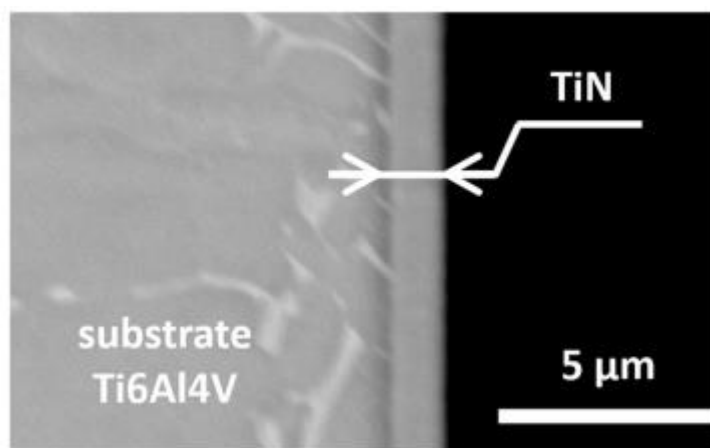


Fig. 2.31 Cross-section of the TiN PVD coated Ti-6Al-4V sample [72].

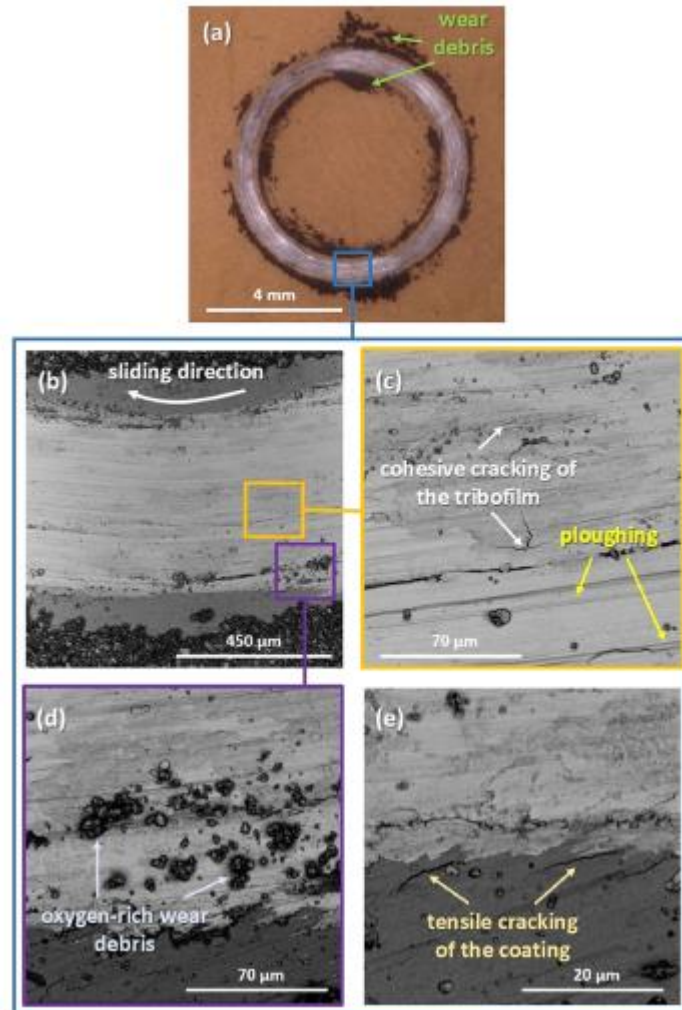


Fig. 2.32 Optical microscope (a) and SEM (b)–(e) images of wear track obtained for TiN coated Ti-6Al-4V alloy after 263.7m sliding distance in dry condition [72].

Applying surface coating to PBF Ti-6Al-4V alloy should also be naturally extended from improving wear resistance of CP Ti-6Al-4V, due to their not significant difference on wear resistance from Li et al.'s study [73]. Li et al. [73] explained that whether hardness higher than 350 HV may result in an increase in wear resistance is unclear, though hardness of SLM Ti-6Al-4V being mainly in martensitic form is above 400 HV. In their study of sliding wear of SLM, electron beam powder bed fusion (EBM) and conventional processed (CP) samples, Li et al. [73] showed no significant difference in wear rate (WR) amongst SLM, EBM and CP Ti-6Al-4V samples.

Study on applying coating to improve tribological improvement of MAM Ti-6Al-4V alloy has only started recently and published work is still rare in the open literature. Kao et al. [74]

applied CN (carbon nitride) and Ti-doped DLC (Ti-C:H) thin films on SLM Ti-6Al-4V which was first nitrided at 900°C before depositing the thin films. A total of six different samples were prepared, namely Ti-6Al-4V alloy (3DT), nitrided Ti-6Al-4V alloy (N3DTs), CN-coated Ti-6Al-4V alloy (CN-3DT), CN-coated nitrided Ti-6Al-4V alloy (CN-N3DTs), Ti-C:H coated Ti-6Al-4V alloy (DLC-3DT), and Ti-C:H-coated nitrided Ti-6Al-4V alloy (DLC-N3DTs). Fig. 2.33 shows the nitride layer is around 8 μ m, and CN or DLC coatings are around 1 μ m on top of nitride layers if such coating were applied. Wear tests using a reciprocating sliding wear tester against 316L stainless steel ball, Ti-6Al-4V ball and Si₃N₄ ball were conducted. Fig. 2.34 clearly shows applying the thin films have reduced the wear depth. Fig. 2.35 gives the examination and appearances of surfaces of DLC-3DT and DLC-N3DTs worn samples. Fig. 2.35(a) and (b) show the wear surface of the DLC-3DT sample. A scooped out surface appearance in Fig. 2.35(a) has indicates the occurrence of severe adhesion wear, and the O content is 30.5 at.% and 38.9 at.% which shows the wear mechanism is one of the severe adhesion wear accompanied by oxidation wear. As seen from Fig. 2.35(c), the wear surface of the DLC-N3DTs sample is smooth and contains only mild scratches, and the main wear mechanism is abrasion wear. Circles 1 and 2 in Fig. 2.35(d) have C contents of 14.2 at.% and 26.1 at.% respectively which is significantly lower than that of the unworn surface (97.7 at.%). Besides, the nitrogen contents in Circles 1 and 2 are 10.6 at.% and 6.9 at.%, respectively which is from the nitride layer. Thus, it is inferred that the DLC coating is broken and the wear scar penetrates almost all of the way through the coating to the underlying substrate (wear depth 1.17 μ m bigger than 1 μ m DLC layer). However, the wear mode(s) leading to failure of the coating has not been clearly explained.

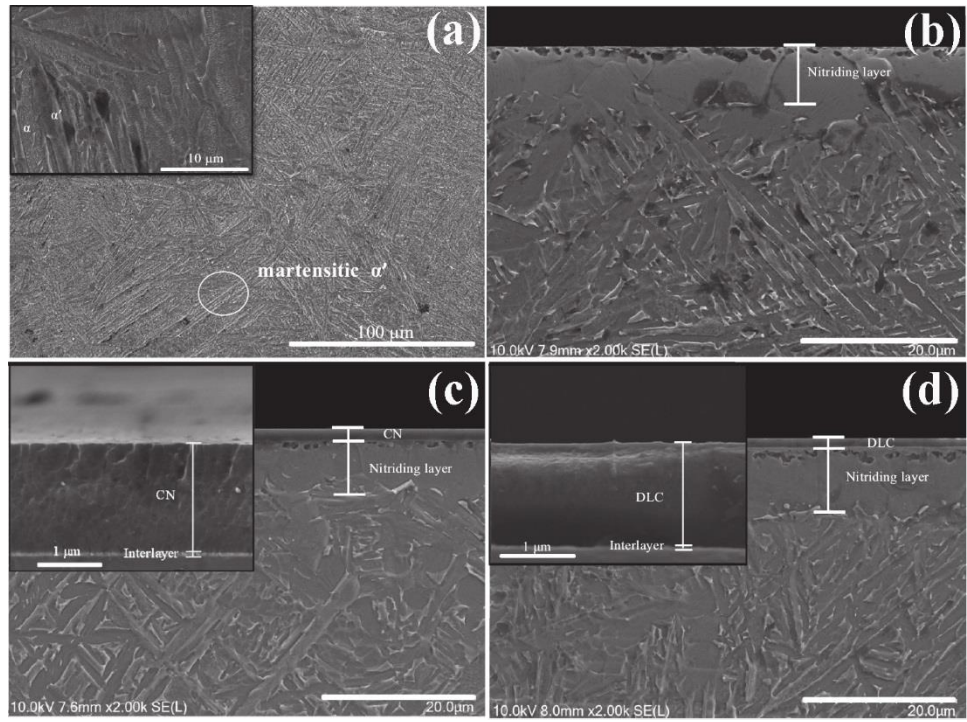


Fig. 2.33 SEM cross-sectional micrographs of: (a) 3DT, (b) N3DTs, (c) CN-N3DTs and (d) DLC-N3DTs [74].



Fig. 2.34 Wear depths of all specimens when sliding against 316L, Si₃N₄ and 3DT balls. (S.D. denotes standard deviation) [74].

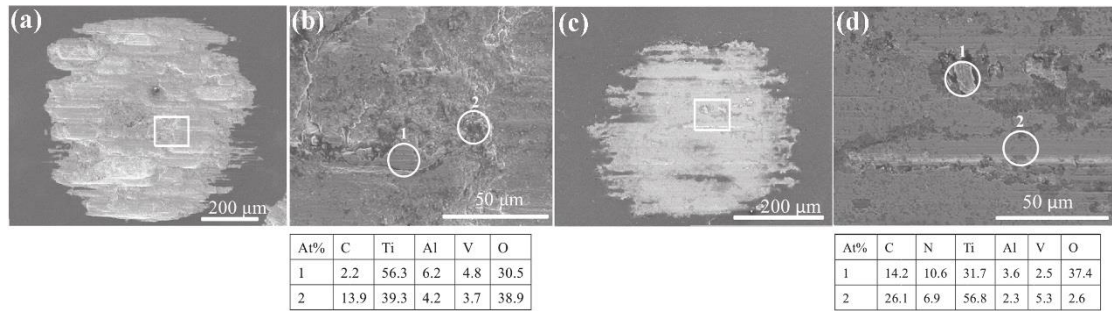


Fig. 2.35 SEM images for wear surfaces on: (a) DLC-3DT, (b) DLC-3DT (1000×), (c) DLC-N3DTs and (d) DLC-N3DTs (1000×) when sliding against 3DT ball, and the EDS analysis results for the regions marked in the corresponding figures (labelled 1 or 2), respectively [74].

By summarizing the studies above, though some of them have noticed the final worn of the PVD coating, and has analyzed the worn surface morphology and chemical contents to try to know the wear process of the PVD coating, however, these studies are all based on the final worn surfaces, not a study until now has well and clearly shown the wear process of PVD coating, since it starts to break to its ultimate failure.

2.4.2 Wear behavior of nitrogen ion implanted Ti-6Al-4V alloy

Apart from PVD coating as the protection method to increase the wear resistance of Ti-6Al-4V alloy, ion implantation is also an important way of improving surface hardness and wear resistance [75][76]. Ion-implantation is usually used to improve the wear resistance of sensitive medical components such as surgical tools and load bearing implants. Unlike the PVD coating that creates a discontinuous layer on top of the base material, ion implantation can provide a gradual transition layer (typically less than 1 μm thickness) by altering the chemical and mechanical properties of the near surface material. This can reduce the risk of delamination of the discontinuous layer resulted from the poor adhesion strength [76][77].

Ion-implantation is a low temperature process that energetic ions are accelerated to the surface of the substrate material and change the surface chemical and physical properties to enhance the wear resistance. At first, a dosage of accelerated ions, which usually contain several KeV to few MeV energy, will pass through the -15 °C beam line with raster scanners (Fig. 2.36). These

raster scanners are applied voltage with vertical and horizontal directions to trap the ions in order to obtain a uniform implanted region. When the ions pass through the beam line and lose all their energy and at the same time incorporated into the substrate material, the surface is implanted [77].

During ion implantation process, the substrate surface will be undergoing changes, some incident ions penetrate a certain depth of the surface material and be implanted, and other ions scatter away (Fig. 2.37). Besides, some substrate material ions can be sputtered by the collision cascade of the incident ions [78]. The type, dosage and energy of the ions are the most important parameters influencing the properties of the implanted surface and ion concentration.

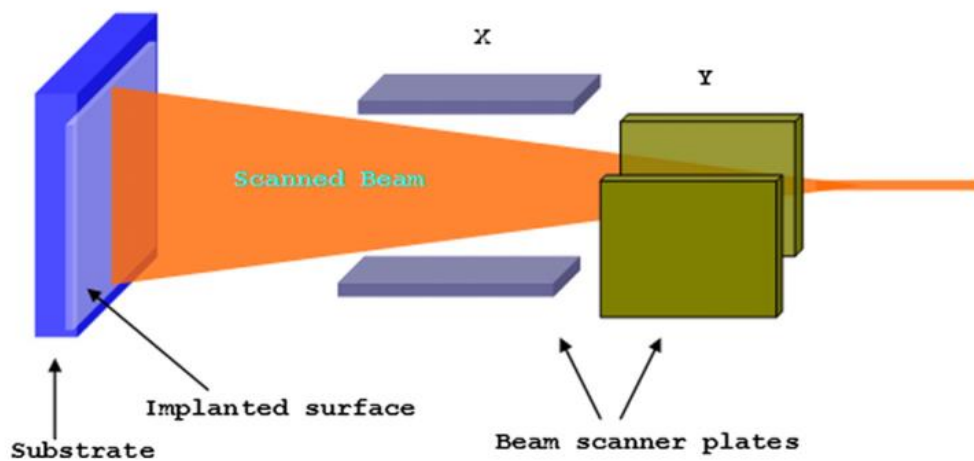


Fig. 2.36 Ion implantation beam scanner [77].

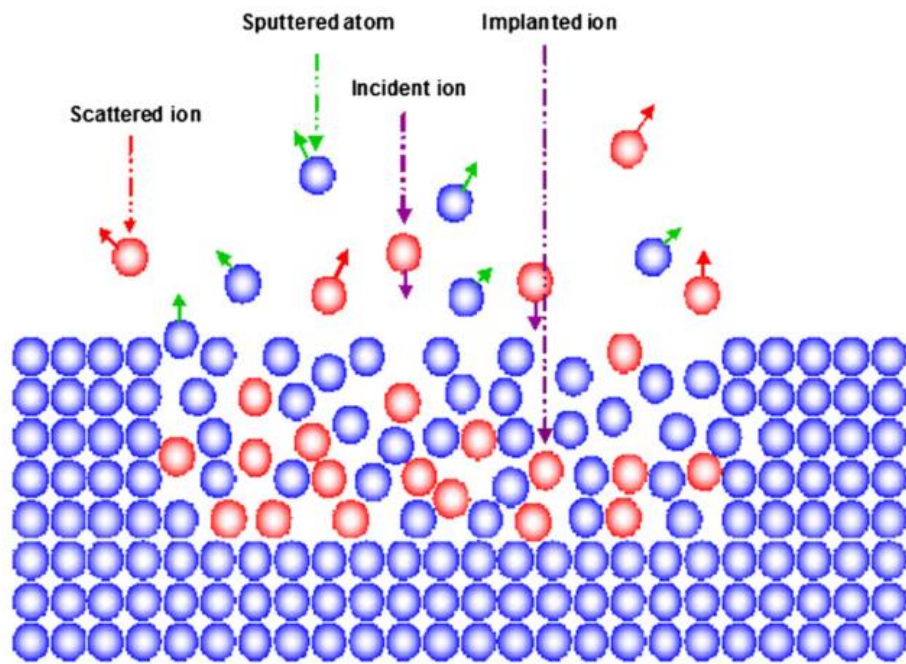


Fig. 2.37 Schematic of ion-solid interactions [77].

Titanium ion implantation can be conducted by Ca, P, C, CO, O, N, Na, Mg, Ag ions and inert ions such as He and Ar. By these types of ions implanted into the titanium alloy surface, the material surface stability, wear and corrosion resistance can be improved. Due to the abundance in nature and the ability to improve surface properties, nitrogen ion implantation has been studied most extensively. There are several articles discussing the ion implantation of Ti-6Al-4V and its influence on wear performance, where the relationship between the dosage of N^+ and wear is discussed in detail.

In the comprehensive review by Rautray et al. [77], it is generally believed that a significant improvement of wear resistance can be achieved by nitrogen ion implantation on Ti-alloys. In this review, a particular example from Boampon et al. [79] on the effect of ion implantation on improving wear resistance has been detailed.

Boampon et al. [79] applied a dose of $2 \times 10^{21} N^+$ ions/m² to Ti-6Al-4V alloy and conducted sliding wear tests on the ion implanted samples with ultra-high molecular weight polyethylene (UHMWPE) pins as counter material. Fig. 2.38 shows the Knoop hardness of ion implanted Ti-6Al-4V compared with as built samples, and it can be observed that ion implantation results in up to two-fold increase in hardness. The wear weight loss also showed that ion implanted

Ti-6Al-4V samples have better wear resistance than the as built Ti-6Al-4V samples (the wear weight loss of ion implanted and as built Ti-6Al-4V samples are $81 \pm 0.06\mu\text{g}$ and $214 \pm 0.08 \mu\text{g}$ respectively, when they slide against UHMWPE pin).

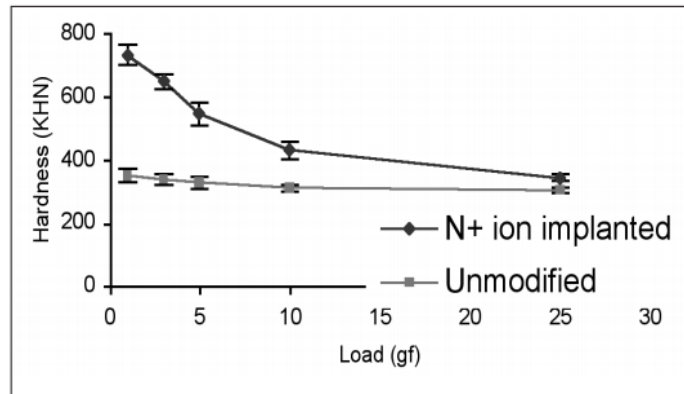


Fig. 2.38 Knoop surface microhardness of Ti-6Al-4V alloy with and without ion implantation [79].

Fig. 2.39 is the comparison of the wear tracks of unmodified and implanted Ti-6Al-4V plates tested against UHMWPE pins. It can be seen from Fig. 2.39(a) that random severe scratches and grooves are the main features of the wear track morphology which shows severe abrasive wear. It could be because of the strong adhesion between UHMWPE and the titanium oxide film, which is in favor of three-body abrasive wear [80-82]. In contrast, testing with UHMWPE/N⁺ ion implanted Ti-6Al-4V couple showed almost no damage in the wear tracks of the Ti-6Al-4V plates as shown in Fig. 2.39(b). It is known that TiN precipitate formed on the Ti-6Al-4V surface can stabilize the outer oxide layer and thus reduce the removal of oxide particles from the surface, which can reduce the wear of both Ti-6Al-4V plate and UHMWPE pin [79]. However, the precise mechanism that retards the onset of abrasive wear is not yet clear [81][83].

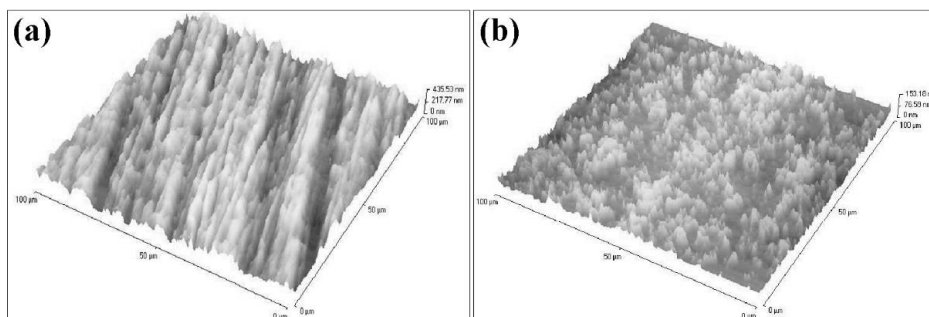


Fig. 2.39 AFM image of worn Ti-6Al-4V surface (a) and N⁺ ion-implanted Ti-6Al-4V surface (b) [79].

The original work where the dose of $2 \times 10^{21} \text{N}^+ \text{ions/m}^2$ was found optimal is from the study of Fabre et al. [84], while Fabre et al.'s work has not been cited particularly when wear resistance was discussed in Rautray et al.'s [77] review. Fabre et al. [84] have conducted Ti-6Al-4V /UHMWPE wear testing based on a range of N^+ dosage, and by their simulation, the maximum concentration was reached at the depth of 70nm from the surface for different N^+ dosages. Fig. 2.40 is the adhesion work measurements. Adhesion work is the free energy change when two surfaces adhere to each other, and it can be used to evaluate the adhesive behavior and strength. In this study, they used heptane liquid, which is an organic liquid, simulating UHMWPE pin to obtain the adhesion work between Ti-6Al-4V and UHMWPE. Fig. 2.40 shows the minimum value is obtained when the N^+ dosage is 2×10^{21} , besides, the measurement of UHMWPE pin wear loss further showed the minimum wear loss value was with the $2 \times 10^{21} \text{N}^+$ dosage test.

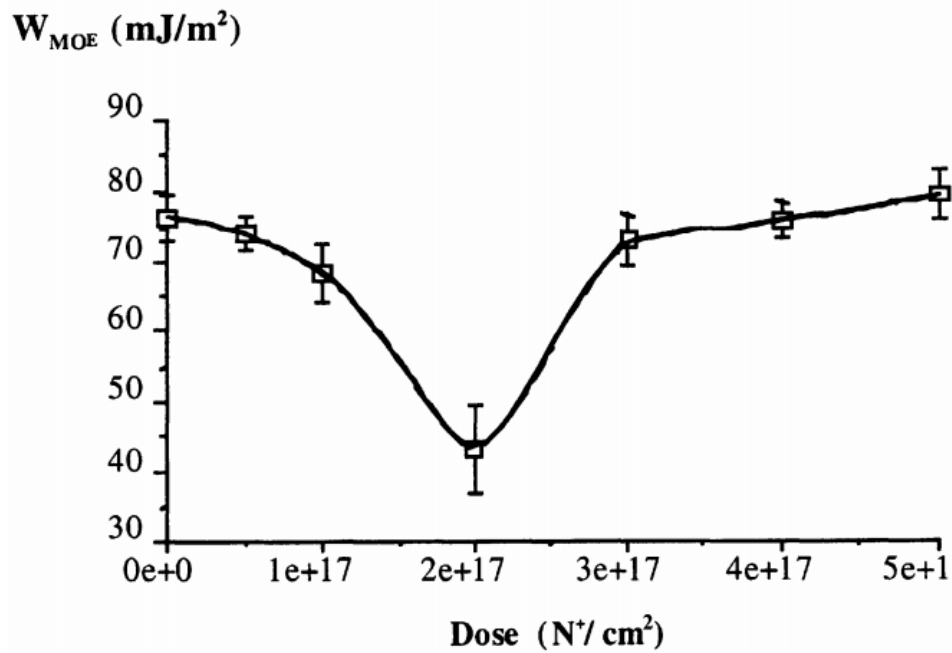


Fig. 2.40 Adhesion work variation of implanted Ti-6Al-4V [84].

It should be noted that the conditions (particularly the accelerating voltage) in Fabre et al.'s work [84] are different from that used in Boampon et al.'s [79] work (Boampon et al. used Zymet Z-100 device and 100KeV voltage, while the device in Fabre et al.'s [84] work is Varian DF4 and the voltage is 40KeV). Besides, [79] and [84] used UHMWPE and ion implanted or unmodified Ti-6Al-4V as wear couple in their sliding wear tests; however, the material properties for ceramic or metal is quite different to polymer material, adhesive and

abrasive wear behaviors during wear tests of Ti-6Al-4V /ceramic or Ti-6Al-4V /metal should be very different from those of Ti-6Al-4V /polymer wear test [73]. Whether Boampon et al. [79] or Fabre et al [84]’s findings could be extended to the current Ti-6Al-4V /WC-Co condition may be viewed uncertain. A further confusion may need to be pointed out that in a recent overview [85] of the topic on surface modification of Ti-alloys, the condition of the dose of $1 \times 10^{21} \text{N}^+ \text{ions/m}^2$ has been referred to as the best condition, citing Rautray et al.’s review [77]. This dose is half the dose mentioned in [79][84] which was stated as the best N^+ ions dose condition.

Three studies about sliding wear testing of pure Ti /ceramic or Ti-6Al-4V /metal couples have also been published and the tests conditions and results are listed in table 2.3. In the study of Budzynski et al. [86] and Kaminski et al. [87], the wear was measured by a cross-sectional area of the track as shown in Fig. 2.42 and 2.43.

Table 2.3 Papers about ion implanted Ti or Ti-6Al-4V samples wear tests.

Paper	Dosage, $\text{N}^+ \text{ions/m}^2$	Accelerating voltage	Sample	Counter material	Wear test	Results
[88]	1×10^{21} , 5×10^{21} , 1×10^{22}	150KeV	high purity titanium	Al_2O_3 ball (10mm diameter)	Liner reciprocating, 0.49N, 6mm stroke, 1.67mm/s, 50 cycles	The worn area of a dose of $5 \times 10^{21} \text{N}^+ \text{ions/m}^2$ is narrower than other dosages (Fig. 2.41)
[86]	1×10^{20} , 1×10^{21} , 1×10^{22}	120 KeV	Ti-6Al-4V	Bearing steel ball (2mm diameter)	Rotatory ball-on-disk, 2000 cycles	ion implantation improved wear resistance with a rapid reduction of wear rate when dosage increase from 1×10^{21} to $1 \times 10^{22} \text{N}^+ \text{ions/m}^2$ (Fig. 2.42)
[87]	1×10^{21}	60 KeV	Ti-6Al-4V	steel ball (2mm diameter)	Rotatory ball-on-disk, 500mN load, 10000 cycles	a slightly higher wear resistance for the implanted samples, but the standard deviation values of their data are significantly higher than the difference in wear resistance (Fig. 2.43)

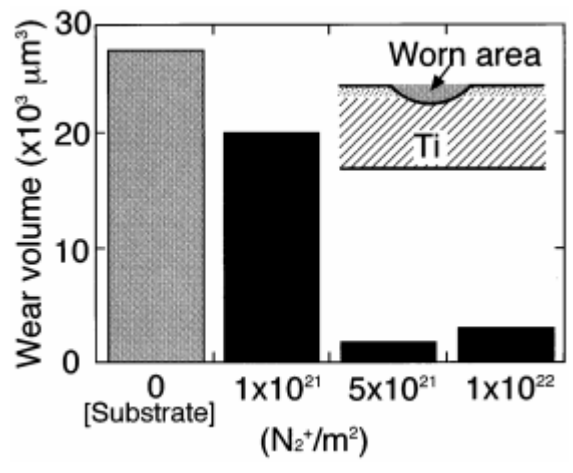


Fig. 2.41 Relation between load and penetration depth of indenter [88].

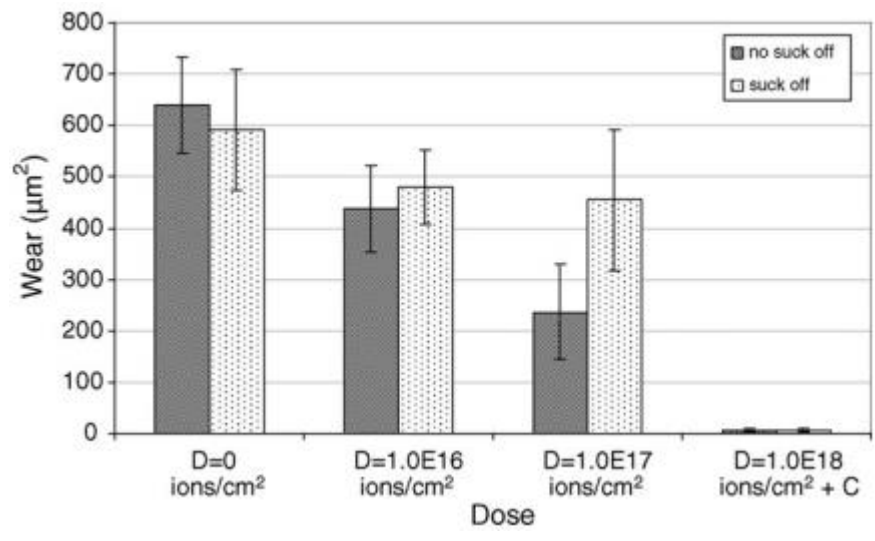


Fig. 2.42 Wear values of implanted and unimplanted samples after 2000 cycles [86].

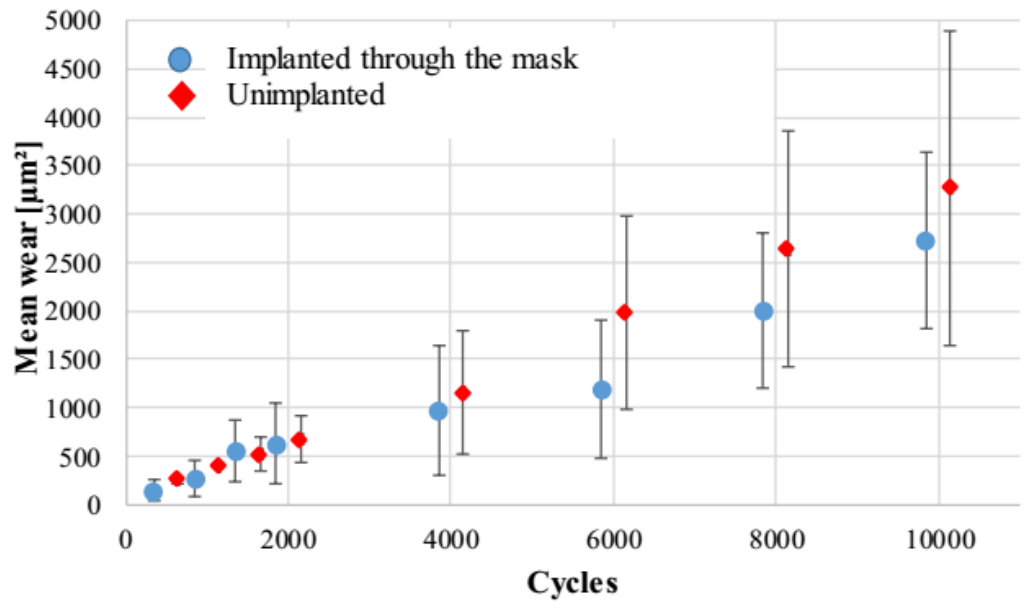


Fig. 2.43 Mean wear of Ti Grade 5 samples with standard deviations [87].

The limited studies and data available, as discussed above, may have suggested that nitrogen ion implantation should provide wear resistance, but when a dosage of $\leq 1 \times 10^{21} \text{N}^+ \text{ions/m}^2$ is applied, the effect is not significant. A dosage of significantly higher than $1 \times 10^{21} \text{N}^+ \text{ions/m}^2$ should result in a significant effect on increasing wear resistance. Our samples both “ $6 \times 10^{17} \text{ at/cm}^2$ of nitrogen”, meaning $6 \times 10^{21} \text{N}^+ \text{ions/m}^2$ supposed to provide wear resistance, but under such dosage, the wear resistance under nitrogen ion implanted Ti-6Al-4V/metal couple should be further investigated and discussed. Besides, not a paper until now has discussed the wear performance of ion-implanted PBF Ti-6Al-4V.

2.5 Summary of the literature review and research questions

The above review of the relevant literature has shown the following:

- Recent data in literature are unclear on whether higher hardness may result in an increase in wear resistance of Ti-6Al-4V, following Archard’s linear relationship. Recent development of both SLM and EBM has shown fully dense parts can be produced by these processes. Although hardness values of parts produced by these powder bed fusion processes are higher than 350 HV, whether these parts are more wear resistant than parts produced by conventional processed and annealed parts is highly uncertain. A further confusion from data of recent wear studies is the hardness values lower than 400 HV reported for SLM processed Ti-6Al-4V alloy in some studies.
- The current understanding on the effect of temperature on wear rate from literature may be viewed contradictory from different studies. A number of studies based on measuring volume loss of the Ti-6Al-4V pin from pin-on-disk experiments have shown that wear rate generally decreases as temperature increases, although it depends also on the level of load applied. On the other hand, a study based on directly measuring the wear volume of the wear track in the disk clearly shows the wear rate is directly proportional to the test temperature. The suggestion of tribo-oxide layer to reduce wear rate also seems unclear from the literature data.

- Two aspects of wear of coated Ti-6Al-4V samples have not been fully understood. The first is the detail of wear mode of the coated samples (coating fracture and detaching or gradual wear), although applying hard coating is generally understood to reduce wear rate in the tested conditions reported. The second is the lack of understanding, comparing SLM samples to the more conventionally processed Ti-6Al-4V samples with the latter considerably lower in hardness, on how the coating performance is affected by the substrate hardness and how the coating may fail as wear testing progresses. Furthermore, although ion implantation is a well-established surface engineering process, wear testing of ion implanted Ti-6Al-4V samples have seldom been conducted.

The above summary shows that wear rate and wear modes of powder bed fusion Ti-6Al-4V alloy are currently insufficiently understood. Considering that powder bed fusion additive manufacturing technology has been advanced considerably in recent years and the powder bed fusion Ti-6Al-4V will be more widely applied, and considering the above identified knowledge gaps, the following research questions are necessary to be addressed:

- Under a representative wear condition, how does the wear rate of martensitic and thus harder Ti-6Al-4V samples of SLM compare with the $\alpha+\beta$ forms of Ti-6Al-4V processed by EBM and CP and what are the deformation and fracture mechanisms contributing to the respective wear rate?
- Following on the above question, what is the effect of temperature on the respective wear rate corresponding to each form of Ti-6Al-4V, what are the surface products and wear debris that may form and how do these products/debris affect wear rate during sliding wear testing at various temperatures?
- How does the martensitic harder Ti-6Al-4V substrate affect the wear process of a hard coating in comparison with the coating on the softer CP substrate and, in general, how does the coating wear or fracture contribute to the measured rate as wear testing progress?
- Given that the SLM Ti-6Al-4V is martensitic which is considerably harder than CP Ti-6Al-4V in $\alpha+\beta$ form, what difference would it be in the nitrogen ion implanted layer in

terms of hardness values and how this implanted layer may affect wear process and wear rate?

Experiments and analyses have been conducted to answer these questions. Detailed description and explanation on the experimental and analytical procedures are given in Chapter 3. Results and discussion are reported from Chapter 4 to Chapter 7, accordingly, following the above research questions.

Chapter 3 Research Methodology

Research methodology is going to be stated in detail in this chapter. By introducing the wear tests environment including the counter material, test equipment and wear conditions for as-built samples, PVD coated and ion-implanted samples, the different manufacturing routes of PBF and CP samples are going to be stated. The PVD coated layer is discussed in this chapter, and the ion implanted dosage and the nitrogen distribution after ion implantation will also be described. Besides, the material structure observation equipment, physical and surface parameters detecting equipment are also going to be introduced.

3.1 Samples, counter material and wear test equipment

Additively manufactured samples of Ti-6Al-4V alloy were made using a SLM machine (AM400, built by Renishaw, UK) and an EBM machine (Q20, built by ARCAM, Sweden). These samples were produced using machine parameters normally for achieving nearly fully dense parts. Parameter values are shown by table 3.1 and 3.2. When the SLM or EBM printers are under working condition, the chamber gas for SLM machine is Ar, while for EBM machine, the chamber is vacuum. The SLM and EBM samples are as-built samples without any post heat treatment. CP samples were sectioned from an annealed titanium grade 5 plate following ASTM B265 according to supplier (Baoji Really Metals and Alloys Co., China). The conventional processed samples were made by annealing after casting and rolling. Their microstructures are shown in Fig. 1.4, showing the typical martensite α' acicular structure in SLM, $\alpha+\beta$ lamellar structure in EBM and structure of “short fibrous” β in α matrix in CP samples. Hardness tests were conducted on these polished samples using a Leco LM-800AT microhardness tester (Fig. 3.1) using a load of 1kgf. Hardness values were determined to be $428\pm 17\text{HV}$ for SLM samples, $359\pm 16\text{HV}$ for EBM samples and $324\pm 8\text{HV}$ for CP samples, based on 10 measurements for each type of samples. Table 3.3 lists the 10 measurements values.

Table 3.1 SLM process parameters.

Parameter	Value
Laser beam radius	35 μ m
Layer thickness	60 μ m
Hatch distance	120 μ m
Laser powers	300W, 400W, 500W (at 800mm/s)
Scan speeds	1000mm/s, 800mm/s, 660mm/s (at 400W)

Table 3.2 EBM process parameters.

	Parameter	Value
Contours	Number of contours	3
	Outer contour offset	0.27mm
	Inner contour offset	0.18mm
	Contour current	9mA
	Contour speed	550mm/s
Hatch	Line offset	0.22mm
	Max current	28mA
	Focus offset	45mA
	Speed function	33

Table 3.3 Micro-hardness test results.

Test	1	2	3	4	5	6	7	8	9	10	Average
SLM	443.5	425.9	411.4	418.8	415.7	429.5	423.9	425.1	444.3	437.6	427.57
EBM	368.4	365.7	370.2	359.2	374.9	358.2	347.5	343.2	350.9	353.8	359.2
CP	317.3	323.2	319.8	324.9	316	333.2	331.4	337.3	314.8	324.5	324.24



Fig. 3.1 Micro-hardness tester.

When conducting the sliding wear tests under room and high temperature, as well as tests for PVD coated and ion implanted samples, the counter ball material was WC-Co (WC: 92%, Co: 8%, 90-92 HRC) and the ball diameter was 10 mm. This counter material has been commonly used for studying the performance of Ti-6Al-4V alloy under sliding wear conditions [38][39][89][90].

A Linear Reciprocating Tribometer (Ducom TR-282, USA) was used and ball on plate configuration was selected to conduct the dry sliding wear tests as shown by Fig 3.2. The sample is tightly fixed into the equipment sample bed, the counter material is grasped by the holder and be driven by a motor to reciprocally move on the sample surface. The normal load is applied on the counter material holder by a cantilever, its value can be changed by the weight in the bottom box of the tribometer which is dropped down through the vertical rod that connected to the cantilever. The real time coefficient of friction (COF) was automatically recorded by the device during the tests. By observing the COF curve, it is convenient to identify the wear surface changes during the wear tests, especially for PVD coated and ion-implanted samples.

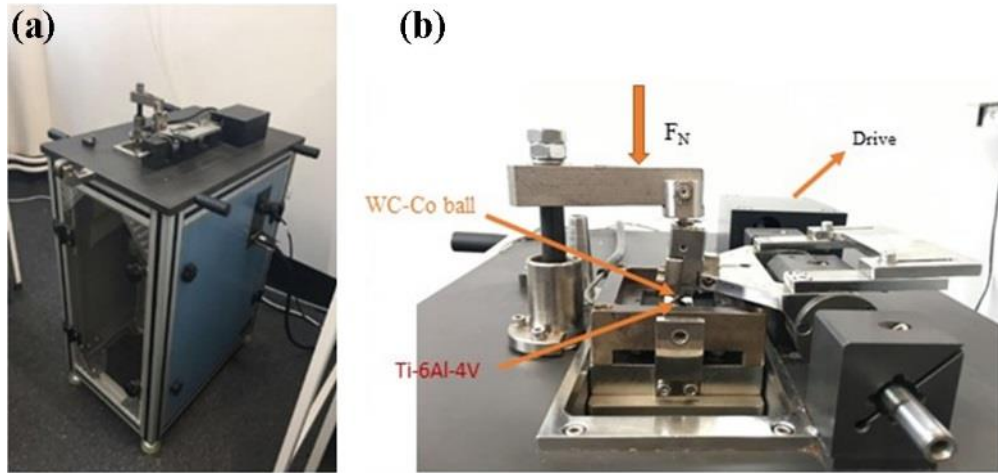


Fig. 3.2 Liner reciprocating tribometer.

3.2 Sample preparation and nanoindentation

All the samples were made or sectioned into 40mm×40mm×5mm in size in order for the samples to fit into the sample holder of the tribometer, and make sure multiple wear tests can be conducted on each sample. Before wear tests or surface treatment (PVD coating or ion-implantation), all wear samples were ground by SiC grinding papers until grit-2400 to achieve an average surface roughness (R_a) of $\sim 0.05\mu\text{m}$ measured using a Taylor Hobson Talysurf profilometer.

If tests need samples coated with physical vapor deposition (PVD), polished samples were then coated using PVD process (Surface Technology Coatings, Melbourne, Australia) with a TiN coating. As shown in Fig. 3.3, the thickness of the coating (h_{Coating}) is $\sim 2.4\mu\text{m}$ and the coating has densely and evenly covered the SLM sample with martensitic structure or CP sample with $\alpha+\beta$ phase structure, respectively.

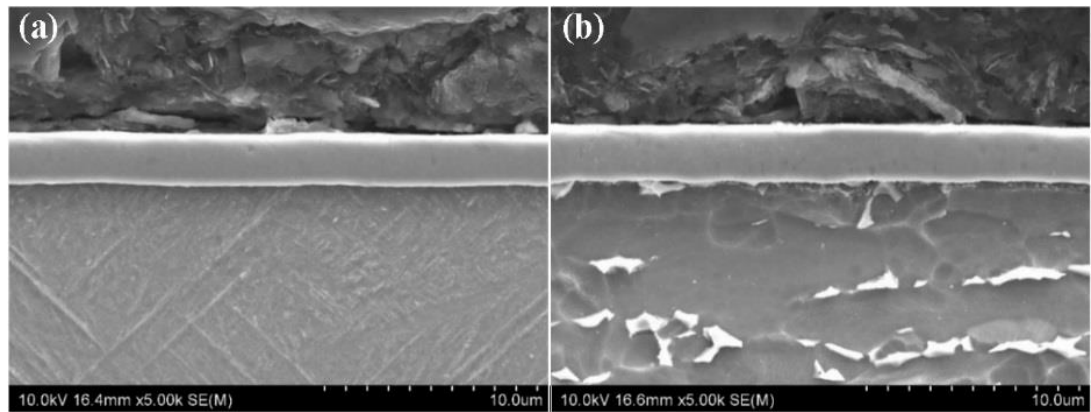


Fig. 3.3 Cross sections of PVD TiN coated on: (a) SLM martensitic and (b) CP $\alpha+\beta$ Ti-6Al-4V samples.

For ion-implantation surface treatment, polished samples were cut into 12mm \times 10mm \times 5mm pieces in order for them to be ion-implanted by GNS Science. The N^+ ions distribution from the top most surface is shown by Fig. 3.4. There are two different implantation processes (N1 or N2), samples under both processes have a total dosage of $6\times 10^{17} N^+/cm^2$ of nitrogen. After ion-implantation, these ion-implanted samples were tightly fixed into a holder with 40mm length before they were ready for wear tests.

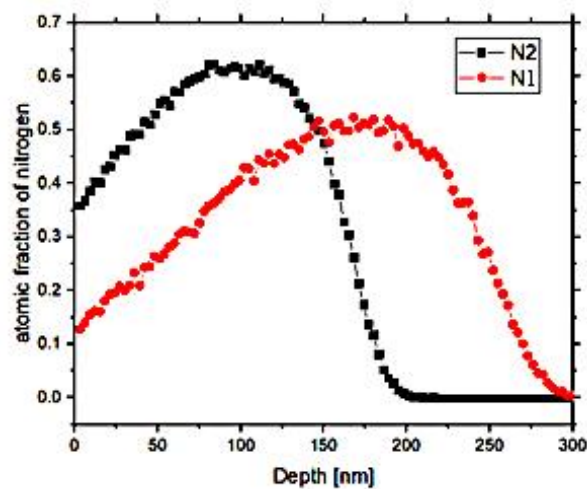


Fig. 3.4 Simulated nitrogen concentration vs. depth for the two implantation processes.

To test the difference of the two ion-implanted methods, as well as to have a comparison with the PVD coating surface treatment, nanoindentation was used. Nanoindentation was conducted by a TI 950 Triboindenter, five test places evenly distributed on the sample surface were selected for each test sample. For each place, six loads were applied (1000 μ N, 2000 μ N, 4000 μ N, 6000 μ N, 8000 μ N, and 10000 μ N) on six points, respectively. How hard a material is measured

by how deep (h_{n-i}) the indenter penetrates under a specific maximum load (P_{max}). The average value of h_{n-i} by 5 times tests under each applied P_{max} was obtained for each test sample. Fig 3.5 present the curves during nanoindentation for a SLM N2 ion-implanted sample.

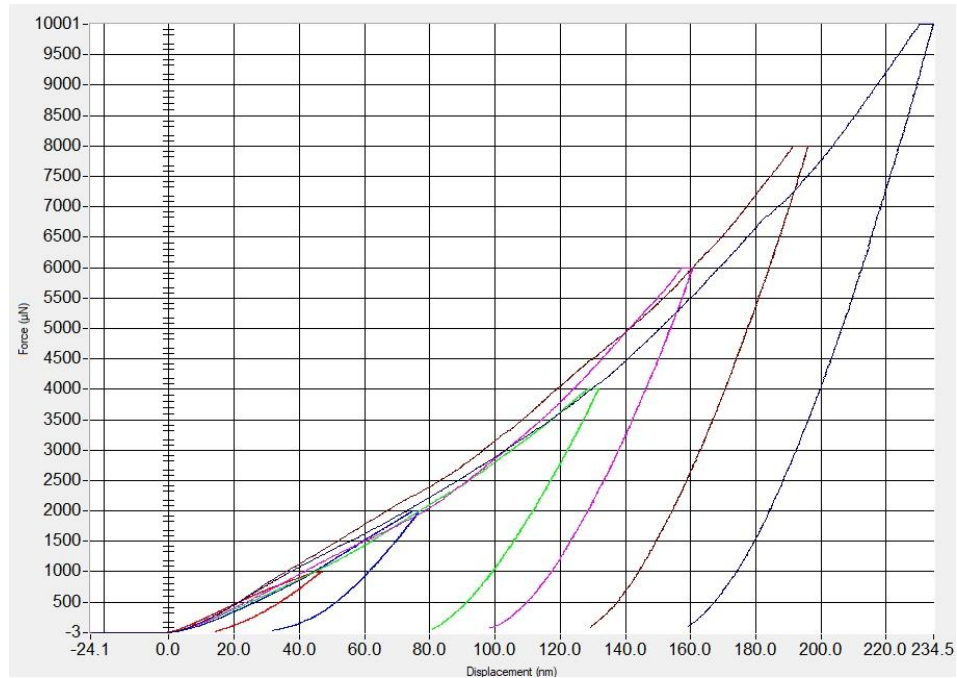


Fig. 3.5 Curves for nanoindentation test of a SLM N2 ion-implanted sample.

3.3 Tests conditions

Tests were conducted using a range of test conditions, as listed in Table 3.4. Duplicate tests were conducted for each condition. Though we used multiple tests conditions for room temperature tests for samples without surface treatment, it must be pointed out that, for high temperature tests, the load and frequency were fixed at 6N and 5Hz, thus the variable is only the temperature. For PVD coated samples tests, the load and frequency were 2N and 5Hz as for the surface treatment samples tests, we are going to focus on the surface coating failure mechanism and not the various wear conditions. Besides, serious wear had occurred using 2N loading for only a short wear distance/time when doing tests for ion-implanted samples. Thus, all tests using ion implanted samples were conducted using 1N load, 2Hz and 40m total wear distance with the sliding stroke of 10mm.

Table 3.4 Sliding wear conditions.

Loads (F_N)	1N, 2N, 6N, 10N
Frequency (f)	2Hz, 5Hz, 8Hz
Sliding stroke	10mm
Sliding distance	500m, 40m
Temperatures	25°C, 200°C, 400°C, 600°C

Different from other tests that run over for their whole sliding distance, tests for PVD coated samples had additional tests after duplicate tests of 500m sliding distance. These tests were conducted to estimate the distance within which the coating is effective in preventing wear loss of Ti-6Al-4V, thus these tests were stopped when the coating was broken. By this monitoring conducted by examining the wear tracks of samples tested for various times, how the coating itself wears and deteriorates was monitored so that the failure mechanisms can be understood.

3.4 Wear measurement

After testing, the samples were first checked by an Olympus SZX9 stereomicroscope (Fig. 3.6), to roughly know the shape of the track or the coating status, and then wear volume (WV) was estimated. This was done by first determining 15 cross sectional profiles evenly distributed along each wear track using a stylus profilometer. The cross-sectional profiles were then converted to cross-sectional areas using ImageJ software. The software can also measure the depth and width of a profile at the same time. The average value of these areas was then multiplied by the track length to yield the wear volume of the track. The conventionally used wear rate (WR) is then taken as the wear volume divided by the sliding distance (500m). For example, Fig. 3.7 is a sectional profile near an end of a wear track from a CP sample after testing under 200°C and 2N load. The area of this profile is 0.024mm², and after gathering all 15 areas of this track, the average area is 0.0496mm², thus wear volume is 0.0496 mm² × 10mm (wear track length)=0.496mm³, wear rate is 0.496 mm³/500m=9.92E-4mm³/m. The depth and width of the profile have been marked in the figure, and the depth and width of a wear track can

help evaluate the shape of the wear track is regular or not (Chapter 4), or consider the coating is failed or not (Chapter 6).

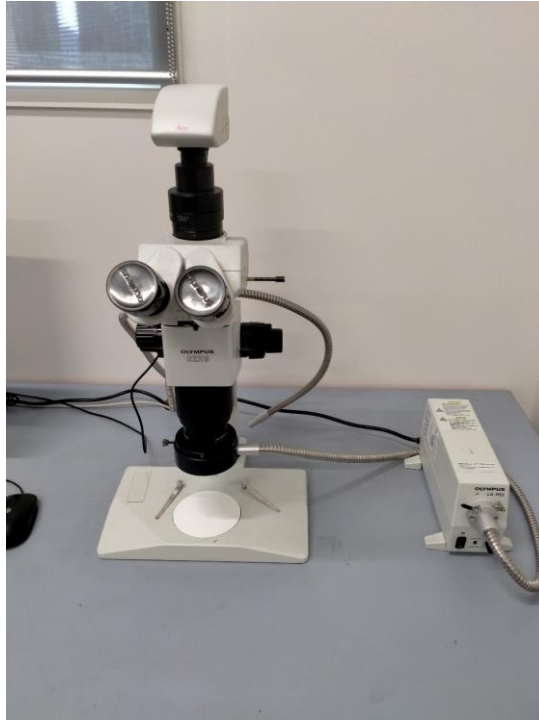


Fig. 3.6 Olympus SZX9 stereomicroscope.

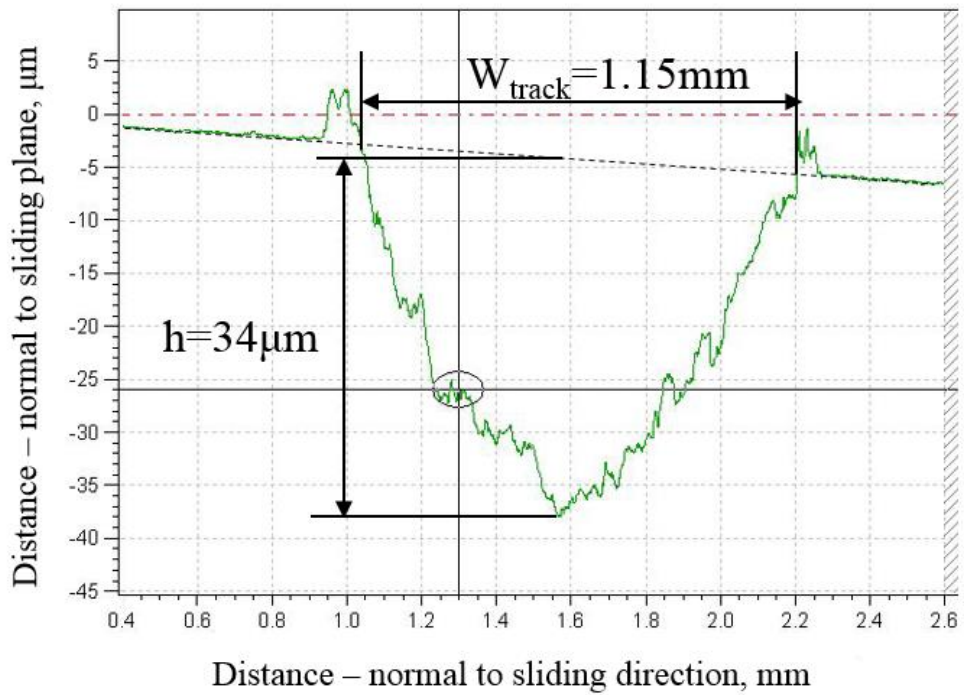


Fig. 3.7 A sectional profile for a CP sample wear track tested under 200°C and 2N load.

After testing and measuring, wear tracks were examined using a Hitachi SU-70 field emission scanning electron microscope (FE-SEM) (Fig. 3.8). For microstructure observation, cross sectional samples of wear tracks were made first by carefully sectioning along the center line in longitudinal direction of each track. However, for examining how the PVD coatings have been thinned during wear testing, cross sectional samples of wear tracks were prepared by cutting normal to the wear track sliding direction.

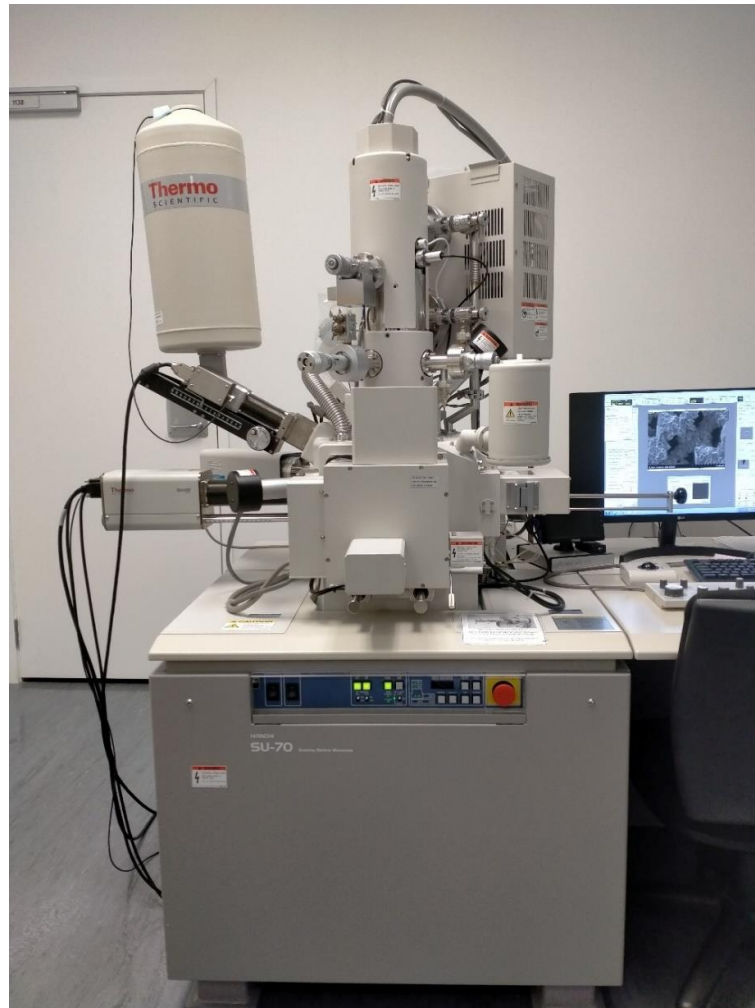


Fig. 3.8 Hitachi SU-70 field emission scanning electron microscope (FE-SEM).

Samples were then mounted using a Struers LoboPress and ground manually with 180, 500 and 1200 grit SiC papers before the final fine polishing using a Struers TegraPol 21 automatic polisher down to $0.03\mu\text{m}$ using colloidal silica suspension (OP-S). Polished samples were then etched using the Kroll solution (2% HF, 5% H₂NO₃, 93% H₂O). Examination of microstructure of the as-received and tested samples was conducted using the FE-SEM.

Chapter 4 Dry Wear Behavior of SLM, EBM and CP Samples

Results and discussion of this thesis starts with the wear behaviors of the alloy processed by SLM, EBM and CP, representing the martensitic and $\alpha(\text{hcp})+\beta(\text{bcc})$ structures and three levels of hardness, during tests at room temperature. Wear rate affected by wear load and frequency (speed) have been determined. Examination of track surface appearance and cross-sectional features of tracks to explain the reasons of wear rate data under various conditions have been conducted. Furthermore, the known mechanical properties of the alloy in various forms of structure have been qualitatively considered to explain how they may have behaved and to have resulted in the various wear rates under the current wear test conditions.

4.1 Wear rate

4.1.1 Wear rate as a function of applied load

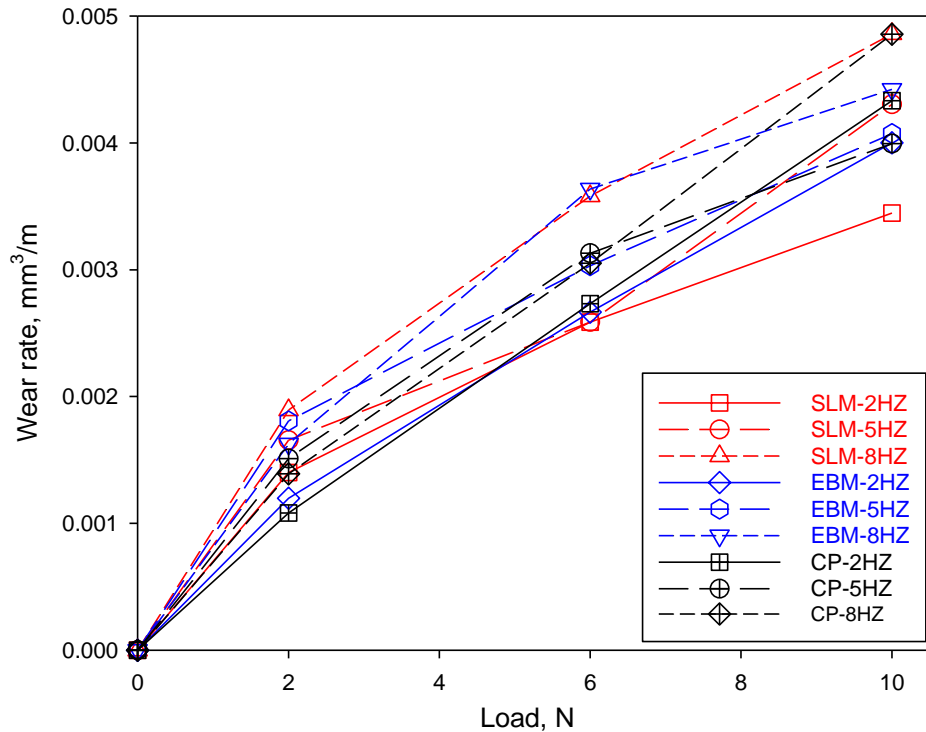


Fig. 4.1 Values of WR plotted as a function of test load.

Values of WR for wear tests with conditions listed in Table 3.4 for as built samples under T_{Rm} in

Chapter 3 are plotted as a function of F_N in Fig. 4.1. Each data point is the average of the WR measurements from the duplicate tests in one test condition. In Fig. 4.1, zero load which should result in zero WR has been included so that the trend of WR change as a function of the increase in F_N can be better evaluated. It is clear that the trend is not linear, meaning:

$$WR = aF_N^n \quad (4.1)$$

where $n \neq 1$. This trend is similar for the three different types of samples although these samples differ in microstructure and hardness. In the plot of WR vs. F_N , n values for the plots differ significantly from 0.51 to 0.88 determined by regression analysis. This variation can be shown not to be the result of the difference in manufacturing route (i.e., SLM, EBM or CP), but may result from not having more tests for each alloy condition in different F_N values, although in each F_N condition duplicate tests were conducted. However, as the primary aim of the present work is to evaluate the comparative performance of the alloy in different microstructural states, the more accurate determination of n values is not considered.

4.1.2 Wear rate as a function of sliding frequency

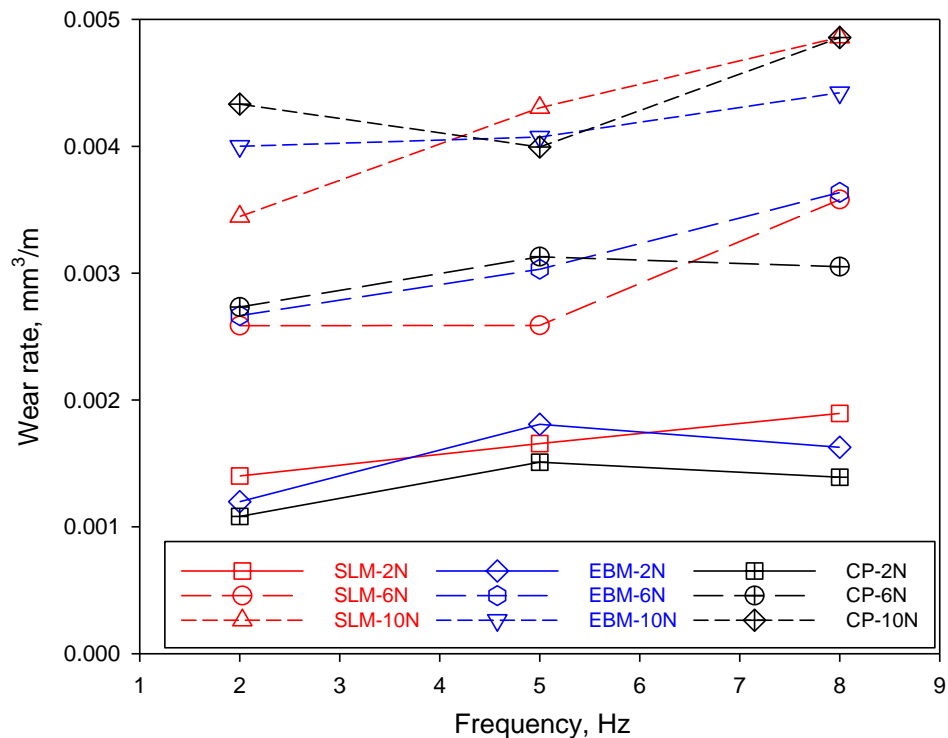


Fig. 4.2 Values of WR plotted as a function of test frequency.

Values of WR for wear tests with conditions listed in Table 3.4 for as built samples under T_{Rm} in Chapter 3 are plotted as a function of f , as can be seen in Fig. 4.2, the effect of f on WR is overall weak. This can be further understood by examining WR values of 6N loading, as an example. A linear regression indicates an increase in WR from $2.7 \times 10^{-3} \text{mm}^3/\text{m}$ at 2Hz to $3.4 \times 10^{-3} \text{mm}^3/\text{m}$ at 8Hz (for $F_N=6\text{N}$). This means that, $\Delta WR/\Delta f = [(3.4 \times 10^{-3} - 2.7 \times 10^{-3}) \text{mm}^3/\text{m}] / 6\text{Hz} = 1.2 \times 10^{-4} (\text{mm}^3/\text{m})/\text{Hz}$. Thus, overall, as f increases, WR increases but at a low rate.

This dependency of WR on f can be compared to how the change of F_N affects WR. It is readily observed in Fig. 4.1 that $\Delta WR/\Delta F \approx 3.2 \times 10^{-4} (\text{mm}^3/\text{m})/\text{N}$ over the range of F_N from 2 to 10N, although the increase is not exactly linear. This means that over the range of $\Delta F_N (=8\text{N})$ used, ΔWR could be $2.6 \times 10^{-3} \text{mm}^3/\text{m}$ ($\gg 7.0 \times 10^{-4} \text{mm}^3/\text{m}$). Thus, the effect of increase in every N causing the increase of WR [$=3.2 \times 10^{-4} (\text{mm}^3/\text{m})/\text{N}$] is stronger than the effect of increase in every Hz [$=1.2 \times 10^{-4} (\text{mm}^3/\text{m})/\text{Hz}$].

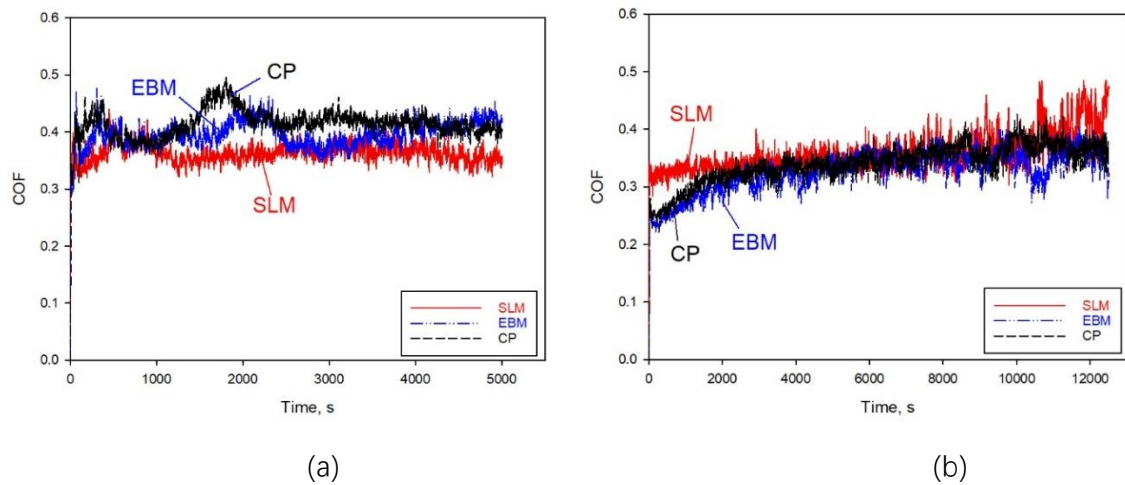


Fig. 4.3 COF values plotted as a function of time for test conditions: (a) 6N at 5Hz and (b) 10N at 2Hz.

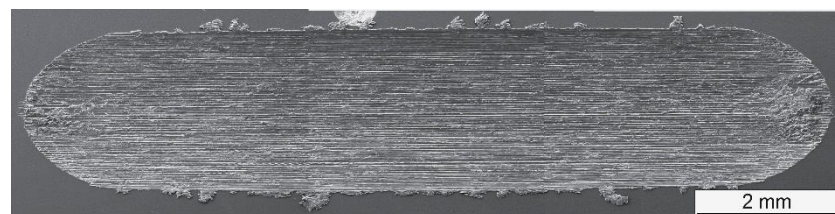
Fig. 4.3 shows COF plotting as a function of testing time for two different test conditions. Values of COF appear not to vary significantly for the three different samples. Examining all COF values conducted in this study has confirmed that COF varies as F_N or f varies, but for each testing condition, COF values of the three samples have not varied significantly. As the primary aim of the present study is to investigate the WR that may be affected by the alloy in different forms of microstructure and thus hardness, not the detailed mechanics of wear, the more extensive COF data are not presented here. Rather, wear tracks and shear deformation relating to WR are examined in more detail, as presented below.

4.2 Wear track surface appearance

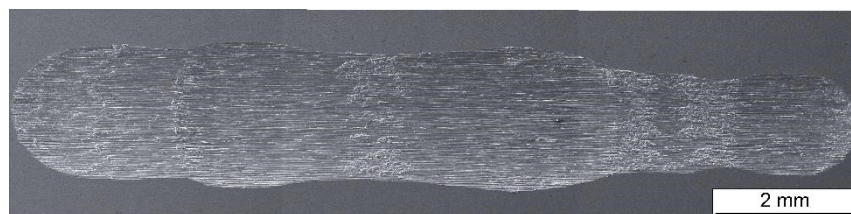
Fig. 4.4 shows four selected track surface images of samples tested at various conditions. Tracks can be quite uniform in width for some cases, as can be seen in Fig. 4.4(a) and Fig. 4.4(b). The image in Fig. 4.4(a) for a SLM sample is however seen smoother with less wear debris smeared on the track comparing to the CP sample in Fig. 4.4(b). The edges of the CP sample wear track (Fig. 4.4(b)) are seen to be decorated intermittently with small flown out pieces and these pieces are largely absent in the SLM sample (Fig. 4.4(a)). In some cases, irregular shape of the track could be observed where the width varies along the length of the track. Fig. 4.4(c) and Fig. 4.4(d) display two wear tracks of highly irregular shapes. This irregularity in track shape has been reported by Niu et al. [4, 5] who present wear tracks in their entirety. As this irregularity is not confined in a particular kind of sample (SLM, EBM or CP), the reason for it is not studied further.



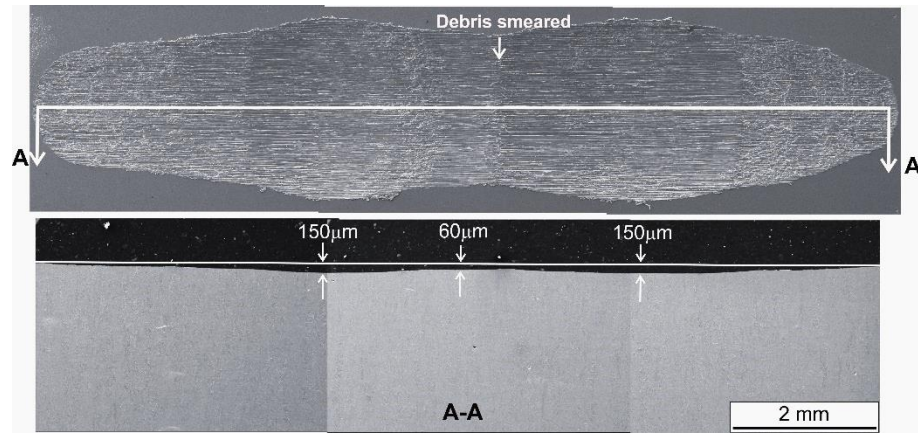
(a)



(b)



(c)



(d)

Fig. 4.4 Appearances of selected wear tracks showing various track features, (a) SLM sample tested at 2Hz and 6N - straight track, (b) CP sample tested at 2Hz and 6N - straight track with edge pieces, (c) SLM sample tested at 5Hz and 2N - width variation, and (d) EBM sample tested at 8Hz and 6N - width and height variations.

Take Fig. 4.4(d) as an example to discuss further the track width (W_{Track}) and its variation. Observing from top, the lower W_{Track} in the mid location of the track in the longitudinal direction should mean a less wear track depth (h), as is also observable in the cross sectional view, which indicates $h \approx 60 \mu m$ in mid-track location in the cross section. The values of h increase on both sides of the mid-track location and the maximum $h \approx 150 \mu m$. This means $\Delta h \approx 150 - 60 = 90 \mu m$, which is much higher than the value of h in mid-track location ($60 \mu m$), and means that this wear track is very “bumpy” along the track length. From the measured sectional profiles, the averaged h and W_{Track} can be obtained and data for all tested samples are plotted in Fig. 4.5. The scatters of the data are quite small and the regression line is quite close to the calculated curve of h - W_{Track} based on the diameter of the ball used. This suggests that debris on track surface has not affected the wear volume and thus WR estimation.

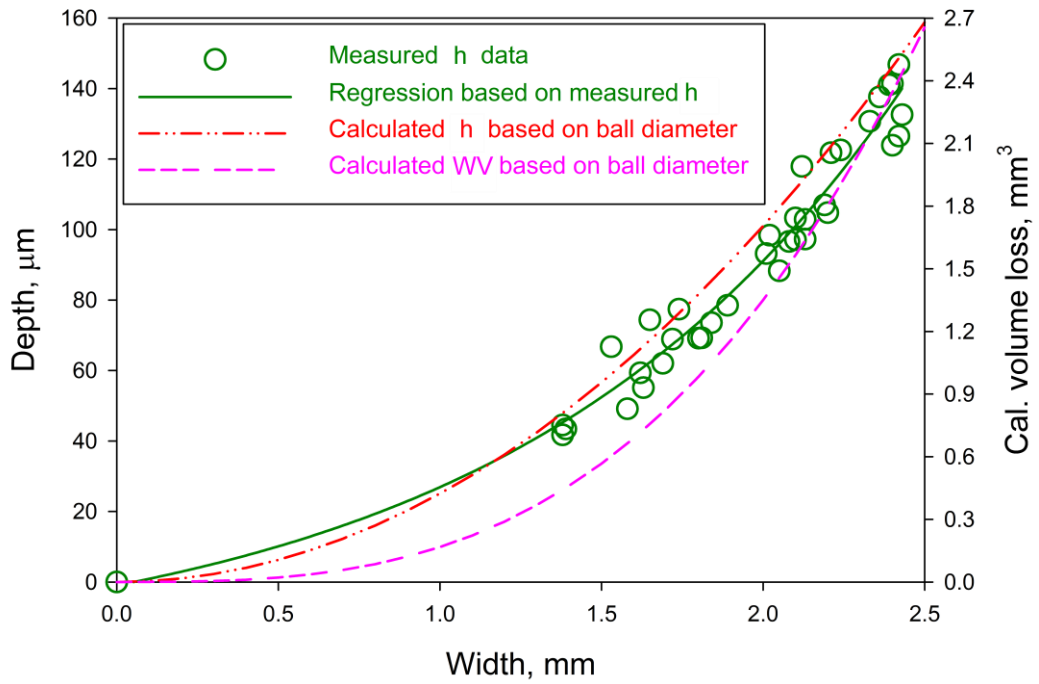


Fig. 4.5 Measured depth, calculated depth and calculated wear volume plotted vs. track width.

Numerically, the measured W_{Track} values and one standard deviation (σ_{WT}) of all samples are plotted in Fig. 4.6(a) and Fig. 4.6(b) as a function of F_N and f , respectively. The trend of increasing W_{Track} as F_N increases in Fig. 4.6(a) is similar to the trend of $WR-F_N$ in Fig. 4.1. The rate (dWR/dF_N) of increase in Fig. 4.1 appears high and the rate (dW_{Track}/dF_N) in Fig. 4.6(a) appears low. This is the result of the more rapid increase in dWR/dW_{Track} when W_{Track} increases, particularly when $W_{\text{Track}} > 1.5$, as shown in Fig. 4.5. The trend of W_{Track} change as f increases in Fig. 4.6(b) is also similar to that in Fig. 4.2. The major features that have been described for the images in Fig. 4.4 can now be explained for all samples in Fig. 4.6(b). Consistent with Fig. 4.4(a) and Fig. 4.4(b), all samples tested at 2Hz (for 9 conditions in Fig. 4.6(b)) have resulted in low σ_{WT} , meaning a low variation of track width. On the other hand, for all samples tested at a high f (8Hz), σ_{WT} values are generally high. The combination of low F_N at 2N and medium f at 5Hz also results in high σ_{WT} values in Fig. 4.6(b) and an examples is illustrated in Fig. 4.4(c), as have already been explained. The combination of mid-high F_N (6N-10N) and medium f at 5Hz has yielded mid-levels of σ_{WT} .

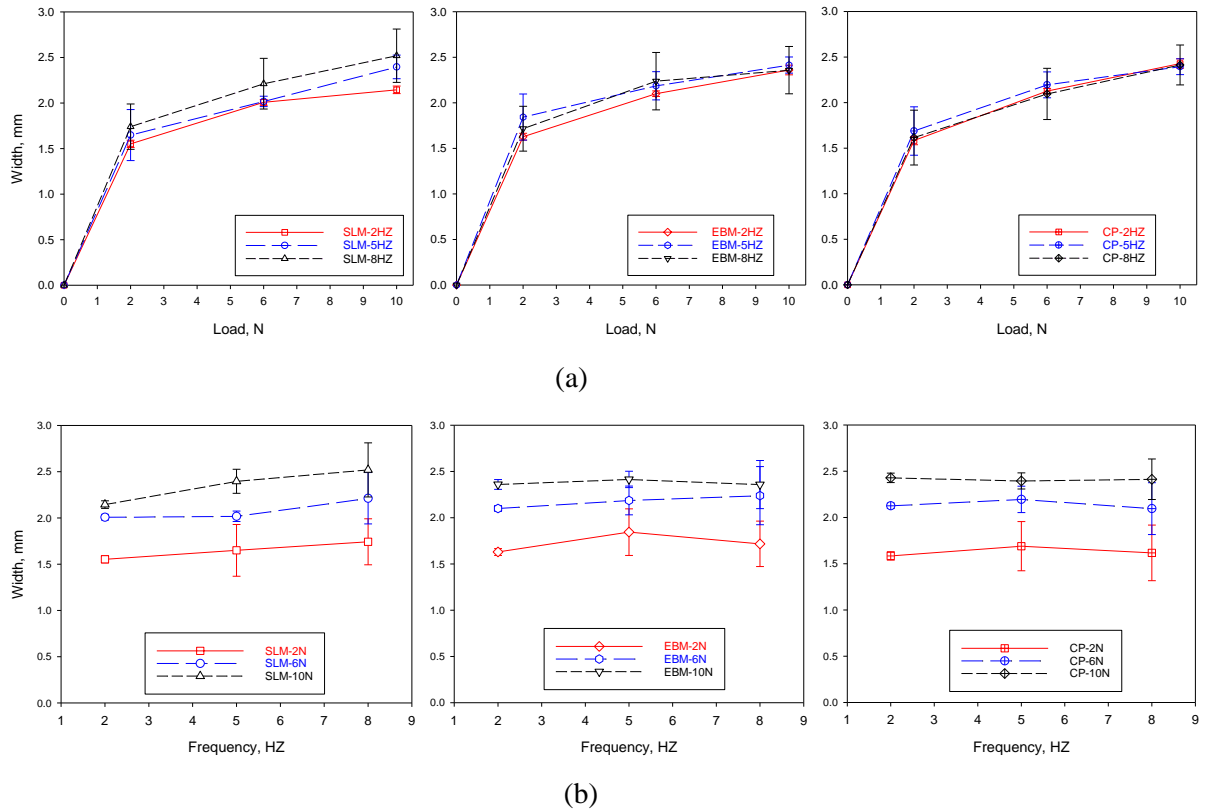


Fig. 4.6 Average measured width and standard deviation values plotted as a function of (a) test load and (b) test frequency.

4.3 Cross sectional features of wear tracks and shear layer

4.3.1 Cross sectional features

Selected cross sectional images are shown in Fig. 4.7, each corresponding to the respective one in Fig. 4.4 taken in the mid-length location of the track. These images reveal that the thickness of the debris is uneven and discontinuous. As observed in Fig. 4.4, the SLM sample tested at 2Hz has less wear debris smeared on the track comparing to the CP sample. This is consistent with what can be observed in the cross sections in Fig. 4.7(a) and Fig. 4.7(b) that wear debris can readily be observed to have been smeared on the surface of the CP sample while little can be observed in the SLM sample. The images in Fig. 4.7(c) and Fig. 4.7(d), where debris layers are not continuous and are not seen to be thick, are taken in hump locations shown in Fig. 4.4(c) and Fig. 4.4(d). This suggests that a hump is locally less worn, but does not strongly relate to the amount or form of debris.

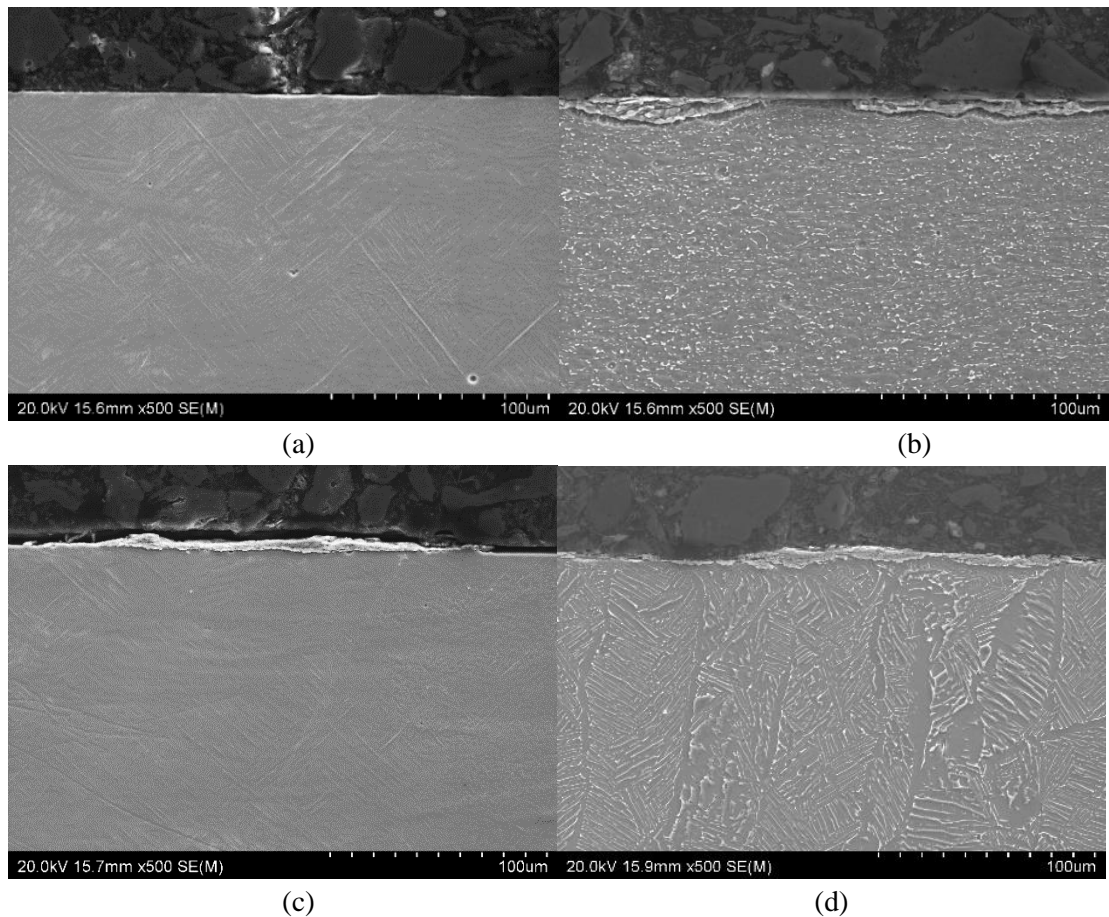
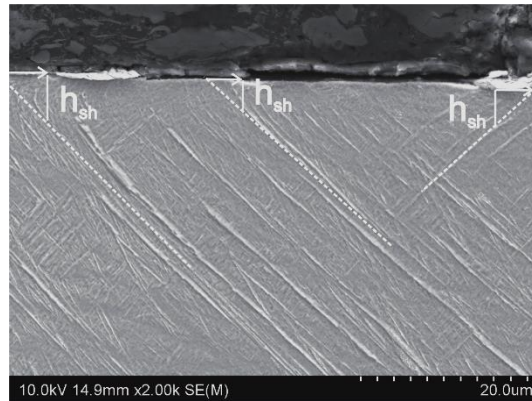


Fig. 4.7 Cross sectional SEM micrographs showing: (a) SLM sample tested at 2Hz and 6N – little debris, (b) CP sample tested at 2Hz and 6N – discontinuous debris layer, (c) SLM sample tested at 5Hz and 2N – uneven and discontinuous debris layer, and (d) EBM sample tested at 8Hz and 6N - uneven and discontinuous debris layer.

4.3.2 Shear layer

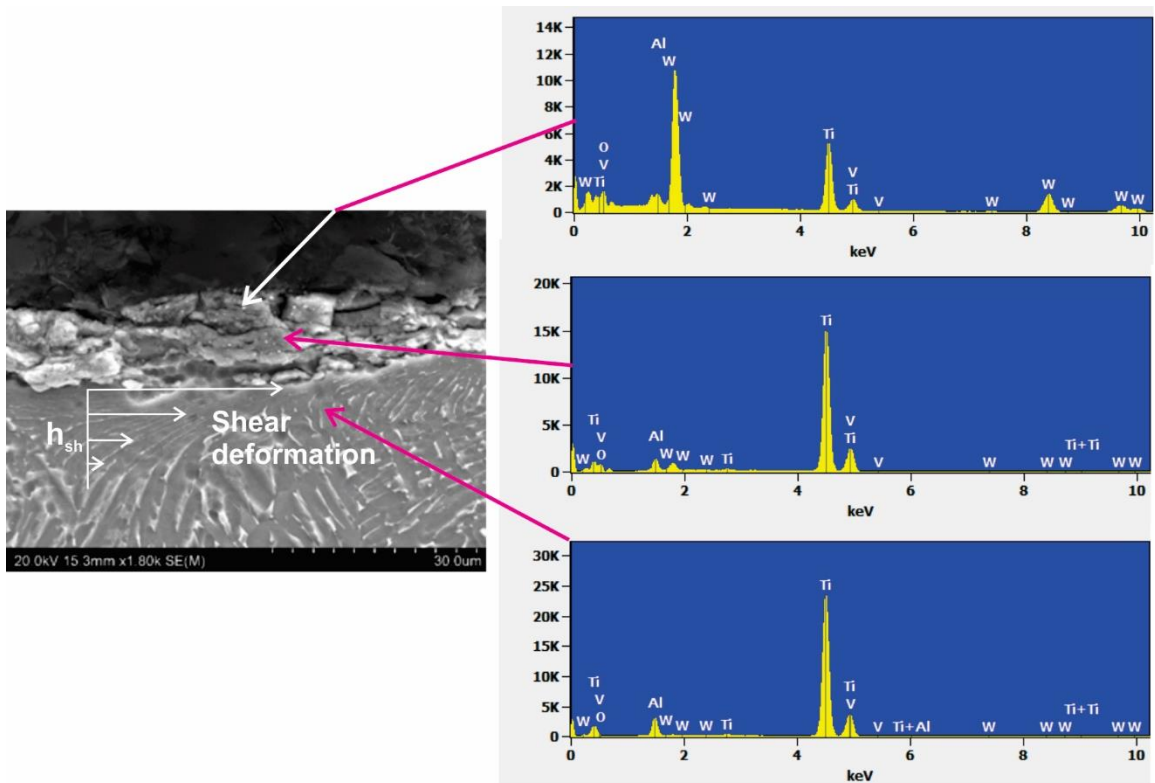
Higher magnification micrographs shown in Fig. 4.8 display a local layer of shear deformation in each sample. The thickness of the shear layer (h_{sh}) can be estimated based on observing the traces of how the shape of the microconstituents have changed. For SLM samples, as has been explained referring to Fig. 1.5(a), primary (long), secondary (short) and even tertiary α' -martensite of acicular shapes (needles in 2D micrograph plane) can be observed. If bending of the needles due to plastic flow has occurred after wear test, deformation during wear test can be inferred. Fig. 4.8(a) is for a tested sample corresponding to a low amount of shear. The dotted lines represent the local orientations of the primary α' -martensite needles. Near the sample surface, needles can be seen to have been bended towards the right. Distance between the

starting point of bending, although it is difficult to locate accurately, to the sample surface is h_{sh} . In Fig. 4.8(a), h_{sh} varies from 4 to 6 μm . This is a low amount of shear (for low f).

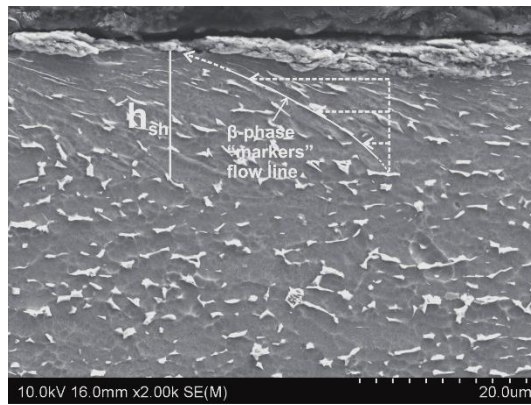


(a)

Fig. 4.8 Examples of surface cross sections of tested samples (a) SLM sample tested at 2Hz and 6N, (b) EBM sample tested at 5Hz and 6N and three EDS spectra of points as indicated and (c) CP sample tested at 5Hz and 2N.



(b)



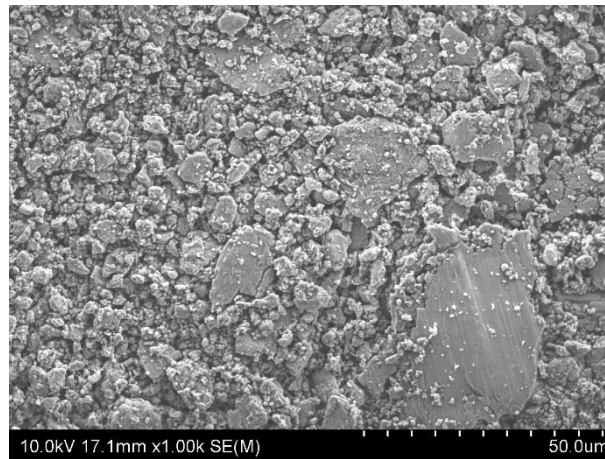
(c)

Fig. 4.8 Cont.

On average, significantly higher ($h_{sh} \gg 6\mu\text{m}$) amounts of shear were found for all other samples ($f \neq 2\text{Hz}$). In EBM samples, shear deformation causing the elongated β -phase particles bending can be readily identified (Fig. 4.8(b)). Deformation causing particle thinning can also be readily seen in these samples. From the observation of how particles have bent and thinned, a shear field can be suggested. It can be seen from Fig. 4.8(b) that h_{sh} is up to $15\mu\text{m}$. The shear layer is characterized by the increasingly thinner β phase particles due to increasingly more extensive shear. Within $\sim 3\mu\text{m}$ from the surface (or the interface with debris), where shear deformation has been very extensive, β -phase particles can no longer be seen. For CP samples, the shorter β -phase particles may have led to some uncertainty in the measurement of shear layer, but the distinctive shear formation can be seen as displayed in Fig. 4.8(c) and h_{sh} can also be approximately estimated.

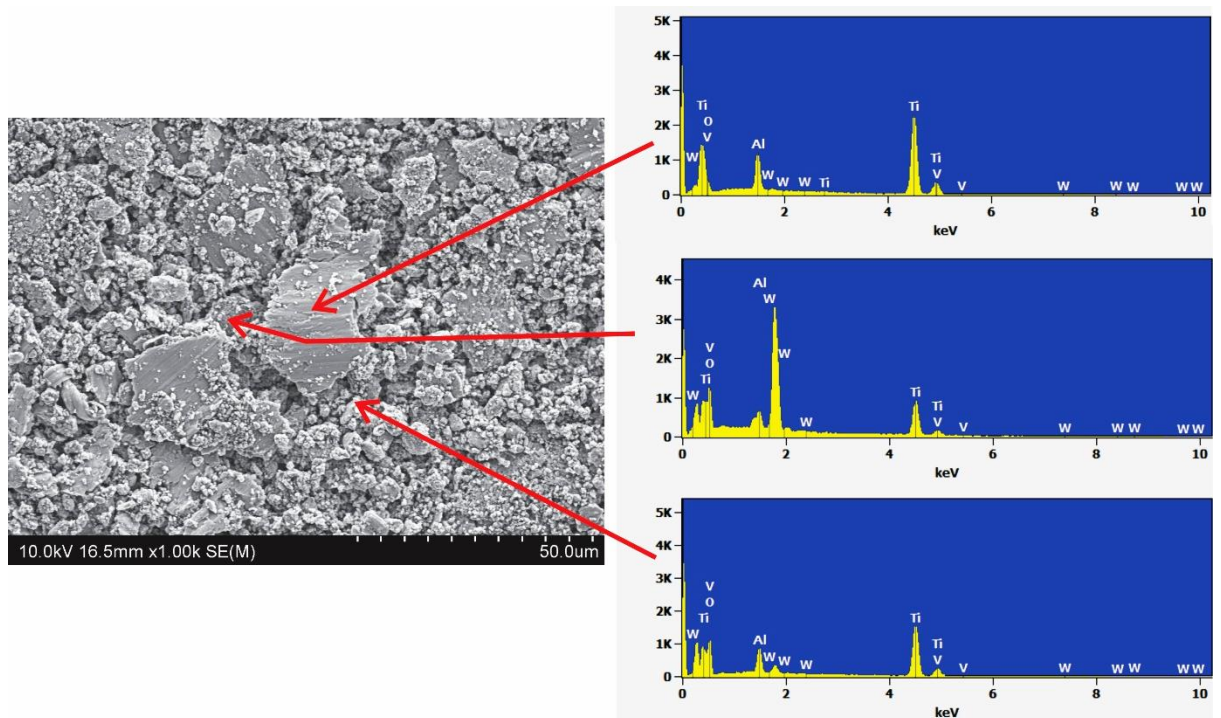
EDS analysis in Fig. 4.8(b) has indicated that the debris is primarily the original Ti-alloy material with a certain degree of oxidation having taken place and some fragmented WC particles distributed. No β phase particles can be identified in debris, and this is expected as the debris is a highly deformed Ti-alloy material with very small grain/particle sizes. Thus, hardness of debris could be higher. Furthermore, extra fine WC particles distributed in the debris may have further increased the hardness of the debris. It is thus reasonable to have observed debris filled pits (an example shown in Fig. 4.7(b)) as the pressing of a small amount of the harder debris under the WC-Co ball during sliding test may have caused debris locally to have indented deep into the Ti-alloy material underneath.

Selected wear debris collected outside the wear tracks are shown in Fig. 4.9, which are quite similar in appearance to debris of tests from other conditions. These debris particles are in a wide range of size. EDS analysis shown in Fig. 4.9(b) on these particles is consistent with that on the debris remained on sample surface shown in Fig. 4.8(b). The particles are primarily Ti-alloy material (top and bottom spectra in Fig. 4.9(b)) and fragmented WC particles have been embedded in the debris (mid spectrum in Fig. 4.9(b)).

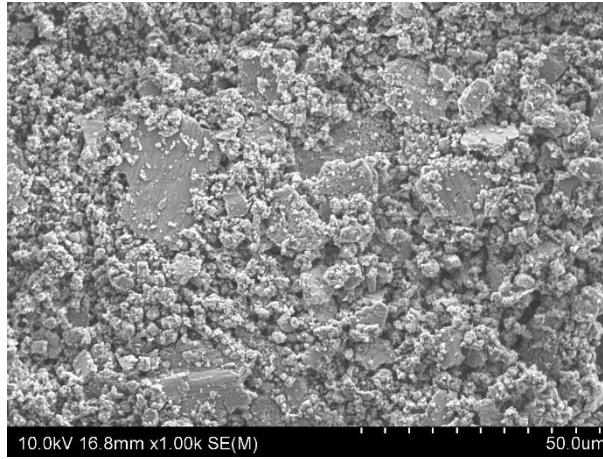


(a)

Fig. 4.9 SEM images of wear debris from tests conducted at $F_N=6N$ and with $f=5Hz$ using (a) SLM, (b) EMB and three EDS spectra of points as indicated, and (c) CP samples.



(b)



(c)

Fig. 4.9 Cont.

For further understanding of the shear deformation leading to wear, as an example, the suggested shear field locally in the sample illustrated in Fig. 4.8(b) is considered for indicating shear strain. Shear distances within the shear layer have been approximately traced using β -phase particles as tracers. However, as has already been explained, within that $\sim 3\mu\text{m}$ heavily deformed shear layer, the shear distance can only be suggested based on the moving direction of β -phase particles outside the heavily deformed thin layer. The estimated/suggested distances are given an x-y coordinate, shown in Fig. 4.10(a) where further measurements can be made to determine the engineering strain (e) values:

$$e = \frac{\sqrt{(\Delta x)^2 + (\Delta y)^2} - \Delta y}{\Delta y} \quad (4.2)$$

Values of e are also given in Fig. 4.10(a) and replotted versus the distance from where $e=0$ in Fig. 4.10(b). The strain has increased to ~ 2 in the region where deformation of β phase particles can be approximately traced and increased more rapidly towards the surface (or the interface with debris) estimated to almost 3.9 (true strain $\epsilon=1.6$). This is a very high amount of deformation. Clearly, a high h_{sh} value indicates a high amount of strain (deformation).

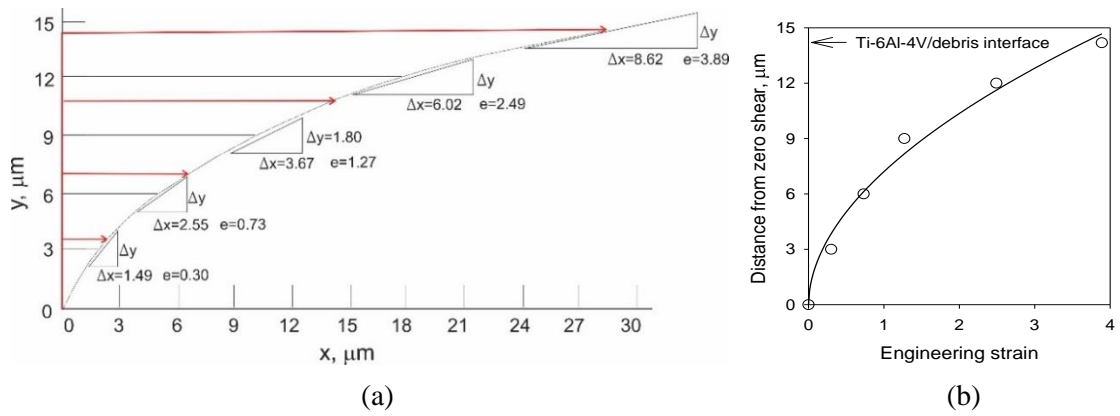
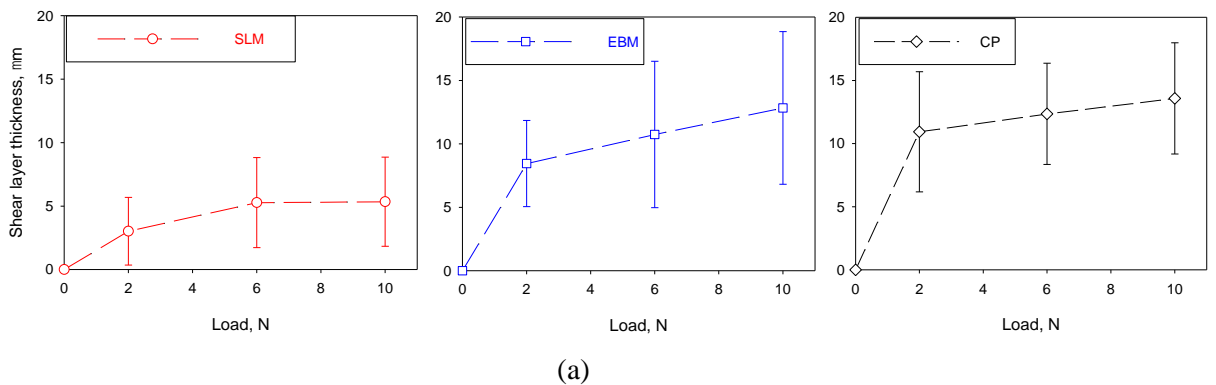


Fig. 4.10 An illustration of shear strain in shear layer, (a) shear distance in the shear field measured in the micrograph in Fig. 4.8(b) and (b) increase in shear strain towards the Ti-6Al-4V/debris interface.

Measurements of h_{sh} have been conducted for samples tested under various F_N values at 5Hz and at various f values under 6N. For each sample, measurement was made by measuring 20 points along the track length under SEM. Values of average h_{sh} and one standard deviation are plotted against F_N and f in Fig. 4.11(a) and Fig. 4.11(b), respectively. A significant feature of the data is that standard deviation values are high, indicating the highly uneven amounts of shear deformation along the wear track. As has already been indicated in Fig. 4.8, in general, average h_{sh} of SLM samples is lower than those of EBM and CP samples. This is clearly shown by the measured values in Fig. 4.11. The figure also shows that h_{sh} value for EBM samples in each condition is generally comparable to that of CP samples in the same condition. Also, in general, increase in either F_N or f tends to slightly increase h_{sh} .



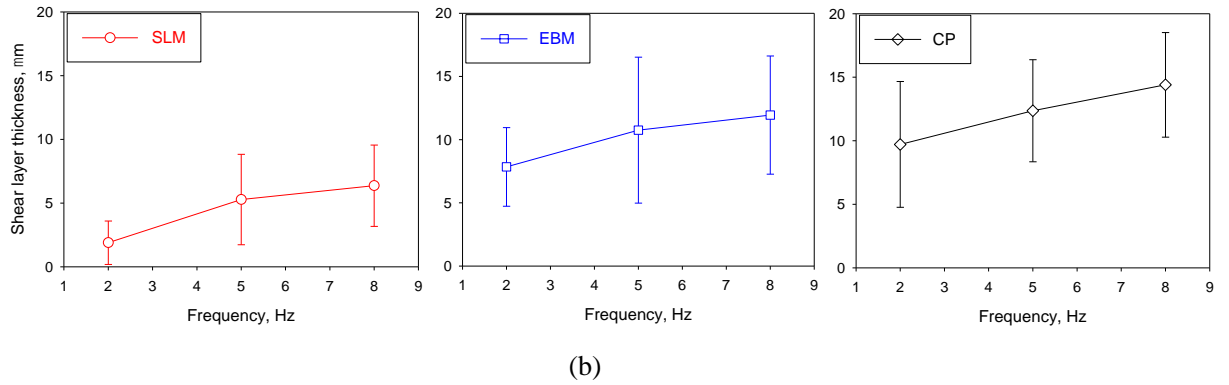


Fig. 4.11 Values of shear layer thickness (h_{sh}) plotted as a function of (a) F_N with $f=5$ Hz and (b) f with $F_N = 6$ N, for SLM, EBM and CP samples as indicated.

4.4 Wear mechanisms governing the measured wear rates

Data in Fig. 4.1 have clearly shown the expected overall trend of increasing WR as F_N increases, although the trend has been found to be non-linear. On the other hand, the effect of f on WR has been shown to be weak, as shown in Fig. 4.2. The major finding in this work, however, is that the three different manufacturing routes of Ti-6Al-4V alloy have resulted in a very similar wear resistance under the wide ranges of F_N and f . This is clearly shown in both Fig. 4.1 and Fig. 4.2 and is despite the significant differences in their hardness (on average 324HV for CP, 359HV for EBM and 428HV for SLM samples) values. As has been explained in Chapter 2 (section 2.2), how hardness relating to the wear resistance of the alloy is an aspect having been evaluated in a number of studies [7][24][51-55][57] and there are disagreements on the relationship. In the present experiments, Archard's equation, where WR decreases as hardness increases, has not been obeyed. The high hardness above 400HV offered by martensite structure in SLM samples has not resulted in a reduction in WR of the alloy. The reason for this is suggested below.

Quantitative treatment cannot be made and only a qualitative discussion may be attempted. Hardness is a measure of resistance to plastic deformation without fracture under a hard indenter and, during wear test, wear originates from deformation and fracture under a moving and hard object. Thus, strength (resistance to deformation) and deformation behavior relating to the two tests need to be considered. This can be aided by a schematic illustration of wear, as shown in

Fig. 4.12(a), where wear is commonly known to be dominantly the combination of adhesive wear and abrasive wear [91]. The contribution of each cannot be estimated but, fundamentally in both adhesive and abrasive wear, wear results from deformation and fracture.

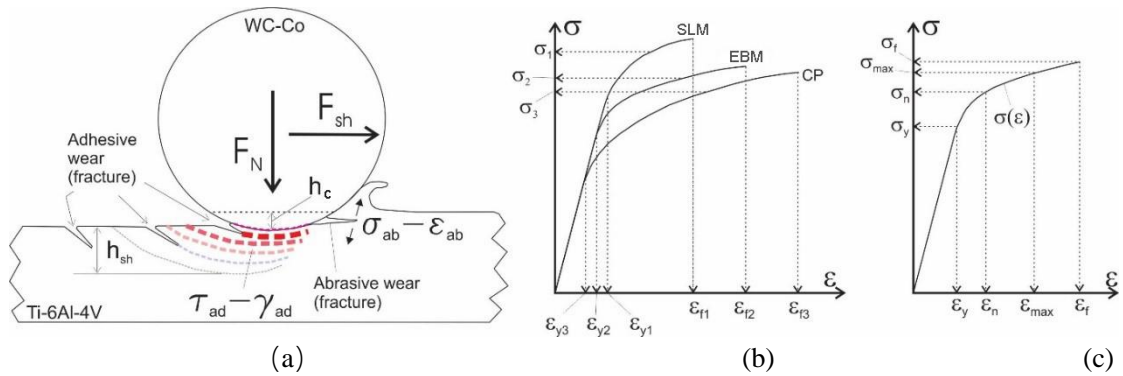


Fig. 4.12 Schematic illustration of (a) sliding wear test with forces, shear stress-strain ($\tau_{ad}-\gamma_{ad}$) field causing adhesive wear, shear layer thickness (h_{sh}), and stress-strain ($\sigma_{ab}-\epsilon_{ab}$) causing abrasive wear indicated, (b) stress-strain curves of Ti-6Al-4V alloy, and (c) stress (σ_n) corresponding to hardness value of the alloy.

The amounts of strain either under wear test loading as indicated in Fig. 4.12(a) or under hardness test loading should relate to the stress-strain ($\sigma-\epsilon$) behaviors, as suggested in Fig. 4.12(b). There has been a large amount of tensile testing on SLM and EBM Ti-6Al-4V samples and data are presented in a recent review by Liu and Shin [25]. It is clear that strength (σ_y and σ_f) and fracture strain (ϵ_f) of SLM samples are higher and lower than the strength and fracture strain, respectively, of EBM samples. However, σ_f and ϵ_f depend on the amount of defects (lack of fusion and porosity). It is reasonable to assume that when $\epsilon_f > 7\%$, ultimate tensile strength (UTS) has almost been reached. Then from the referred review [25], average σ_y , UTS and ϵ_f values for SLM and EBM samples are listed in Table 4.1, together with data from manufacturer for CP samples. Fig. 4.12(b) is thus drawn to schematically illustrate these data, although scale is not in proportion.

Table 4.1 Average tensile strength and elongation values from literature [25] and from manufacturer.

	σ_y (MPa)	UTS, $\approx\sigma_f$, (MPa)	ϵ_f (ϵ_f)
SLM	1038	1172	8.7% (0.08)
EBM	938	1012	12.3% (0.12)
CP	890	1005	14.0% (0.13)

During loading in hardness test, the alloy sample deforms under the indenter with ε ranging from ε_y (maximum elastic strain corresponding to yield strength, σ_y) around the top of indentation to a value ε_{max} (corresponding to a stress, σ_{max}) at the lowest point of indentation. In hardness testing of Ti-6Al-4V alloy, no cracks are observed in the indentation. Thus, ε_{max} is less than ε_f (fracture strain, corresponding fracture strength, σ_f). Then, the hardness value measured should correspond to an “average” value (σ_n) between σ_y and σ_{max} , as schematically illustrated in Fig. 4.12(c), and σ_n can be approximately taken as:

$$\sigma_n = \frac{\int_{\varepsilon_y}^{\varepsilon_{max}} \sigma(\varepsilon) d\varepsilon}{\varepsilon_{max} - \varepsilon_y} \quad (4.3)$$

It is known that work hardening is low in Ti-6Al-4V alloys, as is indicative in σ_y and UTS data in Table 4.1, and thus σ_n should not be considerably higher than σ_y . For SLM Ti-6Al-4V alloy, martensite is the dominant form as shown in Fig. 1.5(a) and thus both yield strength (σ_{y1}) and fracture strength (σ_{f1}) are higher and fracture strain (ε_{f1}) is lower than those of EBM and CP samples. This means, as illustrated in Fig. 4.12(b), $\sigma_1 > \sigma_2 > \sigma_3$.

During wear test, WR greater than zero means ε_{max} in the strain field (near the top surface) reaches ε_f and means that fracture has occurred. Fig. 4.8 and Fig. 4.10 suggest that e_{ah} (strain in adhesive wear region) values on track surfaces can be from 1 to >3 ($\varepsilon_{ah} > 1.4$) and are significantly greater than ε_f (meaning $\varepsilon_{ah} > \varepsilon_f$) values of the alloys listed in Table 4.1. During tensile testing, there is no more deformation when ε_f is reached meaning breaking; but during wear testing, crack initiation does not mean immediate fracture and wear loss. In compression, effective strain (ε_{eff}) of Ti-6Al-4V can be more than 3 [92]. Thus, the amounts of deformation ($e_{ah} > 3$ or $\varepsilon_{ah} > 1.4$) during wear testing of Ti-6Al-4V as seen in Fig. 4.8 and Fig. 4.10 are regarded reasonable. Strength values of the alloy, however, should remain similar and flow stress (σ_{flow1}) for SLM samples should be higher than that (σ_{flow2}) of EBM samples and that (σ_{flow3}) of CP samples.

As shown in Fig. 4.11(a) and illustrated in Fig. 4.10, h_{sh} indicates e . The mean values of h_{sh} in Fig. 4.11(a) indicate indirectly e_{ah} as illustrated approximately in Fig. 4.10 for an example. Values of ε_{ab} in the front deformation zone causing abrasive wear cannot be evaluated but a high

ductility of a material causing high h_{sh} should also cause a high ϵ_{ab} before fracture in the abrasive wear zone. Thus, it may be reasonable that a high h_{sh} meaning a high ϵ_{ah} to cause adhesive wear also means a high ϵ_{ab} to cause abrasive wear. Significantly lower amounts of h_{sh} for SLM samples than those of EBM and CP samples, as shown in Fig. 4.8 and Fig. 4.11, is consistent with the higher strength and lower ductility of the alloy in martensite form. This is also consistent with the low amount of debris in wear tracks as shown in Fig. 4.4 and in Fig. 4.8 for SLM samples. A high amount of debris in a track may mean good ductility and sticking of the worn material to the track but is not directly related to WR. For the higher strength/hardness SLM samples, lower ductility means the deformed material fractures and breaks off more readily, leaving less debris to stick to the track, but WR can still be high.

The effect of increasing F_N on h_{sh} can be examined with data in Fig. 4.11(a). For SLM samples, dh_{sh}/dF_N is high at $1.5\mu\text{m}/\text{N}$ initially (from 0 to 2N), low at $0.5\mu\text{m}/\text{N}$ for F_N from 2 to 6N, and close to zero from 6 to 10N. In comparison, in the initial stage of increasing F_N (from 0 to 2N), dh_{sh}/dF_N at $4.3\mu\text{m}/\text{N}$ is very high for EBM samples and even higher at $5.5\mu\text{m}/\text{N}$ for CP samples. The subsequent dh_{sh}/dF_N values are all very low as F_N increases from 2N, being 0.5 and $0.3\mu\text{m}/\text{N}$ for EBM and CP samples, respectively. Wear loss measured as WR is the result of deformation and tiny pieces fracturing off along the wear track. Thus, the high or very high values of dh_{sh}/dF_N initially as F_N increases should be the major reason for the steep increase in WR as F_N increases from zero load, as is shown in Fig. 4.1. This also means that application of 2N load has caused extensive shear deformation under the WC-Co ball during the current wear test. Increasing F_N increases W_{Track} (Fig. 4.6(a)) and thus WR (Fig. 4.1), but fundamentally the process of deformation to fracture should remain the same.

Examples of shear fields illustrated in Fig. 4.8 and Fig. 4.10 can now be qualitatively extended. For this, average h_{sh} without considering the deviations is discussed. For SLM samples, overall $h_{sh}\approx 5\mu\text{m}$, then $\epsilon_{ah}\approx 0.5$ and ϵ_{ab} can be suggested low. For EBM samples, overall $h_{sh}\approx 11\mu\text{m}$, then $\epsilon_{ah}\approx 2.2$ and ϵ_{ab} can be suggested mid-high. For CP samples, overall $h_{sh}\approx 12\mu\text{m}$, then $\epsilon_{ah}\approx 2.6$ and ϵ_{ab} can be suggested high. Combining these data and the σ - ϵ behaviors illustrated in Fig. 4.12(b), it can be reasoned that a low h_{sh} meaning low ϵ to reach ϵ_f can cause a significant amount of wear loss. This is for the case of SLM samples. On the other hand, for the case of low strength

(lower hardness) if the ductility of the alloy is high, a significantly higher h_{sh} meaning higher ϵ is needed for fracturing and wear loss. This is for the case of EBM and CP samples. The reason why WR being inversely proportional to the hardness of the alloy for both adhesive wear and abrasive wear [91] has not been obeyed in this work is because the suggested relationship has not taken ductility into consideration.

The weak effect of f on WR shown in Fig. 4.2 is now discussed. An increase in f means an increase in the heat generation from friction and deformation per unit time, thus, track temperature should increase with f increase. An increase in temperature means lowering the strength (hardness) but also means increasing the ductility. Lowering strength should mean larger contact area and higher h_{sh} (thus ϵ) under the same loading, thus promoting wear. But a higher ductility allows higher h_{sh} (thus higher ϵ) before fracturing and wear loss. Thus, on balance, the effect of f on WR is not strong. As has been pointed out in the beginning of Chapter 2 (section 2.2), Dong's comprehensive review [12] has suggested that the softness and good ductility of Ti-6Al-4V are the reason for the low resistance of the alloy to both adhesive and abrasive wear. This is, however, not supported by the major finding in this study that WR of the higher strength and hardness (SLM) samples is similar to that of lower strength (EBM and CP) samples of the same alloy. The better ductility of EBM and CP samples, in comparison to SLM samples, has not resulted in a low wear resistance of the alloy. The measured hardness values, strength and ductility following Table 4.1, the present observations and suggested wear behaviors are summarized in Table 4.2. These observations and explanations have contributed to the fundamental understanding of the tribological behaviors, *without a specific application*, of the alloy processed through the three routes.

Table 4.2 Summary of mechanical properties, and the suggested behavior during wear test.

	Hardness, HV	Strength as $(\sigma_y + \sigma_t)/2$, MPa	Ductility	During wear test under a same condition
SLM	428	1105	Low	Wear rate similar as a lower strength & a higher ductility mean a larger amount of deformation without fracture & vice versa
EBM	359	974	Mid	
CP	324	948	Mid-high	

Thus, the wear mechanisms governing the measured wear rates for all three differences in the route of the alloy manufacturing: laser powder bed fusion (SLM), electron beam powder bed fusion (EBM), and conventional processing (CP) can be concluded. For all three types of samples, as expected, increasing F_N increases WR although the rate of increase is non-linear. But the rate of increasing WR as f increases is very low. It has been found that despite the significant differences in their microstructure and hardness, there is no significant difference in WR among the three types of samples when they are tested in the same condition over the wide ranges of loading and frequency. Thus, WR is not inversely proportional to hardness, which varies due to the difference in the three manufacturing routes of the alloy used in this study: high hardness (428HV) in SLM samples, mid-level hardness (359HV) in EBM samples and low hardness (324HV) in CP sample. The reason for WR being not affected by hardness can qualitatively be suggested to be the result of the inverse relationship between strength and ductility of the alloy. Lower hardness and thus lower strength of the alloy has resulted in a larger deformation zone, but higher ductility of the alloy allows for a higher amount of the deformation without having a higher amount of fracture and wear loss.

Chapter 5 Effect of Temperature on Wear Behavior

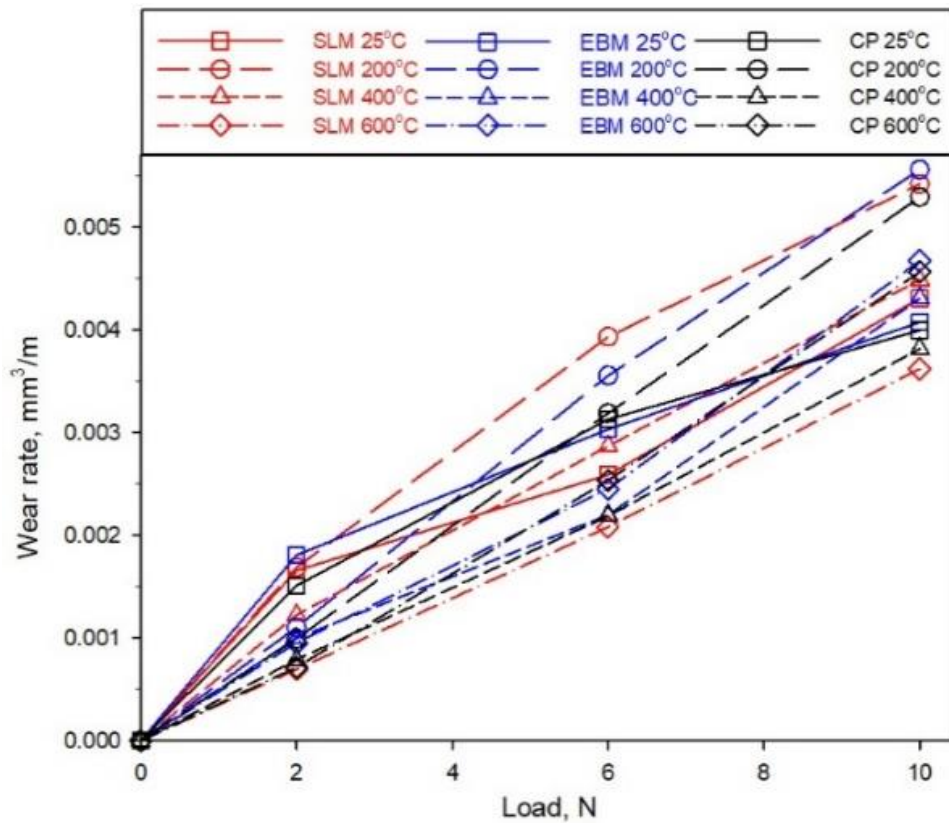
Continuing on the study based on wear tests of SLM, EBM and CP samples conducted at room temperature (T_{Rm}) reported in the previous chapter, in this chapter, the study on the effect of increasing test temperature (T) on wear rate (WR) is reported. WR data for various tests at a wide range of temperatures will first be presented to identify the trend of WR change as T increases. Deviations of track width (W_{Track}) measurement indicating shape irregularly of track will also be presented and discussed. The shape irregularity will then be evidenced by presenting SEM images of wear tracks and the reason for this irregularity will be further discussed. Presentation of the analyses on surface layer to show how increasing T may affect the surface oxide layer and debris will follow. Based on these analyses, the reason will be suggested to explain the observed effect of increasing T on WR .

5.1 Wear rate at various test temperatures

In a similar way to present data of WR values affected by F_N and f in the previous chapter (Fig. 4.1), WR values affected by F_N ranging from 2N to 10N and affected by T from T_{Rm} to 600°C are plotted in Fig. 5.1. Frequency (f) at 5Hz has been the same in this series of test and data for T_{Rm} have been taken from the previous series of study at T_{Rm} . The trend of increasing WR when F_N increases as identified for tests at T_{Rm} (Fig. 4.1) is similar for tests conducted at 200, 400 and 600°C, as is clearly shown in Fig. 5.1(a). Thus, the clear effect of increasing F_N on increasing WR has not been affected by T in the range from T_{Rm} to 600°C. Each range of WR values at a F_N level in Fig. 5.1(a) is not very different but may be seen slightly wider compared to the corresponding range at the same F_N level in Fig. 4.1. This is an indication of either a slight effect by test T or a large scatter at higher T . Also, the lack of a clear difference in WR among the three different material states (SLM, EBM and CP) as identified for T_{Rm} appears to be the same for tests at all temperatures.

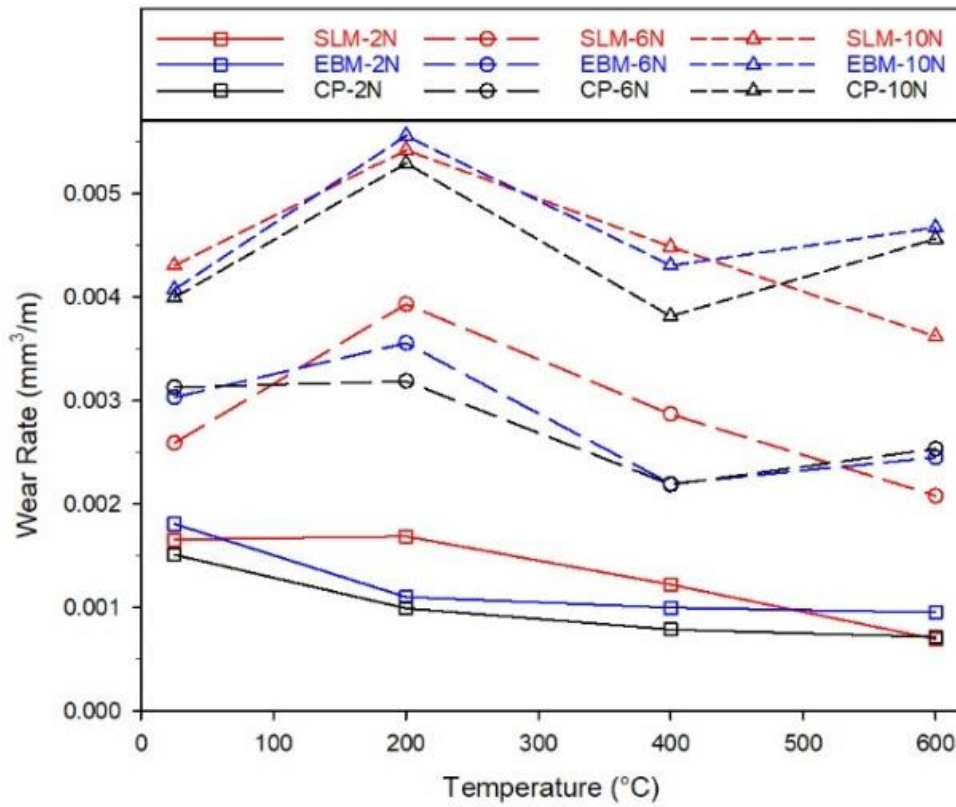
The effect of T on WR is better examined in Fig. 5.1(b). For 2N testing, in general, it could be suggested that there is a weak effect and increasing T reduces WR slightly. There is an

observable effect of T when F_N increases from 2N to 6N that WR is higher at 200°C, but the increase is low. At 10N, the peak WR at 200°C is clear, although the increase in WR is only about 20% compared to the average WR at other temperatures. For $F_N=2N$, the ratio of the highest WR over the lowest WR is < 2 . This ratio decreases as F_N increases. As will be shown (in Chapter 6), for the same testing condition, applying a wear resistance coating reduces WR considerably that an uncoated sample wears 17-33 times faster than one with a coating. Thus, the effect of T on WR as shown in the data in Fig. 5.1b is very small. It may be suggested that T affects the SLM samples slightly differently than it affects EBM and CP samples but, the overall effect may also be viewed weak.



(a)

Fig. 5.1 Values of WR plotted as a function of test loads (a) and test temperatures (b).



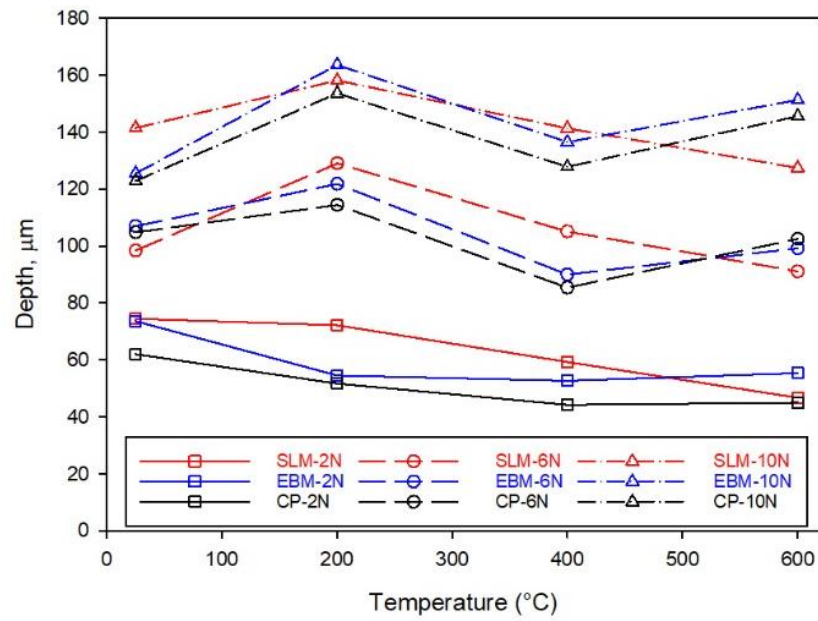
(b)

Fig. 5.1 Cont.

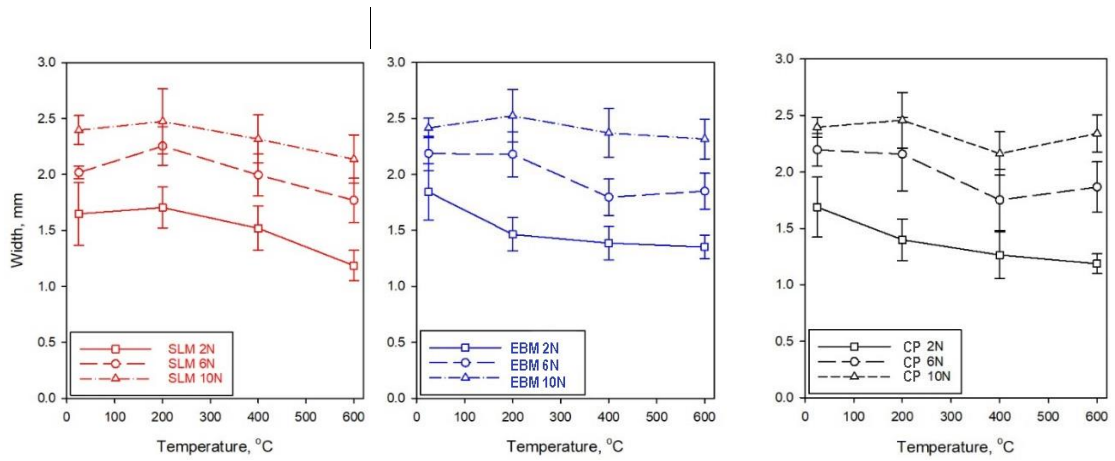
The finding of the insignificant effect of T on WR in the present study is not consistent with the results presented in literature on wear studies of Ti-6Al-4V alloy, although testing conditions differ. As has been described in Chapter 2, the effect of T on WR presented in a number of studies in literature differs from one study to another. Furthermore, as has also been explained, the very large deviation values for some tests in the recent study of Alvi et al. [66] could suggest the effect of temperature on WR to be highly uncertain. In the following, an attempt is made to examine the shape features of the wear tracks and to analyze the wear debris affected by increasing T . These examinations are for identifying the reason for the observed insignificant effect of T on WR determined in our experiments.

Measured values of track depth (h) and track width (W_{Track}) are plotted against T , as shown in Fig. 5.2(a) and Fig. 5.2(b), respectively. Deviation values are provided in the plots of Fig. 5.2(b) for W_{Track} to be referred to when observation on track surface is made using SEM images. Not only the trends of W_{Track} as T increases in Fig. 5.2(b) follow closely those for WR in Fig. 5.1(b), the shape of each curve in Fig. 5.2(a) follows closely the shape of each corresponding curve in

Fig. 5.1(b). The trend of W_{Track} and the shape of each curve plotting W_{Track} against T in Fig. 5.2(b) are not the same as those in Fig. 5.1(b) but the trends and shapes of the curves for each pair (one in Fig. 5.1(b) for WR and the corresponding one in Fig. 5.2(b) for W_{Track}) are still similar. In Fig. 5.2(b), many of the deviation values of W_{Track} are close to 0.5mm, which should be considered high, as max W_{Track} is ~ 2.5 mm. This suggests a high irregularity of track shape.



(a)

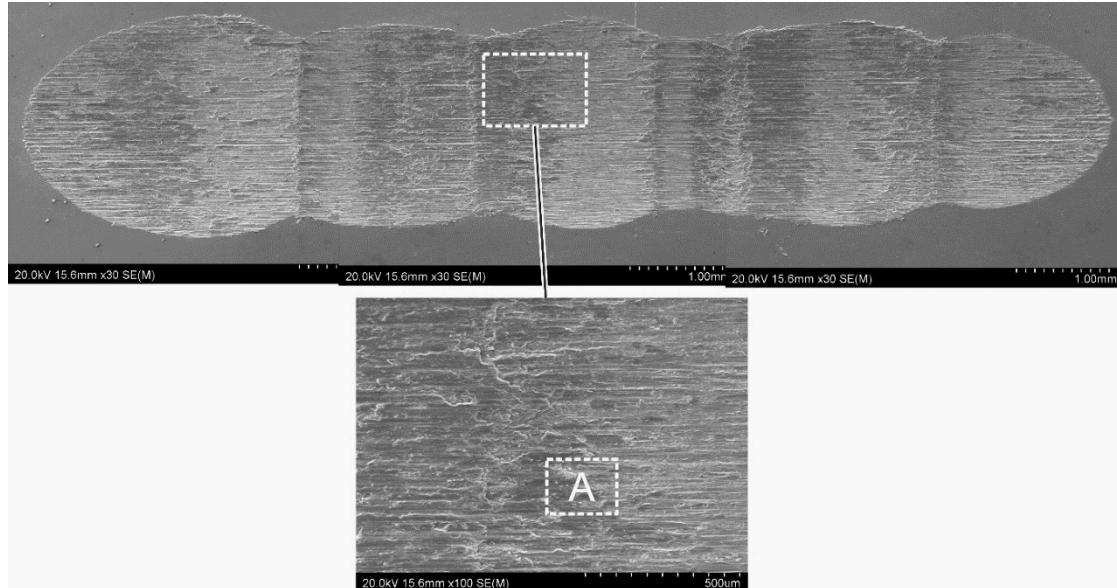


(b)

Fig. 5.2 Measured (a) track depth and (b) track width plotted as a function of test temperature. In (b) standard deviation values are also plotted.

5.2 Wear track appearance and wear debris on track surface

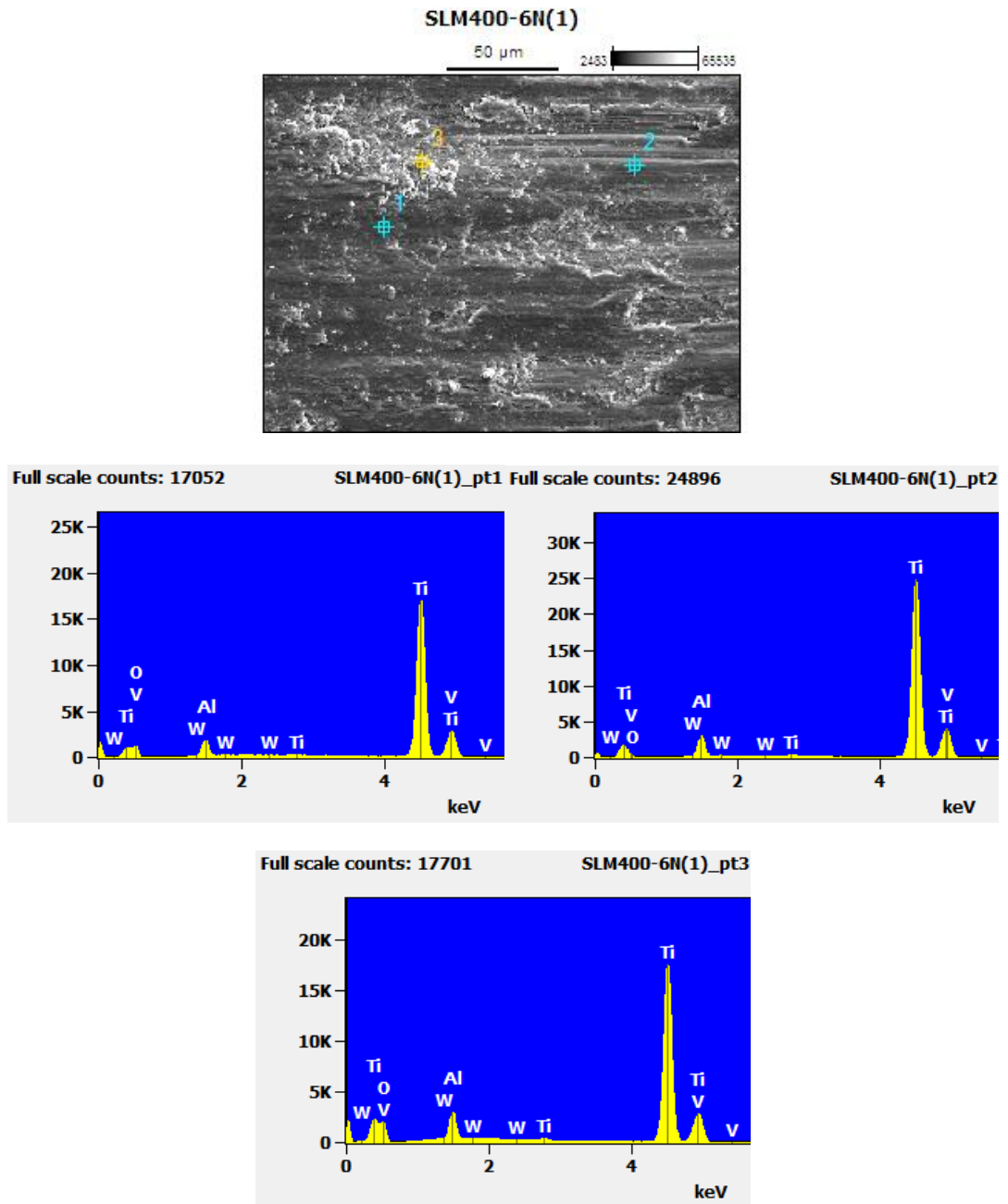
The high irregularity in track shape can be directly shown by SEM images of tracks. An example is given in Fig. 5.3 for the SLM sample tested at 400°C and at 6N, showing W_{Track} to have varied significantly along the track. There are 4 “necks” crossing the track, dividing the track into 5 sections and each with reduced W_{Track} . There appear bands of debris darker in appearance crossing the track transversely. A small area marked “A” in Fig. 5.3(a) is further magnified and shown in the image in Fig. 5.3(b), for which two surface features can be described: one being the smeared debris covering the most of this “A” area, and the other being the freshly worn grooves that are not covered by debris. Two debris smeared points (point 1 and point 3) and one freshly cut (worn) location (point 2) have been EDS analyzed and their EDS spectra are also given in Fig. 5.3(b). A clear different of point 2 to either point 1 or point 3 is the lack of an O peak. The use of the 20kV accelerating voltage resulted in light element peaks to be weak, but the O peak in spectra 1 and 3 are clear. Semi-quantitative analysis has indicated a high oxygen content ~50at% in the debris smeared area, as listed in Table 5.1. Thus, the debris smeared is primarily oxide and the freshly cut location is the Ti-6Al-4V workpiece material.



(a)

Fig. 5.3 SEM images and EDS spectra of the SLM sample tested at 400°C and 6N: (a) the whole wear track with area outlined/shown in a higher magnification and a further high magnified area marked ‘A’ selected for EDS analysis and

(b) EDS spectra from points (1, 2, and 3) marked in the SEM image (of area ‘A’).



(b)
Fig. 5.3 Cont.

Table 5.1 Compositions (at%) from semi-quantitative analysis of the three points in the SEM image and based on the EDS spectra in Fig. 5.3(b).

	O	Al	Ti	V	W
Point 1	51.70	4.55	41.90	1.85	0.00
Point 2	0.00	10.82	85.42	3.76	0.00
Point 3	47.78	7.08	43.15	1.97	0.02

The example given in Fig. 5.4 is for the EBM sample tested at 400°C and at 6N, showing also W_{Track} to have varied significantly along the track also with 4 “necks” dividing the track into 5 sections and with bands of debris darker in appearance crossing the track transversely. A longitudinal cross section is also given to show the corresponding depth irregularity along the track. Similar to the feature that has already been discussed in the previous chapter (Fig. 4.4), the deepest location is $\sim 140\mu\text{m}$ and the smallest depth corresponding to the narrowest neck is $\sim 40\mu\text{m}$. This is consistent with the average depth value of $\sim 90\mu\text{m}$ measured and plotted in Fig. 5.2(a) for this sample tested at 400°C and at 6N.

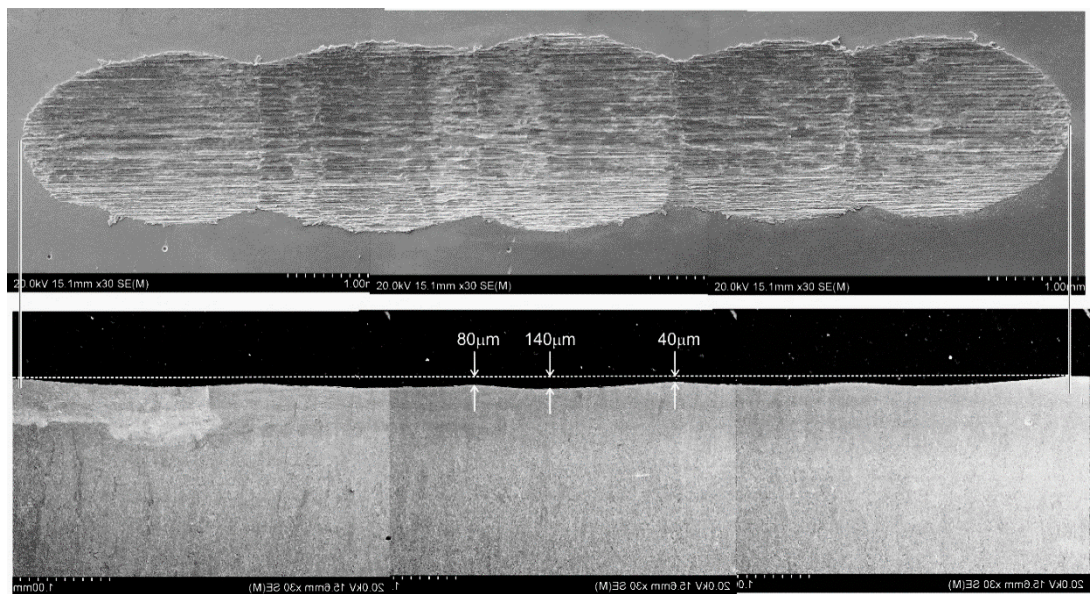


Fig. 5.4 Whole wear track SEM images of EBM sample tested at 400°C and 6N observed from top (top image) and mid cross section (bottom image).

The example given in Fig. 5.5 is for the CP sample tested at 400°C and at 6N, similar to SLM sample shown in Fig. 5.3 and EBM sample in Fig. 5.4, showing also a 4 “necks” track with bands of debris also apparent. The average width of SLM, EBM and CP track measured and plotted in Fig. 5.2 of $\sim 2\text{mm}$ or slightly less with the variations of 0.4-0.5mm are consistent with the tracks observed in Fig. 5.3 to Fig. 5.5. Thus, as has already been explained, the differences in Ti-6Al-4V processing, SLM, EBM or CP, affected little wear track appearance and size. The track shape irregularity has basically been observed in all the tracks at tested temperatures of 200°C, 400° and 600°C under all loads, as can be seen in Appendix 1.

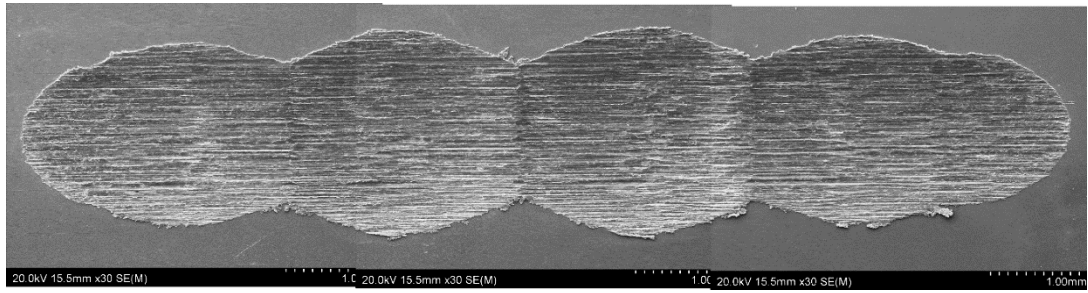


Fig. 5.5 Whole wear track SEM images of CP sample tested at 400°C and 6N, observed from top.

Two further whole track images are presented, one in Fig. 5.6 for the widest track and in Fig. 5.7 for the smallest track, respectively. Clearly, despite of the size difference, shape irregularity and debris bands, some clear and some less clear, in the wider track (Fig. 5.6) or smaller track (Fig. 5.7) are the same as those tracks with mid width values (Fig. 5.3 to Fig. 5.5). The difference in size, comparing the track in Fig. 5.6 to the track in Fig. 5.7 is due to the test load, not due significantly to test temperature, as is proved by all the measured values shown in Fig. 5.2(b). Test load significantly and test temperature does not significantly affect the width, depth and thus the WR and the effect is the same for SLM, EBM and CP samples.

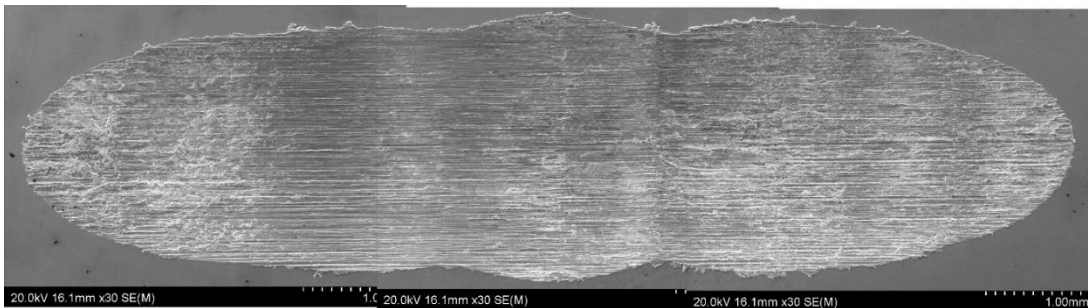


Fig. 5.6 Whole wear track SEM images of EBM sample tested at 200°C and 10N, observed from top.

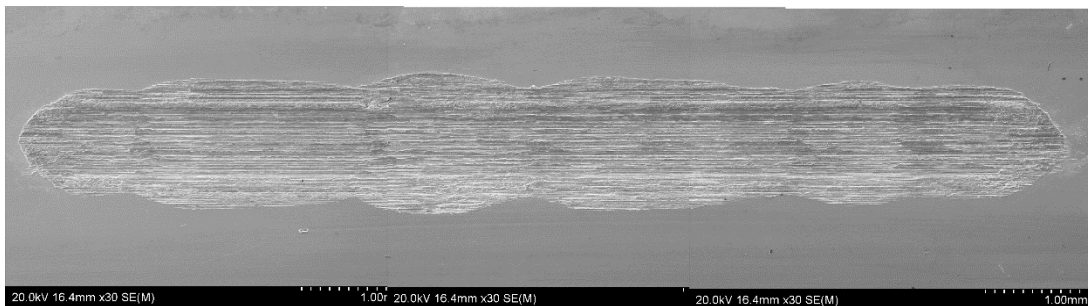


Fig. 5.7 Whole wear track SEM images of SLM sample tested at 600°C and 2N, observed from top.

5.3 Further analysis on wear debris and oxide in cross sections

EDS spectra shown in Fig. 5.3 have indicated the debris in wear tracks tested at a high temperature (400°C) to be high in oxygen content and to be oxide (Table 5.1). More reliable EDS analysis on debris using cross sectional samples have been conducted and data are presented in Fig. 5.8, Fig. 5.9 and Fig. 5.10 for SLM, EBM and CP samples tested at various high temperatures, respectively. The analytical results are however semi-quantitative as no oxide standard samples are available and standard calibration for quantitative analysis could not be thoroughly conducted. The spectra in Fig. 5.8 to Fig. 5.10 for analyses on the debris in cross sections are similar to the spectra shown for point 1 and point 3 in Fig. 5.3 for analyses on the debris from the surface, all showing a definite intensity peak of oxygen.

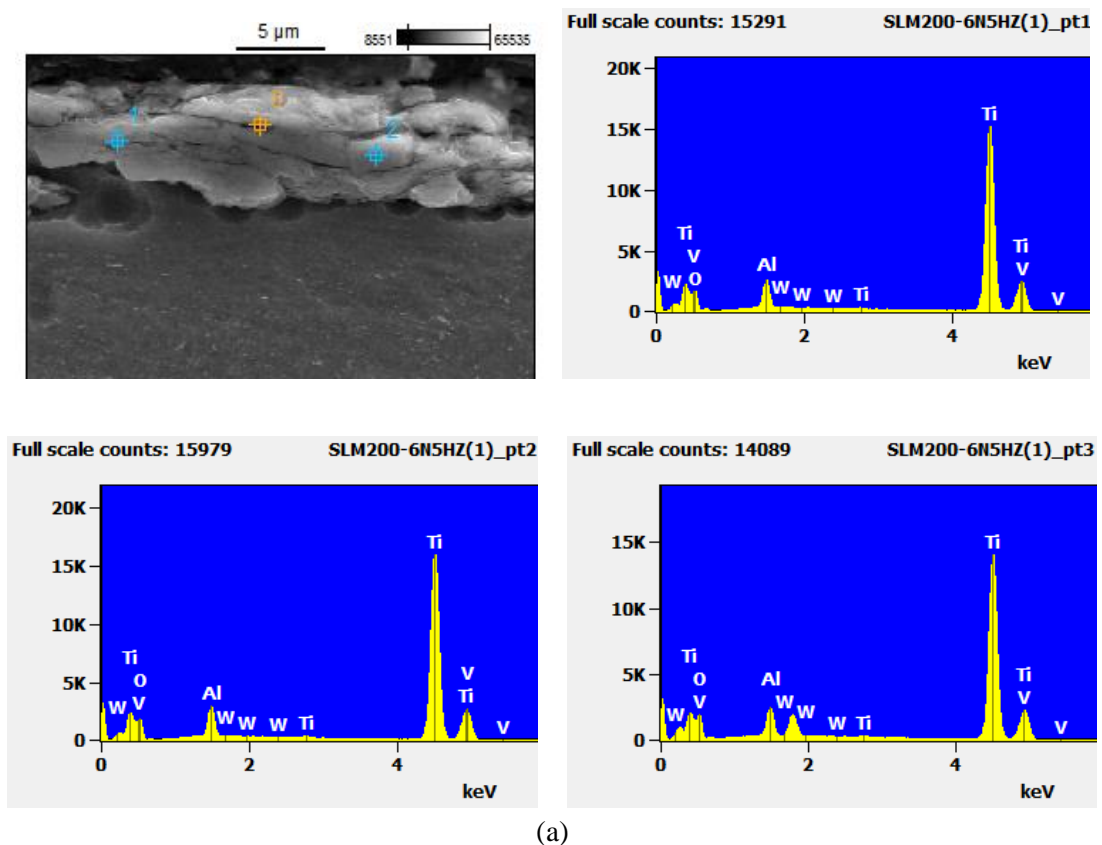
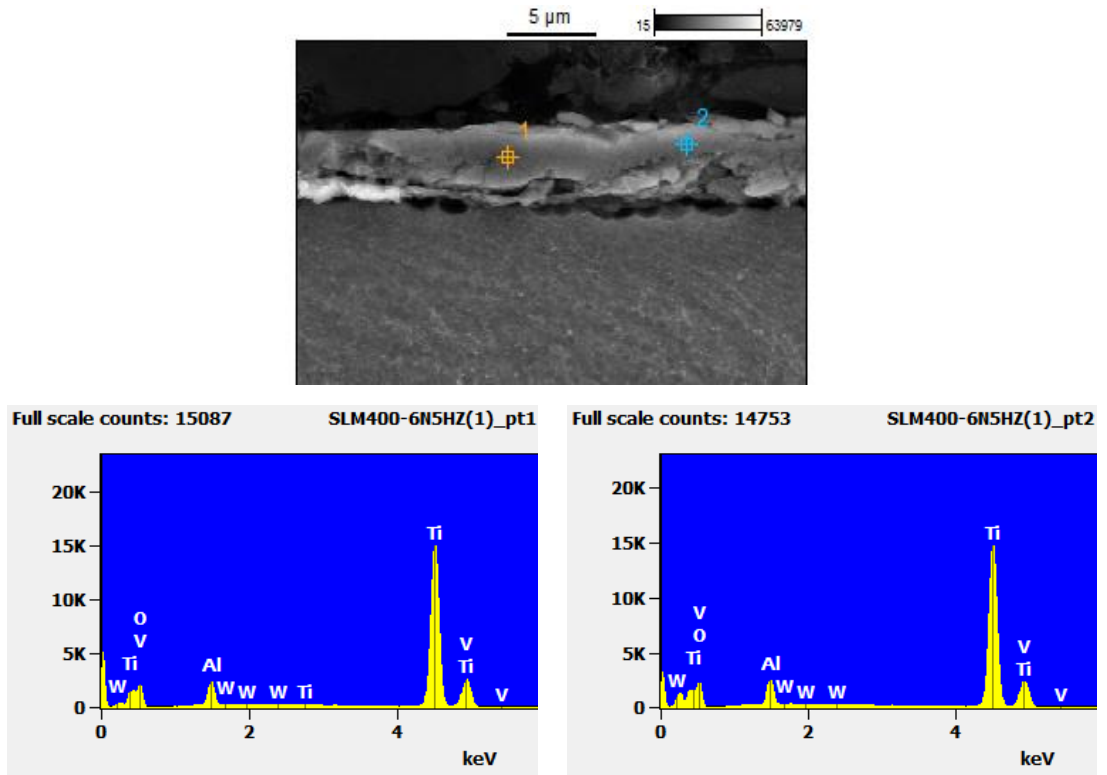
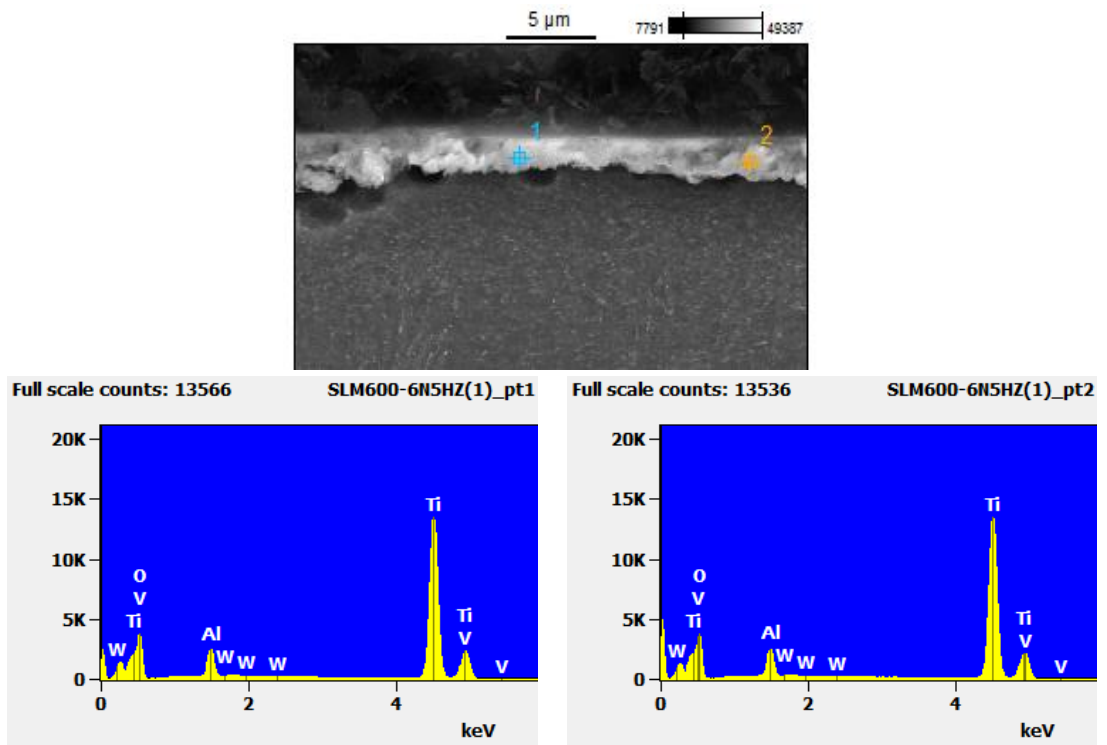


Fig. 5.8 SEM cross sectional images and EDS spectra from analysis of points (1, 2 and 3) marked in the SEM image of SLM samples tested at (a) 200°C, (b) 400°C and (c) 600°C, and under the test load of 6N.

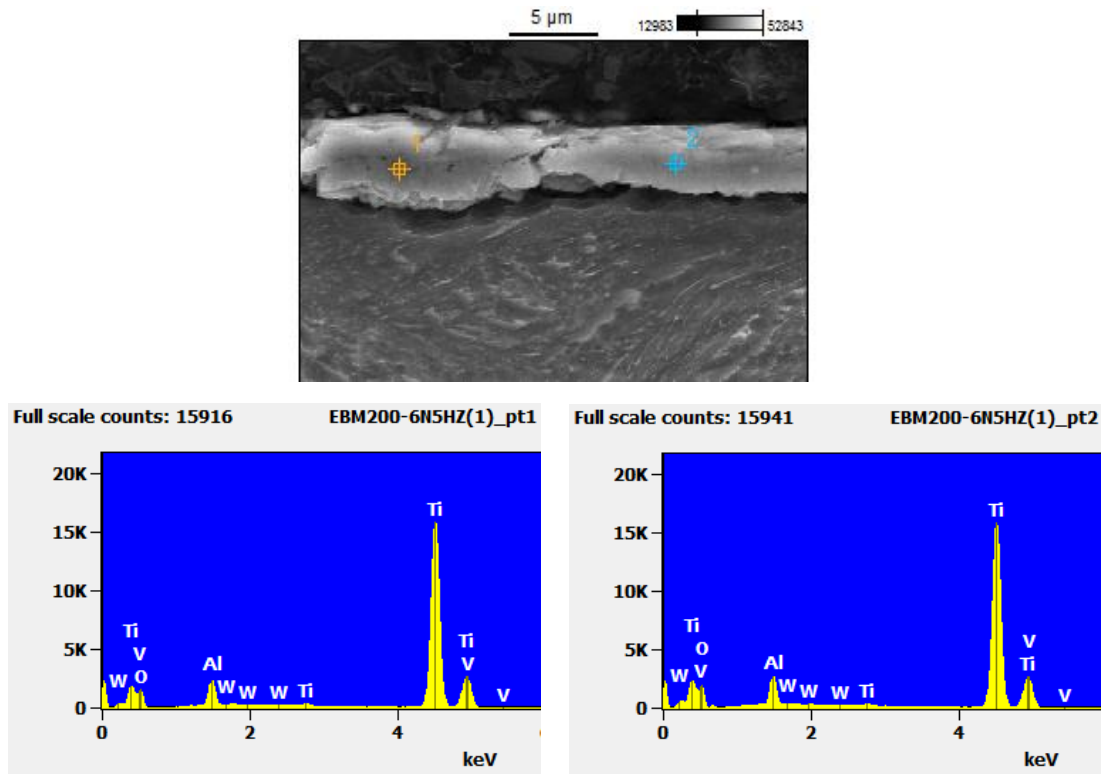


(b)

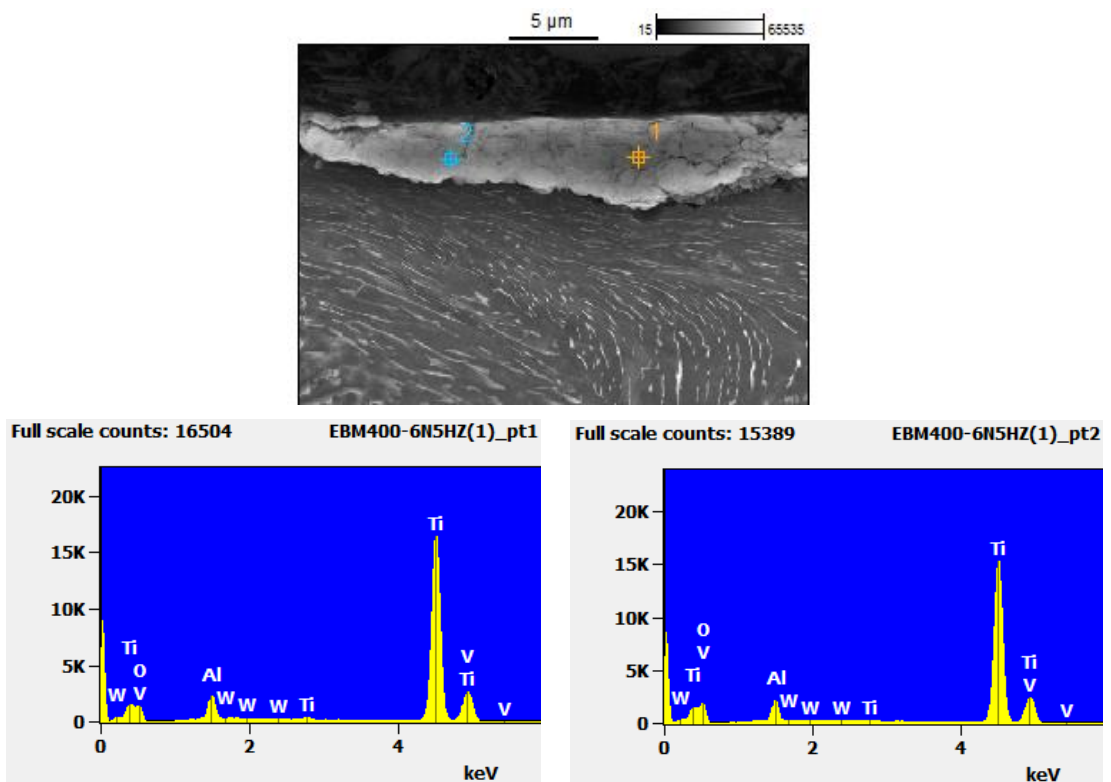


(c)

Fig. 5.8 Cont.

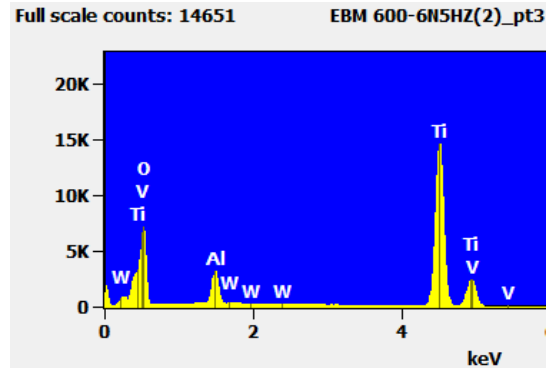
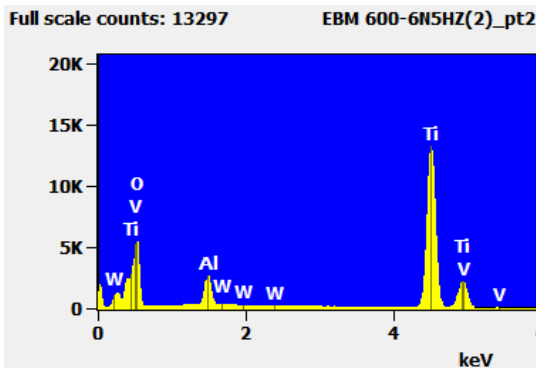
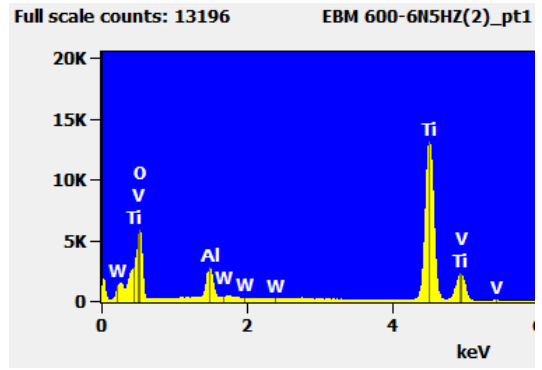
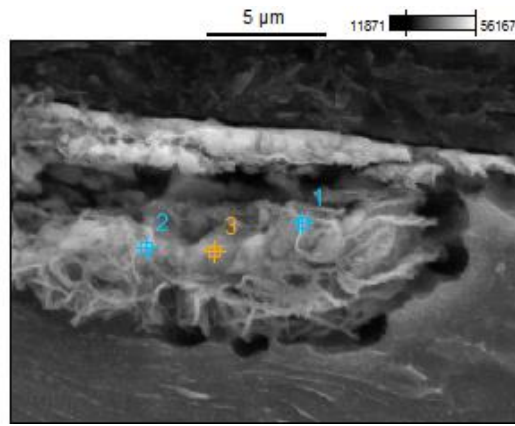


(a)



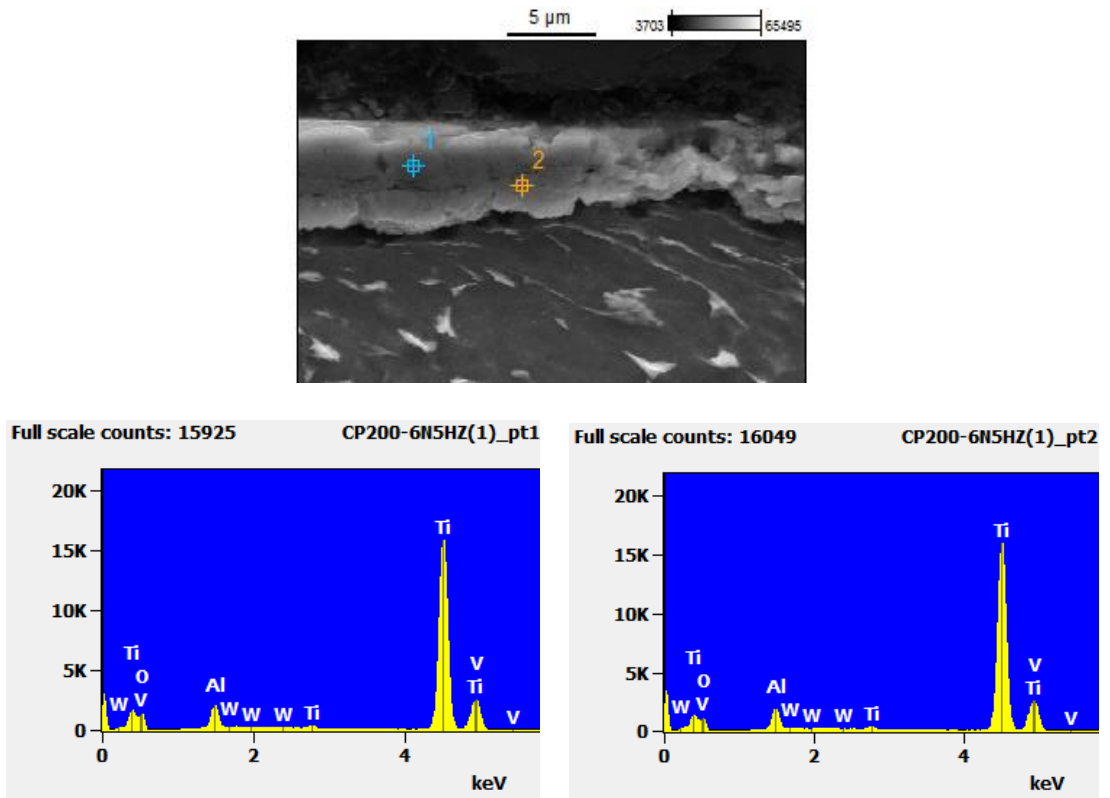
(b)

Fig. 5.9 SEM cross sectional images and EDS spectra from analysis of points (1, 2, and 3) marked in the SEM image of EBM samples tested at (a) 200°C, (b) 400°C and (c) 600°C, and under the test load of 6N.



(c)

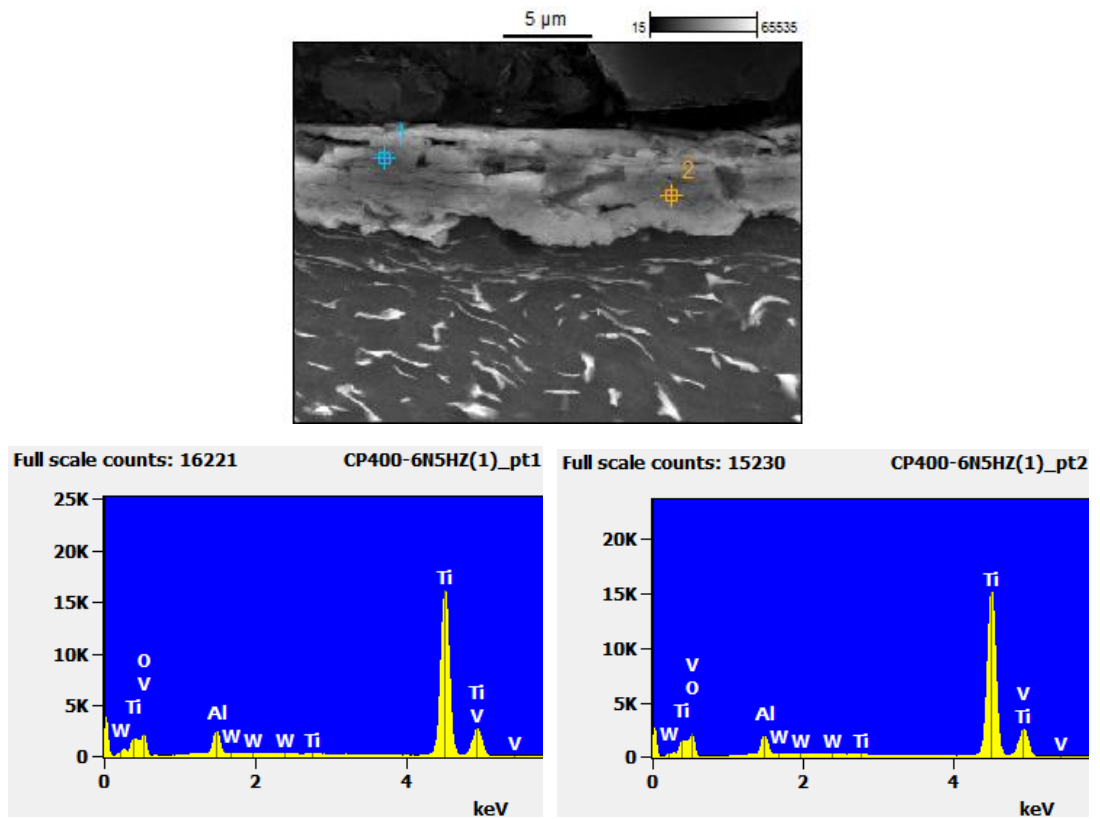
Fig. 5.9 Cont.



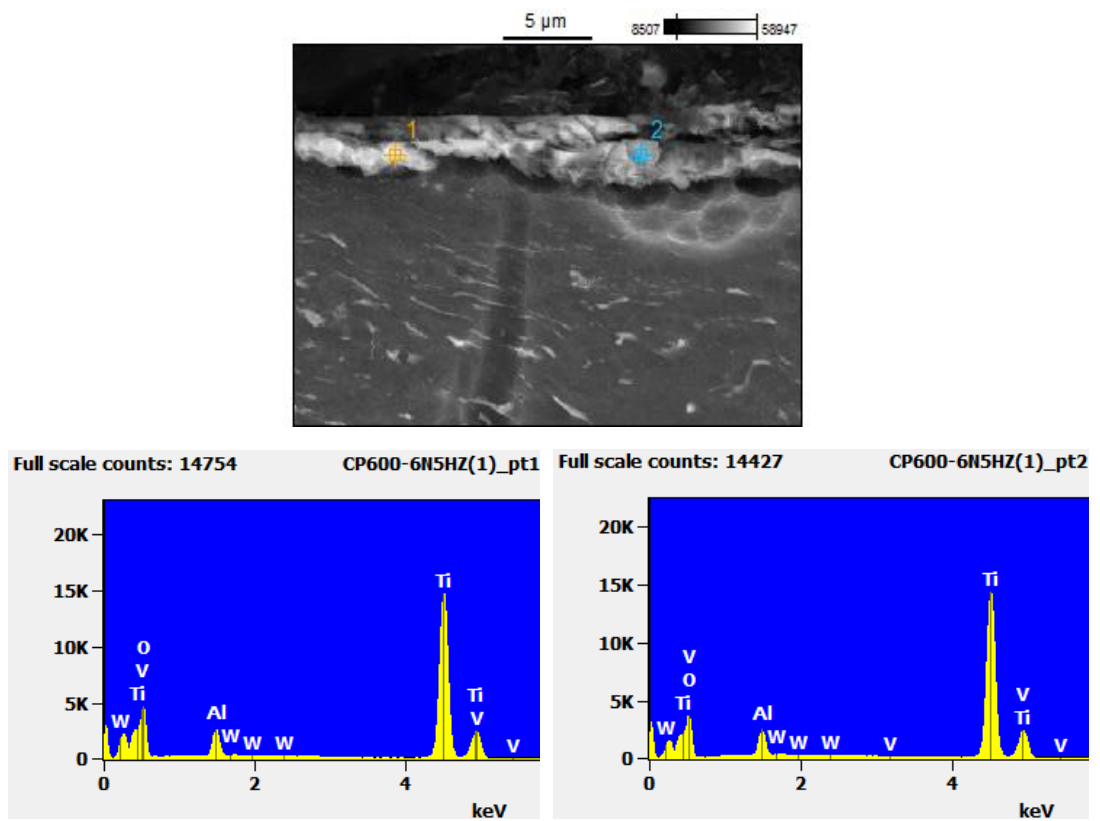
(a)

Fig. 5.10 SEM cross sectional images and EDS spectra from analysis of points (1, 2, and 3) marked in the SEM

image of CP samples tested at (a) 200°C, (b) 400°C and (c) 600°C, and under the test load of 6N.



(b)



(c)

Fig. 5.10 Cont.

EDS spectra in Fig. 5.8 to Fig. 5. 10 are also similar to the spectra for point 1 and point 2 in Fig. 4.8, which debris present in the cross section of a sample tested at room temperature, showing the common oxygen peak in debris. The oxygen peaks Fig. 5.8 to Fig. 5.10 have indicated an increase in oxygen peak intensity as test temperature increases, for SLM, EBM and CP samples. The increase in oxygen peak intensity may not be linear and there seems significantly stronger peaks at 600°C. The compositions of the EDS points based on the semi-quantitative analysis are listed in Table 5.2 and the data of oxygen content as a function of test temperature are plotted in Fig. 5.11. Clearly, the increase in oxygen content in the debris is in a faster rate as temperature increases from 400°C to 600°C than the increase at lower temperatures.

Table 5.2 Compositions (at%) from semi-quantitative analysis of the points in the SEM images and based on the EDS spectra in Fig. 5.8 to Fig. 5.10.

Test cond. & point	O	Al	Ti	V	W
SLM 200°C Point 1 Fig. 5.8a	43.1	7.3	47.5	2.1	0.0
SLM 200°C Point 2 Fig. 5.8a	43.2	7.8	46.8	2.2	0.0
SLM 200°C Point 3 Fig. 5.8a	46.9	6.6	42.9	1.8	1.9
SLM 400°C Point 1 Fig. 5.8b	56.7	5.3	36.3	1.7	0.0
SLM 400°C Point 2 Fig. 5.8b	55.0	5.9	37.3	1.7	0.0
SLM 600°C Point 1 Fig. 5.8c	68.5	4.4	25.8	1.2	0.1
SLM 600°C Point 2 Fig. 5.8c	68.3	4.5	25.9	1.3	0.0
EBM 200°C Point 1 Fig. 5.9a	43.7	6.6	47.3	2.3	0.0
EBM 200°C Point 2 Fig. 5.9a	43.4	7.4	47.1	2.2	0.0
EBM 400°C Point 1 Fig. 5.9b	50.1	5.6	42.4	1.9	0.0
EBM 400°C Point 2 Fig. 5.9b	57.9	4.7	35.8	1.6	0.0
EBM 600°C Point 1 Fig. 5.9c	75.9	3.6	19.5	1.0	0.0
EBM 600°C Point 2 Fig. 5.9c	75.1	3.6	20.2	1.1	0.0
EBM 600°C Point 3 Fig. 5.9c	76.8	3.5	18.7	1.0	0.0
CP 200°C Point 1 Fig. 5.10a	40.4	6.2	51.2	2.2	0.0
CP 200°C Point 2 Fig. 5.10a	34.3	6.5	56.7	2.6	0.0
CP 400°C Point 1 Fig. 5.10b	50.4	5.9	41.7	2.0	0.0
CP 400°C Point 2 Fig. 5.10b	51.9	5.1	41.2	1.9	0.0
CP 600°C Point 1 Fig. 5.10c	69.5	3.9	25.3	1.2	0.0
CP 600°C Point 2 Fig. 5.10c	67.3	4.2	27.2	1.3	0.0

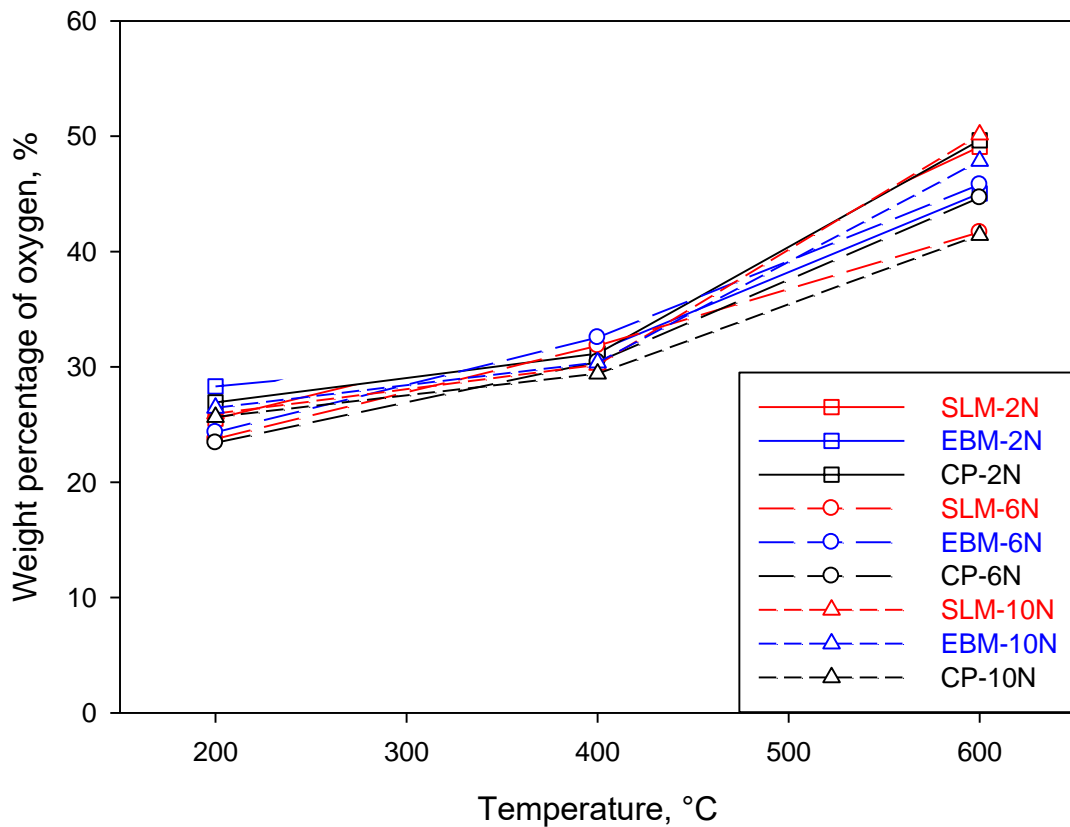


Fig. 5.11 Oxide content determined by EDS-ZAF analysis on wear debris in cross sectional samples plotted vs. tested temperature.

Although the exact forms/structures of the wear debris at the different temperatures have not further analyzed, data in Table 5.2 and Fig. 5.11 may have suggested a change of the structure(s) as test temperature increased. The significant richer in oxygen in debris at 600°C is clear. Thus, it could be probable that at 600°C, the oxygen richer oxide debris may be harder than the oxide formed at lower temperatures and thus provides a high wear resistance although the Ti-6Al-4V underneath has also become lower strength/hardness at higher temperatures.

5.4 Chapter Summary

The present series of experiments and analysis have shown that, in the temperature range from room temperature to 600°C, temperature has not significantly affected the WR, regardless of

what Ti-6Al-4V test sample (SLM, EBM or CP) was used. Wear track characterization and measurements have shown that the wear track appearance and irregularity has not changed when test temperature has changed. It is clear, however, that oxygen is richer in the titanium oxide debris as test temperature increases and the increase in oxygen content is larger from 400 to 600°C than from 200 to 400°C. It is probable that the oxygen richer oxide debris layer at higher temperature may provide a stronger wear resistant although strength/hardness of Ti-6Al-4V is lower. Thus, overall and on balance, temperature does not have a significant effect on WR.

Chapter 6 Wear Behavior of PVD-TiN Coated SLM and CP Samples

Chapters 4 and 5 were about the as-built samples made by SLM and EBM techniques or traditional process. In chapters 6 and 7, tribological performance of SLMed or traditional processed Ti-6Al-4V samples with surface coatings will be discussed. PVD TiN coating is going to be discussed in this chapter and ion implantation is in the next chapter. In Chapter 6, wear loss reflected by wear volume of TiN coated samples is going to be demonstrated compared with uncoated samples. Besides, because wear tests were stopped by different sliding distance to monitor the failure process of the coatings, thus wear volume, wear depth and wear width vs. sliding distance/time will further be discussed. And then, followed by the observation of track surface morphology, the thinning and breaking of the coating and finally the exposing of the sub-material, the mechanism of the coating thinning and breaking until the substrate wear will be revealed in this chapter.

6.1 Wear volume data

6.1.1 Initial data for comparison with uncoated samples

Fig 6.1 shows the comparison of wear rates of both SLM and CP samples with and without coating. For the same wear condition (2N, 5Hz and sliding distance 500m), wear rate for samples that were not coated are $\sim 1.8 \times 10^6 \mu\text{m}^3/\text{m}$ [73], which is 17-33 times higher than the wear rate of the coated samples. Thus, the coating can be viewed effective in reducing wear rate.

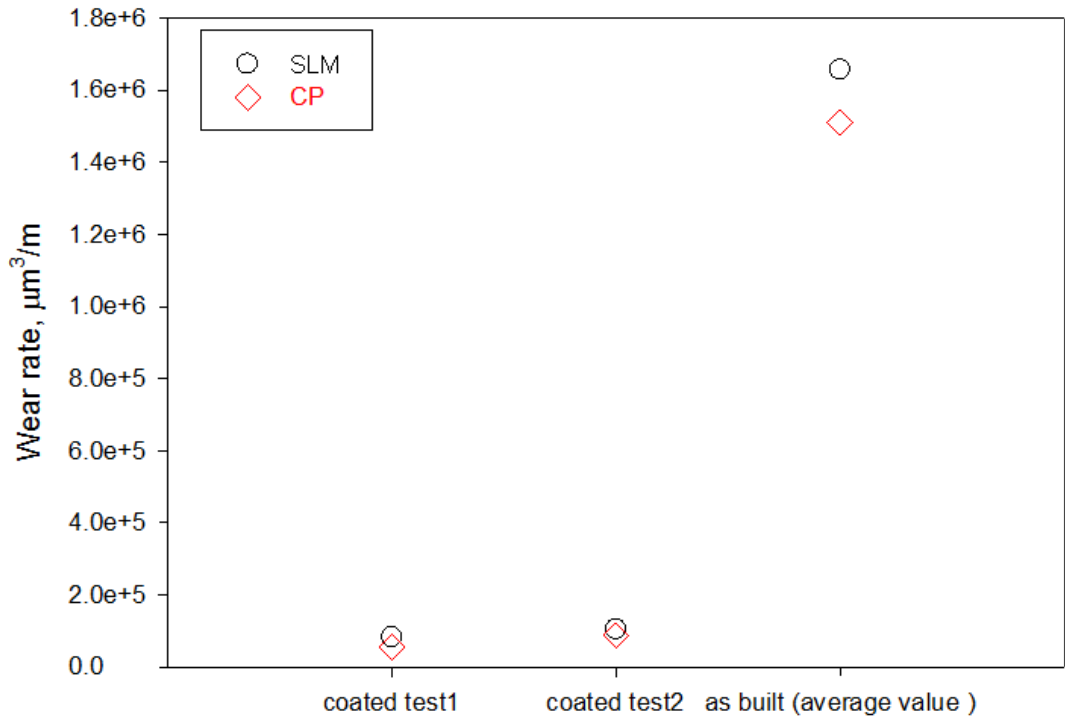


Fig. 6.1 Wear rate for SLM and CP samples with and without PVD coating.

6.1.2 Wear volume, wear depth and wear width vs. sliding distance/time

The overall data of measured wear volume (WV), maximum track depth (h_{Max}) and track width (W_{Track}) plotted as a function of time (t) are presented in Fig. 6.2. The coating on SLM or CP samples appears to have behaved similarly, following the same trends. Fig. 6.2(a) shows that, after a period of increase in WV in a low rate, with WV being $\sim 0.5 \times 10^7 \mu m^3$ for up to 3000s, the increase in WV becomes rapid to $\geq 2.5 \times 10^7 \mu m^3$ at 3800s. For the total sliding distance of 500m, the range of wear rate is $(2.7-5.2) \times 10^7 \mu m^3 / 500m = (5.5-10.4) \times 10^4 \mu m^3/m$. Data in Fig. 6.2(a) also suggests that the protective function has started diminishing severely after $\sim 3000s$ sliding.

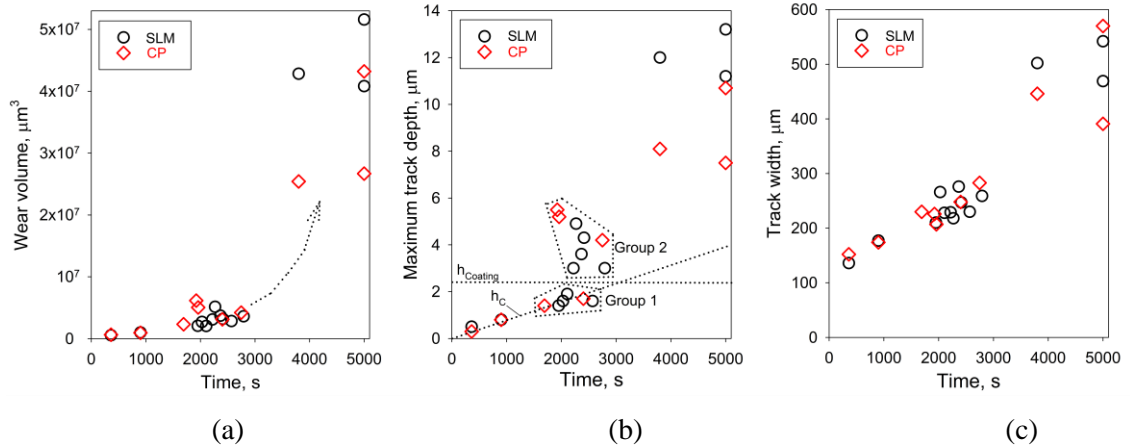


Fig. 6.2 Measured data of (a) WV, (b) h_{Max} and (c) W_{Track} plotted as a function of time for the two types of coated samples. In (b), a horizontal line representing $h_{Coating}$, outline of group 1 data with $h_{Max} < h_{Coating}$, outline of group 2 data with $h_{Max} > h_{Coating}$, a regression line labelled as h_c based on data below $h_{Coating}$ line are drawn.

In order for the coating to be analyzed when it started to fail, the COF trace which was instantly displayed during each wear experiment was closely watched during the tests. The traces of COF for the three tests (900s, 2219s and 5000s) are shown in Fig. 6.3. In the test up to 900s (Fig. 6.3(a)), COF is ~ 0.65 , after the initial rapid rise. This represents the test with no sudden change of signal suggesting no breaking of coating. In the 2219s test (Fig. 6.3(b)), the test was stopped (at 2219s) when a sudden change (a drop in this case) of COF was noticed during the test. This sudden change of COF is suggested to be due to the breaking of the coating in the central region of the track. For 5000s testing (Fig. 6.3(c)), a major change of COF took place at ~ 2592 s and for the remaining time of the test COF is more unstable compared to the initial period before the sudden change at ~ 2592 s.

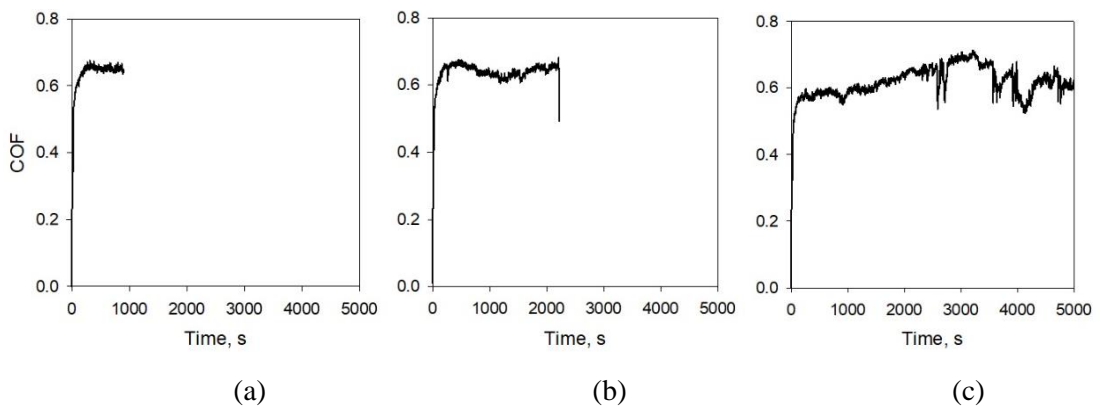


Fig. 6.3 Coefficients of friction during testing of SLM samples for (a) 900s, (b) 2219s and (c) 5000s.

From the $W_{\text{Track}}-t$ graph in Fig. 6.2(c), W_{Track} increases linearly with t although the increase has become slightly more rapid after $\sim 3000\text{s}$. The $h_{\text{Max}}-t$ relationship in Fig. 6.2(b) is however more complicated. It appears that when sliding time increased to $\sim 1700\text{s}$, h_{Max} has become unpredictable. Within the period of $1700-2800\text{s}$, h_{Max} can remain low at $2\mu\text{m}$ or below (group 1 data in Fig. 6.2(b)) or can be high at $3\mu\text{m}$ or above (group 2 data in Fig. 6.2(b)). During the test of a group 2 sample, the test was stopped when there was a clear noise (sudden change) observed in COF trace that was simultaneously being displayed during the test, similar to Fig. 6.3(b). As h_{Coating} before testing is $2.4\mu\text{m}$, which is also indicated in Fig. 6.2(b), a value of $h_{\text{Max}} \geq 3\mu\text{m}$ means the coating has at least locally worn off. Fig. 6.2(b) also shows that at and after 3800s , coating has severely worn off with h_{Max} being many times greater than h_{Coating} .

One of the group 2 h_{Max} values in Fig. 6.2(b) is further explained, as an example, using the corresponding measured trace of cross sectional profile shown in Fig. 6.4. The trace is not smooth, and this may be the result of wear debris present in the wear track as will be shown. If the coating had not failed, the trace should have followed curve B, as is suggested in Fig. 6.4, with track width (W_{Track}) being $315\mu\text{m}$ and $h_{\text{Max}}=2.1\mu\text{m}$. The true trace is however different. In the central location of $94\mu\text{m}$ in width, which is assumed to be the width of the coating having been worn (W_{Worn}), $h_{\text{Max}}=5.3\mu\text{m}$. This value, being considerably greater than the thickness of coating (h_{Coating}), demonstrates the coating having been worn off in the central location of the track.

In general, as $h_{\text{Coating}}=2.4\mu\text{m}$, the remaining thickness of a coating in the central location of a track ($h_{\text{Coat.Tr}}$) of a group 1 sample in Fig. 6.2(b) is equal to or greater than $0.5\mu\text{m}$ ($=h_{\text{Coating}}-h_{\text{Max}}=2.4\mu\text{m}-1.9\mu\text{m}$) with $1.9\mu\text{m}$ being the maximum h_{Max} value of group 1 samples. Thus, no severe damage or only the start of damage of the coating are expected for group 1 tested samples. On the other hand, $h_{\text{Coat.Tr}}=h_{\text{Coating}}-h_{\text{Max}}=2.4\mu\text{m}-3.0\mu\text{m}<0$ in group 2 samples, with $3.0\mu\text{m}$ being the minimum value of group 2 samples. Thus, coating has been severely damaged and that breaking of the coating has taken place in central location of the track are expected in each of the group 2 samples. The two data points for tests just under 2800s (2747s and 2791s) are in group 2 and thus it is highly unlikely the coating can remain undamaged in a test beyond 2800s .

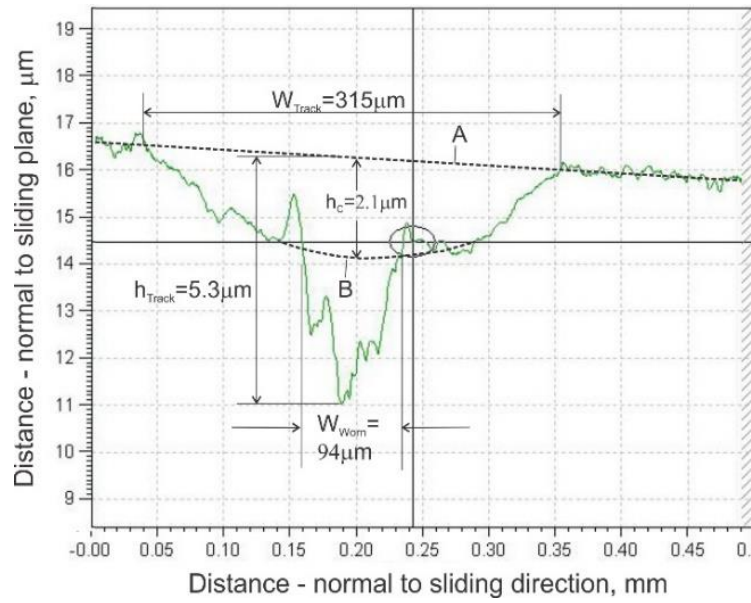


Fig. 6.4 A trace from the profilometry measurement for a CP sample wear track with sliding wear stopped at 2747s.

Line A is the suggested base line and curve B is the suggested trace for the condition that the coating had not fractured in the central location.

A further discussion of wear thinning and the subsequent loss of the protective function of the coating can be aided by the illustration in Fig. 6.5 for the coating which has not completely worn meaning $h_{Max} < h_{Coating}$. Assuming that the WC ball does not wear and only TiN coating wears during sliding, the relationship between h_c and W_{Track} and the relationship between WV and h_c or WV and W_{Track} are:

$$h_c = r - \sqrt{r^2 - \left(\frac{W_{Track}}{2}\right)^2} \quad (6.1)$$

and

$$WV = \left[r^2 \times \sin^{-1} \left(\frac{W_{Track}/2}{r} \right) - \frac{W_{Track} \times (r - h_c)}{2} \right] \times L \quad (6.2)$$

respectively, with r is the radius of the counter ball (5mm) and L is the length of the wear track (10mm).

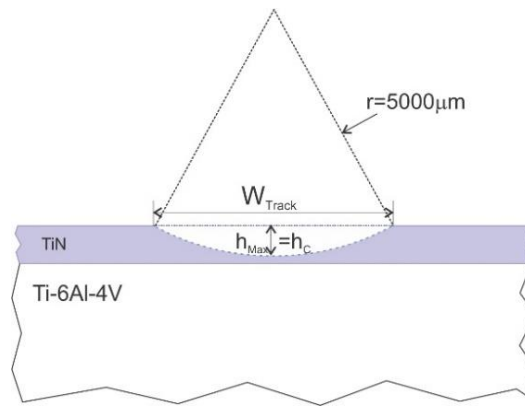


Fig. 6.5 Schematic illustration of a cross section of a wear track showing $h_c (=h_{Max}$ when $h_c < h_{Coating}$). Note: W_{Track} and h_{Max} are not drawn in proportion.

Measured values plotted in Fig. 6.2 are replotted to examine the relationships between h_{max} and W_{Track} in Fig. 6.6(a) and WV and W_{Track} in Fig. 6.6(b), respectively, together with the calculated curves based on equation (6.1) and equation (6.2). It is clear from Fig. 6.6 that the experimental values of h_{max} and WV increase with W_{Track} , as equations (6.1) and (6.2) have predicted, until h_{Max} reaches $2\mu m$. Then, h_{max} itself has become unpredictable due to the possible break of coating locally as illustrated in Fig. 6.4 and the physical features of wear leading to this will be described in the next section. When h_{Max} has become unpredictable due to thinning and locally fracturing of the coating, corresponding to $W_{Track}=(200-300)\mu m$, WV is not significantly affected. Thus, the measured WV values have not departed significantly from the calculated values in Fig. 6.6(b). As wear progresses beyond $h_{max} > h_{Coating} = 2.4\mu m$, both h_{Max} has continued to be and WV has become significantly higher than the respective value predicted by equations (6.1) and (6.2). The physical features leading to this departure are examined next.

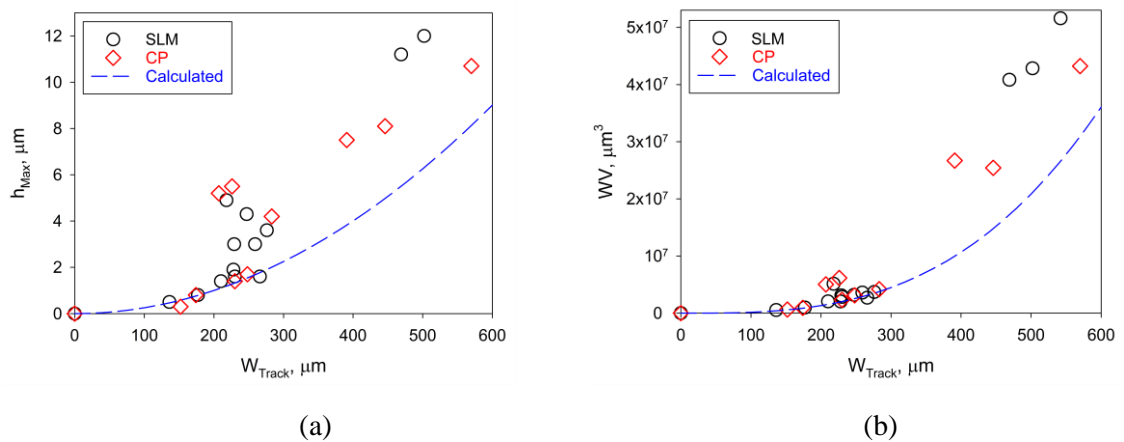


Fig. 6.6 Measured and calculated (a) depth and (b) wear volume plotted against track width for both SLM and CP

samples.

6.2 Track surface, thinning and breaking of coating, and substrate wear

Fig. 6.7 shows the track surfaces of SLM samples tested for up to 5000s. For 900s, W_{Track} is $\sim 200\mu\text{m}$ and the track is quite smooth with fine and faint longitudinal (along the sliding direction) markings and with debris clearly decorating along the track edges and occasionally inside the track. The high magnification image (Fig. 6.7(a), lower right) not only displays clearly the fine debris particles, but also small bands ($\approx 10\mu\text{m}$) roughened in mid location of the track, suggesting locally chipping in coating surface may have started. Since the coating as a whole has not been damaged and has not become discontinuous for Ti-6Al-4V to be exposed, the debris must be the result from the coating wear.

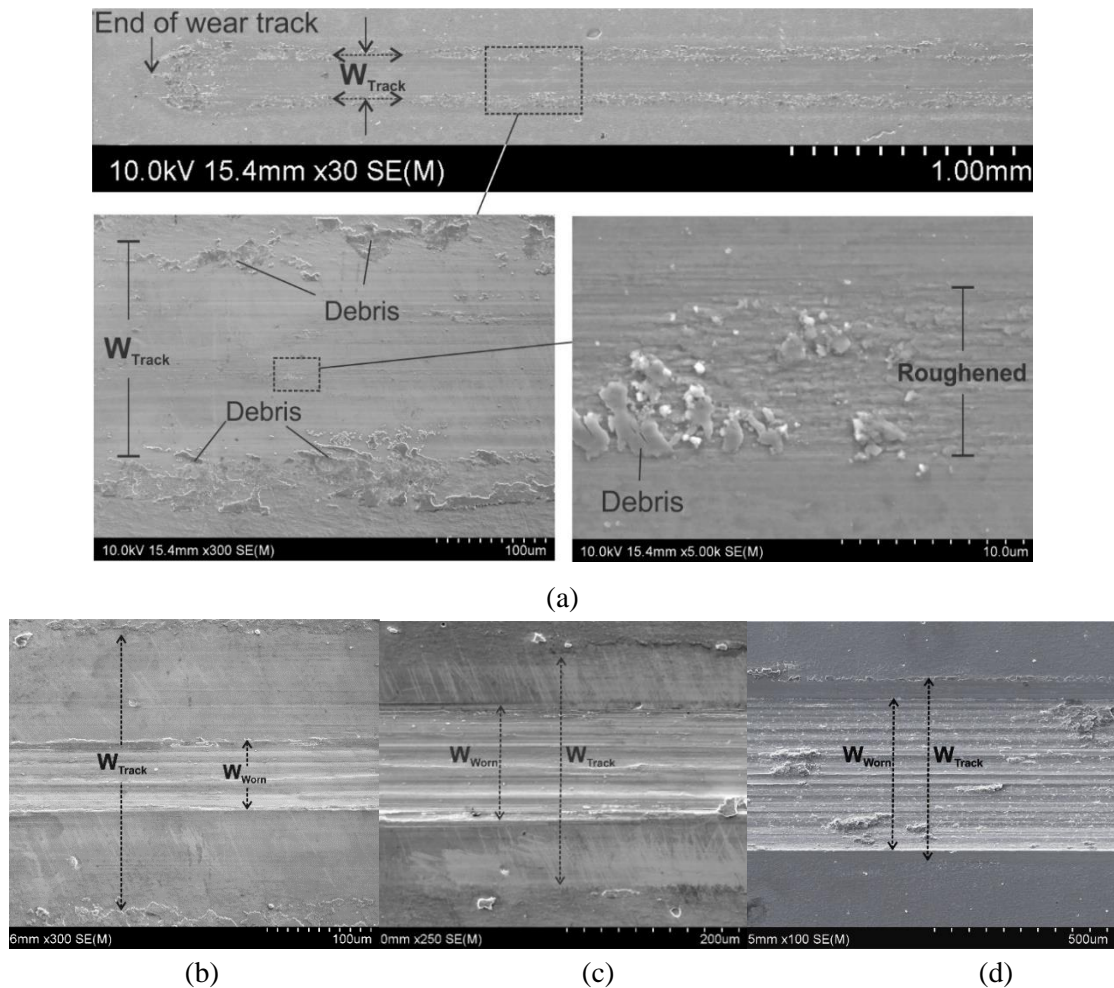
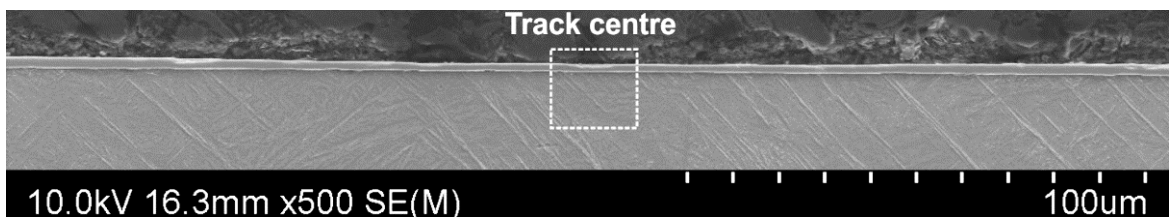


Fig. 6.7 SEM images of track surfaces of SLM samples tested for (a) 900s and (b) 2219s, (c) 2268s and (d) 5000s.

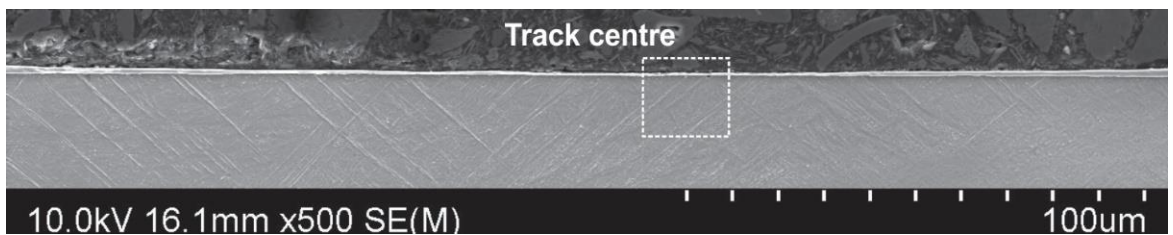
For the test at 2219s (Fig. 6.7(b)), W_{Track} has increased and there is a band of heavy marking/scribing with a width marked as W_{Worn} , suggesting that a section of coating has worn

off exposing Ti-6Al-4V. As can be estimated from the image (Fig. 6.7(b)), $W_{\text{Worn}}/W_{\text{Track}} \approx 64\mu\text{m}/265\mu\text{m}=24\%$. The other test sample (Fig. 6.7(c)) for a similar test time shows almost the same W_{Track} value, but a significant increase in W_{Worn} with $W_{\text{Worn}}/W_{\text{Track}} \approx 138\mu\text{m}/266\mu\text{m}=52\%$. In comparison, the $W_{\text{Worn}}/W_{\text{Track}}$ value detected in Fig. 6.4 is $(94\mu\text{m}/315\mu\text{m})=30\%$. On the other hand, as shown in Fig. 6.2(b), there are a number of tests (group 1) for 1700-2600s where $h_{\text{Max}} < 2\mu\text{m}$, suggesting that W_{Worn} is zero and thus $W_{\text{Worn}}/W_{\text{Track}}$ is zero. This means that while W_{Track} increases linearly with time in that 1700-2800s period, as shown in Fig. 6.2(c), the time for the coating to break and for h_{Max} value to increase significantly is unpredictable. Beyond 2800s, relatively, W_{Worn} has increased considerably more than W_{Track} has, with $W_{\text{Worn}}/W_{\text{Track}} \approx 440\mu\text{m}/512\mu\text{m}=86\%$ for test at 5000s (Fig. 6.7(c)).

The progression of thinning and breaking of coating can be better illustrated with cross sectional images shown in Fig. 6.8. As can be observed in Fig. 6.8(a), at 900s, the coating in track central ($h_{\text{Coat.Tr}}$) is thinner than the coating on both sides of the track where the coating thickness remains as h_{Coating} . From Fig. 6.8(d), $h_{\text{Coat.Tr}} \approx 1.6\mu\text{m}$ and from Fig. 3.3, $h_{\text{Coating}} \approx 2.4\mu\text{m}$. A slightly chipping off in the coating is observable in Fig. 6.8(d), consistent with what can be observed locally in high magnification image in Fig. 6.7(a), as explained before. In a sample tested for 2105s (Fig. 6.8(b) and Fig. 6.8(e)), which is one of the samples where coating has not broken, $h_{\text{Coat.Tr}} \approx 0.5\mu\text{m}$. In a sample tested for 2219s (Fig. 6.8(c) and Fig. 6.8(f)), which is a sample where coating has broken, $h_{\text{Coat.Tr}} = (0.3-0.4)\mu\text{m}$ in the section having already broken.



(a)



(b)

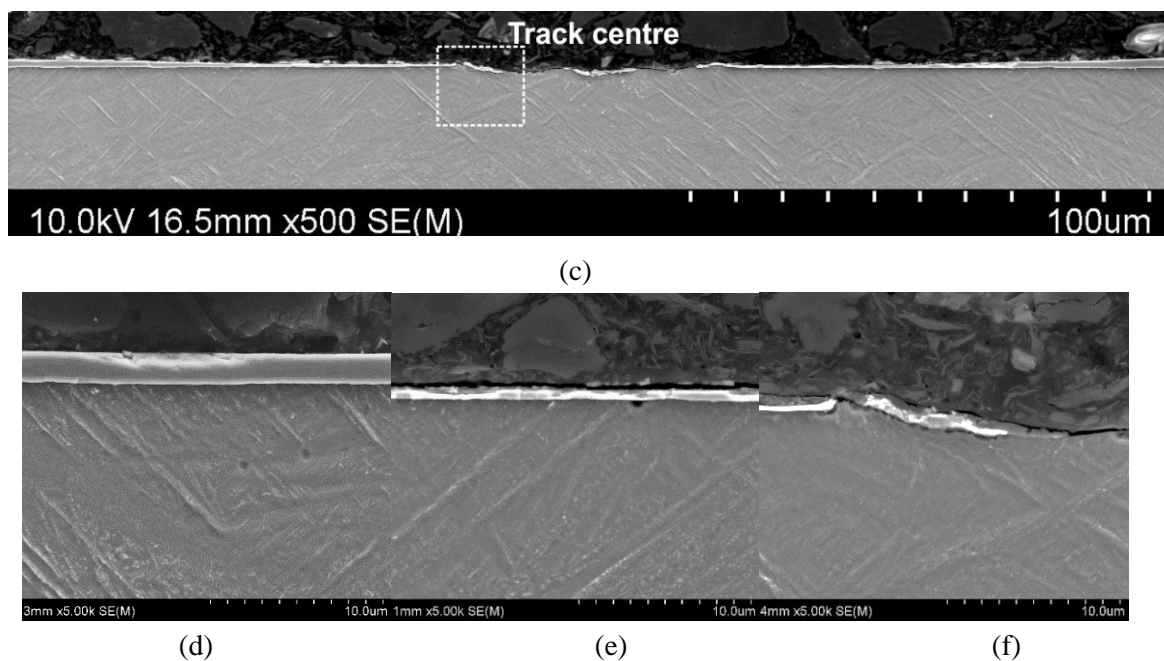


Fig. 6.8 SEM micrographs of track cross sections of SLM samples tested for (a) 900s, (b) 2105s, and (c) 2219s, (d), (e) and (f) are high magnification micrographs in local area marked with a small square in (a), (b) and (c), respectively.

For CP samples tested for 900s (Fig. 6.9(a)), similar to SLM samples (Fig. 6.7(a)), coating has also remained intact ($W_{\text{worn}}=0$) with debris on both sides of the track and also distributed within the track. For both cases, W_{Track} is similar ($190\mu\text{m}$ for SLM sample and $200\mu\text{m}$ for CP sample). Energy dispersive spectroscopy (EDS) has revealed that wear debris particles of TiN coating contain a high amount of oxygen. This is shown by an example of EDS spectra in Fig. 6.9(a) showing that coating itself is Ti and N rich with little oxygen and in debris spot oxygen has been enriched. It is then reasonable to suggest that debris forms during wear of coating has been converted to oxide under the condition of temperature increase and abandon of oxygen in air. Thermodynamically, oxide is more stable than nitride at high temperature [93].

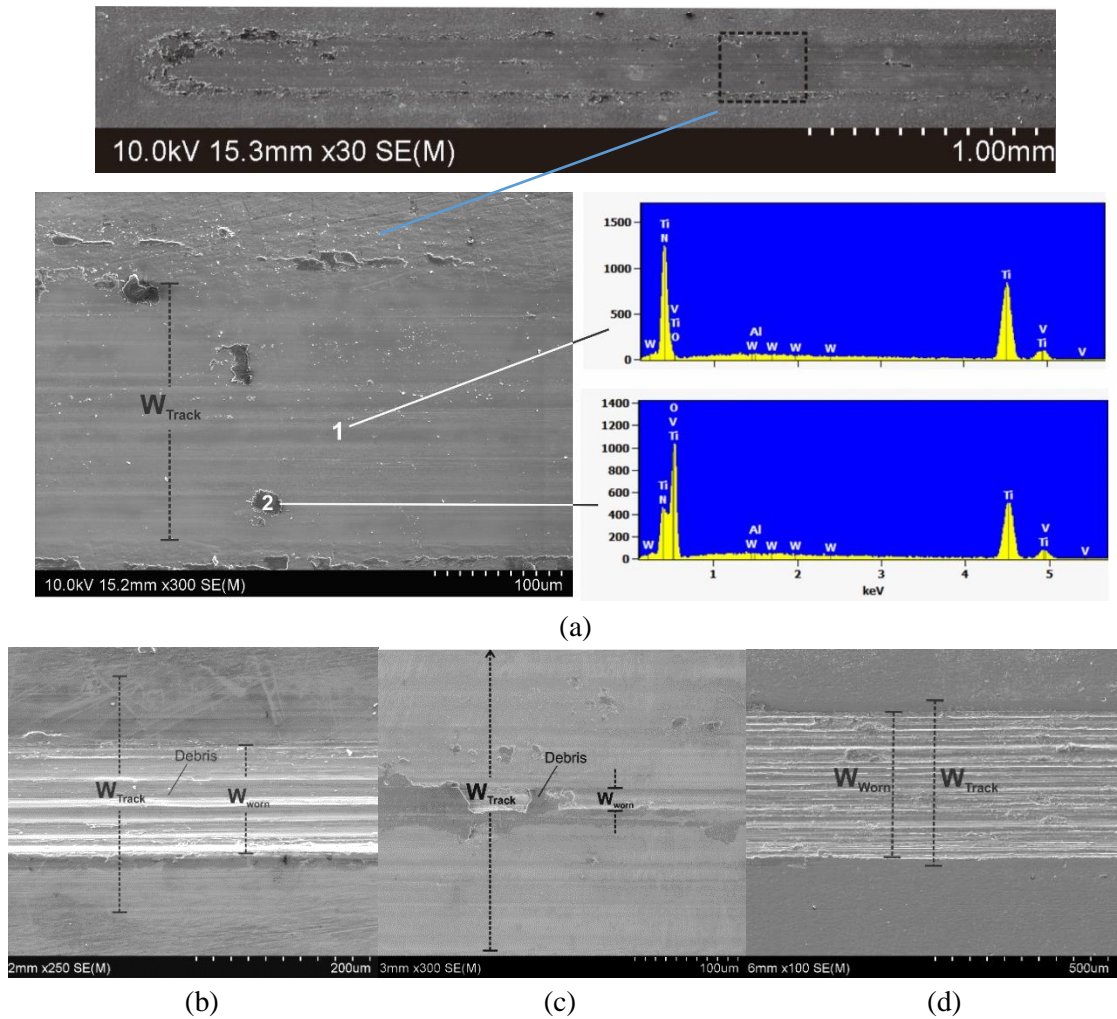


Fig. 6.9 SEM images of track surfaces of CP samples tested for (a) 900s and (b) 1958s, (c) 2401s and (d) 5000s. In

(a), two EDS spectra from the spots indicated as 1 and 2 are shown.

As has already been explained for SLM samples, in the period of 1700-2800s, the coating has been thinned to $(0.5-0.6)\mu\text{m}$ and below, but when the coating breaks in the central location is unpredictable within this period. This is the same for CP samples and a pair of samples are shown in Fig. 6.9(b) and Fig. 6.9(c). For the sample tested for 1958s (Fig. 6.9(b)), break of coating has well taken place and thus $W_{\text{worn}}/W_{\text{Track}} \approx 125\mu\text{m}/275\mu\text{m} = 46\%$ is high. On the other hand, for the sample tested for 2401s (Fig. 6.9(c)), breaking must have only just occurred and thus $W_{\text{worn}}/W_{\text{Track}} \approx 22\mu\text{m}/285\mu\text{m} = 8\%$ is low. The narrowly worn groove ($\sim 22\mu\text{m}$ in width) along the sliding direction is filled by debris in some sections. For long testing time at 5000s, $W_{\text{worn}}/W_{\text{Track}} \approx 425\mu\text{m}/477\mu\text{m} = 89\%$, similar to that of SLM. Cross section images in Fig. 6.10(a) and c shows the thinning of coating at 900s with chipping of coating apparent. Fig. 6.10(b) and d illustrate that the local groove narrowly worn in Fig. 6.9(c) is the result of local material

including both the thinned coating and the substrate Ti-6Al-4V below having been pressed downward.

The role of debris on local wear is now discussed further. TiN has very high hardness and is thus used as the coating to protect Ti-6Al-4V from wear. Debris due to the wear of TiN coating, as illustrated in Fig. 6.9(a), is oxygen rich. Titanium oxides may be very high in hardness and the very hard debris, if not removed to sides, can act as the hard third body taking part in the abrasive wear process. The filling of debris observed in Fig. 6.9(c) and locally both the thinned coating and the Ti-6Al-4V substrate having been indented shown in Fig. 6.10(d) suggest that debris can locally press the material (both thinned coating and Ti-6Al-4V) or assist the wearing of the material. Thus, h_{Max} is significantly higher than $h_{Coating}$ although it is only locally in the central region the coating has started to break.

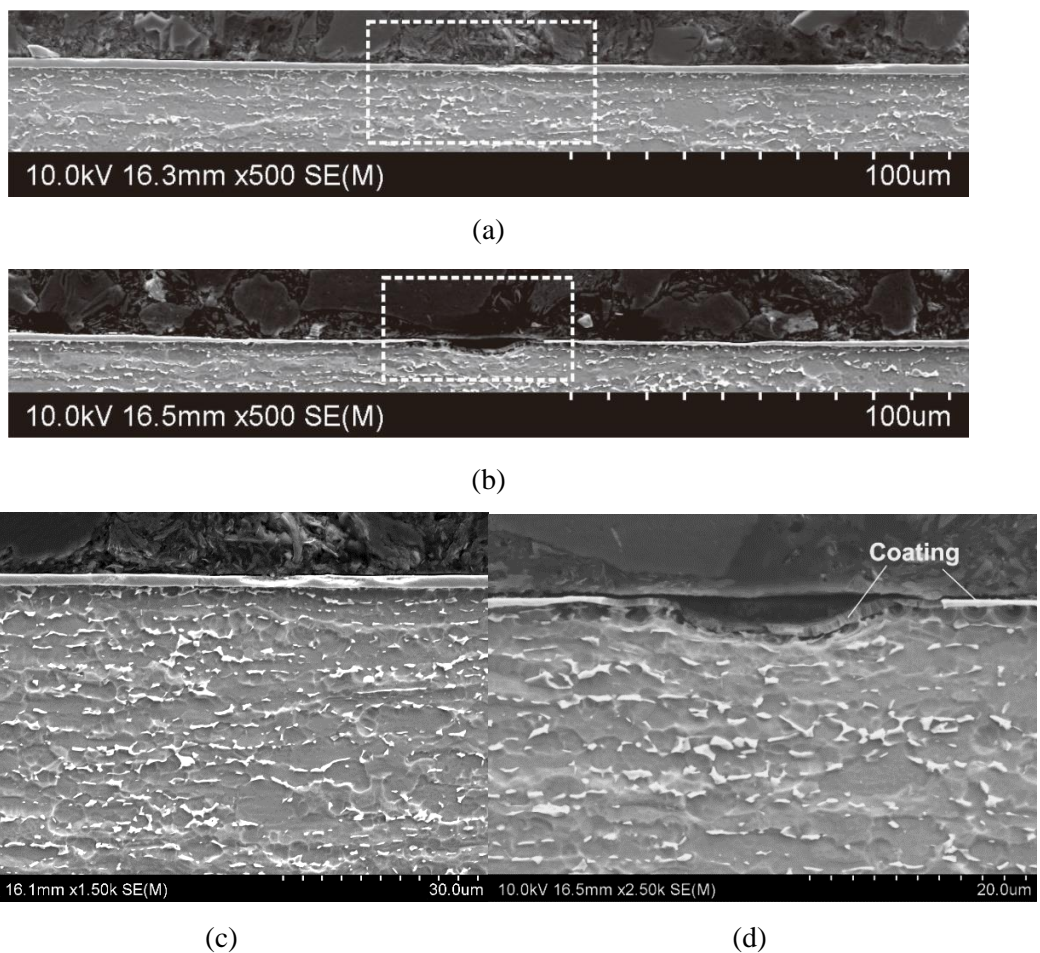


Fig. 6.10 SEM micrographs of track cross sections of CP samples tested for (a)900s and (b) 2401s, (c) and (d) are high magnification micrographs in local area marked with a small square in (a) and (b), respectively.

Two data sets of SLM group 1 in Fig. 6.2(b) may further imply the role of debris in wear process. In the test for 2105s in group 1, $h_{\text{Max}}=1.9\mu\text{m}$ (see also Fig. 6.8(b) and Fig. 6.8(e) for cross sectional images). This means $h_{\text{Coat.Tr}}=h_{\text{Coating}}-h_{\text{Max}}=2.4\mu\text{m}-1.9\mu\text{m}=0.5\mu\text{m}$ without coating break. In the other test in group 1 when $t=2567\text{s}$, $h_{\text{Max}}=1.6\mu\text{m}$, meaning $h_{\text{Coat.Tr}}=h_{\text{Coating}}-h_{\text{Max}}=2.4\mu\text{m}-1.6\mu\text{m}=0.8\mu\text{m}$ also without coating break. On the other hand, in group 2 data, $h_{\text{Coat.Tr}}<0$, coating has broken and debris may assist the wear of substrate Ti-6Al-4V locally, so that $h_{\text{Max}}>3\mu\text{m}$. As shown in Fig. 6.8(f) and Fig. 6.10(b), after coating has broken locally, discontinued coating with $(0.3-0.4)\mu\text{m}$ in thickness can still be seen. It can thus be suggested that when $h_{\text{Coat.Tr}}=0.5\mu\text{m}$, debris may have an important role causing local break of the coating.

6.3 Mechanism and subsequence of coating protection and deterioration

The overall process of how TiN PVD coated Ti-6Al-4V substrate wears in the present experiments can be summarized, as illustrated in Fig. 6.11. For test time less than 1700s, generally, $h_{\text{Max}}=h_{\text{C}}<2\mu\text{m}$ as predicted by the h_{C} line in Fig. 6.2(b). The coating which is being thinned during testing within this period would not be damaged (Fig. 6.11, top), thus, providing a complete protection of Ti-6AL-4V. In the period 1700-3000s, as predicted by the h_{C} line in Fig. 6.2(b), $h_{\text{Coat.Tr}}$ decreases with t . However, coating can be damaged well before 3000s (but after 1700s) (Fig. 6.11 mid). The hard coating debris may cause the damage of the coating when it has become thin. The damaged location can result in high h_{Max} , as debris acts as third body to wear the Ti-6Al-4V below, thus $h_{\text{Max}}>h_{\text{C}}$ and $h_{\text{C}}<h_{\text{Coating}}$. At 3000s, $h_{\text{Max}}>h_{\text{C}}$ and $h_{\text{C}}=h_{\text{Coating}}$. At this point of time, coating outside W_{Worn} and within W_{Track} still provides a strong protection. Beyond 3000s, $\Delta W_{\text{Worn}}/\Delta t$ is becoming increasingly higher and higher and $W_{\text{Worn}}/W_{\text{Track}}$ is moving towards 1 as coated area for wear protection is becoming increasingly less and less. Well beyond 3000s (Fig. 6.11 bottom), WV due to h_{max} is considerably higher than the predicted WV due to h_{C} , as is also shown in Fig. 6.6(b).

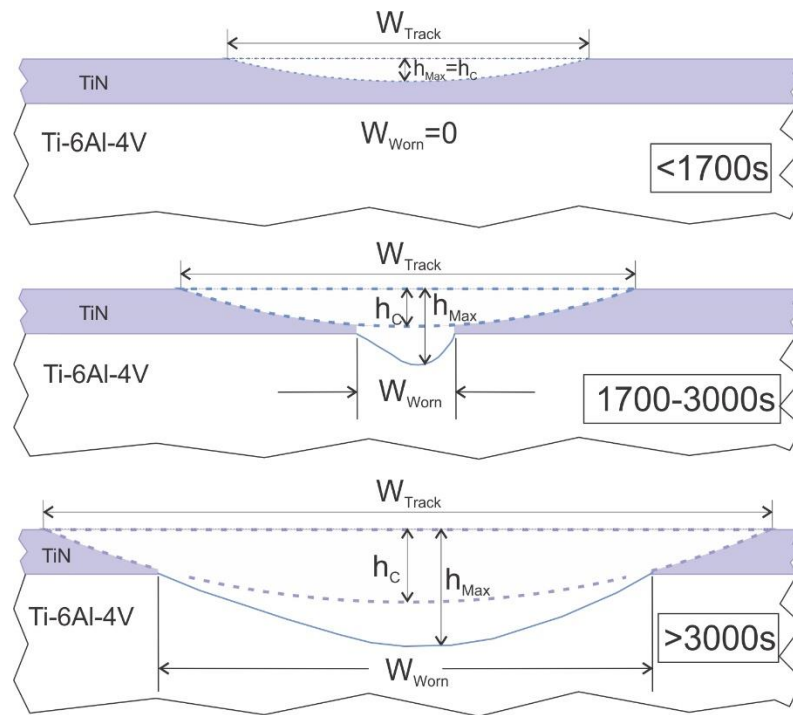


Fig. 6.11 Schematic illustration of wear track before (top schematic) and after the coating having locally broken in mid track (mid schematic), respectively, and continuation of wear with the portion of coating resisting wear becoming less and less (bottom schematic).

Thus, in summary, three sequential stages of wear deterioration during dry linear reciprocating wear tests using WC-Co as counter material have been identified, for both coated Ti-6Al-4V samples processed either by SLM or by a conventional process (CP). They are: Stage I - pure wear thinning of coating, Stage II - locally breaking of the thinned coating in central location of track, and Stage III - widening of width of the section that the coating has been worn. Stage I is a slow process with Ti-6Al-4V completely protected and, thus, thickness of TiN coating (h_{Coating}) is primarily the determining factor for how well the coating can protect Ti-6Al-4V against wear. For $h_{\text{Coating}} \approx 2.4 \mu\text{m}$, it has been found that Stage II started at a point when the wear depth (h_{Max}) reached $1.9 \mu\text{m}$ or slightly lower. Within this point or a little after, the coating in the central location breaks. Debris may assist significantly the breaking process. When breaking occurs, h_{Max} becomes higher than $3 \mu\text{m}$ as locally wear rate of Ti-6Al-4V has become high. However, in Stage II, the locally high wear rate has not affected significantly the wear volume of the sample. Into Stage III, the width of the coating totally worn (W_{Worn}) increases more rapidly than the increase in the width of wear track (W_{Track}) with time. Thus, the protection function rapidly diminishes in Stage III.

Chapter 7 Wear behavior of nitrogen ion implanted SLM and CP samples

After studying the effect of PVD TiN coating on wear resistance as reported in the previous chapter, wear tests at room temperature on SLM and CP samples implanted with nitrogen ions were conducted. This was followed by examining the wear tracks and COF traces in order to explain the wear rate data obtained. To further explain the effect of ion implantation on wear rate as shown by the results of wear tests, depth profiles of hardness were determined using nanoindentation. The details of these results will be presented and discussed in this chapter, followed by the suggestion on how effective ion implantation is for reducing wear rate.

7.1 Wear test data and track examination

7.1.1 Comparative wear rate data

As has been explained in Chapter 3 (section 3.3), loading of wear tests for ion implanted samples needed to reduce to 1N. This is because, unlike the tests for PVD TiN coated samples, serious wear had occurred using 2N loading for only a short wear distance/time. Thus, all tests using ion implanted samples were conducted using 1N load, 2Hz and 40m total wear distance with the length of the track kept the same as other experiments at 10mm. Wear rate data are presented in Fig. 7.1. For each N-sample condition, it was planned to conduct duplicate tests. However, for N1-SLM condition, the second test resulted in zero wear rate, meaning non-measurable loss. Thus, two more tests were conducted for this condition. Again, a significant amount of wear was detected in one test and non-measurable wear loss was found in the other, as shown in Fig. 7.1(a). For all other conditions, as shown in Fig. 7.1, significant wear has taken place for the set wear distance and wear loss could readily be measured for each sample of duplicate tests for each condition.

Comparing data for CP samples in Fig. 7.1(a) to data in Fig. 7.1(c) suggests that the protection to wear by N1 implantation treatment is not very significant for CP samples, as the averaged wear rate value $((0.00028+0.00055)/2=0.00042\text{mm}^3/\text{m})$ for CP-N1 samples is only slightly lower than that $((0.00052+0.0006)/2=0.00056\text{mm}^3/\text{m})$ of non-implanted samples. Referring back to the 4 tests of N1-SLM samples with the average wear rate value of $0.00017\text{mm}^3/\text{m}$ $(=(0.00027+0+0.0004+0)/4)$, compared to $(0.00058+0.00062)/2=0.00060\text{mm}^3/\text{m}$ for non-implanted SLM samples (Fig. 7.1(c)), it can be suggested that a protection is detected from

N1 treatment. Two tests out of four recorded zero wear rate and two others have started wear quite severely for N1 treated SLM samples. A suggestion for this could be that with this treatment and for the testing period (1000s) used, protection by the implantation layer can last before or after the 1000s period. If the protection is lost well within the 1000s, severe wear has then occurred, and a significant wear rate has resulted. On the other hand, protection can last more than 1000s and thus wear rate is zero.

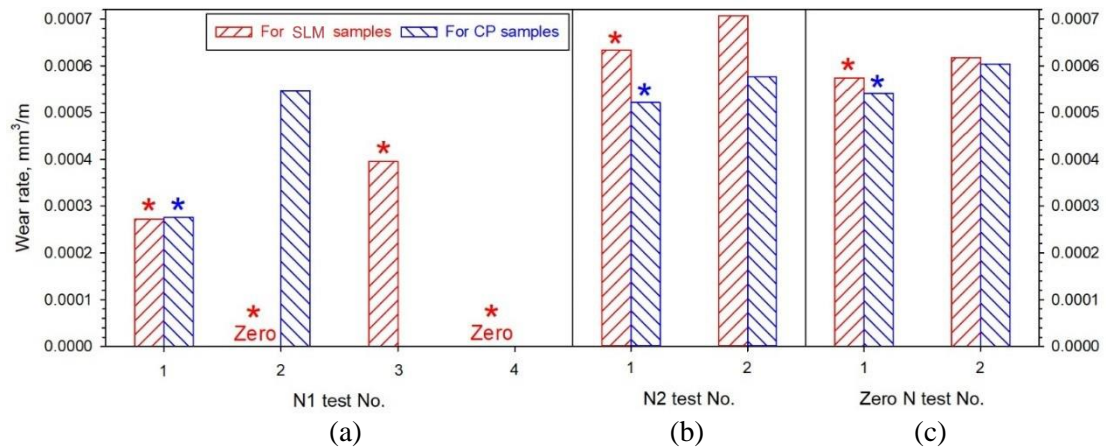


Fig. 7.1 Wear rate of eight tests conducted with $F=1N$ and $f=5Hz$ for 40m and on samples with (a) N1 and (b) N2 nitrogen concentration profile after ion implantation and (c) with samples without ion implantation. Note: data with * mean their track appearances will be shown.

Comparing data in Fig. 7.1(b) to data in Fig. 7.1(c) suggests that N2 implantation condition does not provide protection, under the wear testing condition used. This non-protection could however be from two possibilities. The first is that the N2 condition is the same as non-implantation condition, meaning that the implanted nitrogen does not provide a sufficient hardening effect to reduce wear. The second is the protection period being too short to have affected the overall wear loss in the test period. These possibilities for the measured data presented in Fig. 7.1 will be explored in detail later when COF traces recorded during testing and hardness profiles from nanoindentation measurement on the samples are presented and discussed.

7.1.2 Track surface appearance

Following the sequence of the four wear rate data (with sample 2 and sample 4 being zero) for SLM-N1 tests in Fig. 7.1(a), the four tracks in the same sequence are shown in Fig. 7.2 correspondingly, displaying the two (a and c) clearly worn and the other two (b and d) having worn little. Features of the worn tracks are similar to the worn tracks described in previous

chapters. For the two little worn tracks, tiny and darker pieces decorate and distribute along the tracks. These are wear debris during the initially light wear period before the severe wear had started, similar to the wear debris before coating break when PVD TiN coated samples were tested, as described in last chapter. This indicates the existence of protection by N1 treatment although the protection may not be strong.

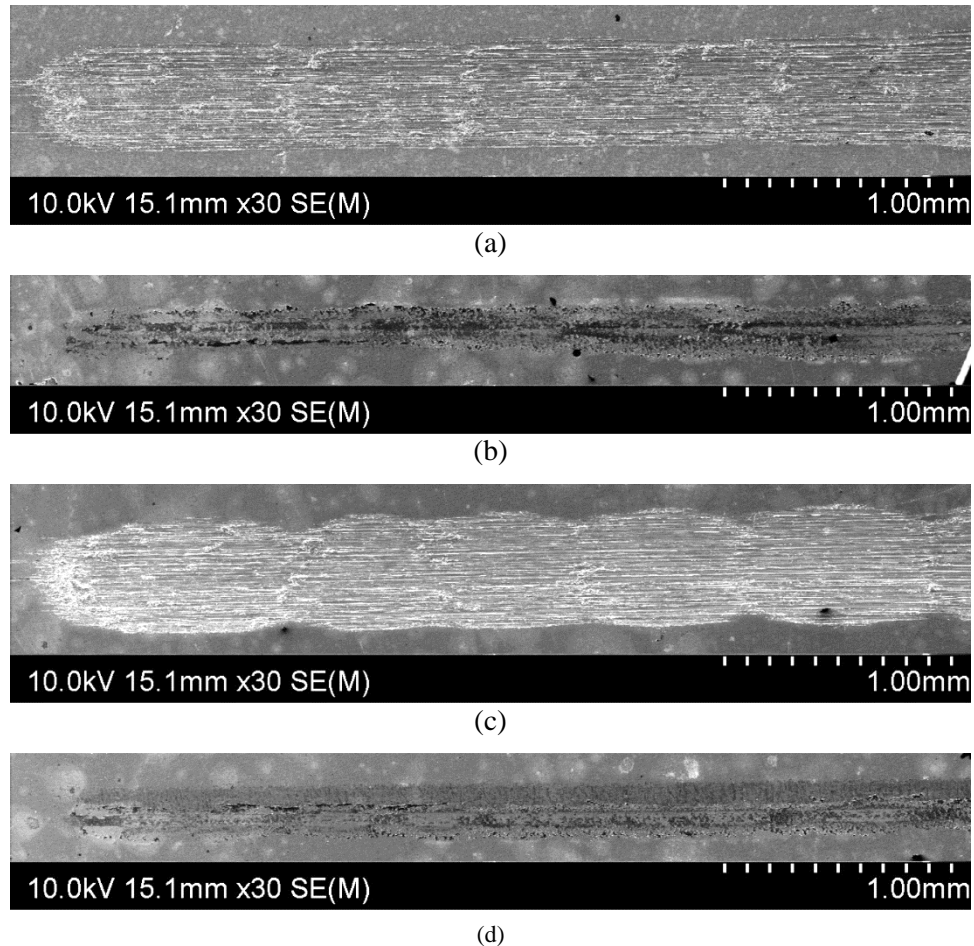


Fig. 7.2 SEM images of SLM-N1 sample wear tracks after (a) first, (b) second, (c) third and (d) fourth experiments.

The tiny and darker wear debris is examined further and SEM images taken in track 4 of SLM-N1 samples, which is a zero wear rate track, are shown in Fig. 7.3. Fig. 7.3(a) displays the discontinuous and thin debris patches in an area of the track. Fig. 7.3(b) shows locally in a high magnification the area covered by debris (feature of blue point 1), the area clear of debris (feature of blue point 2) and a small area clearly worn (feature of yellow point 3). Supporting this can be seen by the corresponding three EDS spot analyses in Fig. 7.3(c) to Fig. 7.3(e). Debris, point 1 in Fig. 7.3(b) and spectrum in Fig. 7.3(c), containing a high oxygen peak is consistent with the initial debris being oxygen rich as described and explained in the last Chapter (section 6.2). EDS spectrum for point 2 and EDS spectrum for point 3 in Fig. 7.3(d) and Fig. 7.3(e), respectively, are largely the same except for the peak of nitrogen. The nitrogen peak in Point 2 is quite strong and the peak in Point 3 is significantly weaker, although the peak has

been made slightly uncertain due the Ti L peak. The very weak N peak in Point 3 is consistent with the local area/spot having been worn and thus the initially N rich top layer having lost.

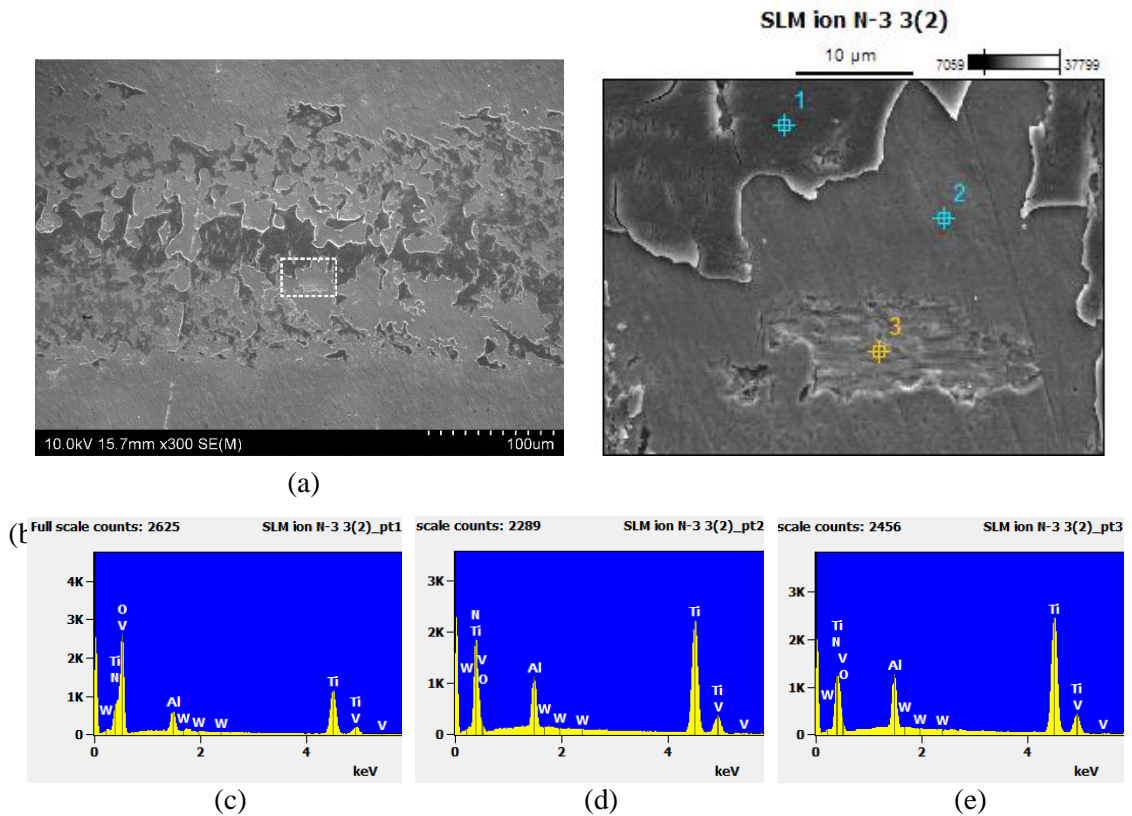


Fig. 7.3 SEM images (a) and (b) in higher magnifications taken in SLM-N1 track from the second test and EDS spectra in locations of (c) point 1, (d) point 2 and (e) point 3 as indicated in (b).

For all other non-SLM-N1 tracks, the appearances of the first of the two tested tracks are shown in Fig. 7.4 and their corresponding wear loss data are indicated (with *) in Fig. 7.1. Only the track CP-N1 is seen noticeably narrower than others in Fig. 7.4, consistent with the lower wear rate in comparison to the wear rate data of N2 and non-treated samples plotted in Fig. 7.1. Although the individual wear rate may differ from one to another, overall, the tracks displayed in Fig. 7.4 are similar and are similar to track 1 and track 3 of SLM-N1 samples in Fig. 7.2. This means that for all these other samples, severe wear had well started before the end of the test period. In other words, N1 for CP samples and N2 for both SLM and CP samples had provided only very low or basically no protection to wear, given the test condition that has been used.

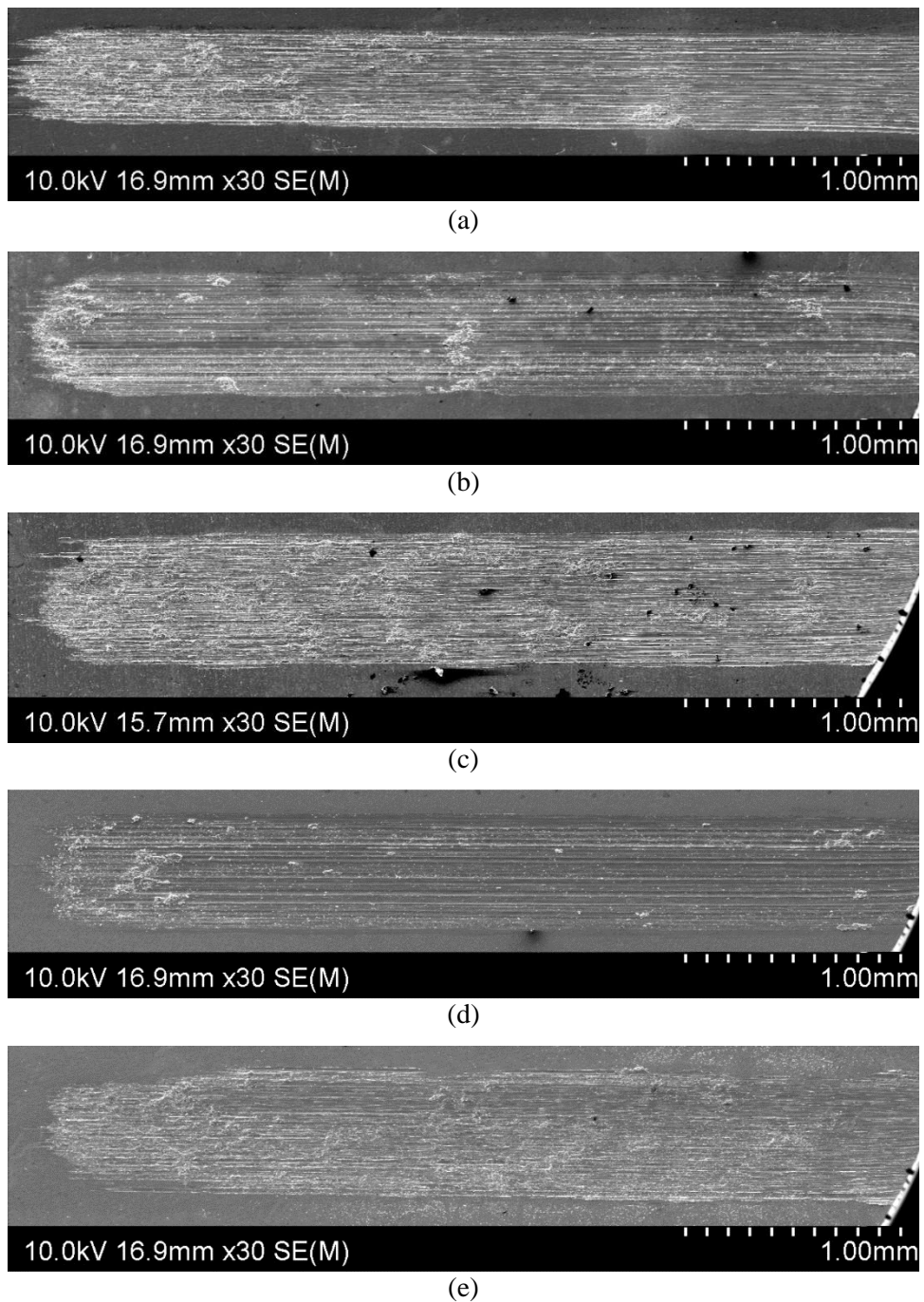


Fig. 7.4 SEM images of wear tracks of (a) CP N1, (b) SLM N2, (c) CP N2, (d) SLM non-treated and (e) CP non-treated samples, after the first respective wear experiment.

7.1.3 COF and wear process

The amount of wear loss that has been measured and the appearance of the wear track that can be observed, as presented and described above for each track, have shown the end result of each test. In an attempt to identify how ion implantation may have provided wear protection, similar to the evaluation of COF traces to reveal the wear protection and breaking of PVD TiN coating

as described in last chapter (section 6.1.2), COF traces are plotted in Fig. 7.5 for examination. In this present case, all traces of tests are presented. Fig. 7.5(a) and Fig. 7.5(b) are for test 1 and test 2, respectively, of SLM-N1 and CP-N1 samples. Fig. 7.5(c) is for the two further SLM-N1 tests. Fig. 7.5(d) and Fig. 7.5(e) are for test 1 and test 2, respectively, of SLM-N2 and CP-N2 samples. Fig. 7.5(f) and Fig. 7.5(g) are for non-treated SLM and CP samples also for test 1 and test 2 in sequence.

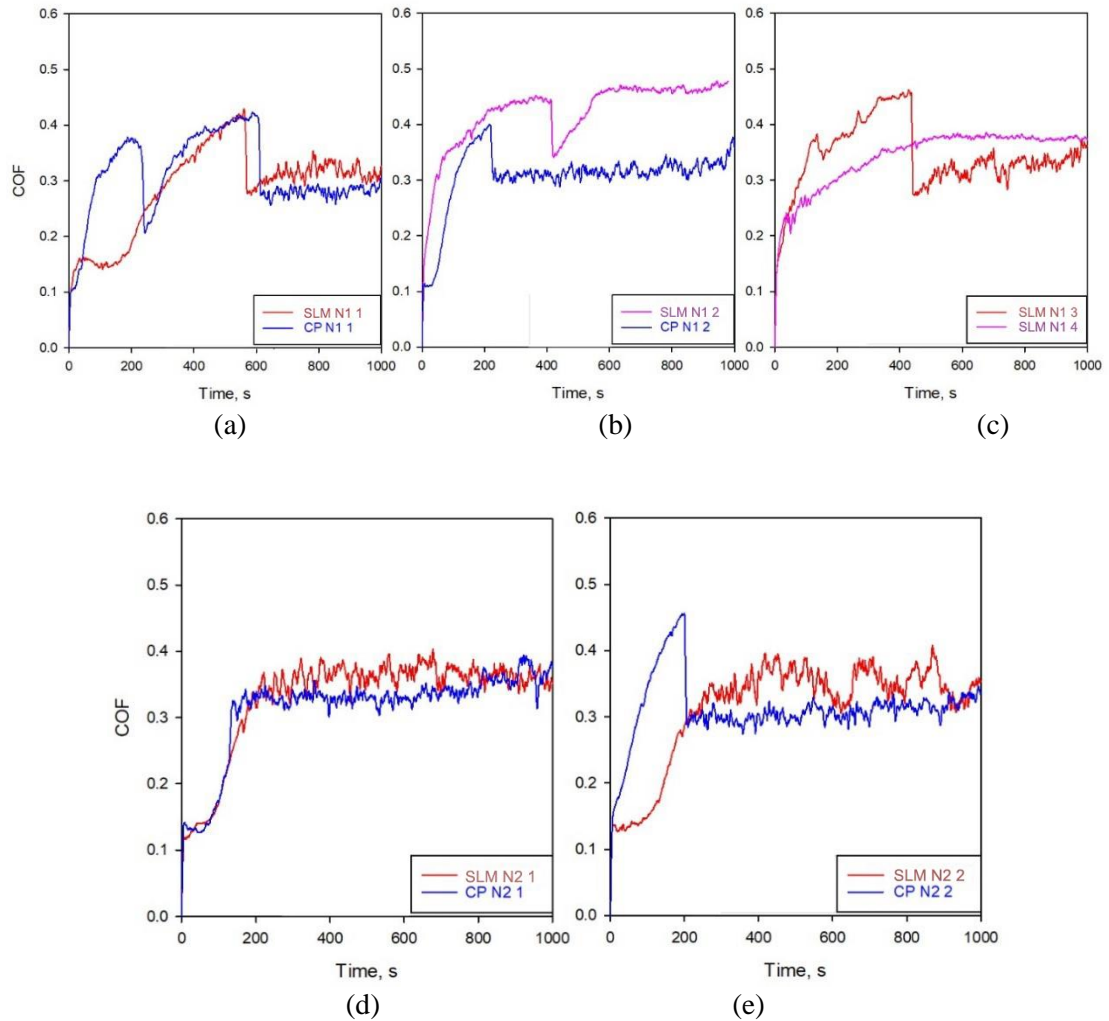


Fig. 7.5 COF plots for (a) SLM and CP N1 first tests, (b) SLM and CP N1 second tests, (c) SLM N1 the third and fourth tests, (d) SLM and CP N2 first tests, (e) SLM and CP N2 second tests, (f) SLM and CP non-treated sample first tests, and (g) SLM and CP non-treated sample second tests.

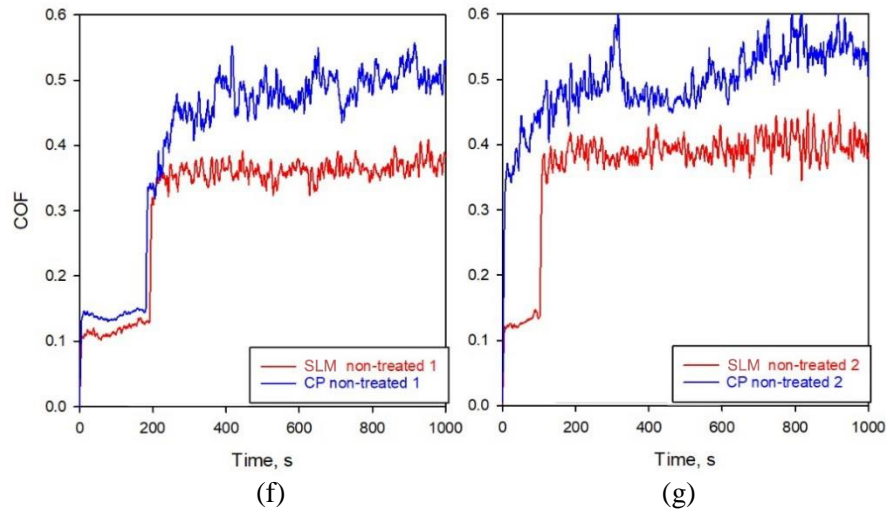


Fig. 7.5 Cont.

In Fig. 7.5(a), following the interpretation for tests of PVD TiN coated samples in the last chapter, both N1 test 1 samples had lost protection by the end of the test period and the severe wear process started similarly at ~ 600 s for both, although for CP-N1, there was a dip of the trace earlier at ~ 250 s. A feature in the COF traces is the amount of “noise” in the traces before and after the change at ~ 600 s. About stick-slip according to Dong’s study [35], “noisy” COF signals are closely resulted from the strong adhesion feature of titanium. It can be suggested that a change of a less noisy to a noisy COF signals after the dip of a COF curve is the result of the implantation layer loss and thus the loss of wear protection. Returning to the discussion on trace N1 curves in Fig. 7.5(a), before ~ 600 s, the amount of noise is small and after the dip at ~ 600 s, the noise has become significantly higher. Thus, it can be reasonably certain that the protection has started to loss after the COF dip at ~ 600 s and severe wear of Ti-6-Al-4V started.

For test 2 (Fig. 7.5(b)), the trace of SLM-N1 test 2 is quite smooth despite of a dip at ~ 400 s. This relatively smooth COF trace corresponding to zero wear loss (Fig. 7.1(a) and Fig. 7.2(b)) supports the suggestion of the relatively smooth region of a COF trace and in this case the whole trace being relatively smooth to be an indication of zero wear process. The N implantation has provided a strong protection for the test period (1000s) for this sample. On the other hand, for CP-N1 test 2, the protection had lost early and at ~ 200 s severe wear had started and thus the final wear loss is high ($0.00055\text{mm}^3/\text{m}$), comparable to the averaged wear rate value ($0.00056\text{mm}^3/\text{m}$) of the two tests using CP samples without implantation treatment (Fig. 7.5(f) and Fig. 7.5(g)). This is consistent with the severely worn track appearances of CP samples, without or with N implantation, in Fig. 7.4.

The higher amount of loss for CP-N1 test 2 than that of CP-N1 test 1 shown in Fig. 7.1 is also consistent with the dip of the COF trace for the CP-N1 sample in test 2 (Fig. 7.5(b)) earlier than

that of the CP-N1 sample in test 1 (Fig. 7.5(a)). Although the trace is not very smooth before the dip, a large dip in the COF trace of SLM-N1 test 3 at ~450s (Fig. 7.5(c)) also corresponds to the loss of protection and thus a relatively high amount of wear loss for the sample (Fig. 7.1(a)). On the other hand, the smooth trace without a dip for SLM-N1 test 4 (Fig. 7.5(c)) is consistent with the zero wear rate of the sample (Fig. 7.1(a)).

As shown in Fig. 7.5(d) to Fig. 7.5(g), COF traces for samples of N2 and non-treated conditions are similar in that for the major part of the test period, after ~200s, the traces are highly noisy. The amount of noise and the COF values for CP non-treated samples can be seen higher. The noisy traces corresponding to the high amount of wear loss for each test in Fig. 7.1(b) and Fig. 7.1(c) have further suggested that N2 treatment has provided little protection for the test period. Overall, the COF traces can thus be seen to have corresponded well with the wear loss data and the trace appearance examination that N1 treatment has provided a small degree of protection particularly for SLM samples but N2 conditions has provided little.

7.2 Further analysis on effect of ion implantation on wear

As the purpose of surface coating/treatment to reduce wear is to increase the hardness of the surface region, to understand the reason why N1 treatment has provided a little and N2 treatment has provided little wear protection, near surface hardness profiles have been determined and examined, so that suggested reasons for the findings from current tests can be provided.

7.2.1 Hardening profile resulting from ion implantation

The distance to the surface that hardness may be affected by N implantation is up to 300nm, as the N concentrations profiles have shown in Chapter 3 (section 3.2). Thus, hardness profiles have been obtained by using nanoindentation and the procedure has been described in Chapter 3 (section 3.2). For comparison purpose, measurements were also made using a TiN PVD coated CP sample. Hardening data and profiles for various samples based on nanoindentation tests are presented in Fig. 7.6. How hard a material is is measured by how deep (h_{n-i}) the indenter penetrates under a specific maximum load (P_{max}). For a given material surface, as the load increases the indenter penetrates deeper. Thus, in general, the higher the $\Delta P_{max}/\Delta h_{n-i}$ the harder the material is.

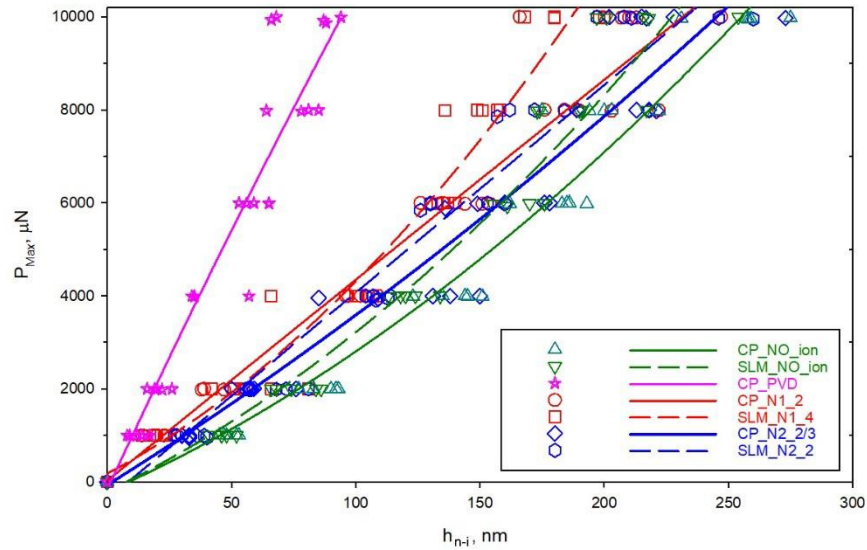


Fig. 7.6 P_{Max} vs. h_{n-i} from nanoindentation measurements for various samples.

The distinctive feature in Fig. 7.6 is that, for P_{Max} up to $10000\mu N$, the $P_{max}-\Delta h_{n-i}$ curve for the PVD TiN coated sample is away from the rest $P_{max}-\Delta h_{n-i}$ curves. As the curve is very steep meaning $P_{max}/\Delta h_{n-i}$ is very high in comparison to others, hardness of the PVD TiN coating is viewed considerably harder than all the other surfaces. Carefully observing can further identify that, within the other group of curves, the one for non-treated CP sample is one with the lowest $P_{max}/\Delta h_{n-i}$ (slope of the curve). A slightly higher average slope for the non-treated SLM sample than non-treated CP sample can also be identified. This is reasonable as microhardness of SLM (being 428HV on average) is significantly higher than that of CP samples (being 324HV on average). The $P_{max}-\Delta h_{n-i}$ curves for three other samples (CP N1, SLM N2 and CP N2) are close to one for the SLM non-treated sample (and far away from the PVD curve), meaning that the increase in hardness after the N treatment is very small. For the SLM N1 sample curve, in comparison to all non-PVD coated samples, slightly higher $P_{max}/\Delta h_{n-i}$ values in 5000-10000 μN load region can be viewed more certain.

From the discussion above on nanoindentation data in Fig. 7.6, it can be suggested that N1 implantation on CP samples and N2 implantation on both SLM and CP samples have had an insignificant effect on surface hardening. Thus, as shown in Fig. 7.1 and Fig. 7.4, N1 treatment for CP samples and N2 treatment for both SLM and CP samples have provided little wear protection. A weak hardening effect by N1 implantation on SLM samples can be detected. For this reason, as also shown in Fig. 7.1 to Fig. 7.5, a weak wear protection by N1 treatment on SLM samples has been registered.

7.2.2 Effectiveness of ion implantation on wear reduction

Clearly, ion implantation in the present study has not resulted in a significant increase in hardness with the only exception of SLM sample which has shown a weak increase in hardness in the top 200nm surface region. From a limited number of studies and data available in literature (Chapter 2.4.2), nitrogen ion implantation should provide wear resistance but when a dosage of $\leq 1 \times 10^{21} \text{N}^+ \text{ions/m}^2$ is applied the effect is not significant. A dosage of significantly higher than $1 \times 10^{21} \text{N}^+ \text{ions/m}^2$ should result in a significant effect on increasing wear resistance. As explained in Chapter 3 (section 3.2), our samples of both N1 and N2 treatment were doped with $6 \times 10^{17} \text{at/cm}^2$ of nitrogen, meaning $6 \times 10^{21} \text{N}^+ / \text{m}^2$. However, the N implantation treatment only had a weak or little effect on wear protection. It may thus be concluded that in general N implantation does not provide a significant effect on increasing hardness to significantly higher values and to a significant depth, thus, having an insignificant effect on wear protection.

Chapter 8 Conclusions

In this study, dry linear reciprocating wear tests using WC-Co counter material have been extensively conducted to evaluate the wear resistance of Ti-6Al-4V alloy by wear rate measurement and examination of the tested samples. The alloy has been processed using powder bed fusion, both laser powder bed fusion (SLM) and electron powder bed fusion (EBM), and by a conventional process (CP). Tests have also conducted on samples coated with TiN using physical vapor deposition (PVD) and surface treated using nitrogen ion implantation. The following conclusions can be drawn from this study:

Uncoated and non-treated samples tested at room temperature

1. For all three types of samples (SLM, EBM and CP samples), as expected, the effect of increase in every N causing the increase of WR is $3.2 \times 10^{-4} (\text{mm}^3/\text{m})/\text{N}$ over the range of F_N from 2 to 10N, although the rate of increase is non-linear. But the rate of increasing in every Hz causing the increase of WR is $1.2 \times 10^{-4} (\text{mm}^3/\text{m})/\text{Hz}$ over the range from 2Hz to 8Hz, which is very low compared with the rate of increasing F_N .
2. The insignificant difference in WR among the three types of samples has shown that WR is not inversely proportional to hardness, which varies due to the difference in the three manufacturing routes of the alloy used in this study: high hardness (428HV) in SLM samples, mid-level hardness (359HV) in EBM samples and low hardness (324HV) in CP samples.
3. The reason for WR being not affected by hardness can qualitatively be suggested to be the result of the inverse relationship between strength and ductility of the alloy. Lower hardness and thus lower strength of the alloy has resulted in a larger deformation zone, but higher ductility of the alloy allows for a higher amount of deformation without having a higher amount of fracture and wear loss.

Uncoated and non-treated samples tested at temperatures up to 600°C

4. Same as testing at room temperature and as expected, at higher testing temperature, increasing F_N increases WR. Regardless of what samples (SLM, EBM or CP samples) are used. Depending on F_N , increasing test temperature up to 600°C affects insignificantly WR: WR decreased from ~0.0017 to 0.0009 mm³/m at 2N, varied from ~0.0035 to ~0.0022 mm³/m at 6N and varied from ~0.0055 to 0.0040 mm³/m at 10N over the temperature range from room temperature to 600°C. The shapes of tracks tested at high temperatures are similar to those tested at room temperature.
5. For all three types of samples, it is probable that the oxygen richer oxide debris layer at higher temperature may provide a stronger wear resistant although strength/hardness of Ti-6Al-4V should be lower at a higher temperature.

PVD TiN uncoated samples tested at room temperature

6. Tests on PVD TiN coated SLM or CP samples have shown that WR rate of coated samples is 17-33 times lower than the WR of the uncoated samples. Thus, the coating can be viewed effective in reducing wear rate, until the coating fails.
7. It has been identified that wear deterioration of coating follows in three sequential stages. They are:

Stage I - pure wear thinning of coating, which is a slow process, and the thickness of the coating is the determining factor of the protection of wear.

Stage II - locally fracturing of the thinned coating in central location of track when the wear depth (h_{Max}) reached 1.9mm or slightly lower. Debris may assist significantly the fracturing process at this stage. When fracturing occurs, h_{Max} becomes higher than 3 μ m as locally wear rate of Ti-6Al-4V has become high, but has not affected significantly the wear volume of the sample.

Stage III - widening of width of the section that the coating has been worn, when the width of the coating locally worn (W_{Worn}) increases more rapidly than the increase in the width of wear track (W_{Track}) with time, the protection function rapidly diminishes.

8. Monitoring during the tests with coefficient of friction (COF) has been found to be an effective way detecting the onset of coating break, which results in a sudden jump of the COF value. This is supported by both track surface and cross-sectional examination of the tested samples.

Nitrogen ion implanted samples tested at room temperature

9. Overall, even using low test load at 1N, treating SLM and CP samples with nitrogen ion implantation has not resulted in a significant reduction in WR although N1 treatment (the peak value of N^+ atomic fraction is at 175nm depth from the surface) of SLM samples may have provided wear resistance for a short period of time.
10. The insignificant effect of N implantation on WR reduction can be attributed to the insignificant effect of N implantation in the increase in hardness within the normally affected depth of ~200nm, the only exception of SLM sample showing a weak increase in hardness in the 200nm surface region. The slight effect of N implantation on SLM samples is supported by the COF traces of the tests.
11. Our samples were doped with $6 \times 10^{21} N^+ / m^2$ of nitrogen, this dosage of nitrogen is much higher than the dosage which should increase wear resistance significantly recorded in the limited data in literature. However, this N implantation surface treatment has not provided a significant effect on increasing hardness in the top 200-300nm and reducing WR.

References

- [1] I. Inagaki, T. Tsutomu, S. Yoshihisa, and A. Nozomu, "Application and Features of Titanium for the Aerospace Industry," *Nippon steel sumitomo Met. Tech. Rep.*, no. 106, pp. 22–27, 2014.
- [2] M. A. Elias, C.N., Lima, J.H.C., Valiev, R., and Meyers, "Biomedical applications of titanium and its alloys Biological Materials Science 46-49," no. March, pp. 1–4, 2008.
- [3] M. Geetha, A. K. Singh, R. Asokamani, and A. K. Gogia, "Ti based biomaterials, the ultimate choice for orthopaedic implants - A review," *Prog. Mater. Sci.*, vol. 54, no. 3, pp. 397–425, 2009.
- [4] H. J. Rack and J. I. Qazi, "Titanium alloys for biomedical applications," *Mater. Sci. Eng. C*, vol. 26, no. 8, pp. 1269–1277, 2006.
- [5] M. Yamada, "An overview on the development of titanium alloys for non-aerospace application in Japan," *Mater. Sci. Eng. A*, vol. 213, no. 1–2, pp. 8–15, 1996.
- [6] K. Zhuravleva *et al.*, "Production of Porous β -Type Ti-40Nb Alloy for Biomedical Applications: Comparison of Selective Laser Melting and Hot Pressing," *Materials (Basel)*, vol. 6, no. 12, pp. 5700–5712, 2013.
- [7] J. Tong, C. R. Bowen, J. Persson, and A. Plummer, "Mechanical properties of titanium-based Ti–6Al–4V alloys manufactured by powder bed additive manufacture," *Mater. Sci. Technol. (United Kingdom)*, vol. 33, no. 2, pp. 138–148, 2017.
- [8] ASM, "Introduction to Selection of Titanium Alloys," *Titan. A Tech. Guid.*, vol. 180, pp. 5–11, 2000.
- [9] S. Z. Wen and P. Huang, *Principles of Tribology*, 3rd ed. Beijing: Tsinghua University Press, 2008.

- [10] S. Yerramareddy and S. Bahadur, "Effect of operational variables, microstructure and mechanical properties on the erosion of Ti-6Al-4V," *Wear*, vol. 142, no. 2, pp. 253–263, 1991.
- [11] K. G. Budinski, "Tribological properties of titanium alloys," *Wear*, vol. 151, no. 2, pp. 203–217, 1991.
- [12] H. Dong, *Tribological properties of titanium-based alloys, in Surface Engineering of Light Alloys*. Woodhead Publishing Limited, Oxford, 2010.
- [13] L. S. Morais *et al.*, "Titanium alloy mini-implants for orthodontic anchorage: Immediate loading and metal ion release," *Acta Biomater.*, vol. 3, no. 3 SPEC. ISS., pp. 331–339, 2007.
- [14] S. Singh, S. Ramakrishna, and R. Singh, "Material issues in additive manufacturing_ A review," *J. manu*, vol. 25, pp. 185–200, 2017.
- [15] N. Ur Rahman *et al.*, "An Overview: Laser-Based Additive Manufacturing for High Temperature Tribology," *Front. Mech. Eng.*, vol. 5, no. April, pp. 1–15, 2019.
- [16] D. Herzog, V. Seyda, E. Wycisk, and C. Emmelmann, "Additive manufacturing of metals," *Acta Mater.*, vol. 117, pp. 371–392, 2016.
- [17] W. E. Frazier, "Metal additive manufacturing: A review," *J. Mater. Eng. Perform.*, vol. 23, no. 6, pp. 1917–1928, 2014.
- [18] X. Tan *et al.*, "Graded microstructure and mechanical properties of additive manufactured Ti-6Al-4V via electron beam melting," *Acta Mater.*, vol. 97, pp. 1–16, 2015.
- [19] T. DebRoy *et al.*, "Additive manufacturing of metallic components – Process, structure and properties," *Prog. Mater. Sci.*, vol. 92, pp. 112–224, 2018.

- [20] J. Suryawanshi, K. G. Prashanth, and U. Ramamurty, "Mechanical behavior of selective laser melted 316L stainless steel," *Mater. Sci. Eng. A*, vol. 696, no. April, pp. 113–121, 2017.
- [21] H. Attar *et al.*, "Mechanical behavior of porous commercially pure Ti and Ti-TiB composite materials manufactured by selective laser melting," *Mater. Sci. Eng. A*, vol. 625, pp. 350–356, 2015.
- [22] T. Keller *et al.*, "Application of finite element, phase-field, and CALPHAD-based methods to additive manufacturing of Ni-based superalloys," *Acta Mater.*, vol. 139, pp. 244–253, 2017.
- [23] A. Liebisch and M. Merkel, "On the numerical simulation of the thermal behavior during the selective laser melting process," *Materwiss. Werksttech.*, vol. 47, no. 5–6, pp. 521–529, 2016.
- [24] W. Toh, E. Liu, P. Wang, S. Tor, M. Nai, and X. Tan, "Microstructure and Wear Properties of Electron Beam Melted Ti-6Al-4V Parts: A Comparison Study against As-Cast Form," *Metals (Basel)*, vol. 6, no. 11, p. 284, 2016.
- [25] S. Liu and Y. C. Shin, "Additive manufacturing of Ti6Al4V alloy: A review," *Mater. Des.*, vol. 164, p. 107552, 2019.
- [26] P. K. Gokuldoss, S. Kolla, and J. Eckert, "Additive manufacturing processes: Selective laser melting, electron beam melting and binder jetting-selection guidelines," *Materials (Basel)*, vol. 10, no. 6, 2017.
- [27] T. Craeghs, L. Thijs, F. Verhaeghe, J.-P. Kruth, and J. Van Humbeeck, "A study of the microstructural evolution during selective laser melting of Ti-6Al-4V," *Acta Mater.*, vol. 58, no. 9, pp. 3303–3312, 2010.
- [28] S. Li, H. Hassanin, M. M. Attallah, N. J. E. Adkins, and K. Essa, "The development of TiNi-based negative Poisson's ratio structure using selective laser melting," *Acta Mater.*,

vol. 105, pp. 75–83, 2016.

- [29] H. K. Rafi, N. V. Karthik, H. Gong, T. L. Starr, and B. E. Stucker, “Microstructures and mechanical properties of Ti6Al4V parts fabricated by selective laser melting and electron beam melting,” *J. Mater. Eng. Perform.*, vol. 22, no. 12, pp. 3872–3883, 2013.
- [30] W. Xu *et al.*, “Additive manufacturing of strong and ductile Ti-6Al-4V by selective laser melting via in situ martensite decomposition,” *Acta Mater.*, vol. 85, pp. 74–84, 2015.
- [31] P. A. Kobryn and S. L. Semiatin, “The Laser Additive Manufacture of Ti-6Al-4V,” no. September, pp. 40–42, 2001.
- [32] T. Ahmed and H. J. Rack, “Phase transformations during cooling in $\alpha + \beta$ titanium alloys,” *Mater. Sci. Eng. A*, vol. 243, no. 1–2, pp. 206–211, 1998.
- [33] F. X. Gil Mur, D. Rodríguez, and J. A. Planell, “Influence of tempering temperature and time on the α' -Ti-6Al-4V martensite,” *J. Alloys Compd.*, vol. 234, no. 2, pp. 287–289, 1996.
- [34] L. Facchini, E. Magalini, P. Robotti, A. Molinari, S. Höges, and K. Wissenbach, “Ductility of a Ti–6Al–4V alloy produced by selective laser melting of prealloyed powders,” *Rapid Prototyp. J.*, vol. 16, (6), pp. 450–459, 2010.
- [35] Y. T. Lee and G. Welsch, “Young’s modulus and damping of Ti6Al4V alloy as a function of heat treatment and oxygen concentration,” *Mater. Sci. Eng. A*, vol. 128, no. 1, pp. 77–89, 1990.
- [36] L. E. Murr *et al.*, “Microstructure and mechanical behavior of Ti-6Al-4V produced by rapid-layer manufacturing, for biomedical applications,” *J. Mech. Behav. Biomed. Mater.*, vol. 2, no. 1, pp. 20–32, 2009.
- [37] L. H. Mair, T. A. Stolarski, R. W. Vowles, and C. H. Lloyd, “Wear: Mechanisms, manifestations and measurement. Report of a workshop,” *J. Dent.*, vol. 24, no. 1–2, pp.

141–148, 1996.

- [38] Q. Niu, X. Zheng, M. Chen, and W. Ming, “Study on the tribological properties of titanium alloys sliding against WC-Co during the dry friction,” *Ind. Lubr. Tribol.*, vol. 66, no. 2, pp. 202–208, 2014.
- [39] Q. L. Niu, X. H. Zheng, W. W. Ming, and M. Chen, “Friction and Wear Performance of Titanium Alloys against Tungsten Carbide under Dry Sliding and Water Lubrication,” *Tribol. Trans.*, vol. 56, no. 1, pp. 101–108, 2013.
- [40] S. Kumar and J. P. Kruth, “Wear performance of SLS/SLM materials,” *Adv. Eng. Mater.*, vol. 10, no. 8, pp. 750–753, 2008.
- [41] M. Ramezani, K. Khanlari, T. Neitzert, P. Kelly, and P. Cao, “Comparison of the reciprocating sliding wear of 58Ni39Ti-3Hf alloy and baseline 60NiTi,” *Wear*, vol. 408–409, no. May, pp. 120–130, 2018.
- [42] K. Khanlari, M. Ramezani, P. Kelly, P. Cao, and T. Neitzert, “Reciprocating Sliding Wear Behavior of 60NiTi As Compared to 440C Steel under Lubricated and Unlubricated Conditions,” *Tribol. Trans.*, vol. 61, no. 6, pp. 991–1002, 2018.
- [43] Q. Y. Zhang, Y. Zhou, L. Wang, X. H. Cui, and S. Q. Wang, “Investigation on tribo-layers and their function of a titanium alloy during dry sliding,” *Tribol. Int.*, vol. 94, pp. 541–549, 2016.
- [44] Y. S. Mao, L. Wang, K. M. Chen, S. Q. Wang, and X. H. Cui, “Tribo-layer and its role in dry sliding wear of Ti-6Al-4V alloy,” *Wear*, vol. 297, no. 1–2, pp. 1032–1039, 2013.
- [45] X. X. Li, Y. Zhou, X. L. Ji, Y. X. Li, and S. Q. Wang, “Effects of sliding velocity on tribo-oxides and wear behavior of Ti-6Al-4V alloy,” *Tribol. Int.*, vol. 91, pp. 228–234, 2015.
- [46] M. Lou and A. T. Alpas, “High temperature wear mechanisms in thermally oxidized

- titanium alloys for engine valve applications,” *Wear*, vol. 426–427, no. September 2018, pp. 443–453, 2019.
- [47] L. Yong, Y. Dezhuang, H. Shiyu, and Y. Zhuyu, “Dry Sliding Wear of Ti-6Al-4V Alloy at Low Temperature in Vacuum,” *Prot. of Materials Struct. from Sp. Environ.*, no. 3, pp. 309–316, 2006.
- [48] M. Dutt Sharma and R. Sehgal, “Dry Sliding Friction and Wear Behavior of Titanium Alloy (Ti-6Al-4V),” *Tribol. Online*, vol. 7, no. 2, pp. 87–95, 2012.
- [49] M. Fellah, M. Labaiz, O. Assala, L. Dekhil, and A. Iost, “Tribological behavior of Ti-6Al-4V and Ti-6Al-7Nb alloys for total hip prosthesis,” *Trends Biomater. Artif. Organs*, vol. 29, no. 1, pp. 22–30, 2015.
- [50] D. Gu *et al.*, “Densification behavior, microstructure evolution, and wear performance of selective laser melting processed commercially pure titanium,” *Acta Mater.*, vol. 60, no. 9, pp. 3849–3860, 2012.
- [51] F. BARTOLOMEU *et al.*, “Wear behavior of Ti6Al4V biomedical alloys processed by selective laser melting, hot pressing and conventional casting,” *Trans. Nonferrous Met. Soc. China (English Ed.)*, vol. 27, no. 4, pp. 829–838, 2017.
- [52] C. Palanisamy, S. Bhero, B. Abiodun Obadele, and P. Apata Olubambi, “Effect of build direction on the microhardness and dry sliding wear behavior of laser additive manufactured Ti-6Al-4V,” *Mater. Today Proc.*, vol. 5, no. 1, pp. 397–402, 2018.
- [53] N. W. Khun, W. Q. Toh, X. P. Tan, E. Liu, and S. B. Tor, “Tribological Properties of Three-Dimensionally Printed Ti–6Al–4V Material Via Electron Beam Melting Process Tested Against 100Cr6 Steel Without and With Hank’s Solution,” *J. Tribol.*, vol. 140, no. 6, p. 061606, 2018.
- [54] J. Ryu, S. Shrestha, G. Manogharan, and J. Jung, “Sliding Contact Wear Damage of EBM built Ti6Al4V: Influence of Process Induced Anisotropic Microstructure,” *Metals*

(*Basel*)., vol. 8, no. 2, p. 131, 2018.

- [55] W. Zhang *et al.*, “Superior Wear Resistance in EBM-Processed TC4 Alloy Compared with SLM and Forged Samples,” *Materials (Basel)*., vol. 12, no. 5, p. 782, 2019.
- [56] Y. Zhu, X. Chen, J. Zou, and H. Yang, “Sliding wear of selective laser melting processed Ti6Al4V under boundary lubrication conditions,” *Wear*, vol. 368–369, pp. 485–495, 2016.
- [57] P. Chandramohan, S. Bhero, B. A. Obadele, and P. A. Olubambi, “Laser additive manufactured Ti–6Al–4V alloy: tribology and corrosion studies,” *Int. J. Adv. Manuf. Technol.*, vol. 92, no. 5–8, pp. 3051–3061, 2017.
- [58] A. P. Semenov, “Tribology at high temperatures,” *Tribol. Int*, vol. 28, pp. 45–50, 1995.
- [59] M. S. Rahman, J. Ding, A. Beheshti, X. Zhang, and A. A. Polycarpou, “Elevated temperature tribology of Ni alloys under helium environment for nuclear reactor applications,” *Tribol. Int.*, vol. 123, no. December 2017, pp. 372–384, 2018.
- [60] J. Hardell, S. Hernandez, S. Mozgovoy, L. Pelcastre, C. Courbon, and B. Prakash, “Effect of oxide layers and near surface transformations on friction and wear during tool steel and boron steel interaction at high temperatures,” *Wear*, vol. 330–331, pp. 223–229, 2015.
- [61] M. T. Whittaker, W. Harrison, P. J. Hurley, and S. Williams, “Modelling the behavior of titanium alloys at high temperature for gas turbine applications,” *Mater. Sci. Eng. A*, vol. 527, no. 16–17, pp. 4365–4372, 2010.
- [62] D. Rugg, M. Dixon, and J. Burrows, “High-temperature application of titanium alloys in gas turbines. Material life cycle opportunities and threats – an industrial perspective,” *Mater. High Temp.*, vol. 33, no. 4–5, pp. 536–541, 2016.
- [63] X. H. Cui, Y. S. Mao, M. X. Wei, and S. Q. Wang, “Wear Characteristics of Ti-6Al-4V

Alloy at 20-400°C,” *Tribol. Trans.*, vol. 55, no. 2, pp. 185–190, 2012.

- [64] D. Kumar, B. Lal, M. F. Wani, J. T. Philip, and B. Kuriachen, “Dry sliding wear behavior of Ti–6Al–4V pin against SS316L disc in vacuum condition at high temperature,” *Tribol. - Mater. Surfaces Interfaces*, vol. 13, no. 3, pp. 182–189, 2019.
- [65] X. Liang, Z. Liu, and B. Wang, “Physic-chemical analysis for high-temperature tribology of WC-6Co against Ti–6Al–4V by pin-on-disc method,” *Tribol. Int.*, vol. 146, no. February, p. 106242, 2020.
- [66] A. Sajid, N. Magnus, A. Marta-Lena, and A. Farid, “Tribological performance of Ti6Al4V at elevated temperatures fabricated by electron beam powder bed fusion,” *Tribol. Int.*, vol. 153, p. 1006658, 2021.
- [67] A. Baptista, F. Silva, J. Porteiro, J. Míguez, and G. Pinto, “Sputtering physical vapour deposition (PVD) coatings: A critical review on process improvement and market trend demands,” *Coatings*, vol. 8, no. 11, 2018.
- [68] M. Y. P. Costa, M. O. H. Cioffi, H. J. C. Voorwald, and V. A. Guimares, “An investigation on sliding wear behavior of PVD coatings,” *Tribol. Int.*, vol. 43, no. 11, pp. 2196–2202, 2010.
- [69] C. Liu, Q. Bi, and A. Matthews, “Tribological and electrochemical performance of PVD TiN coatings the femoral head of Ti-6Al-4V artificial joints,” *Surf. Coatings Technol.*, vol. 163–164, pp. 597–604, 2003.
- [70] G. Cassar, S. Banfield, J. C. A. B. Wilson, J. Housden, A. Matthews, and A. Leyland, “Tribological properties of duplex plasma oxidised, nitrided and PVD coated Ti-6Al-4V,” *Surf. Coatings Technol.*, vol. 206, no. 2–3, pp. 395–404, 2011.
- [71] C. Martini and L. Ceschini, “A comparative study of the tribological behavior of PVD coatings on the Ti-6Al-4V alloy,” *Tribol. Int.*, vol. 44, no. 3, pp. 297–308, 2011.

- [72] M. Łępicka, M. Grądzka-Dahlke, D. Pieniak, K. Pasierbiewicz, K. Kryńska, and A. Niewczas, “Tribological performance of titanium nitride coatings: A comparative study on TiN-coated stainless steel and titanium alloy,” *Wear*, vol. 422–423, no. January, pp. 68–80, 2019.
- [73] H. Li, M. Ramezani, and Z. W. Chen, “Dry sliding wear performance and behavior of powder bed fusion processed Ti–6Al–4V alloy,” *Wear*, vol. 440–441, no. July, p. 203103, 2019.
- [74] W. H. Kao, Y. L. Su, J. H. Horng, and C. Y. Chang, “Tribological, electrochemical and biocompatibility properties of Ti6Al4V alloy produced by selective laser melting method and then processed using gas nitriding, CN or Ti-C:H coating treatments,” *Surf. Coatings Technol.*, vol. 350, no. July, pp. 172–187, 2018.
- [75] F. Z. Cui and Z. S. Luo, “Biomaterials modification by ion-beam processing,” *Surf. Coatings Technol.*, vol. 112, no. 1–3, pp. 278–285, 1999.
- [76] P. Sioshansi and E. J. Tobin, “Surface treatment of biomaterials by ion beam processes,” *Surf. Coatings Technol.*, vol. 83, no. 1–3, pp. 175–182, 1996.
- [77] T. R. Rautray, R. Narayanan, and K. H. Kim, “Ion implantation of titanium based biomaterials,” *Prog. Mater. Sci.*, vol. 56, no. 8, pp. 1137–1177, 2011.
- [78] S. E. Maksimov and B. L. Oksengendler, “Sputtering of atoms during ion bombardment of media containing nanosized particles in the near-surface region,” *Tech. Phys. Lett.*, vol. 41, no. 2, pp. 187–190, 2015.
- [79] D. K. Boampong, S. M. Green, and A. Unsworth, “N⁺ ion implantation of Ti6Al4V alloy and UHMWPE for total joint replacement application.,” *J. Appl. Biomater. Biomech.*, vol. 1, no. 3, pp. 164–16471, 2003.
- [80] F. Alonso, A. Arizaga, S. Quinton, J. J. Ugarte, J. L. Viviente, and J. I. Oñate, “Mechanical properties and structure of Ti-6Al-4V alloy implanted with different light

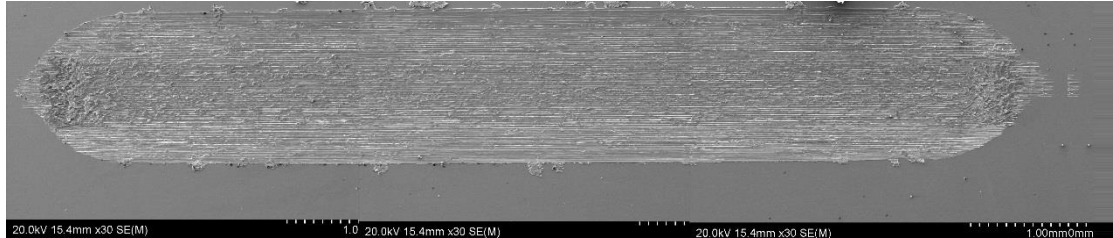
- ions,” *Surf. Coatings Technol.*, vol. 74–75, no. PART 2, pp. 986–992, 1995.
- [81] H. Ji, L. Xia, X. Ma, and Y. Sun, “Tribological performance of Ti-6Al-4V plasma-based ion implanted with nitrogen,” *Wear*, vol. 246, no. 1–2, pp. 40–45, 2000.
- [82] Y. Itoh, A. Itoh, H. Azuma, and T. Hioki, “Improving the tribological properties of Ti-6Al-4V alloy by nitrogen-ion implantation,” *Surf. Coatings Technol.*, vol. 111, no. 2–3, pp. 172–176, 1999.
- [83] H. Schmidt, A. Schminke, and D. M. Rück, “Tribological behavior of ion-implanted Ti6Al4V sliding against polymers,” *Wear*, vol. 209, no. 1–2, pp. 49–56, 1997.
- [84] A. Fabre, L. Barrallier, F. Torregrosa, and L. Roux, “Ion beam implantation and plasma immersion ion implantation. Application on nitrided Ti-6Al-4V titanium alloy,” *Microsc. Microanal. Microstruct.*, vol. 8, no. 6, pp. 413–422, 1997.
- [85] L. C. Zhang, L. Y. Chen, and L. Wang, “Surface Modification of Titanium and Titanium Alloys: Technologies, Developments, and Future Interests,” *Adv. Eng. Mater.*, vol. 22, no. 5, pp. 1–37, 2020.
- [86] P. Budzynski, A. A. Youssef, and J. Sielanko, “Surface modification of Ti-6Al-4V alloy by nitrogen ion implantation,” *Wear*, vol. 261, no. 11–12, pp. 1271–1276, 2006.
- [87] M. Kaminski, P. Budzynski, M. Wiertel, and A. Drozdziel, “Use of nitrogen ion implantation for modification of the tribological properties of titanium alloy Ti6Al4V,” *IOP Conf. Ser. Mater. Sci. Eng.*, vol. 421, no. 3, 2018.
- [88] S. Fukumoto, H. Tsubakino, S. Inoue, L. Liu, M. Terasawa, and T. Mitamura, “Surface modification of titanium by nitrogen ion implantation,” *Mater. Sci. Eng. A*, vol. 263, no. 2, pp. 205–209, 1999.
- [89] Y. Dai, C. Zhang, J. Luo, Y. Yang, and Y. Wang, “Friction and wear performance of titanium alloy against tungsten carbide lubricated with phosphate ester,” *Tribol. Int.*, vol.

95, pp. 27–34, 2015.

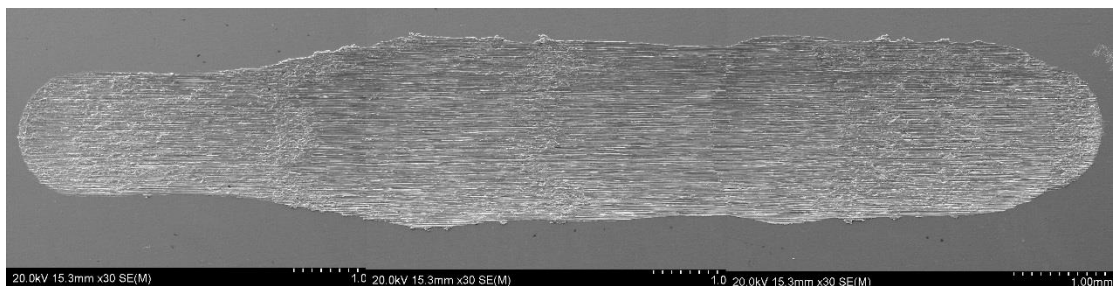
- [90] Y. Yang, C. Zhang, Y. Dai, and J. Luo, “Tribological properties of titanium alloys under lubrication of SEE oil and aqueous solutions,” *Tribol. Int.*, vol. 109, no. November 2016, pp. 40–47, 2017.
- [91] K. Kato and K. Adachi, “Wear mechanisms,” In: B. Bhushan, Chapter 7 in *Modern Tribology Handbook, Volume 1: Principles of Tribology*: CRC Press, 2001.
- [92] Q. Zhao, G. Wu, and W. Sha, “Deformation of titanium alloy Ti-6Al-4V under dynamic compression,” *Comput. Mater. Sci.*, vol. 50, no. 2, pp. 516–526, 2010.
- [93] Y. C. Chim, X. Z. Ding, X. T. Zeng, and S. Zhang, “Oxidation resistance of TiN, CrN, TiAlN and CrAlN coatings deposited by lateral rotating cathode arc,” *Thin Solid Films*, vol. 517, no. 17, pp. 4845–4849, 2009.

Appendix

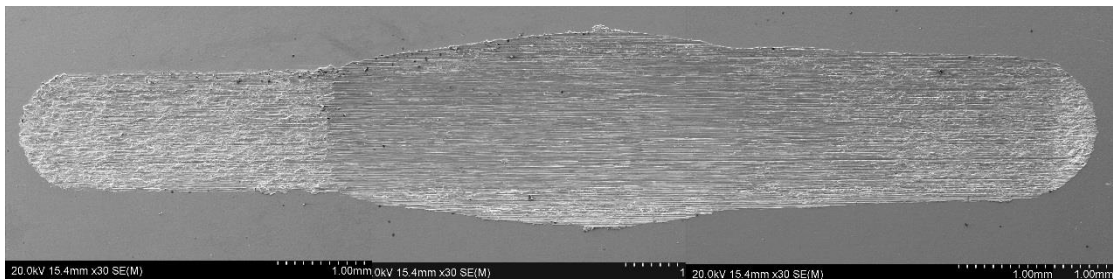
Appendix 1 Whole wear tracks from top view



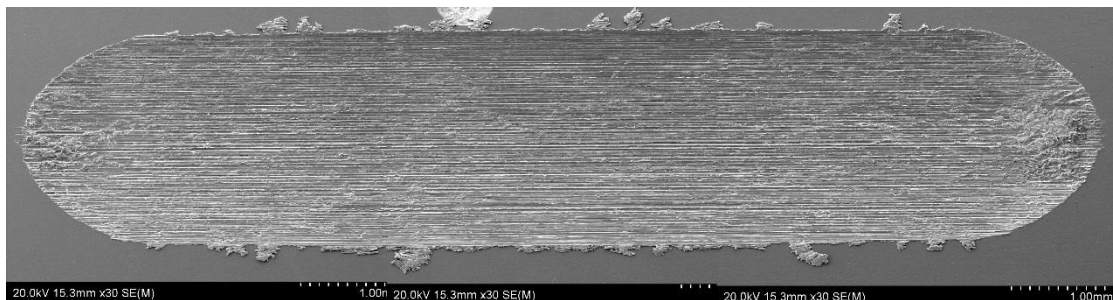
TR_m-CP-2N-2Hz



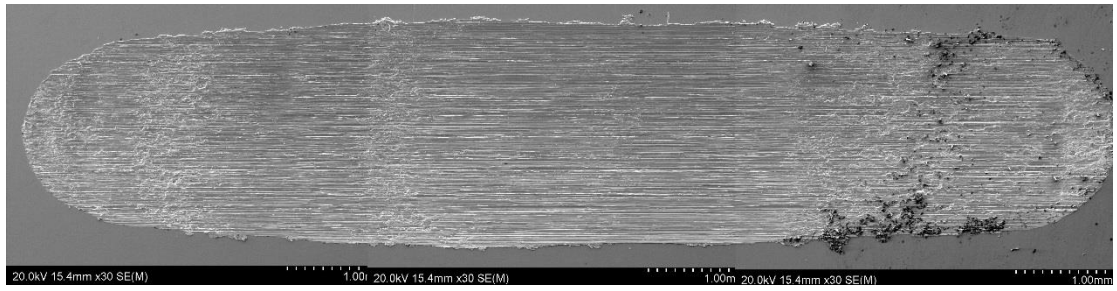
TR_m-CP-2N-5Hz



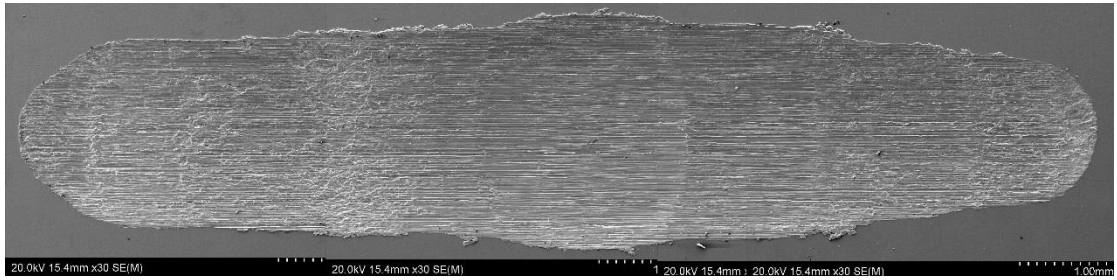
TR_m-CP-2N-8Hz



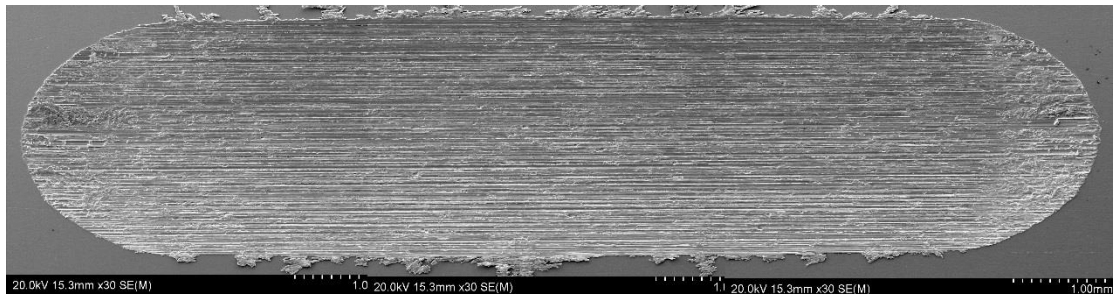
TR_m-CP-6N-2Hz



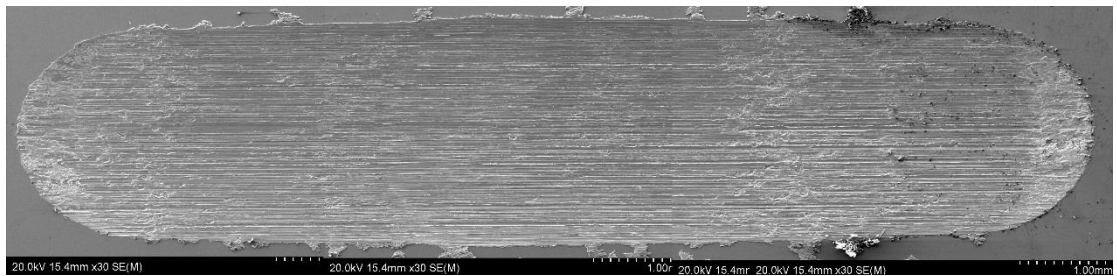
$T_{Rm-CP-6N-5Hz}$



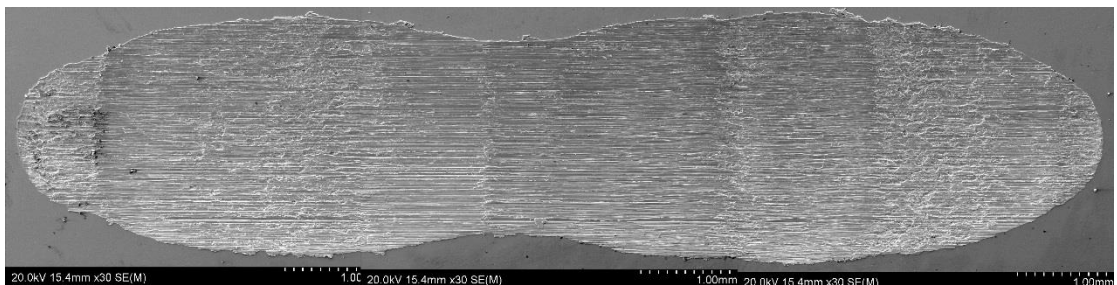
$T_{Rm-CP-6N-8Hz}$



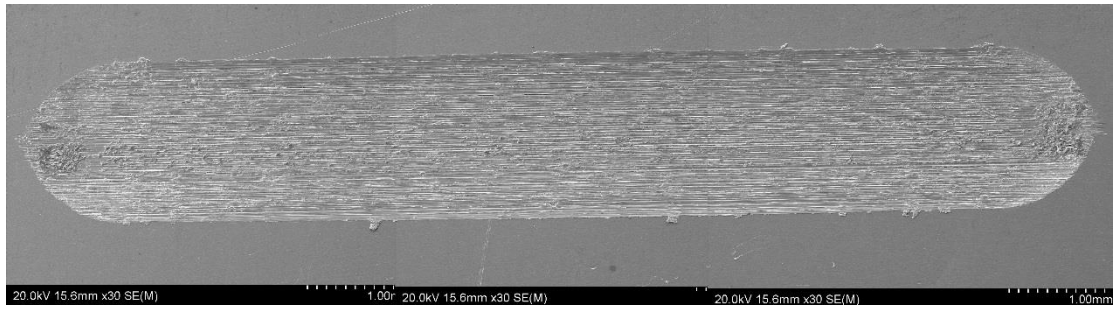
$T_{Rm-CP-10N-2Hz}$



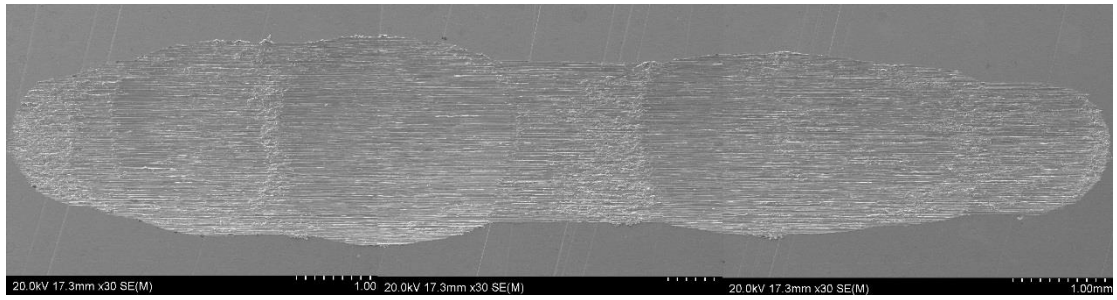
$T_{Rm-CP-10N-5Hz}$



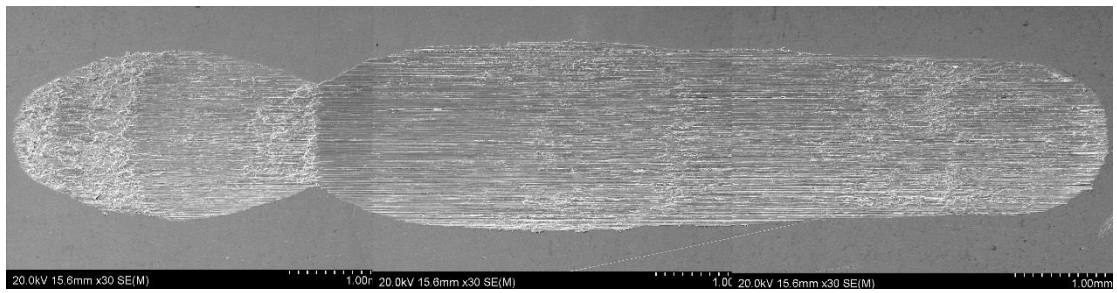
$T_{Rm-CP-10N-8Hz}$



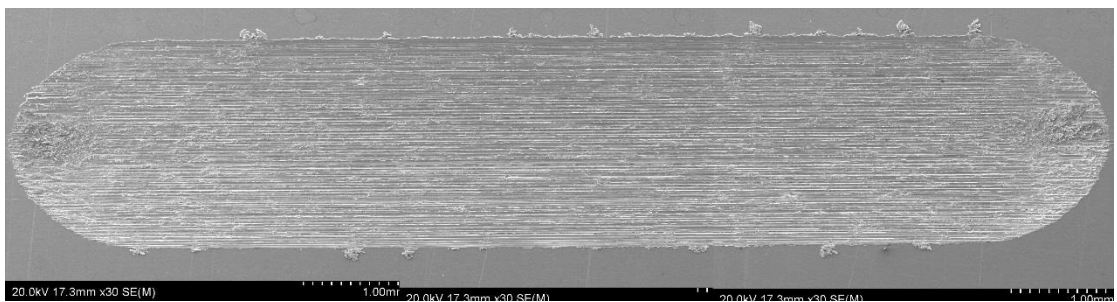
T_{Rm} -EBM-2N-2Hz



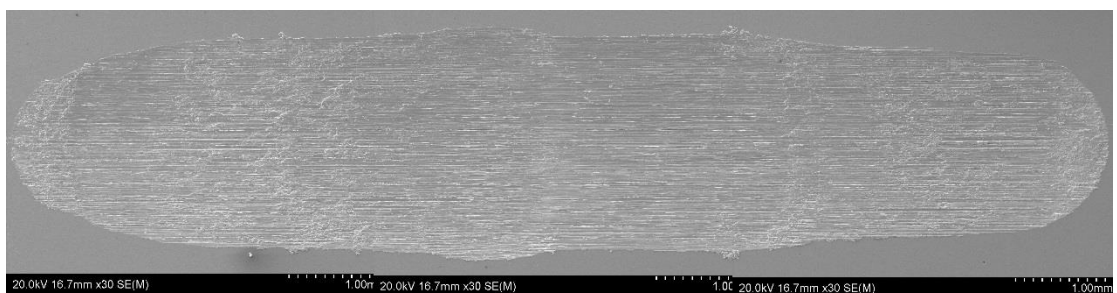
T_{Rm} -EBM-2N-5Hz



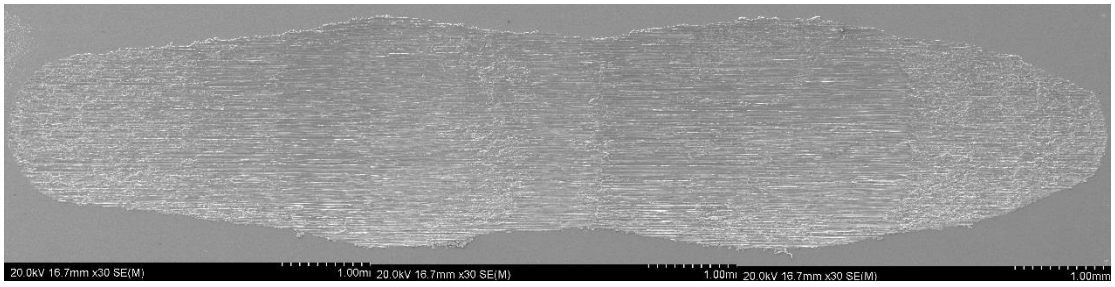
T_{Rm} -EBM-2N-8Hz



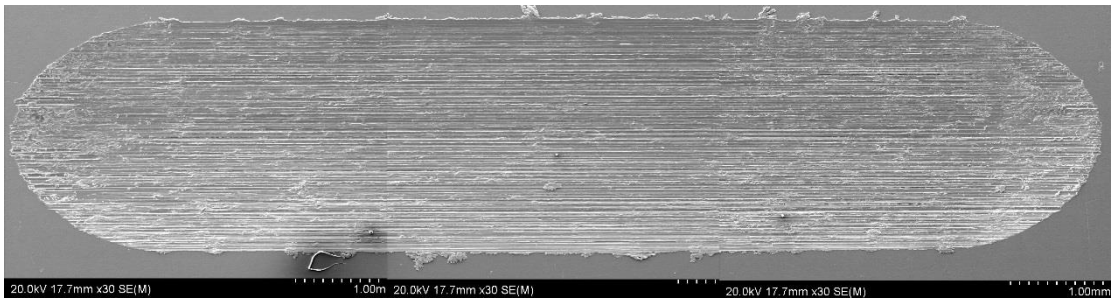
T_{Rm} -EBM-6N-2Hz



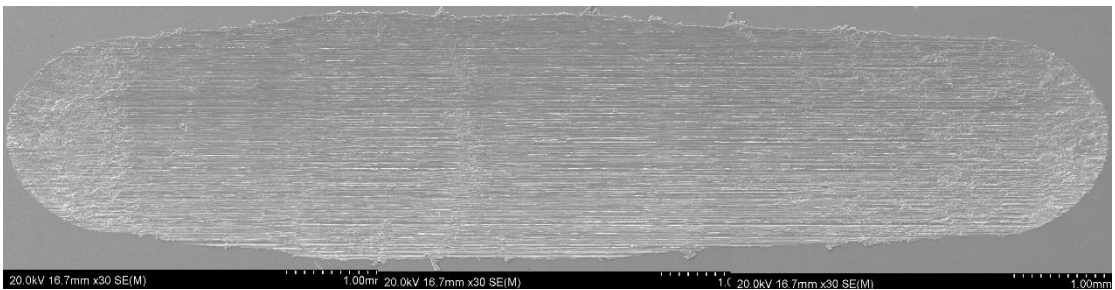
T_{Rm} -EBM-6N-5Hz



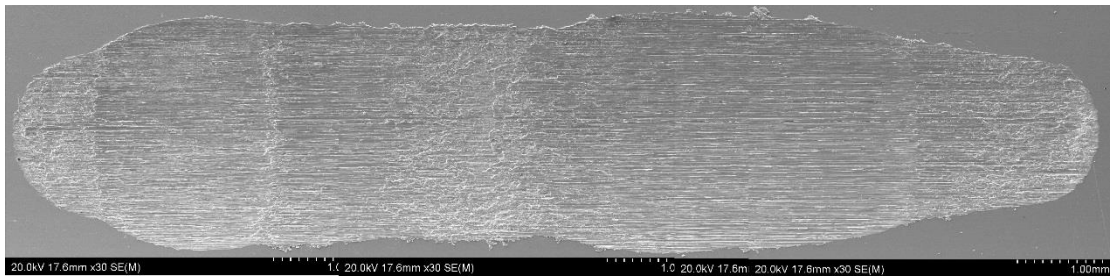
T_{Rm}-EBM-6N-8Hz



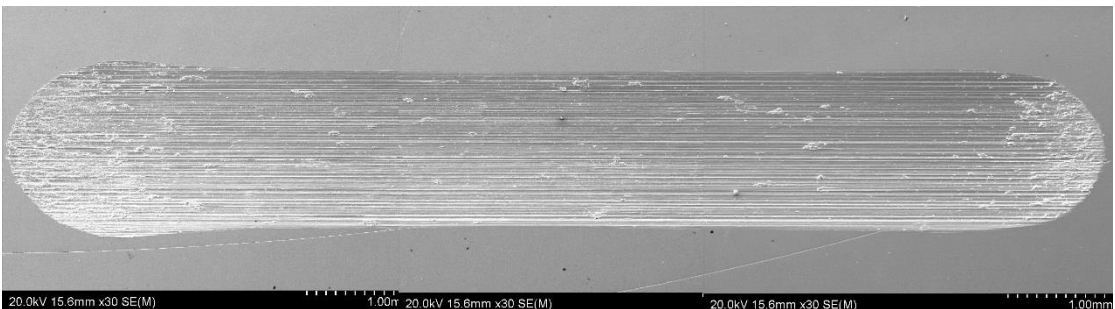
T_{Rm}-EBM-10N-2Hz



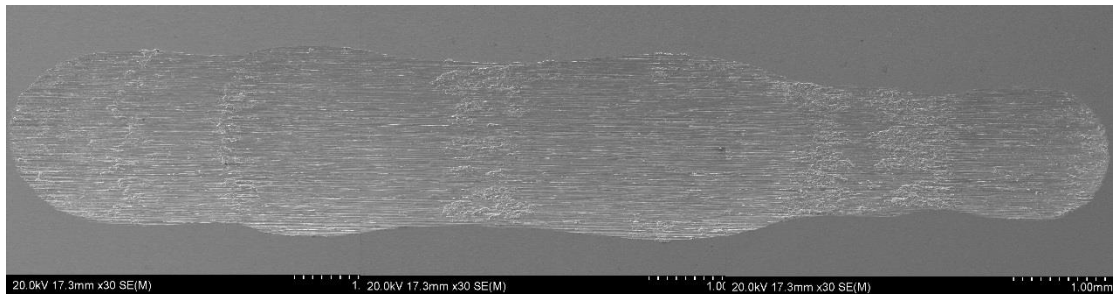
T_{Rm}-EBM-10N-5Hz



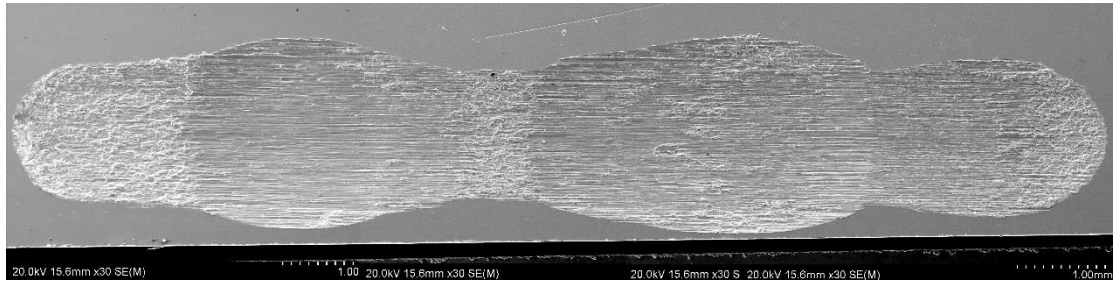
T_{Rm}-EBM-10N-8Hz



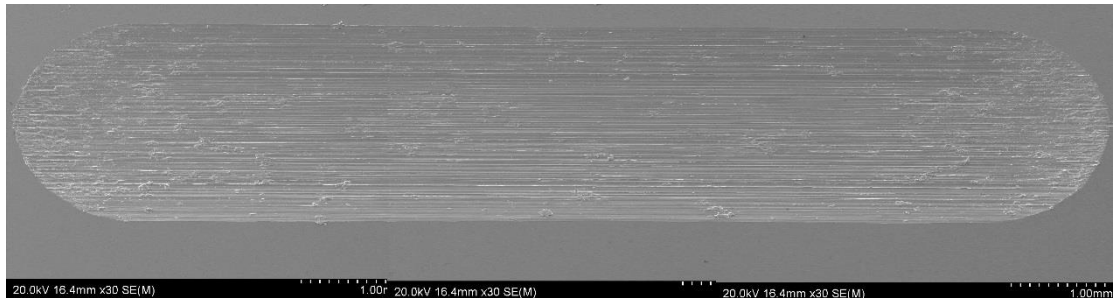
T_{Rm}-SLM-2N-2Hz



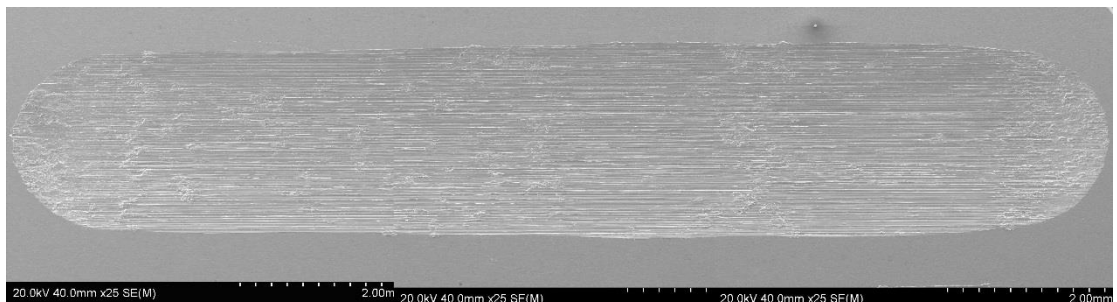
T_{Rm}-SLM-2N-5Hz



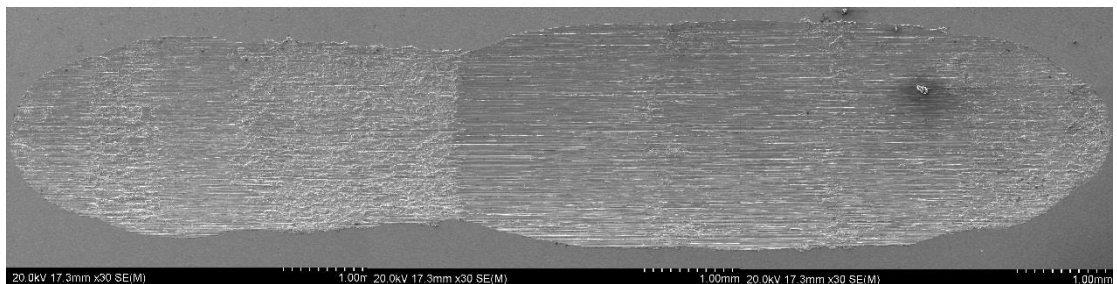
T_{Rm}-SLM-2N-8Hz



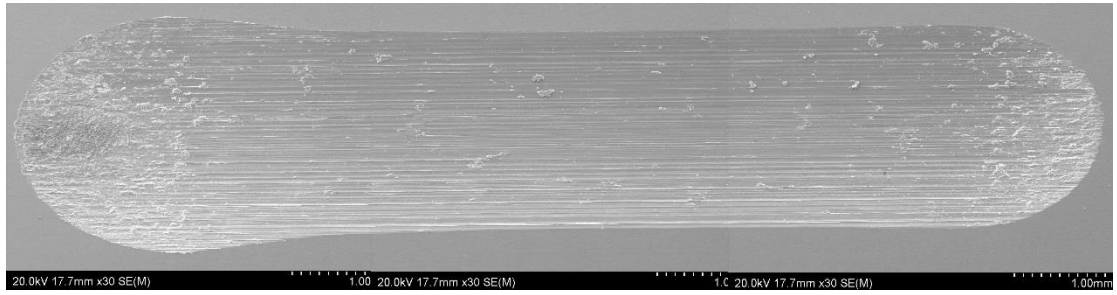
T_{Rm}-SLM-6N-2Hz



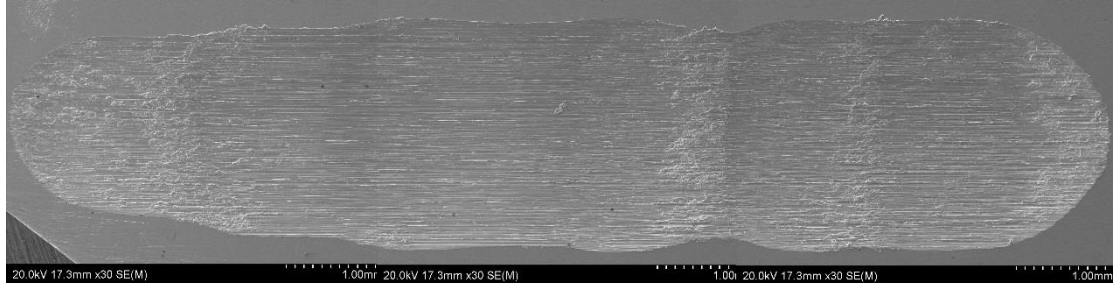
T_{Rm}-SLM-6N-5Hz



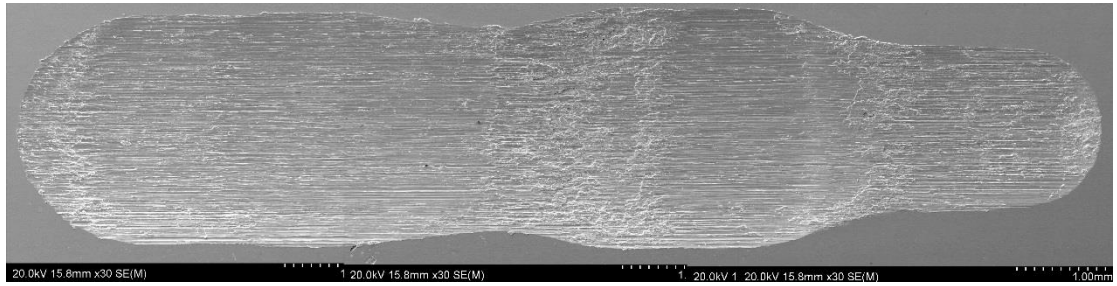
T_{Rm}-SLM-6N-8Hz



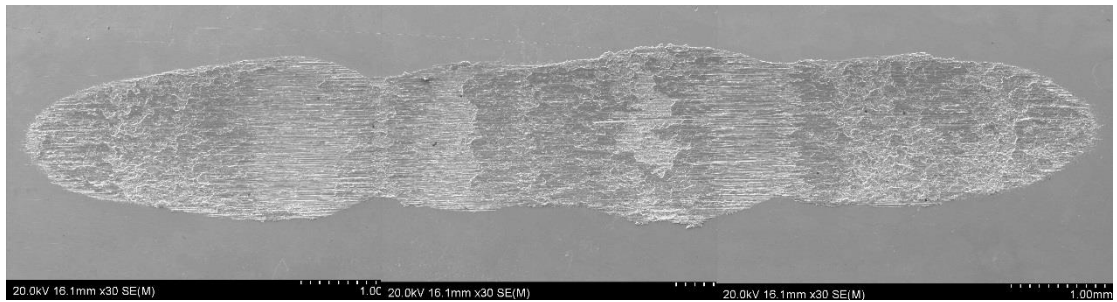
TR_m-SLM-10N-2Hz



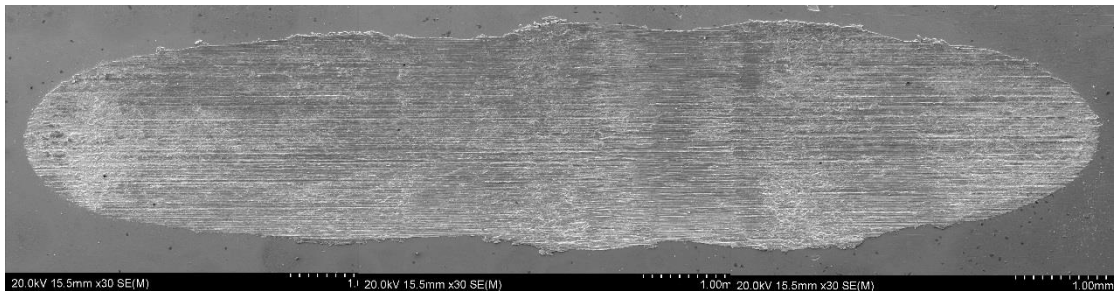
TR_m-SLM-10N-5Hz



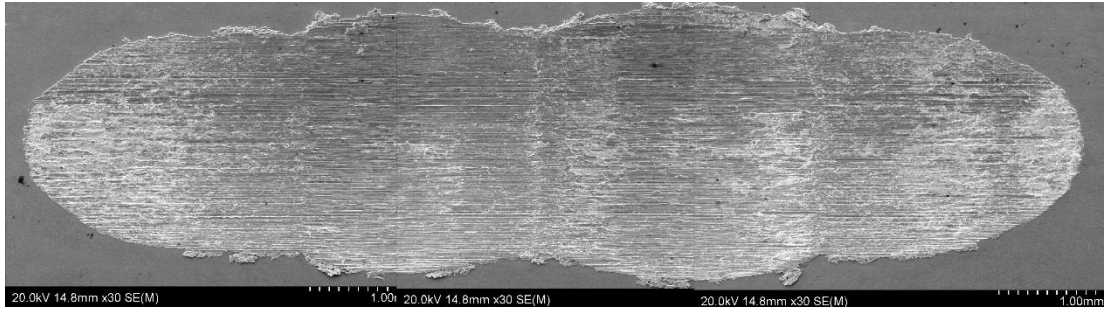
TR_m-SLM-10N-8Hz



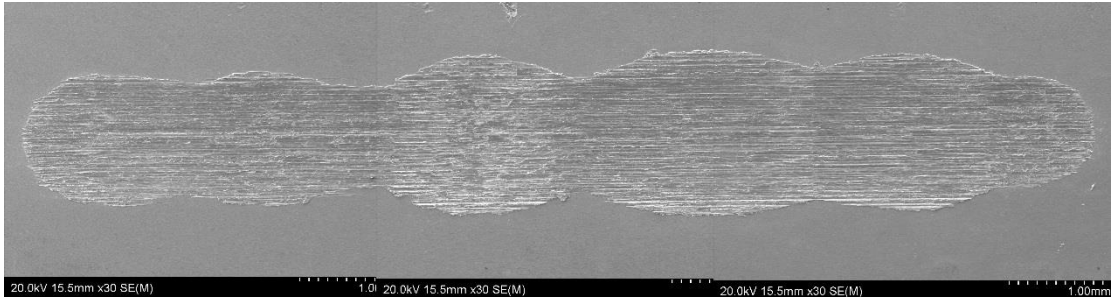
CP-200°C-2N



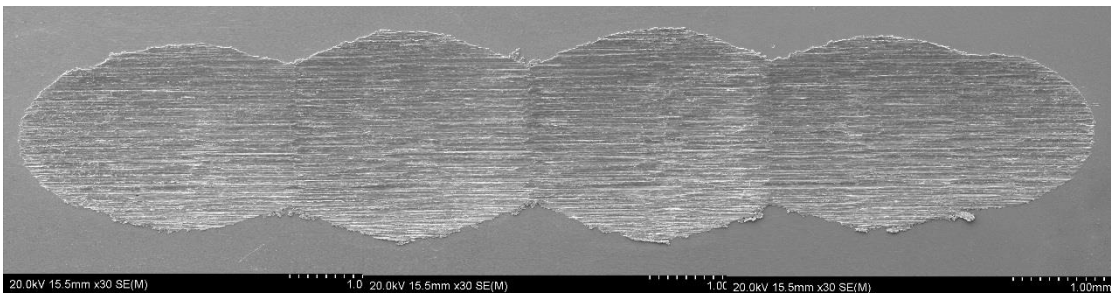
CP-200°C-6N



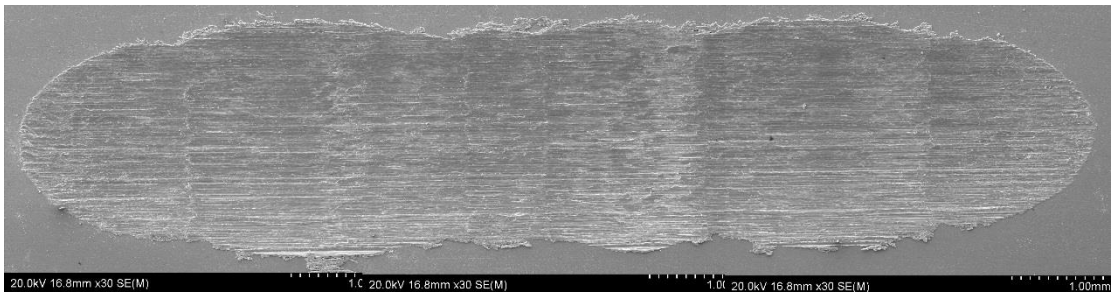
CP-200°C-10N



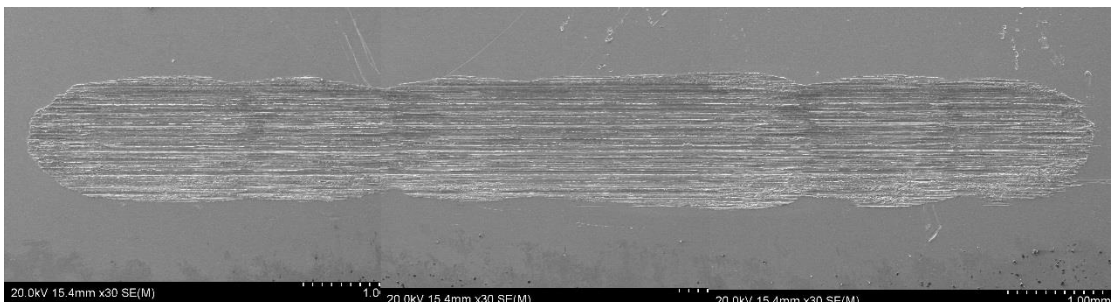
CP-400°C-2N



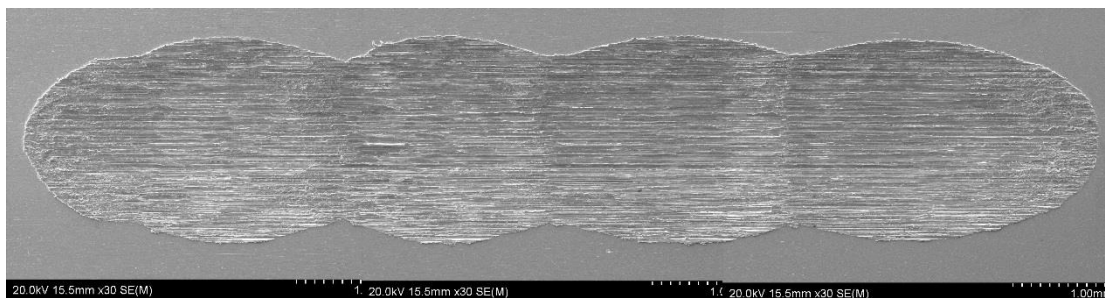
CP-400°C-6N



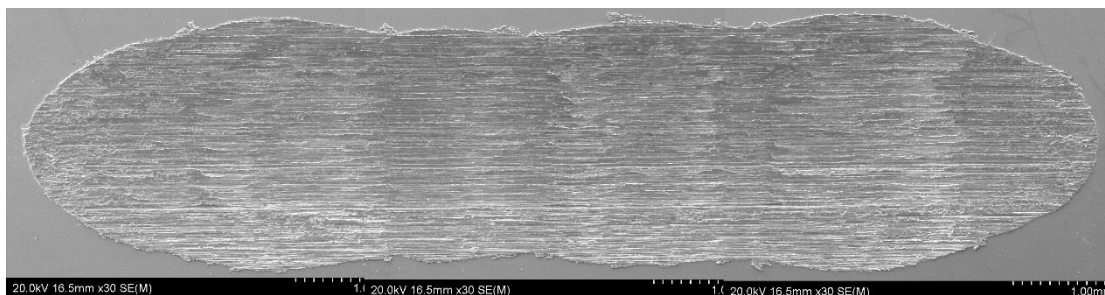
CP-400°C-10N



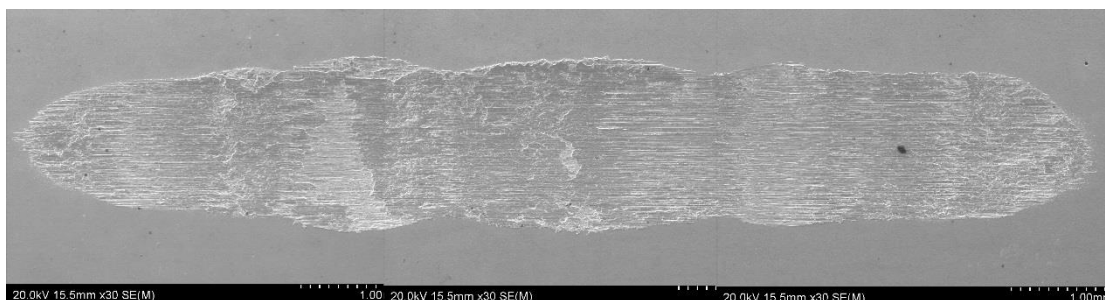
CP-600°C-2N



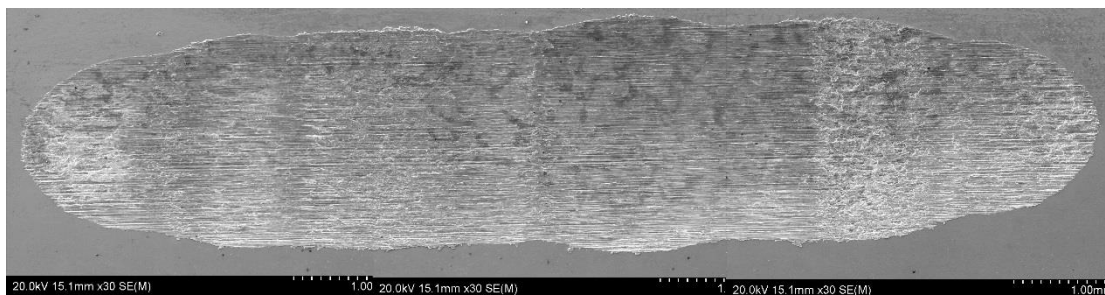
CP-600°C-6N



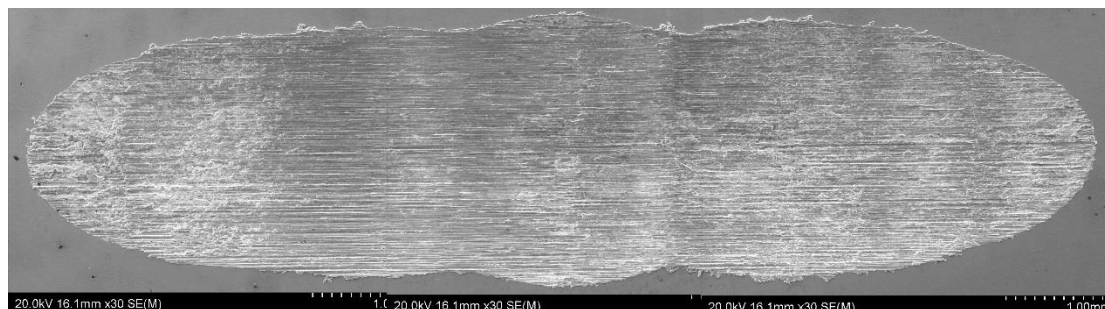
CP-600°C-10N



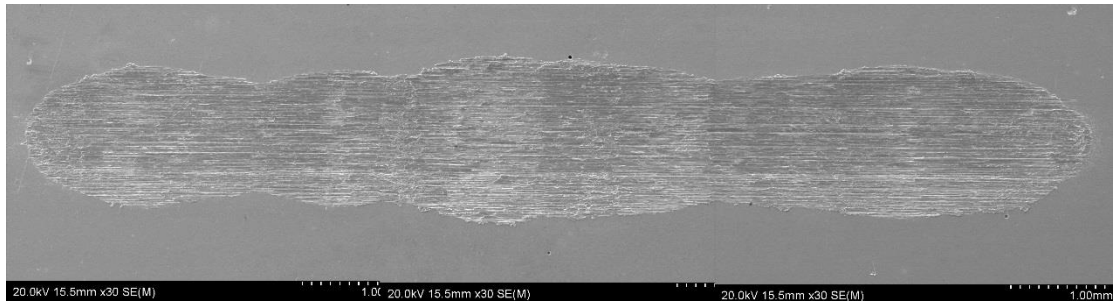
EBM-200°C-2N



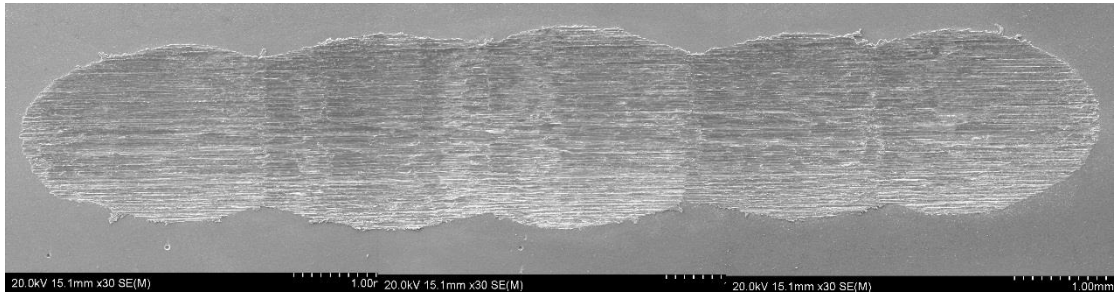
EBM-200°C-6N



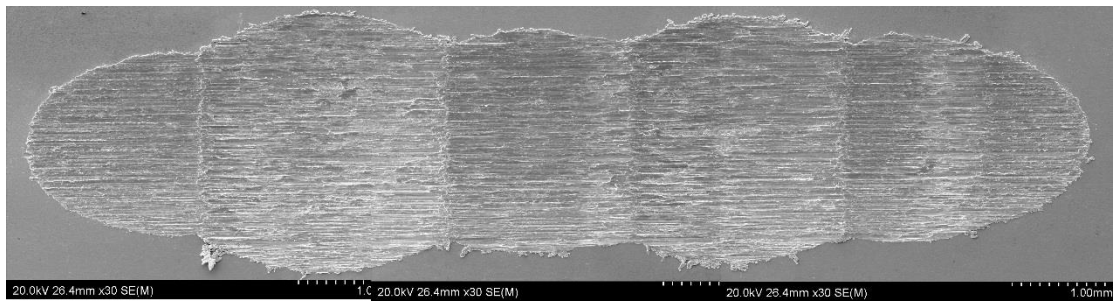
EBM-200°C-10N



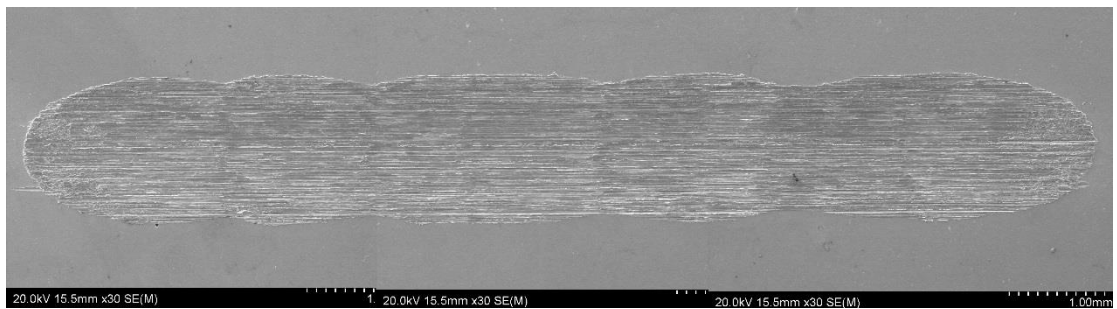
EBM-400°C-2N



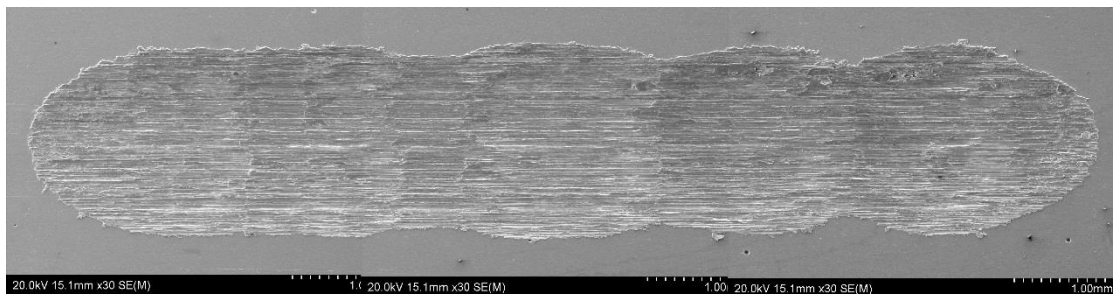
EBM-400°C-6N



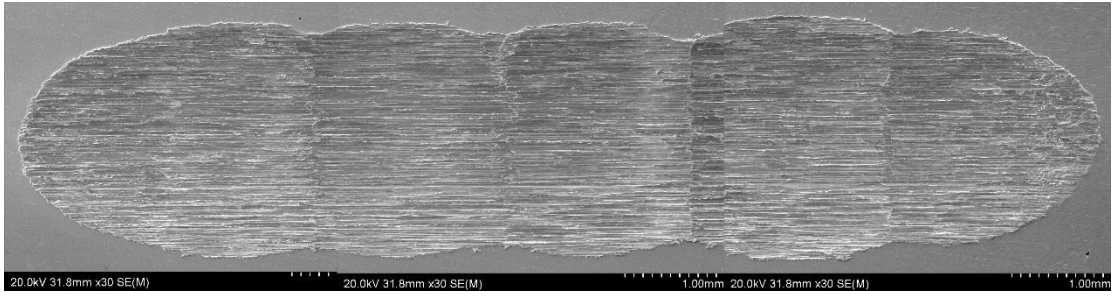
EBM-400°C-10N



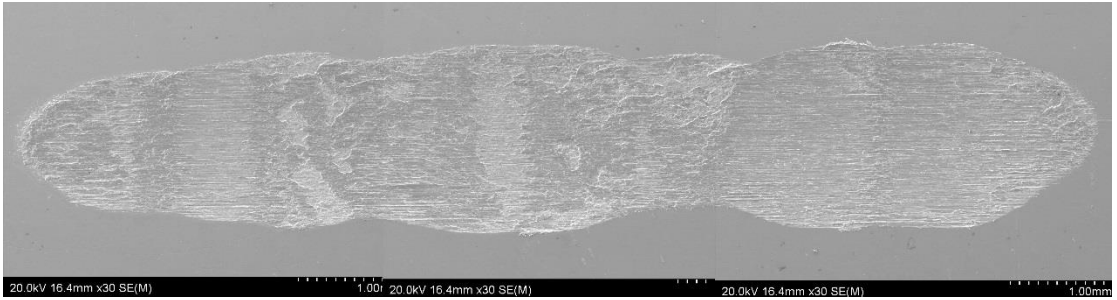
EBM-600°C-2N



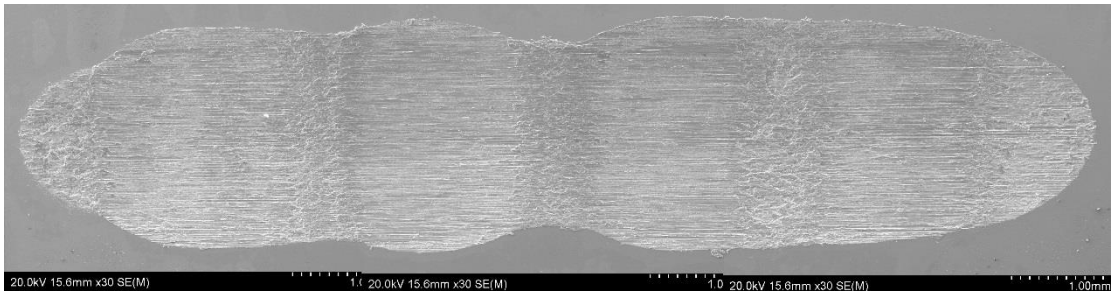
EBM-600°C-6N



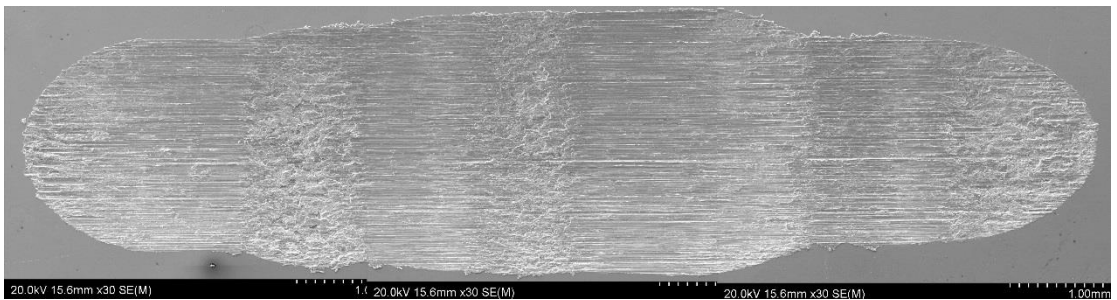
EBM-600°C-10N



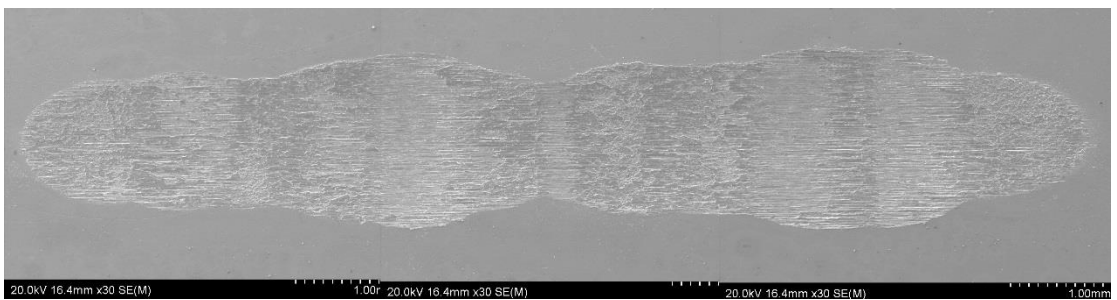
SLM-200°C-2N



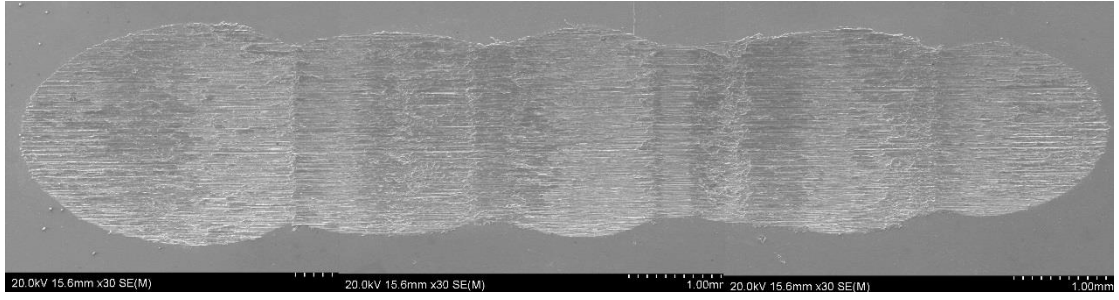
SLM-200°C-6N



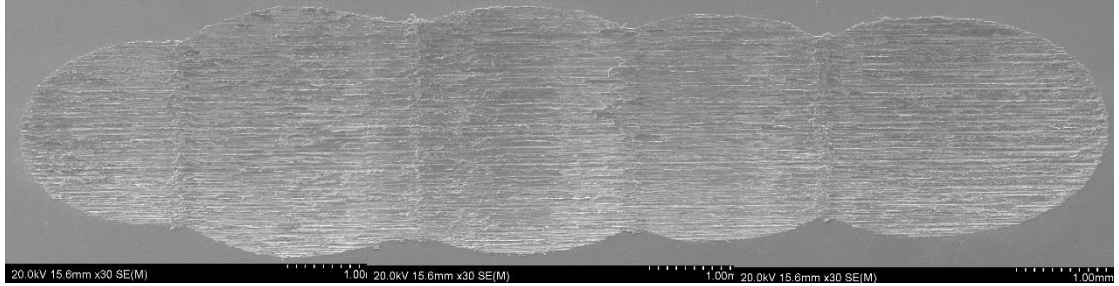
SLM-200°C-10N



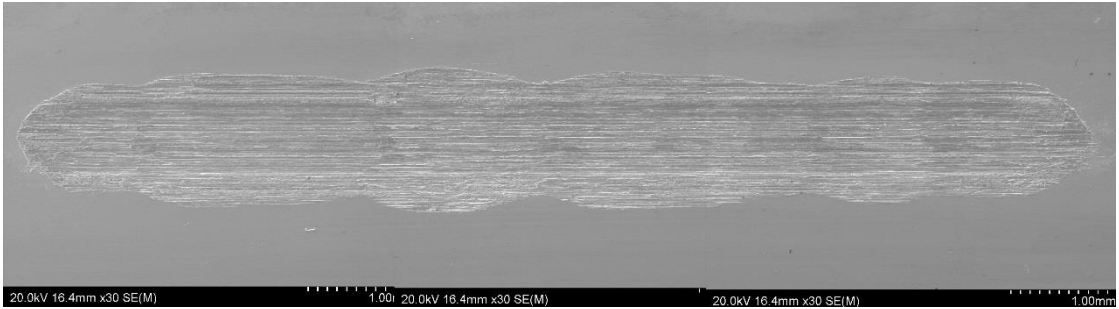
SLM-400°C-2N



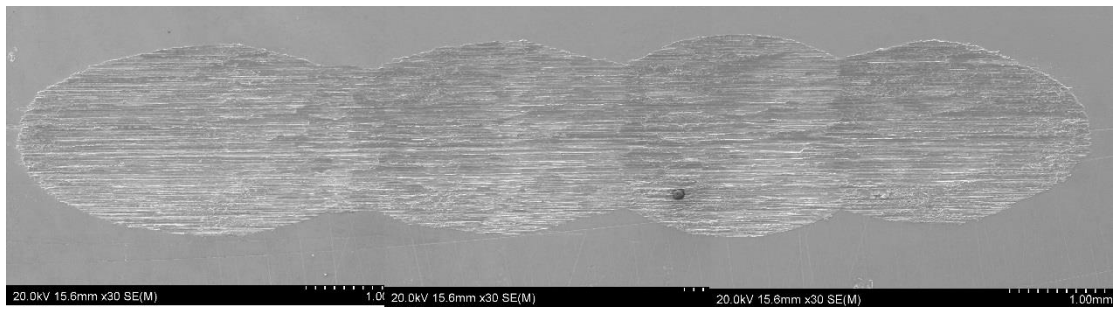
SLM-400°C-6N



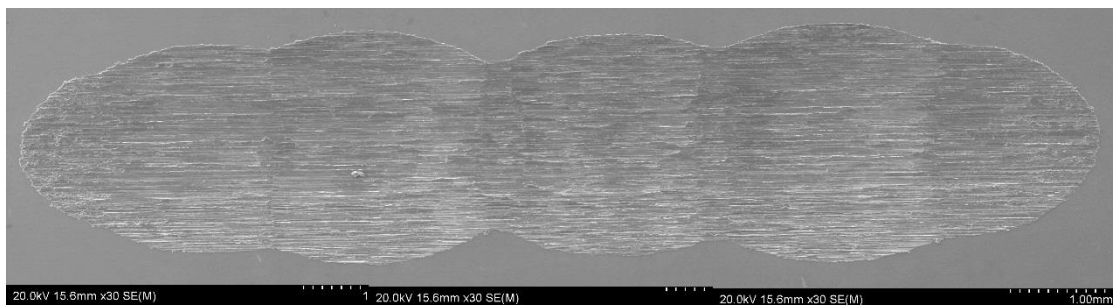
SLM-400°C-10N



SLM-600°C-2N



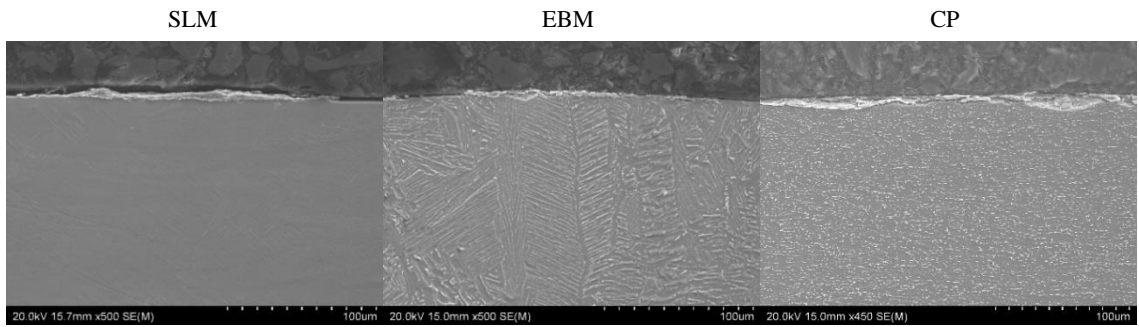
SLM-600°C-6N



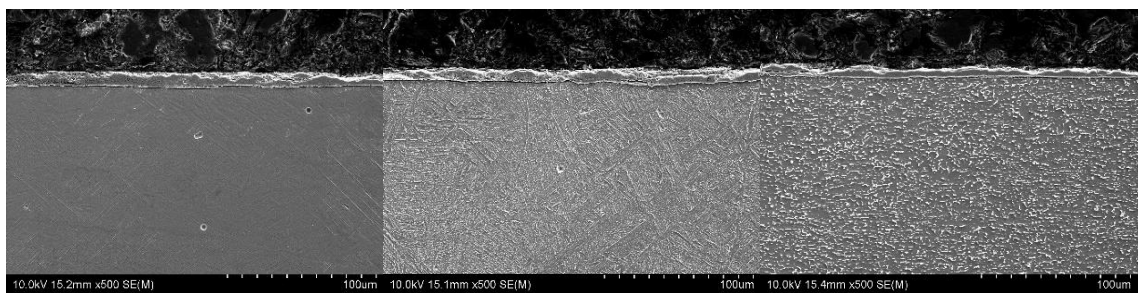
SLM-600°C-10N

Appendix 2 Cross-sections of worn tracks

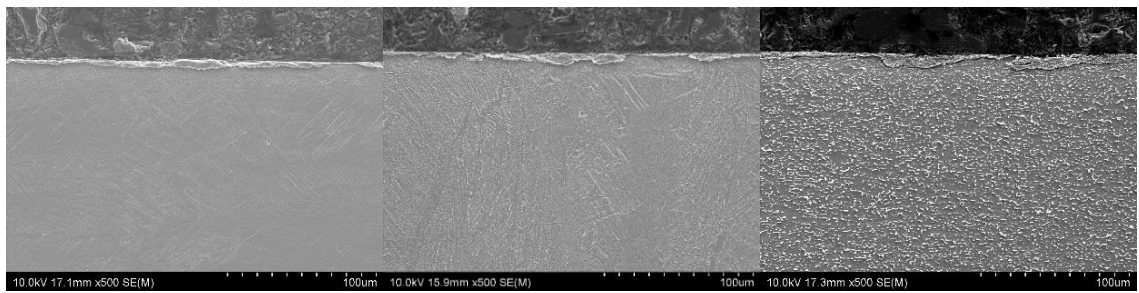
2N 5HZ



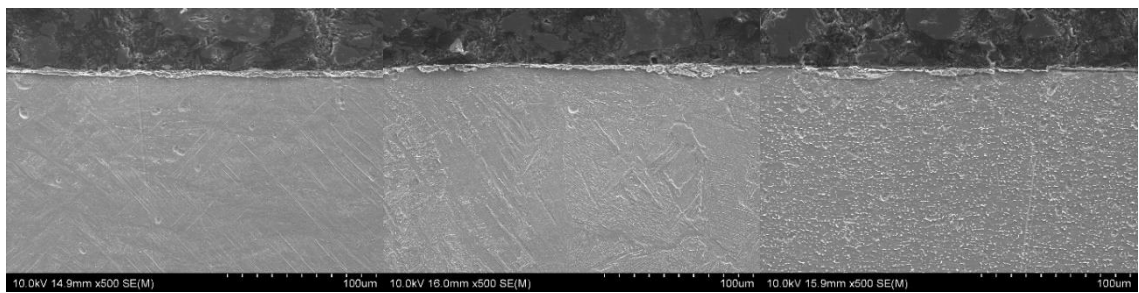
25°C



200°C

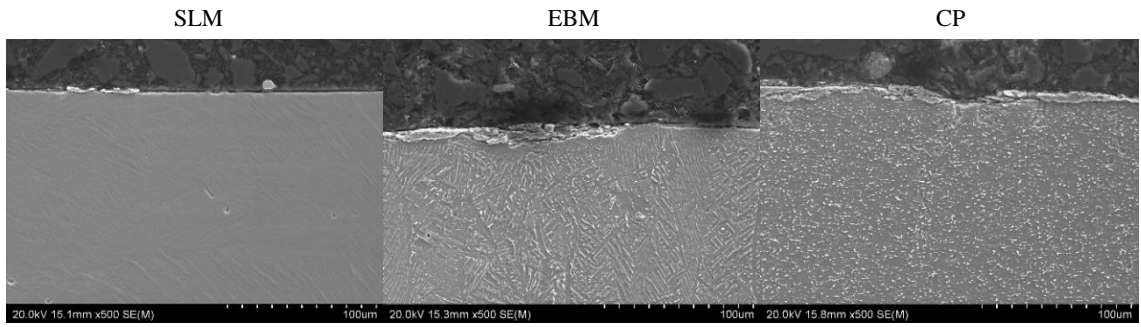


400°C

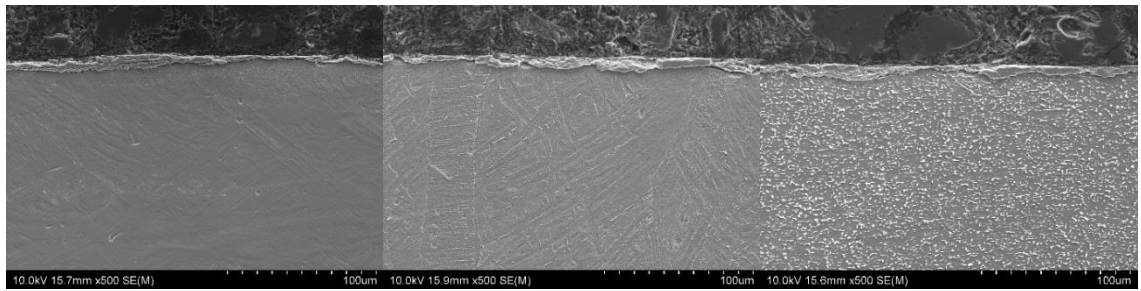


600°C

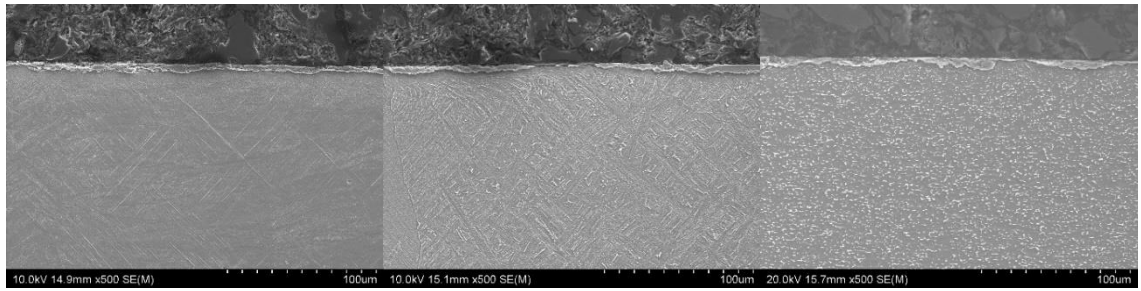
6N 5HZ



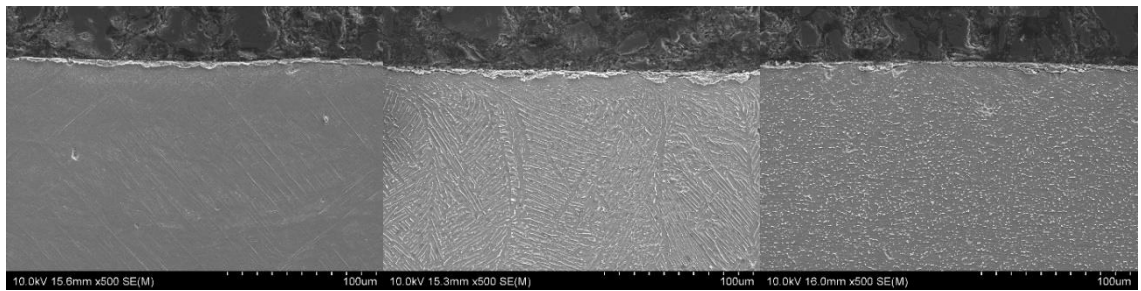
25°C



200°C



400°C



600°C

